(2)

STUDY ON MICROSTRUCTURE CONTROL AND CRITICAL CURRENT DENSITY OF SUPERCONDUCTING MATERIALS

SANG-SOO OH

KYOTO UNIVERSITY
1992

STUDY ON MICROSTRUCTURE CONTROL AND CRITICAL CURRENT DENSITY OF SUPERCONDUCTING MATERIALS

Submitted in Partial Fulfillment of the
Requirement for the Degree of
Doctor of Engineering
in Department of Metallurgy
Kyoto University
1992

by
SANG-SOO OH

Preface

In the present thesis, I reported the results of my studies on the microstructure control and critical current density of superconducting materials, which have been carried out under the supervision of Professor Kozo Osamura at the Department of Metallurgy in Kyoto University during April, 1987 ~ March, 1992. During the years I spent in my studying, I received many valuable advice, warmest encouragement and guidance from many people. I wish to express my sincere gratitude to all those who contributed in various ways for the completion of this thesis.

I am very grateful to Professor Kozo Osamura of Kyoto University for his hearty support with generous humanity and his constant encouragement have been invaluable these past years. I think this work would have not been possible if without his warm-hearted support. Thanks to his help in various ways, I spent truly fruitful years in Kyoto university.

I wish to express my sincere gratitude to Professors Masaharu Yamaguchi and Masayuki Siga of Kyoto University for their helpful discussions and suggestions during reviewing this thesis. I wish to thank Associate Professor Shojiro Ochiai and Dr. Hiroshi Okuda of Kyoto University for their enthusiastic discussions and advice.

I also wish to thank Messrs. T. Unezaki and I. Nakagawa for their helpful technical assistance on EPMA and SEM.

I wish to express my gratitude to Dr. K. Watanabe, K. Kudo, K. Sai and Y. Ishikawa at Tohoku University for their help in the critical current measurements. I am grateful to all the members of Professor Osamura's research group, especially Messrs. S. Yoshida, M. Kamo and T. Kubota for their support and discussions.

I am gratified to express my deepest appreciation to Professor Hyun–Kee Cho, Kyungpook National University, for making it possible to study abroad and for giving affectionate advice and for continual encouragement to finish this study. I wish to thank for their financial support of the Ministry of Education, Science and Culture, Japan, during my stay in Japan. Finally, I would like to thank to my parents and lovely wife for their love, support, persistent patience, and well-understanding during the years it took to complete this dissertation.

Sang–Soo Oh

Kyoto, Japan
March 1992

Contents

Chapter 1

General introduction

1.1 History of superconducting materials

1.1.1 Metallic superconductors

In 1911, three years after the success in liquefaction of helium(1908), Kamerlingh Onnes observed [1] that the electrical resistivity of solid Hg suddenly dropped to zero when it was cooled below about 4.2 K. This startling discovery was recorded as the origin of development of superconductor. According to this discovery, it was made clear that a superconductor exhibits infinite conductivity ($1/R = \infty$), which is most important property of superconductor. As shown in figure 1.1, superconductivity only occurs in the region below the critical surface constructing from three parameters, critical current (I_c), critical transition temperature (T_c) and critical magnetic field (H_c). The history in development of superconductors has been carried out by the efforts to improve three parameters of superconducting state. After discovery of superconductivity, numerous superconducting materials have been discovered in metallic system and the study to make clear the mechanism of superconductivity has continuously progressed.

In 1933, Meissner and Ochsenfeld [2] found that a bulk specimen in superconducting state exhibits the perfect diamagnetism, with the magnetic induction $B = 0$. This has been called Missener effect and recognized to be very important as characteristic magnetic property of superconductor. Hardy *et al.* [3] first discovered superconductivity in A15 type intermetallic compound, V_3Si in 1953. According to this discovery, the study to search

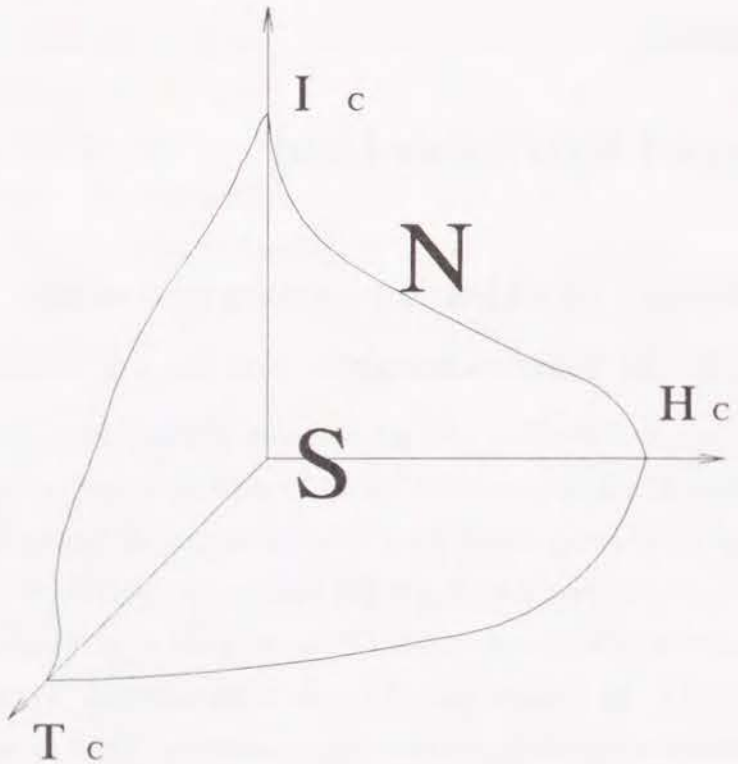

Figure 1.1 Superconducting state region which is defined by three critical parameters.

for new superconductor in A15 type compounds or alloys had started and the existence of type II superconductor, which is different from the type I superconductor in the point of critical magnetic field was made clear in 1950's. Matthias *et al.* [4] pointed out that the critical transition temperature, T_c strongly depends on the average electron valency (Z) per atom and T_c becomes high at Z = 4.7 or 6.7. Due to this Matthias's empirical rule, Nb_3Sn and V_3Ga were discovered in 1954 and 1957, respectively.

For application of the superconductor to magnet technology, Kunzler [5] first succeeded to produce a superconducting wire of Nb_3Sn compound in 1961. Here, the powder metallurgical technique was adopted for preparation of the wire. Using the magnet prepared from Nb_3Sn, 7 T as magnetic field could be generated experimentally. The period of applied superconductivity is suggested to have been started by this success. Searching for new superconductor in intermetallic compound system was progressed intensively till the appearance of Nb_3Ge, which exhibited highest T_c of 23 K in metallic systems [6]. On the other hand, in alloy system, Nb-Zr superconducting wire was prepared for selling by SUPERCON Co. in 1961. Two years after that, Nb-Ti superconducting wire which has been widely used for superconducting magnet up to date was prepared by Westinghouse. Comparing with A15 compounds, these alloy systems are excellent in working ability. It was known that the critical current density (J_c) of Nb-Ti superconductor depends on the microstructure change by composition, the degree of cold-working and the heat-treatment condition [7]. α - Ti precipitates which appear during thermomechanical treatment were known to play a important role to exhibit the strong pinning effect against the movement of flux line. The improvement in production of alloy superconducting wire has been continuously progressed by the optimization of thermomechanical treatment. Recently, the fine multi filamentary Nb-Ti superconducting wire was developed for improving A.C loss and stabilization in operating and widely used as coil in MRI,MAGLEV,SOR and Nuclear fusion reactors etc.

Comparing with the alloy superconductor like Nb-Ti, the properties of T_c and H_{c2} for intermetallic superconductors are high. However, the developments of A15 type com-

pound superconductor was late by the difficulty of working ability. In the latter part of 1960's, various kinds of production techniques for intermetallic superconducting wire such as Nb_3Sn and V_3Ga were developed earnestly and superconducting magnet could be successfully produced by using these compound superconducting materials. Recently, Nb_3Al, $PbMo_6S_8$ appeared as new intermetallic superconductors for generating high magnetic field and the production technique has been intensively studied [8,9,10]. The physical properties of typical metallic superconducting materials are listed in table 1.1

Table 1.1 Superconducting properties of typical metallic superconductors.

Materials	Critical temperature T_c(K)	Upper critical field H_{c2}(T)
Nb-Ti	~ 9	~ 12
Nb_3Sn	18.2	24
V_3Ga	16.8	21
Nb_3Ge	23.1	-
Nb_3Al	17.5	30
$PbMo_6S_8$	12.6	60

1.1.2 High temperature superconductors

The trend of superconductor developments has been largely changed by Bednortz and Mü ller's pioneering discovery [11] of Ba-La-Cu-O superconductor in 1986. The possibility of high T_c was realized first in ceramic material and the race for development of high temperature superconductor(HTSC) was opened with large scale after this great discovery. In 1987, Wu *et al.* [12] succeed to prepare the ceramic superconductor of Y-Ba-Cu-O ($T_c = 90 \sim 95$ K). The transition temperature exhibited almost the same value by substitution Y for other rare earth element such as Ce,Pr,Tb. This material has a characteristic that oxygen tend to be deficient. Therefore, the supplement of oxygen into specimen during heat treatment is necessary. Since the discovery of Y-Ba-Cu-O superconductor, many

scientists searched for other materials with tetragonal crystal structures containing CuO chains or CuO_2 planes.

In 1988, Maeda *et al.* [13] discovered Bi-Sr-Ca-Cu-O (BSCCO) superconductor which is consisted of high T_c (110 K) and low T_c (85 K) phase. The low T_c phase and the high T_c phase can be expressed by general chemical formula $Bi_2Sr_2Ca_{n-1}Cu_nO_x(x = 2n + 4 + \delta)$ with n = 2 and 3, respectively. Figure 1.2 shows the ideal structure of BSCCO oxides with n = 1,2 and 3. These crystal structures are similar each other, differing only in the number of $Ca - CuO_2$ slabs inserted between double Bi-O layers. The low T_c phase has two CuO_2 layers and one Ca layer while the high T_c phase has three CuO_2 and two Ca layers. It was known that T_c increases with increasing n up to 3. Takano *et al.* reported [14] that the formation of high T_c phase is enhanced by the Pb addition. Encouraged by the discovery of BSCCO, Tl-Ba-Ca-Cu-O superconductor was newly found by the efforts of Sheng *et al.* [15]. T_c of $Tl_2Ba_2Ca_2Cu_3O_{10+x}$ is recorded to 125 ~130 K as the best data in cuprate HTSCs. The crystal structure of Tl-based cuprate superconductors are very similar with BSCCO. They also have three kinds of crystal structure based on the number of CuO_2 and Ca layer. In cuprate HTSCs, superconductivity was recognized to occur in the CuO_2 lattice involved in perovskite type block and sensitively depends on the number of CuO_2 planes.

1.2 Superconducting properties

For the superconductors, a critical transition temperature, T_c, is defined below which the electrical resistivity goes to zero. When a material is held at temperatures lower than T_c, a small fraction of conduction electrons with energies at or close to the Fermi level, enter an ordered state involving pairs of correlated electrons, which are called Cooper pairs and all of them behave as one macro–quantum with the same energy and momentum state and then superconducting state becomes to be realized. At the critical transition temperature T_c, the thermal energy becomes strong enough to destroy the ordering of electron pairs and a material whose temperature is above T_c is said to be in normal state.

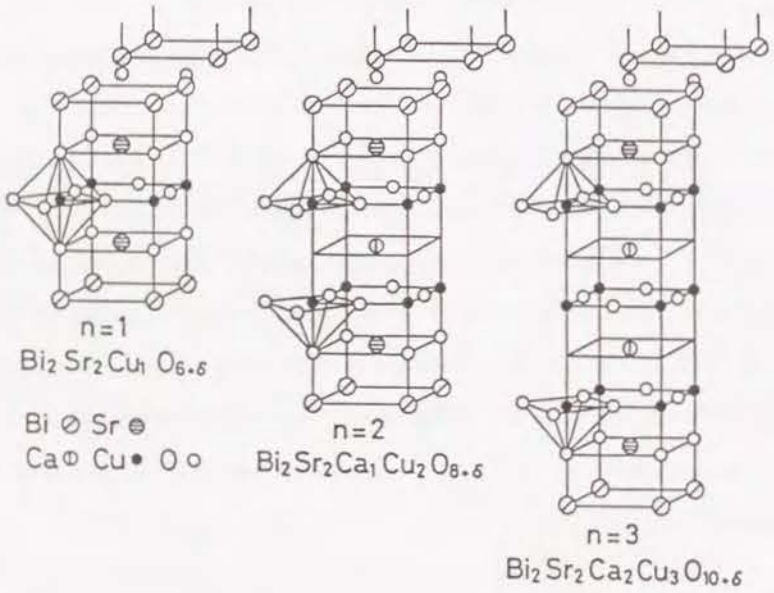

Figure 1.2 Ideal crystal structures of $Bi_2Sr_2Ca_{n-1}Cu_nO_{2n+4+\delta}$.

T_c of alloy and elements has been known [16] to be expressed as a function of electron density at Fermi level, Debye temperature and electron–lattice interaction. Additionally, the microstructure and purity of superconductor are the most important factors that determine the sharpness of the transition. Superconductivity can also be destroyed by increasing the magnetic field above a critical value. Under applied magnetic field, superconductors exhibit two types of behavior as shown in figure 1.3. Type I superconductor exhibits the complete Meissner effect and the superconductivity is destroyed when the specimen becomes normal conductor above the thermodynamic critical magnetic field H_c. Generally, H_c is known to be very low. In the case of Type II superconductor, the quantized flux penetrate the specimen and form flux line lattice (FLL) [17] above the lower critical magnetic field, H_{c1} lower than the H_c. The specimen is in a mixed state (vortex state) between H_{c1} and upper magnetic field H_{c2}, and it has superconducting electrical properties up to H_{c2}. Above H_{c2} the specimen became a normal conductor. Usually, alloys and transition metals tend to be Type II superconductor and they are characterized by a high critical magnetic field and a high critical current density, compared to the Type I superconductor. Considering the application of Type II superconducting materials into magnet, critical current density, J_c is most important property. J_c of Type II superconductor is associated with critical temperature and magnetic field and sensitively affected by microstructure. J_c in magnetic fields is mainly determined by pinning property of the superconducting material. As shown in figure 1.4, Lorentz force acts on flux line lattice(FLL) when a current flows through superconductor along a direction normal to an applied magnetic field in a mixed state and the voltage occurs due to movement of flux line. However, real superconductors contain crystal imperfections such as dislocations as well as other types of inhomogenities such as surfaces, second-phase precipitates,etc. FLL tend to have preferred arrangements with respect to inhomogenities in material and finite force is required to move FLL from their preferred location. The force which opposes motion is referred to as *pinning force*. The presence of pinning force implies that the Lorentz force must exceed a critical value before flux motion will occur.

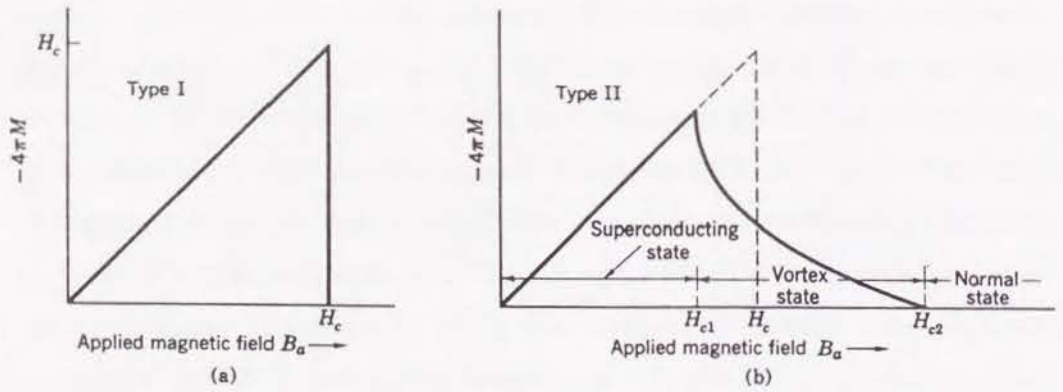

Figure 1.3 Magnetization vs applied magnetic field for two types of superconductors.

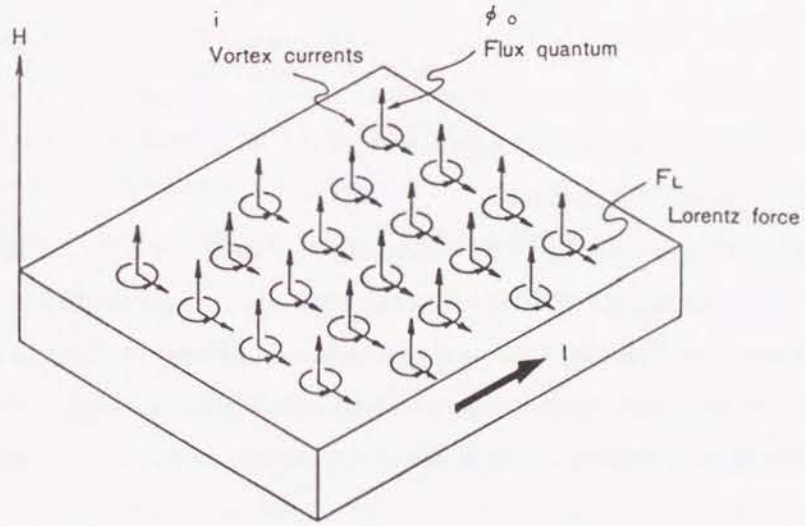

Figure 1.4 Illustration of the Lorentz force F_L in the presence of a flowing current for Type II superconductor.

The pinning force per unit volume, global pinning force density is expressed [18] by

$$F_p = J_c \times B \tag{1.1}$$

The superconductors can carry a finite loss–free current before the occurrence of dissipative loss by FLL flow.

1.3 Purposes of this study

In the application of superconducting materials, the improvement of critical current density, J_c in magnetic fields is indispensable. In the case of Type II superconducting materials, J_c depends on the it's microstructure and it can be controlled by the various factors such as heat treatment conditions, cold workings, addition of other elements in preparing the superconducting materials.

Even though, A15 type compound superconducting materials such as Nb_3Sn and V_3Ga are practically used in magnet coil, some ambiguities had remained about the field dependence of J_c. It was known that the V_3Ga compound exhibits different magnetic properties as comparing with the Nb_3Sn. In the meaning of improvement of J_c in magnetic field, the correlation between field dependence of J_c and microstructure of compound is necessary to make clear.

For producing superconducting wire such as Nb_3Sn and V_3Ga, bronze method is practically used. In Chapter 2, the mechanism of crystal growth and superconducting properties of bronze processed V_3Ga compound as well as the influence of third element additions have been investigated. For various V_3Ga compound specimens prepared with addition of Zr or Mg and without addition, the microstructure change by heat treatment and it's influence to critical current density, especially in magnetic field was investigated in Chapter 2.

Since the discovery of Bi-(Pb)-Sr-Ca-Cu-O(BPSCCO) high temperature superconductor, many efforts have been carried out to prepare the high quality material. Among various technologies to prepare BPSCCO, *melt-quenching-method* which was first tried

by Komatsu is very convenient to obtain dense material. Superconducting phase is obtained by annealing of amorphous B(P)SCCO ceramics formed during melt–quenching process. In Chapter 3, crystallization process and microstructure change as well as superconducting properties of melt–quenching processed B(P)SCCO were investigated.

Because of multi component system, polycrystalline BPSCCO material which is consisted of superconducting phases and impurity phases is obtained during sintering. It was known that the superconducting properties sensitively depends on morphology of impurity phases and volume fraction of superconducting phase. In Chapter 4, phase relation of BPSCCO appeared at various temperature ranges and behavior of formation and growth for high T_c phase were investigated in detail.

B(P)SCCO high temperature superconductor is most attractive material in the field of superconducting wire because the critical current density has been improved continuously up to date by the optimization of preparation condition.

Recently, research and developments for B(P)SCCO superconducting coil have been widely carried out. Among various production techniques for superconducting wires of HTSC, "powder–in–tube technique" has been recognized as most powerful means because microstructure control is possible by optimizing TMT conditions. Furthermore, this technique has been considered to be advantageous for processing the brittle superconducting ceramics by adopting Ag which is superior in ductility and thermal stability. In Chapter 5 $\sim$ 8, the studies were concerned with mainly microstructure control and critical current density of Ag sheathed BPSCCO tapes prepared by "powder–in–tube technique" In Chapter 5, microstructure controlling factors such as heat treatment temperature and cooling rate were changed in TMT process for producing Ag sheathed BPSCCO tapes and it's relation to critical current density was investigated. In Chapter 6, macro and microstructure change for the Ag sheathed BPSCCO tapes prepared with various cold working conditions and the relation between work instability and critical current density was investigated. Also, magnetic field dependence of J_c and I - V characteristic were investigated in detail. In Chapter 7, microstructure change appeared by changing nominal

composition and it's influence to critical current density were investigated. In Chapter 8, microstructure change by addition of other elements, Sn, Ba and Mg and its influence to superconducting properties, especially magnetic field dependence of J_c were studied.

References

1. H. Kamerlingh Onnes : Commun. phys. Lab. Leiden, 1226, 124C(1911).
2. W. Meissner and R. Ochsenfeld : Naturwissenschaften, **21**(1933)787.
3. G. Hardy and J. K. Hulm : Phys. Rev., **89**(1953)884.
4. B. T. Matthias *et al.* : Phys. Rev., **95**(1954)1435.
5. J. E. Kunzler : Rev. Mod. Phys., **36**(1961)1.
6. J. R. Gavaler : Appl. Phys. Lett., **23**(1973)480.
7. M. Wake, M. Kobayashi, K. Tsuchiya, H. Hirabayashi, H. Wada, K. Inoue, K. Itoh, K. Tachikawa, K. Ishibashi and K. Tachikawa : IEEE Trans. Mag., **MAG-19**(1983)552.
8. K. Togano, H. Kumakura, Y. Yoshida and K. Tachikawa : IEEE Trans. Mag., **MAG-21**(1985)463.
9. K. Togawa, H. Kumakura, T. Takeuchi and K. Tachikawa : IEEE Trans. Mag., **MAG-19**(1983)414.
10. Y. Kimura : Phys. Stat. Sol.(a), **69**(1982)187.
11. J. G. Bednorz and K. Mü ller : Z. Phys., **B64**(1986)189.
12. M. K. Wu, J. R. Ashburn, C. J. Torng, P. H. Hor, R. L. Meng, L. Lao, Z. J. Huang, Y. Q. Wang and C. W. Chu : Phys. Rev. Lett, **58**(1987)908.
13. H. Maeda, Y. Tanaka, M. Fukutomi and T. Asano : Jpn. J. Appl. Phys. **27**(1988)L209.
14. M. Takano, J. Takada, K. Oda, H. Kitaguchi, Y. Miura, Y. Ikeda, Y. Tomii and H. Mazaki : Jpn. J. Appl. Phys., **27**(1988)L1041.
15. Z. Z. Sheng and A. M. Hermann : Nature, **322**(1988)55.

16. J. Bardeen, L. N. Cooper and J. R. Schrieffer : Phys. Rev., **108**(1957)1175.

17. A. A. Abricosov : Sov. Phys.-JETP, **5**(1957)1174.

18. M. Tinkham : Introduction to Superconductivity(McGraw–Hill, New York).

Chapter 2

Crystal growth and microstructure dependence of critical current density for bronze-processed V_3Ga compound

2.1 Introduction

Since V_3Ga compound was discovered as one of A15 type compound superconductors in 1957, a lot of efforts have been expended on fabrication of superconducting wire or tape. In 1967, Tachikawa reported [1] that the V_3Ga composite tape can be successfully prepared by the diffusion reaction between vanadium tape and Ga which is coated on the surface of vanadium tape and this composite tape was practically applied to superconducting magnet for generating high magnetic field. The relationship between the microstructure and the critical current density of V_3Ga composite tape has been investigated by Nembach and Tanaka *et al.* [2,3] and due to their results, it was revealed that the grain boundary acts as a primary pinning center against flux flow. From the microstructure investigation, Livingston, Scalan and Tanaka *et al.* made clear [4–6] that the critical current density depends on grain size.

Recently, the production of V_3Ga multifilamentary composite wire becomes possible [7] by establishment of *bronze process*. In the bronze process, V_3Ga compound is formed by the diffusion reaction between the bronze(Cu-Ga) matrix and vanadium filament and the

compound layer grows into vanadium by the diffusion of Ga element from Cu-Ga alloy during heat treatment. Hughes *et al.* [8] investigated about the formation of A15 compound from the view point of solid state reaction. Growth mechanism of A15 compound was also intensively investigated by many groups [9–11]. For the improvement of critical current density of V_3Ga compound, a refinement of microstructure by the optimization of heat treatment condition or addition of third element has been expected. From this viewpoint, many attempts have been made and the critical current density of V_3Ga compound has been considerably improved [12–14].

In the field of pinning theory, many studies have been earnestly carried out since Kramer model in 1973 [15]. Evetts *et al.* [16] newly proposed the formula which express field dependence of pinning force by modifying the Kramer model. Zerweck and Welch [17,18] suggested, respectively electron scattering model for compound type superconductor. In spite of many studies, however, it can be said that some ambiguities about magnetic field dependence of critical current density especially in high magnetic field and pinning mechanism of V_3Ga compound still remains.

In this study, influence of Mg and Zr addition on the microstructure and the growth of V_3Ga compound prepared with various heat treatment conditions was investigated in detail. The correlation between the magnetic field dependence of critical current density and the microstructure change of V_3Ga due to Mg and Zr addition was investigated. For investigating the pinning mechanism of V_3Ga compound, elementary pinning force was evaluated by using direct summation model.

2.2 Experimental

Bronze ingots with various compositions of Cu-18at% Ga-1at% M(M=None,Zr, Mg) were prepared in an induction furnace under vacuum. By repeating the process of cold rolling and annealing at 973 K in vacuum, finally sheet type Cu-Ga-M specimens with size of 0.8 mm thickness, 10 mm width and 55 mm length were prepared. One side surface of this specimen was fully polished by emery papers and buffer with Al_2O_3 paste.

Sandwich type specimens were made by inserting the vanadium foil with thickness of 0.2 mm between two sheets of Cu-Ga-M alloys after polishing. This sandwich type specimen was put into stainless tube and one end of this tube was welded. The stainless tube was pressed at 973 K for 10 min with pressure of 250 MPa, where the stainless tube was evacuated by using rotary and diffusion vacuum pumps. After that, the sandwich type specimens were cut into small pieces. The specimens were sealed in evacuated quartz tube and annealed at 923 and 973 K for 80 $\sim$ 2000 ks. After heat-treatment, layer thickness of V_3Ga compound was measured by optical microscope. Microstructure of fracture surface for V_3Ga compound was observed by scanning electron microscope. Grain size of V_3Ga compound was measured from the scanning electron micrograph of fracture surface by using intersect method. Here, two kinds of grain size d_n, and d_p were defined against the direction of crystal growth of V_3Ga compound layer. The critical current in magnetic fields (2 - 23 T) at 4.2 K was measured in HFLSM in Tohoku university, where magnetic fields were applied normal ($\perp$) or parallel(//) to the surface of specimen . Sample configuration along with definition of direction of applied magnetic field and grain size were schematically presented figure 2.1. The electric circuit for measurement of critical current in magnetic field were schematically presented in figure 2.2, where a water cooling magnet or a hybrid type magnet was used for generating magnetic field. The critical current, I_c was defined with criterion of 1 μV/cm. After measuring the cross-section area, S of compound layer which is normal to transport current direction, critical current density was calculated by $J_c = I_c/S$.

2.3 Results and discussion

2.3.1 Crystal growth

When V_3Ga is prepared by bronze process, the compound layer is formed at interface between bronze layer and vanadium layer during heat treatment. Ga atom in bronze layer diffuse to compound layer, and react with vanadium atom, then V_3Ga compound layer forms and grows. Figure 2.3 shows annealing time dependence of compound layer

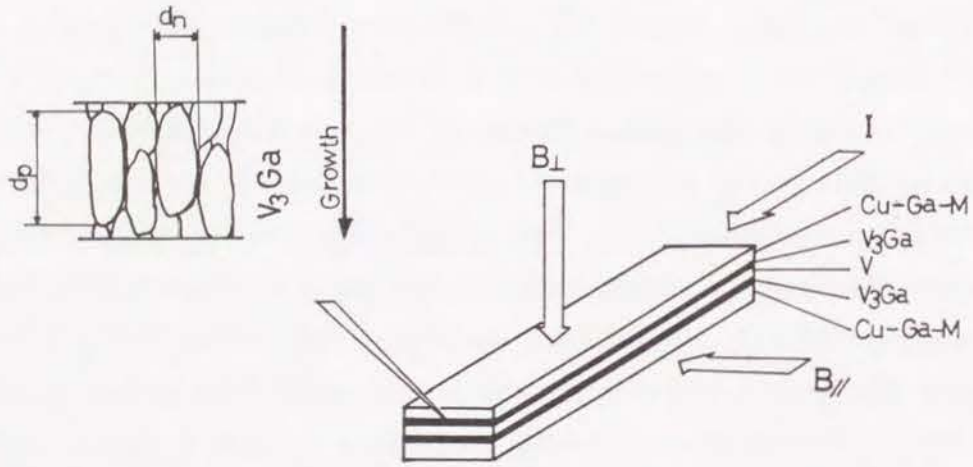

Figure 2.1 Sample configuration at critical current measurement in magnetic filed and the definition of grain size.

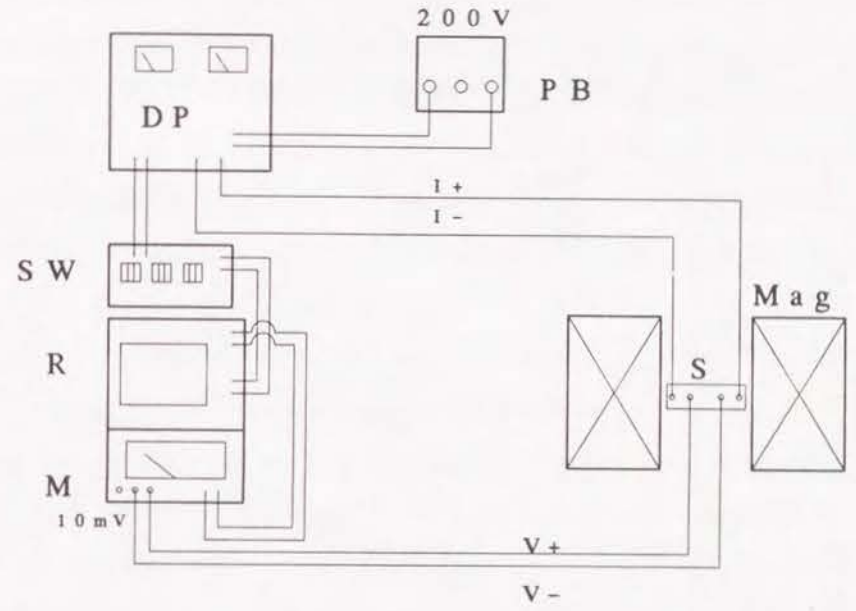

DP: D.C Supplier

PB: Power Box

SW: Sweeper

M: Micrometer

R: Recorder

Mag: Magnet

S: Specimen

Figure 2.2 Schematic illustration of the electric circuit for critical current measurements in magnetic field at 4.2 K.

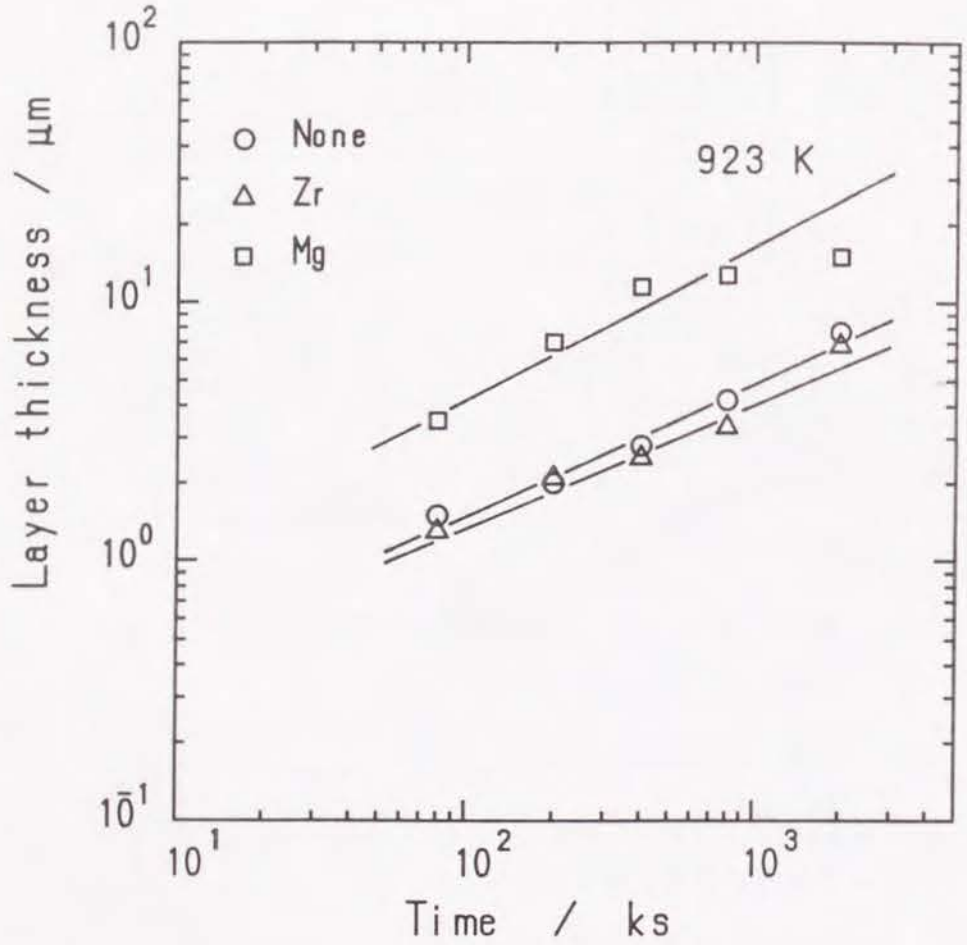

Figure 2.3 Compound layer thickness as a function of annealing time for the specimen annealed at 923 K.

thickness for specimens annealed at 923 K. Among three kinds of specimens, layer thickness of Mg additive specimen was found to be largest. The compound layer of Zr additive specimen is found to become thinner than that of none additive specimen. According to above results, it was found that Mg and Zr acts as promoting and impeding element against growth of V_3Ga compound layer, respectively. Figure 2.4 shows the annealing time dependence of compound layer thickness for specimen annealed at 973 K. Comparing with results from figure 2.3, it was observed that annealing at high temperature is effective to obtain the thick V_3Ga compound layer.

Figure 2.5 shows the annealing time dependence of grain size ,d_n, where the data are indicated with average value. For all the specimens, grain size continuously increased with increasing annealing time. It was found that grain growth of V_3Ga is enhanced at high temperature as indicated by the data for Mg additive specimen. Grain size of Mg additive specimen was observed to be larger than other ones at same annealing condition. On the other hand, it was found that the grain size of compound is become to small by Zr addition. For the grain size, d_p, annealing time dependence is shown in figure 2.6. Comparing with result of d_n shown in figure 2.5, it was found that grains tend to columnar for all the specimens. This tendency is found to become outstanding by Mg addition and long period annealing.

Figure 2.7 shows the microstructure of fracture surface in compound of various specimens. It was found that the grain morphology of V_3Ga compound layer is changed by heat treatment condition and additive element. For the Zr additive specimen, it was found that grains changed to columnar by high temperature heat treatment. For the Mg additive specimen annealed at 973 K, equaxed small grains were observed together with large columnar grains.

In general, time dependence of layer thickness of V_3Ga compound,l can be expressed by the following equation.

$$l = kt^n \tag{2.1}$$

Rate constant, k and time exponent, n for three kinds of specimens annealed at 923

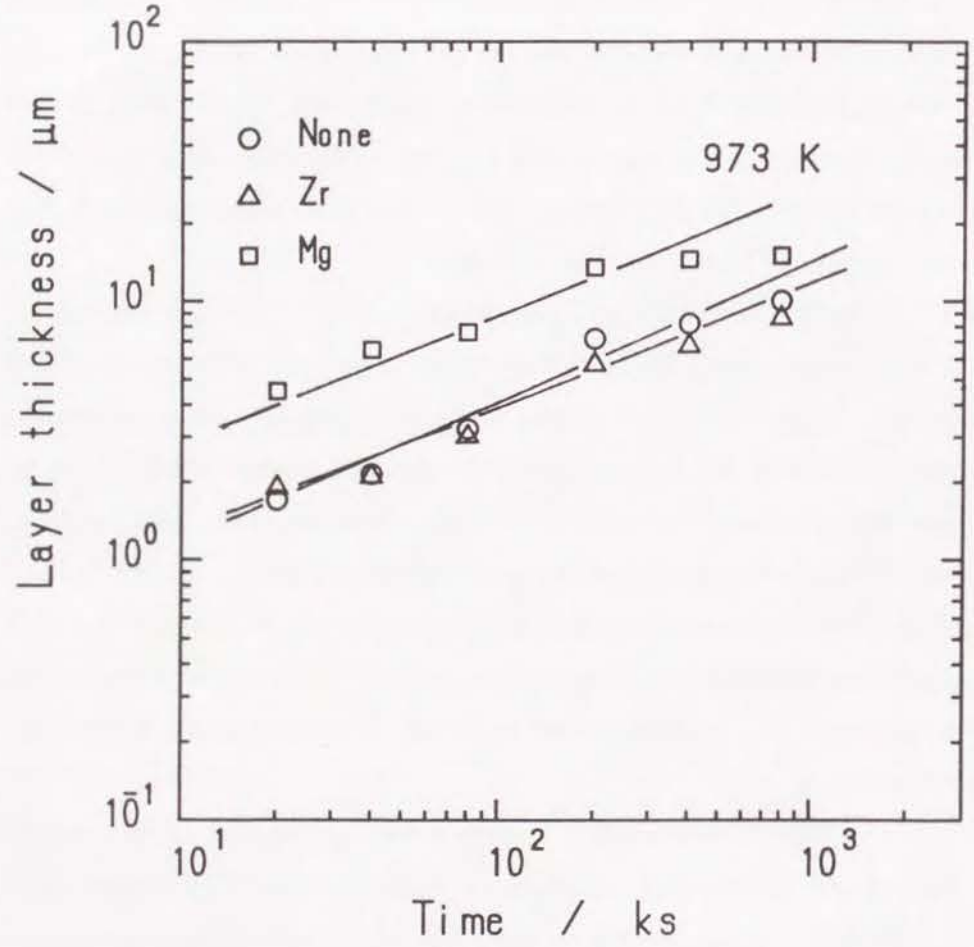

Figure 2.4 Compound layer thickness as a function of annealing time for the specimen annealed at 973 K.

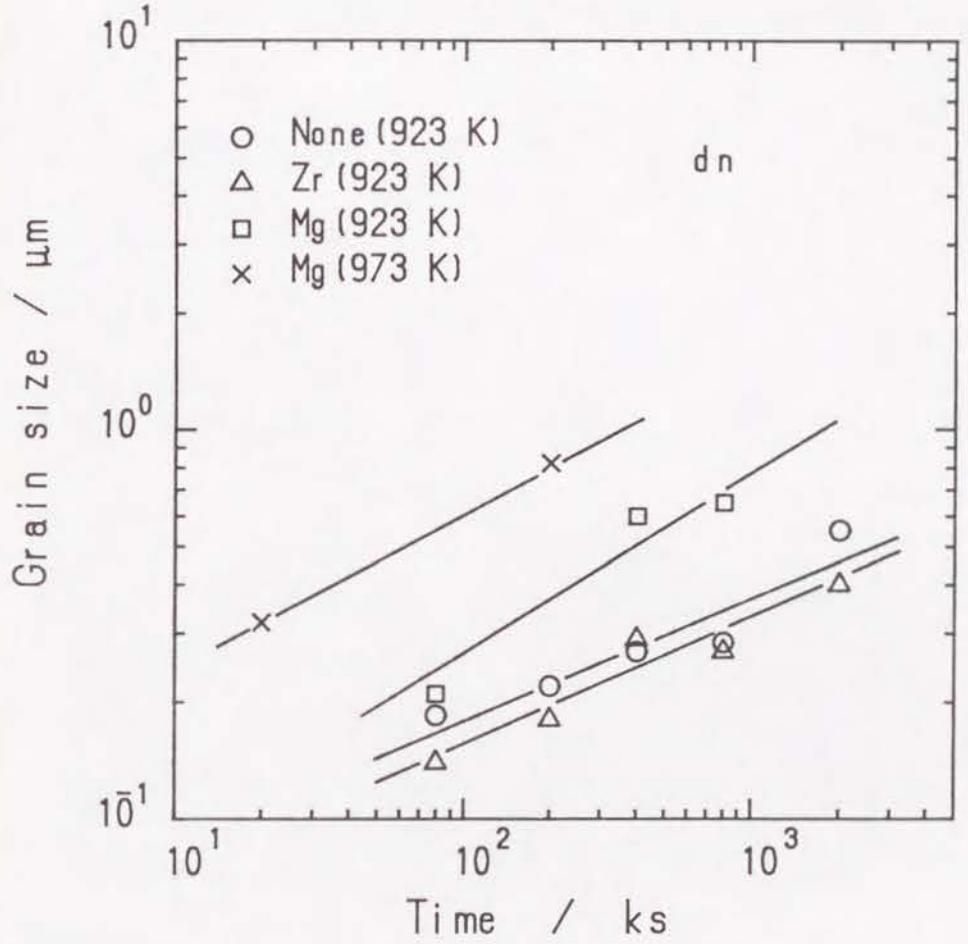

Figure 2.5 Grain size of compound, d_n as a function of annealing time.

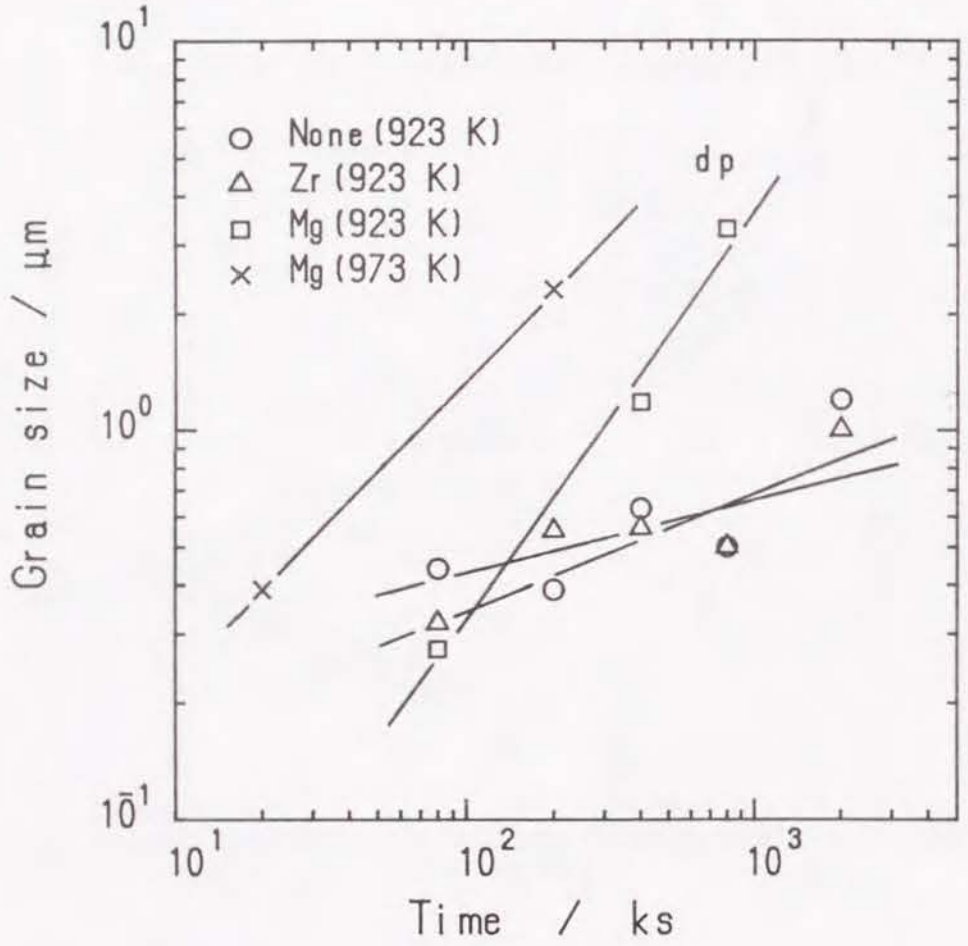

Figure 2.6 Grain size of compound, d_p as a function of annealing time.

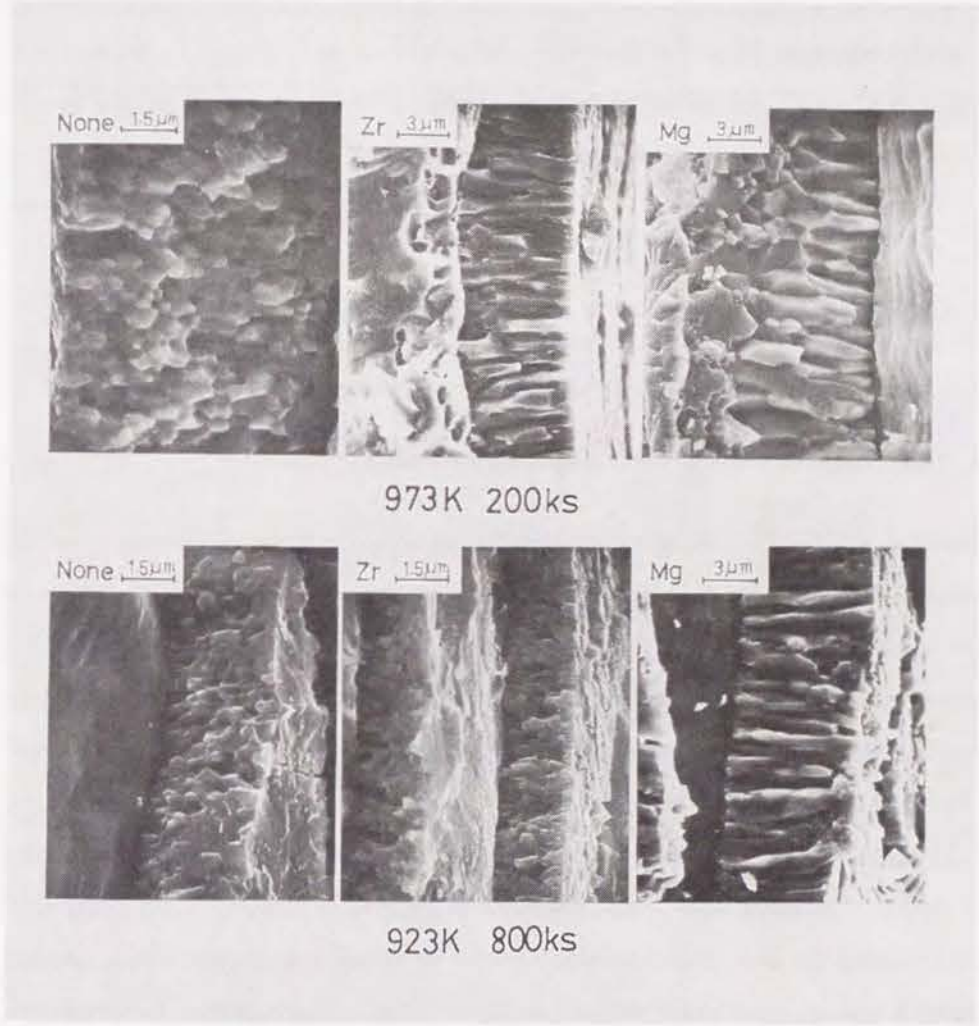

Figure 2.7 Scanning electron micrographs of fracture surface for V_3Ga compound layer of various specimens.

and 973 K, respectively were summarized in table 2.1, where the data for the Mg additive specimen in the region of saturation as shown in figure 2.3, 4 were omitted. It was found that time exponent, n is close to 0.5 for all the specimens. This implies that the V_3Ga compound grows parabolically with respect to annealing time. Assuming that the change of solute concentration in bronze matrix is negligibly small, several processes are considered to control the overall rate of layer growth as follow.

1. Diffusion of Ga in the bronze layer
2. Chemical reaction of Ga and V at reaction interface
3. Grain boundary diffusion of Ga in the V_3Ga compound layer
4. Bulk diffusion of Ga in the V_3Ga compound layer

In previous studies, [19,20] it was made clear that layer thickness of compound which is calculated with assuming that the growth of compound layer is controlled by process 1 was found to be much thicker than that measured experimentally. Since time exponent, n is 1 for the case that surface chemical reaction controls overall reaction of V_3Ga growth, then it is insufficient to explain the present experimental data. In order to reach reaction interface Ga can pass through V_3Ga compound layer by two diffusion paths, grain boundary and bulk in compound. For the grain boundary diffusion in compound, Farrell [9] investigated it in detail. According to it, time exponent n becomes 0.33 because the total area of grain boundary for high diffusion path decreases by coarsening of grain during annealing. Judging from that time exponent is close to 0.5 for all the specimens, bulk diffusion of Ga in compound is considered to control the growth of V_3Ga compound layer.

2.3.2 Magnetic field dependence of critical current density

Figure 2.8 shows the magnetic field dependence of critical current density, J_c for the specimen annealed at 973 K for 200 ks, where magnetic field is applied to normal to surface of specimen. For all the specimens, J_c decreased monotonously with increasing

Table 2.1 Rate constant, k and time exponent, n in formula expressing growth of compound layer $l = kt^n$.

Temperature	System	Rate constant, k	Time exponent, n
923 K	Cu-18at%Ga/V	0.14	0.52
	Cu-18at%Ga-1at%Zr/V	0.15	0.48
	Cu-18at%Ga-1at%Mg/V	1.02	0.58
973 K	Cu-18at%Ga/V	0.34	0.52
	Cu-18at%Ga-1at% Zr/V	0.46	0.45
	Cu-18at%Ga-1at% Mg/V	1.75	0.41

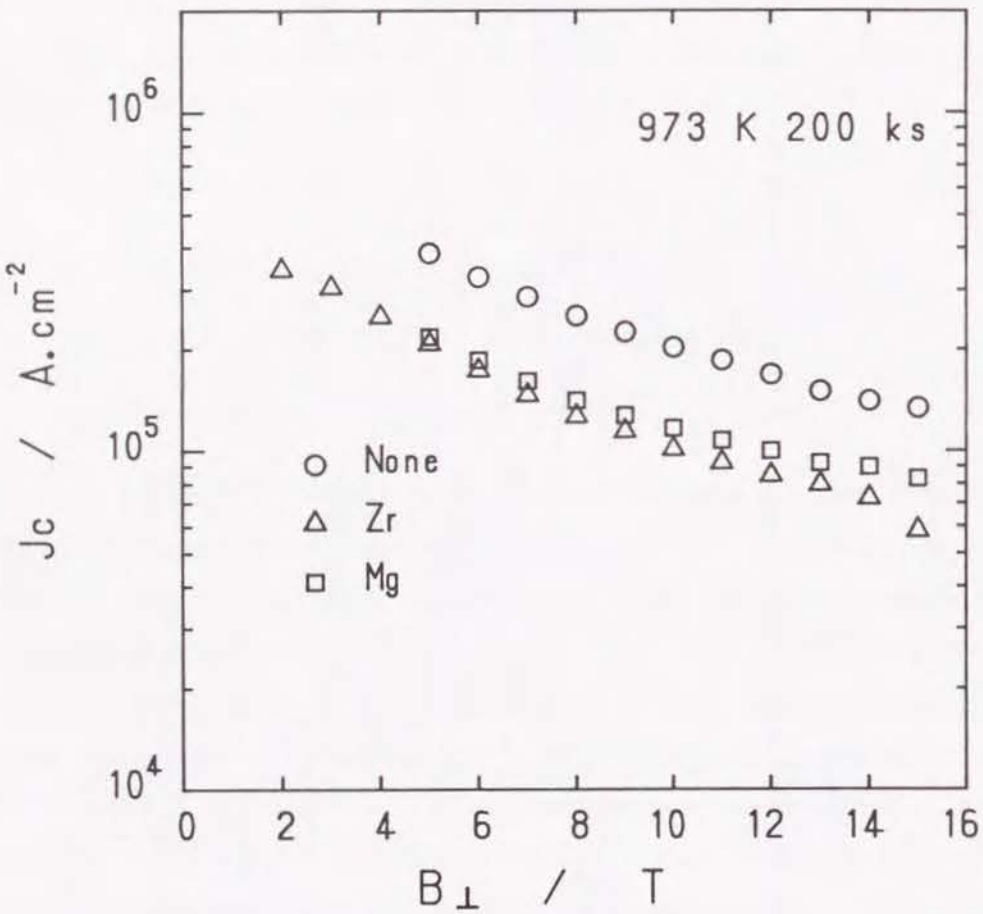

Figure 2.8 Critical current density as a function of magnetic field($B \perp$) for specimens annealed at 973 K for 200 ks.

the field. J_c of none additive specimen is found to be higher than that of other kind of specimens. Magnetic field dependence of J_c for the specimen annealed at 923 K for 80 ks is shown in figure 2.9. J_c of Mg additive specimen shows the highest value among three kind of specimens. Magnetic filed dependence of J_c is found to be improved by Mg addition for the specimen annealed at 923 K for 80 ks. On the other hand, Zr addition turned out to be no effective. Comparing with the result from figure 2.8, it was found that the J_c decreased drastically with increasing magnetic field. Mg additive specimen exhibited higher J_c in all range of magnetic field than that of specimen annealed at 973 K for 200 ks. On the other hand, J_c appeared high in low magnetic field below 10 T for none additive and Zr additive specimen annealed at 923 K for 80 ks. Figure 2.10 shows magnetic field dependence of J_c for none additive specimen annealed at 923 K for various times. Within the range of magnetic field below than 12 T, it is found that the shorter time annealing, the higher J_c is obtained. In the range of magnetic field above 12 T, J_c increased by long time annealing.

Figure 2.11 shows magnetic field dependence of J_c for the specimen annealed 923 K for 80 ks, where magnetic field is applied parallel to the surface of specimen. Comparing with result from figure 2.9, for all the specimens, J_c appeared low in all range of magnetic field. As shown in figure 2.5,6 and 7, V_3Ga grains were similar to columnar and they exhibited different grain size as d_p and d_n. Due to this, effective area of grain boundary which interacts with flux line as pinning center is altered with direction of applied magnetic field.

Therefore, J_c becomes high when the magnetic field is applied normal to surface of specimen, (parallel to direction of grain growth). This is consistent with result [7] of Tanaka *et al.*

Magnetic field dependence of J_c for the Mg additive specimen annealed at 923 K for 100 ks and 973 K for 400 ks, respectively is shown in figure 2.12. J_c for the specimen annealed at 923 K decreased gradually with increasing magnetic field and dropped drastically over 15 T, while J_c for the specimen annealed at 973 K did not change so much till 17 T with

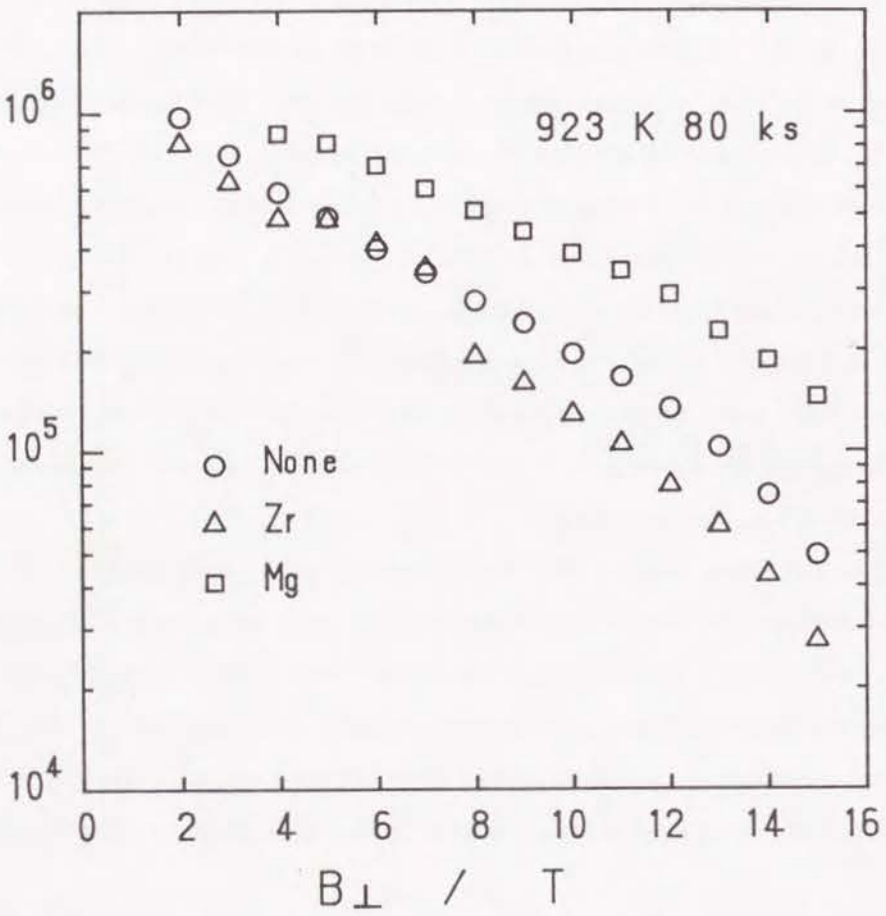

Figure 2.9 Critical current density as a function of magnetic field($B \perp$) for specimens annealed at 923 K for 80 ks.

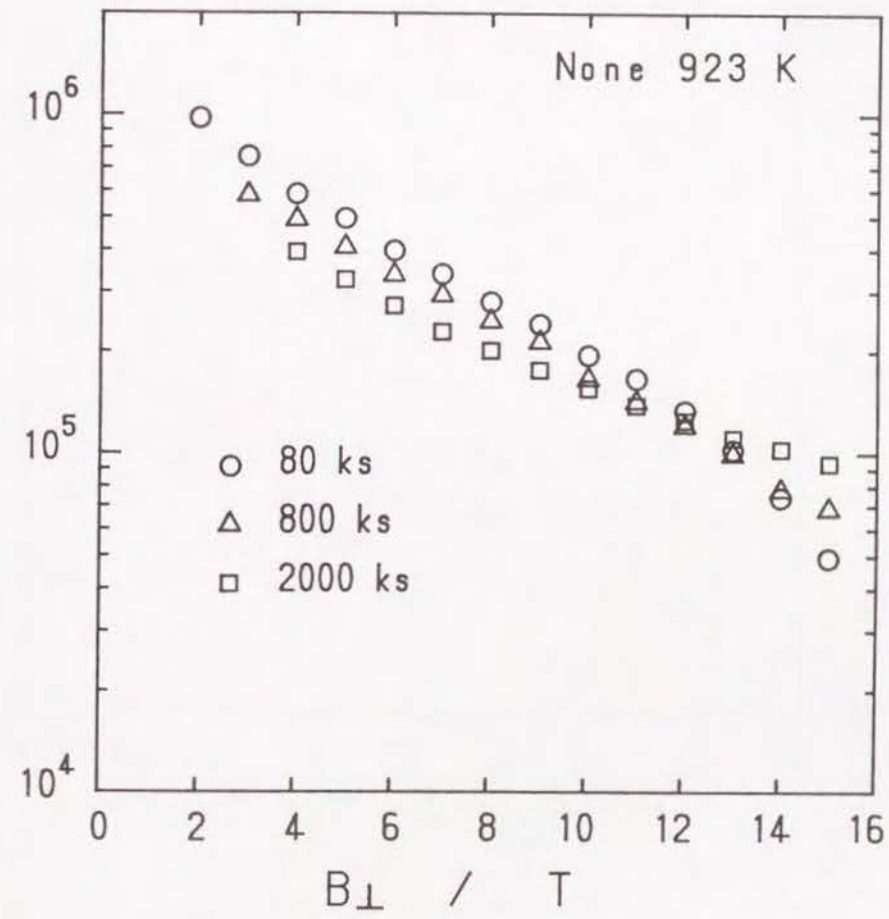

Figure 2.10 Critical current density as a function of magnetic field($B \perp$) for none additive specimens annealed at 923 K for various times.

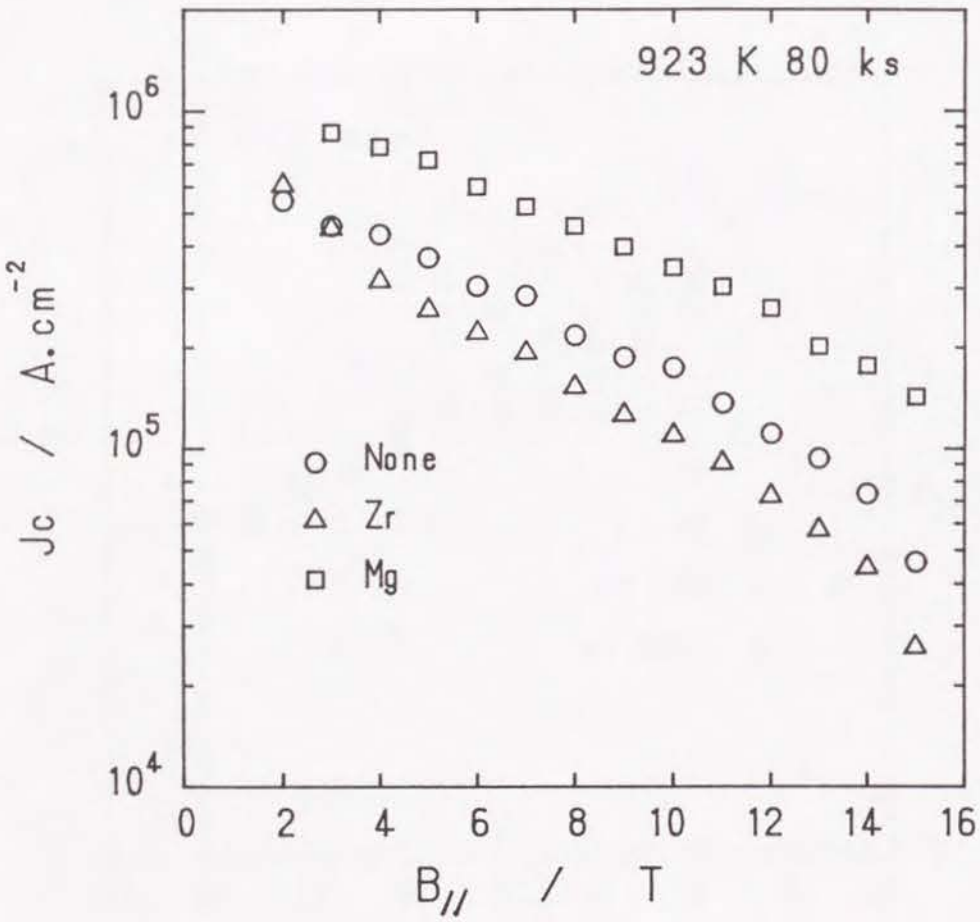

Figure 2.11 Critical current density as a function of magnetic field($B_{//}$) for specimens annealed at 923 K for 80 ks.

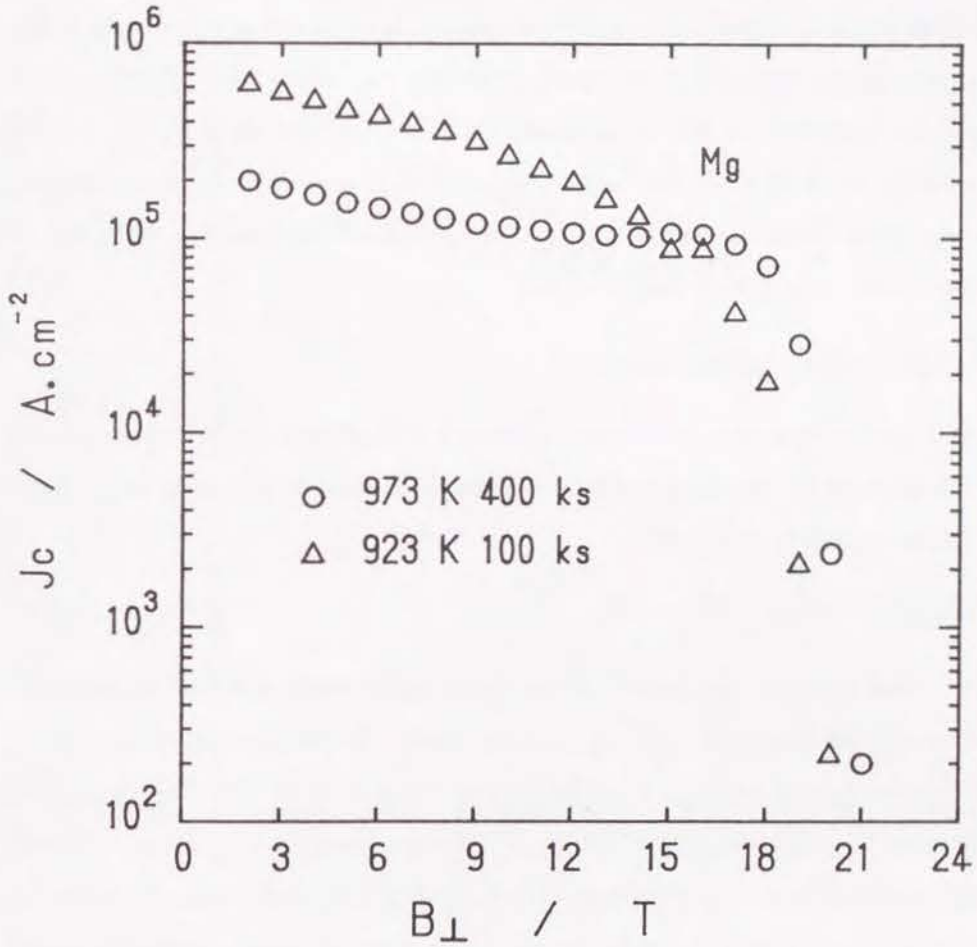

Figure 2.12 Critical current density as a function of magnetic field($B \perp$) for Mg additive specimens.

increasing the magnetic field. It can be considered that high field property is improved by high temperature and long time annealing.

Figure 2.13 shows magnetic field dependence of J_c for the various kind of specimens annealed at 973 K for 400 ks. For all the specimens, J_c decreased monotonously in the range of low magnetic field and decreased drastically over about 16 T. None additive specimen the exhibited the highest J_c among three kinds of specimens in the range of magnetic field below 16 T. In the range of magnetic field over 16 T, J_c of Mg additive specimen appeared high. According to this, it was found that Mg addition is effective to the improvement of J_c in high magnetic field.

2.3.3 Pinning mechanism

When a current flows in a mixed-state superconductor along a direction normal to an applied magnetic field, the quantized flux lines are acted upon by a Lorentz force. Here, Lorentz force density is given by [21]:

$$F_L = J_t B \tag{2.2}$$

where J_t and B are current density and average magnetic field in sample, respectively. The maximum loss-free current density, J_c is determined by the maximum force density (global pinning force density,F_p) acted by pinning center such as defect, which opposes the flux motion by F_L, where $F_p = J_c B$. From the above consideration, it can be known that high critical current density is obtained by increasing the global pinning force density. Global pinning force density F_p can be expressed with formula of direct summation model [22],

$$F_p = n_v f_p \tag{2.3}$$

where, n_v and f_p are number of pinning interaction per unit volume and elementary pinning force, respectively. Therefore, it can be known that critical current density directly depends on n_v and f_p. As shown in figure 2.7, it was found that the grain of Mg additive specimen became coarse by long time annealing at 973 K. The result that J_c for Mg

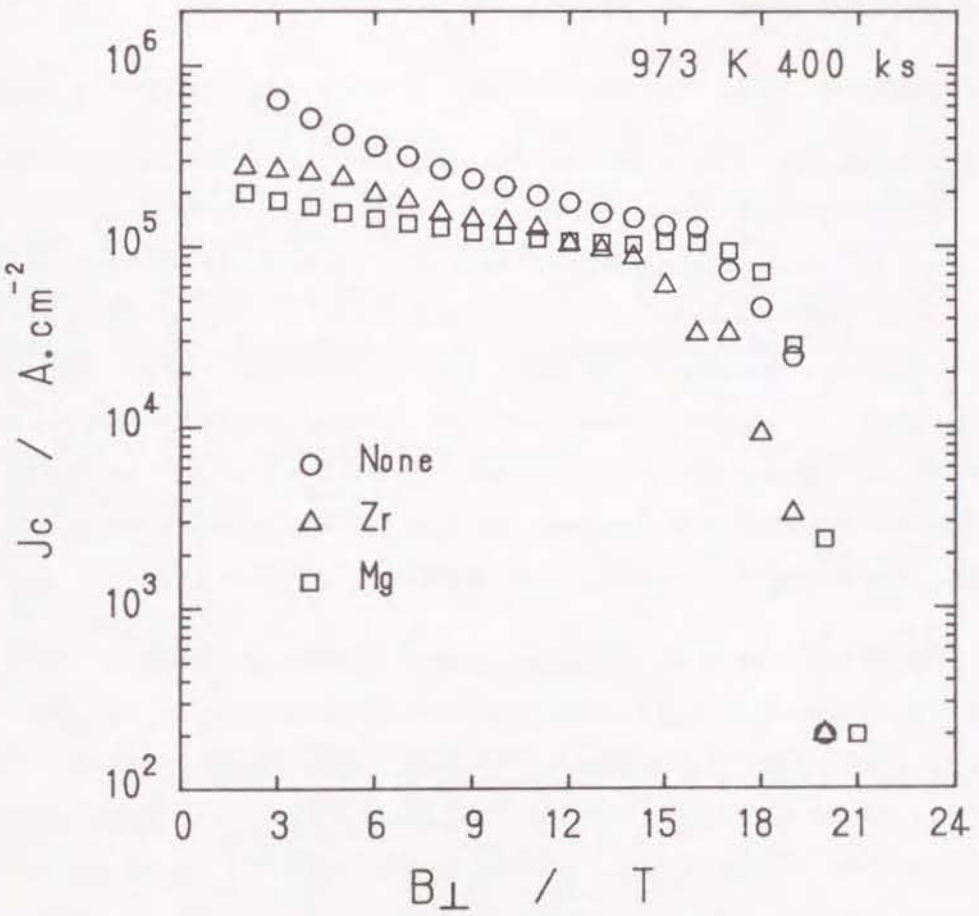

Figure 2.13 Critical current density as a function of magnetic field($B \perp$) for specimens annealed at 973 K 400 ks.

additive specimen annealed 973 K for 200 ks is lower than that for Mg additive specimen annealed 923 K for 80 ks is attributed to a decrease in the number of n_v by grain coarsening. Elementary pinning force per unit length can be calculated as follow by using direct summation model.

$$f_p^* = F_p d_n a_f \tag{2.4}$$

Here, d_n and a_f are grain size and the distance between the two flux lines penetrated. The calculated values of f_p^* for specimens annealed at 923 K for 80 ks are listed table 2.2. It was found that elementary pinning force becomes largest for Mg additive specimen among three kinds of specimens and its value become small when the applied magnetic field became high. According to this, improvement of J_c is considered to be attributed to the increase of elementary pinning force. The values of f_p^* listed in table 2.2 are similar to reported values from Zerweck and Welch [17,18] which were calculated theoretically by electron scattering model. Therefore, pinning for V_3Ga compound is thought to be resulted from the electron scattering at grain boundary.

Table 2.2 Calculated elementary pinning force of various specimens.

Cu-18 at%Ga-1at %M/V	None	Zr	Mg
Grain size, $d_n(\mu m)$	0.186	0.138	0.210
$f_p^*(10^{-4}N/m)$ at 6 T	0.89	0.68	1.77
$f_p^*(10^{-4}N/m)$ at 15 T	0.02	0.009	0.08

Kramer suggested [15] that magnetic field dependence of critical current density can be described theoretically by considering elastic interaction between the flux line and pinning center. According to his theory, the pinning force in high magnetic field is limited by shearing flow of FLL and shearing flow does not depends on microstructure. Evetts *et al.* [16] suggested that the critical shearing process of flux depends on the morphology of grain in compound, then Kramer's formula was modified as following equation, where grain size is involved.

$$F_p = 7.4 \times 10^4 B_{c2}(1-b)^2/\kappa d \tag{2.5}$$

From above equation(2.5), following convenient form can be derived to determine B_{c2}.

$$J_c^{1/2} B^{1/2} \propto B_{c2} - B \tag{2.6}$$

B_{c2} can be obtained by plotting $J_c^{1/2}B^{1/2}$ against B (Evetts-Plummer plot). Figure 2.14 shows the results of Evetts-Plummer plot and the values of B_{c2}, which were obtained by extrapolating in the range of high magnetic field are indicated. For the Mg additive specimen, B_{c2} was found to increase by high temperature and long time annealing. Among three kinds of specimens annealed at 973 K for 400 ks, Mg additive specimen exhibited highest B_{c2} of 21.06 T. According to this, Mg addition is thought to be effective to increase of B_{c2}.

Magnetic field dependence of global pinning force density is known to be normalized by using following equation [23].

$$F_p = F_{p,max} b^p (1-b)^q \tag{2.7}$$

Here, $b = B/B_{c2}$. Figure 2.15 shows the $F_p/F_{p,max}$ vs B/B_{c2} for the Mg additive specimen. For the specimen annealed at 923 K for 100 ks, global pinning force density reached maximum at $b = 0.4$ and decreased gradually with increasing induced field, while for the case of specimen annealed at 973 K for 400 ks, global pinning force density gradually increased and reaches maximum at $b = 0.8$. According to this, it is confirmed that magnetic field dependence of global pinning force density depends on heat treatment condition. By fitting the present data to above equation, p and q are found to become 0.96 and 1.45, respectively for the specimen annealed at 923 K for 100 ks. However, it was found that the data for the specimen annealed at 973 K for 400 ks could not be fitted with above equation. It was reported that the pinning force for Nb_3Sn decreased with following same scaling curve in high magnetic field. However, from the present experimental results it was made clear that the pinning force in V_3Ga does not follow same scaling curve. The appearance of sharp peak near B_{c2} is resulted from so called peak-effect [24], while broad

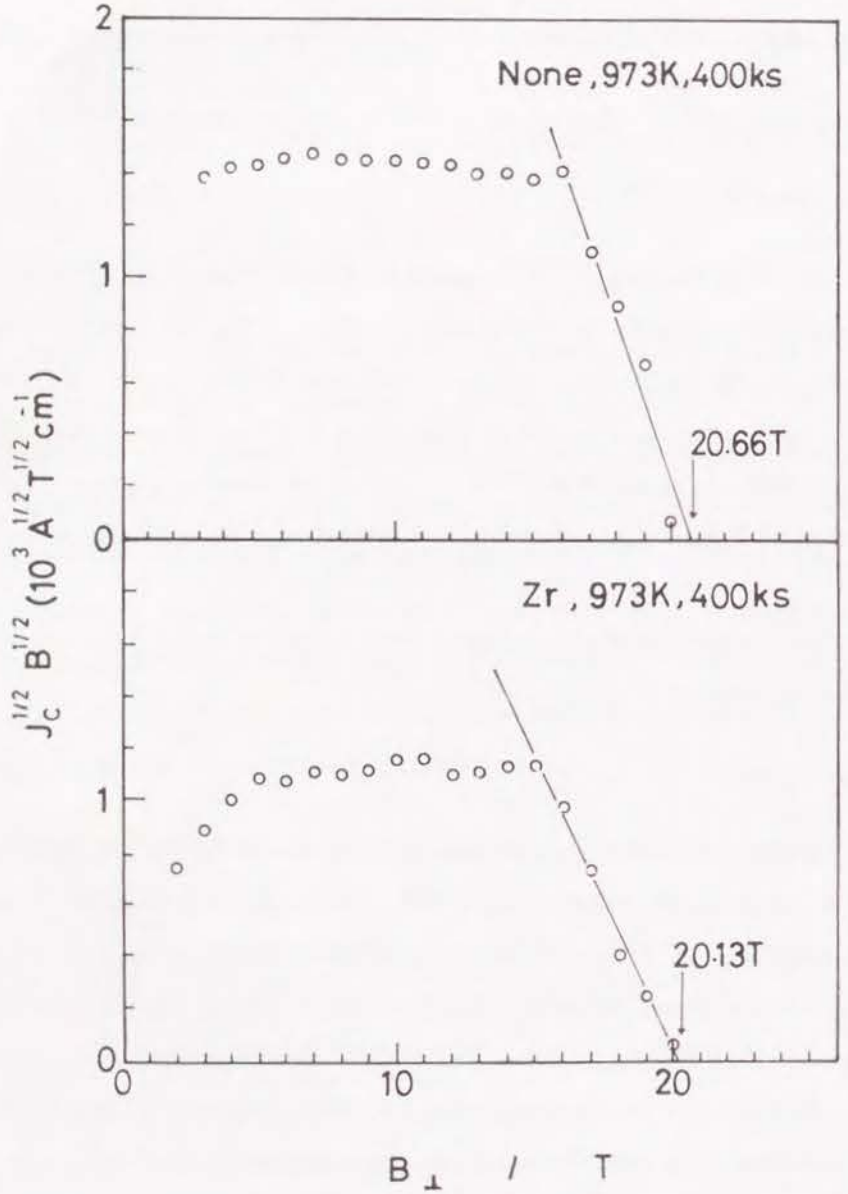

Figure 2.14(a) $J_c^{1/2}B^{1/2}$ vs magnetic field($B \perp$) for none or Zr additive specimens, where B_{c2} is derived by extrapolation.

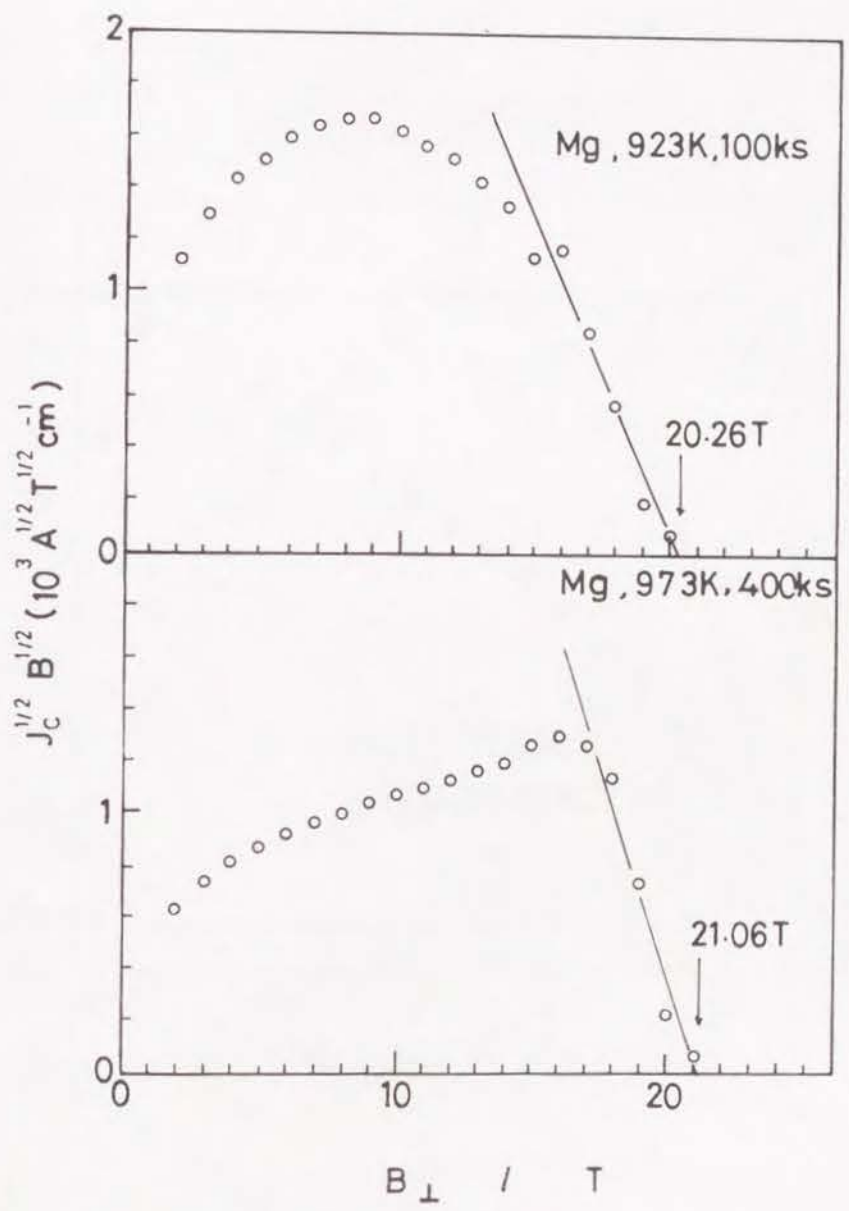

Figure 2.14(b) $J_c^{1/2}B^{1/2}$ vs magnetic field($B \perp$) for Mg additive specimens, where B_{c2} is derived by extrapolation.

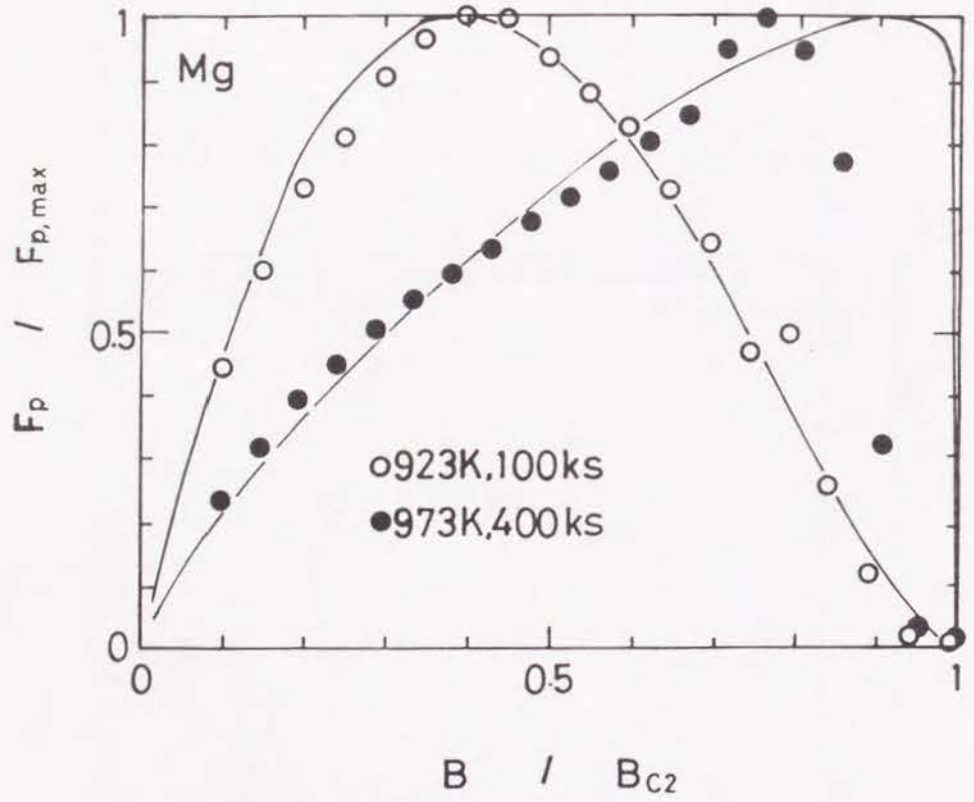

Figure 2.15 Normalized global pinning force ($F_p/F_{p,max}$) vs induced field (B/B_{c2}).

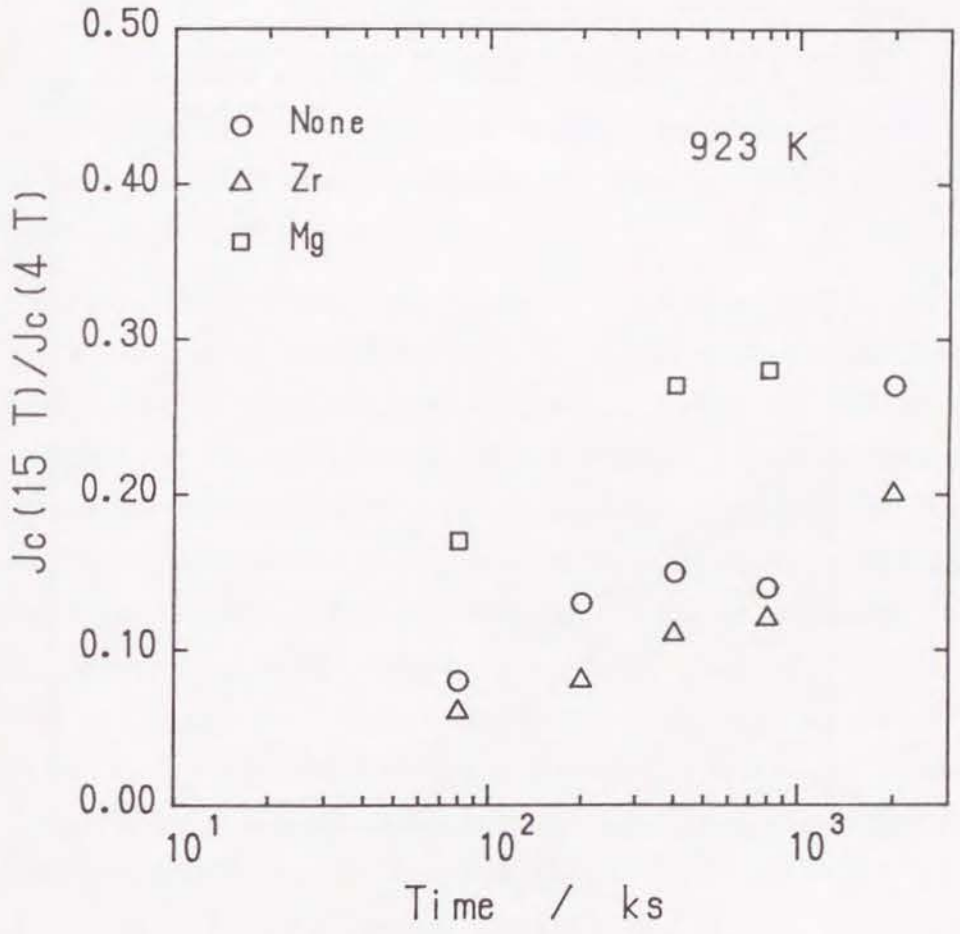

Figure 2.16 Normalized critical current density, J_c (15 T)/J_c (4 T) vs annealing time for various specimens.

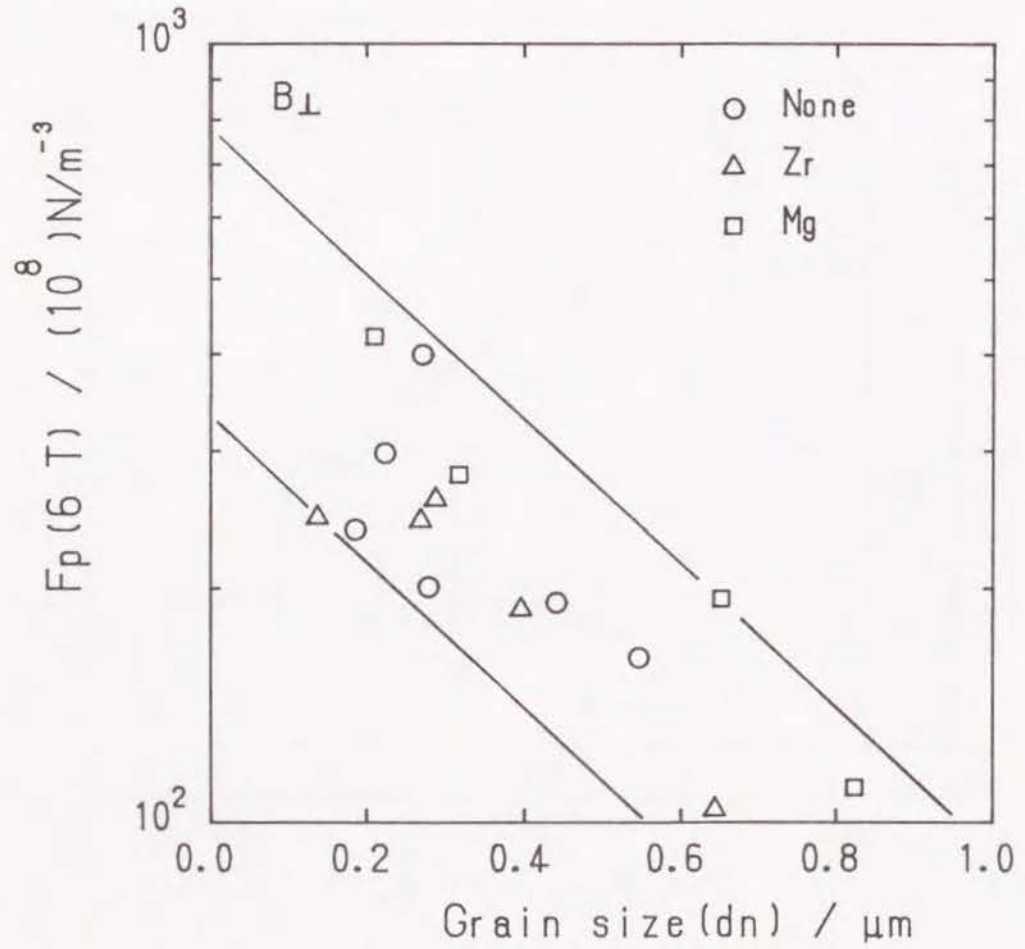

Figure 2.17 Global pinning force, F_p (6 T) as a function of grain size d_n for various specimens.

peak appeared at region of low magnetic field is related with grain boundary pinning mechanism. Even though ambiguities exist about the mechanism of peak-effect, there is a possibility that another fine defects distributed periodically in grain strongly interacts with FLL near B_{c2}. It was known [2] that martensite transformation occurred when V_3Ga is cooled below around 20 K. If fine defects can be formed in grain by the martensite transformation, they can act as pinning centers in high magnetic field. However the microstructure of compound after martensite transformation and the condition of transformation are not clear yet.

For investigating the dependence of annealing time on magnetic field property of J_c, the ratio of J_cs at low field(4 T) and high field(15 T) against annealing time was plotted in figure 2.16. For all the specimens, the ratio of J_c increased with increasing the heat treatment time. This implies that the degradation ratio of J_c with respect to increase of magnetic field becomes small for the specimen annealed for long time. Two factors are thought to be associated with this. B_{c2} is considered to be increased by long time annealing because the stoichiometry of compound is improved by long time heat treatment, then the improvement of magnetic field property was thought to be resulted from an increase of B_{c2} by long time heat treatment. Since the coarsening of grain in compound occurs during long time annealing, J_c at region of low magnetic field decreased because of decrease of total area of grain boundary, while J_c at region of high magnetic field increases due to peak effect for the specimen with a coarse grain.

Figure 2.17 shows the grain size dependence of global pinning force density(at 6 T) for various specimens, where magnetic field is applied to surface of specimen. It was observed that global pinning force density decreased with increasing grain size for any additive specimen. According to this, it can be confirmed that global pinning force density becomes to increase for the V_3Ga with fine grain because pin density which directly influence on global pinning force density in low magnetic field increases. The values of global pinning force are shown to be scattered with some extent because the V_3Ga compound of present specimen are consisted of large grain and small grain.

2.4 Conclusion

Crystal growth of V_3Ga compound as well as the relationship between microstructure and critical current density or global pinning force for V_3Ga prepared with addition of Zr and Mg element were investigated in detail. The conclusions obtained by present study could be summarized as follow.

1. Crystal growth of V_3Ga compound was enhanced by Mg addition.
2. Overall growth of V_3Ga compound layer was confirmed to be controlled by bulk diffusion in compound layer.
3. V_3Ga grains tend to columnar and this tendency is enhanced by Mg addition.
4. Critical current density is improved by Mg addition because of increase in elementary pinning force and B_{c2} .
5. The degradation ratio of J_c in high magnetic field becomes small for the long time annealed specimen
6. In low magnetic field, global pinning force density increased linearly with decreasing grain size.

References

1. K. Tachikawa and Y. Tanaka : Jpn. J. Appl. Phys., **6**(1967)782.
2. E. Nembach and K. Tachikawa : J. Less-Common Metals, **19**(1969)359.
3. Y. Tanaka and K. Tachikawa : J. Less-common Metals, **37**(1974)177.
4. Y. Tanaka, Y. Furuto, M. Ikeda, I. Inoue, T. Suzuki and S. Meguro : Cryogenics, APRIL(1977)233.
5. J. D. Livingston : Phys. stat. sol.,(a)**44**(1977)295.
6. R. M. Scalan, W. A. Fietz and E. F. Koch : J. Appl. Phys., **46**(1975)2244.
7. Y. Tanaka, K. Ito and K. Tachikawa : J. Japan. Inst. Metals, **40**(1976)514.
8. D. Dew-Hughes and T. S. Luhman : J. Mater. Sci., **13**(1978)1868.
9. H. H. Farrell, G. H. Gilmer and M. Suenaga : J. Appl. Phys., **45**(1974)4025.
10. M. Suenaga , Proc. of *Int. Cryogenic Materials Conf.* Kobe, Japan, 1982, ed. by K. Tachikawa and A. Clark (Butterworth press).
11. K. Osamura, S. Ochiai, S. Kondo, M. Namatame and M. Nosaki : J. Mater. Sci., **21**(1986)1509.
12. D. Dew-Hughes : J. Appl. Phys., **49**(1978)327.
13. Y. Yoshida and K. Tachikawa : Appl. Phys. Lett., **27**(1975)632.
14. K. Tachikawa, Y. Tanaka, Y. Yoshida, T. Asano and Y. Iwasa : IEEE Trans. on Mag., **MAG-15**(1979)391.
15. E. J. Kramer : J. Appl. Phys., **44**(1973)1360.

16. J. E. Evetts and C. J. G. Plummer , Proc. of *Int. Sum. Flux pinning and Electronic properties in Superconductors.*, Fukuoka, Japan, Ed. by T. Matsushita (Matsukura press)

17. G. Zerweck : J. Low. Temp. Phys., **42**(1981)1.

18. D. O. Welch : IEEE Trans. on Mag., **MAG-21**(1985)827.

19. K. Kawaguchi, S. S. Oh, S. Ochiai and K. Osamura : J. Japan. Inst. Metals, **52**(1988)886.

20. K. Osamura, S. Ochiai and S. S. Oh : J. Jpn. Copper and Brass Res. Assoc., **27**(1988)127.

21. M. Tinkham : Introduction to Superconductivity(MaGraw–Hill, New York)1975.

22. T. Matsushita : Jpn. J. Appl. Phys., **20**(1981)1955.

23. J. W. Ekin : IEEE Trans. on Mag., **MAG-17**(1981)658.

24. A. M. Campbell and J. E. Evetts : Adv. Phys., **21**(1972)199.

Chapter 3

Superconducting property and microstructure of Bi(Pb)-Sr-Ca-Cu-O prepared by melt quenching method

3.1 Introduction

Since Maeda *et al.* [1] discovered a high temperature Bi-Sr-Ca-Cu-O superconductor, many attempts have been carried out to prepare high quality specimen. For the sintered bulk prepared by conventional solid state reaction, the critical current density was known to be very low due to the existence of impurity phases and the poor density. Komatsu *et al.* reported [2] first that a dense superconducting ceramic can be obtained by melt-quenching method and superconducting phase is crystallized from amorphous state during annealing.

In the present Bi-Sr-Ca-Cu-O system, three kinds of perovskite superconducting phases are known to exist [3], as characterized by their ideal chemical compositions; $Bi_2Sr_2CuO_x$(2201) superconducting phase, $Bi_2Sr_2CaCu_2O_x$(2212) low T_c phase and $Bi_2Sr_2Ca_2Cu_3O_x$(2223) high T_c one. Takano *et al.* reported [4] that the Pb addition and prolonged heat treatment is most effective to increase the volume fraction of 2223 high-T_c phase. However, it was known to be difficult [5] to obtain 2223 high-T_c phase as major one by using the melt-quenching and annealing technique. Another problem is that some impurity phases appear easily with superconducting phases in the Bi-Sr-Ca-Cu-O system.

It is important to make clear the phase relationship between the superconducting phases and the impurity ones in order to produce only the 2223 high-T_c single phase. However, the details have been scarcely reported till now. In this study, Bi(Pb)-Sr-Ca-Cu-O superconductors were prepared by melt-quenching method and superconducting property was investigated. Also, in order to clarify the relationship among various phases appeared during crystallization from the amorphous state obtained by melt-quenching. The influence of Pb addition on crystallization process and thermal stability of superconducting phases have been investigated in detail.

3.2 Experimental

Oxide or carbonate powders of high purity Bi_2O_3, $SrCO_3$, $CaCO_3$, CuO and PbO were mixed and ground for 3.6 ks. The nominal compositions of the mixtures investigated were $Bi_2Sr_2Ca_2Cu_3O_x$, $Bi_{1.8}Pb_{0.2}Sr_2Ca_2Cu_4O_x$ and $Bi_{1.6}Pb_{0.4}Sr_2Ca_2Cu_3O_x$. The mixture was melted in high purity alumina crucible at 1443 K, at which the specimen was kept only for a short time of 0.6 ks, because of avoiding serious reaction of the melt with crucible. The melt was poured onto a Cu plate and pressed by another Cu plate. Black colored glossy sheet ceramic with about 0.5 mm thickness was obtained by this procedure. Critical temperature, T_c and current, I_c were measured by so called 4 terminal method. The criterion of 1 μV / cm was used for definition of I_c. In order to examine the phase change during crystallization process, the thermogravimetry and the differential thermal analysis (TG-DTA, Rigaku TAS 100 system) were performed in air with heating rate of 5 K/min. In order to investigate the microstructure change, the specimen was heated with same heating rate as TG-DTA measurements and then quenched into liquid nitrogen. This heat treatment is called the HT1, as shown schematically in figure 3.1. On the other hand, the isothermal heat-treatment, which is called the HT2, was performed at various temperatures in air and quenched into liquid nitrogen. The identification of phases existed was investigated by means of X-ray powder diffractometer (Philips PW1700 system, XRD) and electron probe microanalyser (EPMA). The microstructure was observed mainly by

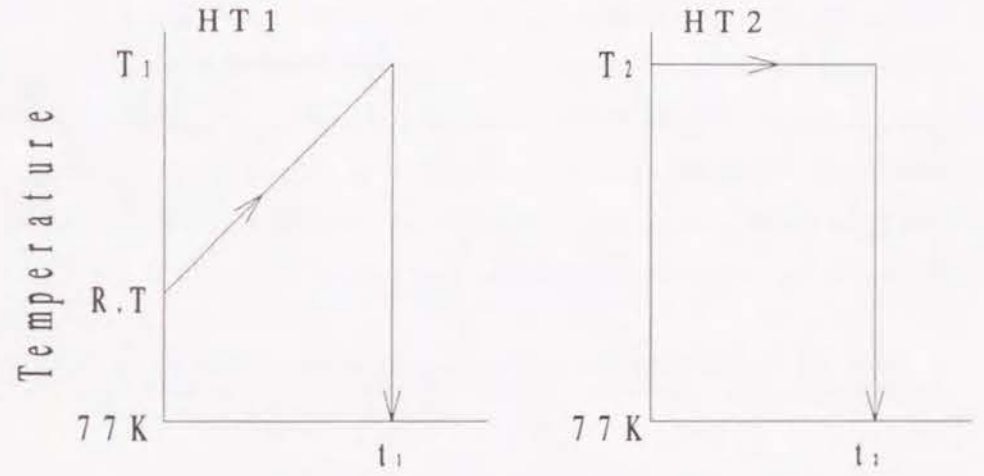

Figure 3.1 Schematic illustration of two kinds of heat treatments employed in present experiment.

the scanning electron microscope(SEM).

3.3 Results and discussion

3.3.1 Superconducting property

Temperature dependence of resistivity for $Bi_{1.8}Pb_{0.2}Sr_2Ca_2Cu_3O_x$ specimen annealed at 1118 K for 604.6 ks was measured and its result was shown in figure 3.2. The resistivity began to drop drastically near 110 K and the $T_{c,off}$, at which resistivity becomes zero is observed to be 98 K. According to this, it is thought to be that high T_c phase exists in the bulk and its grains are connected in almost whole region of specimen.

Critical temperatures for $Bi_{1.8}Pb_{0.2}Sr_2Ca_2Cu_4O_x$ specimen annealed at 1118 K for various times were measured and its results are listed in table 3.1. $T_{c,off}$ was observed to increase with increasing the annealing times, excluded the case of 864 ks. Comparing with the T_c for the $Bi_{1.8}Pb_{0.2}Sr_2Ca_2Cu_3O_x$ specimen annealed at 1118 K for 604.6 ks, T_c is found be low for the specimens with higher mole ratio of Cu.

Table 3.1 Critical transition temperature, $T_{c,off}$ for $Bi_{1.8}Pb_{0.2}Sr_2Ca_2Cu_4O_x$

Annealing time / ks	$T_{c,off}$/K
172.8	78
345.6	82.5
518.4	87
691.2	89
864.4	85

Figure 3.3 shows the microstructure of polished surface for $Bi_{1.8}Pb_{0.2}Sr_2Ca_2Cu_4O_x$ specimen heat treated at 1118 K. White colored needle-like superconducting phase which was grown anisotropically was observed with impurity phases in the specimen annealed

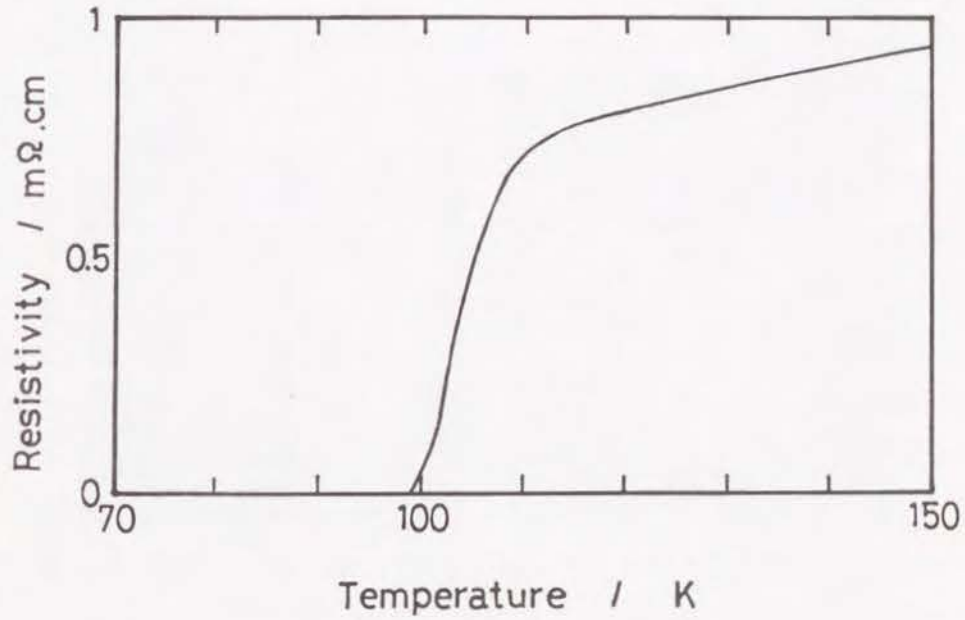

Figure 3.2 Temperature dependence of resistivity for $Bi_{1.8}Pb_{0.2}Sr_2Ca_2Cu_3O_x$ specimen annealed at 1118 K for 604.6 ks.

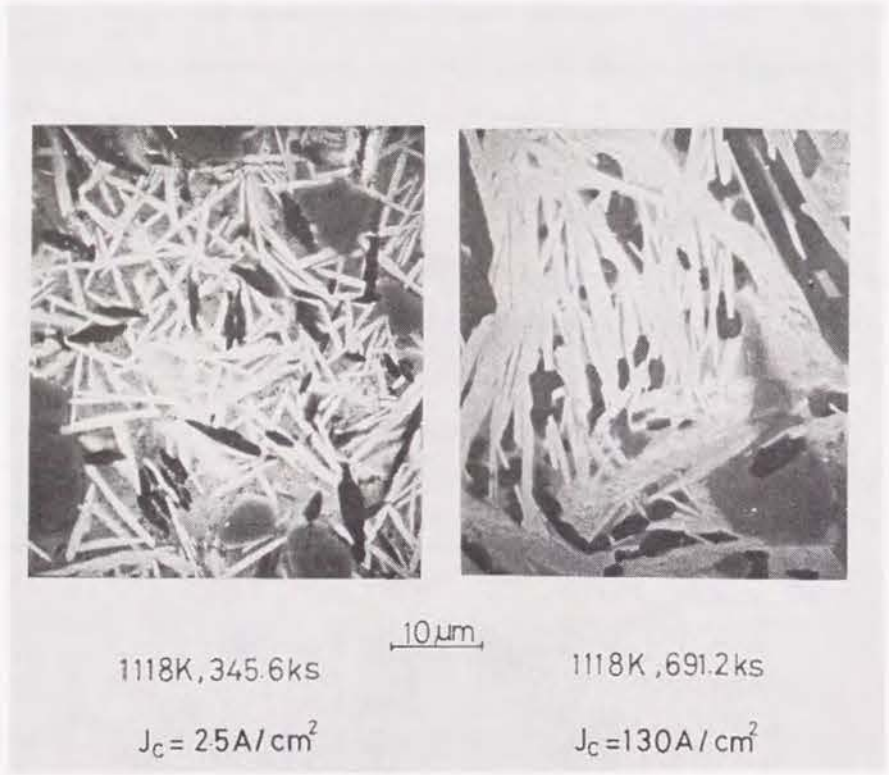

Figure 3.3 Scanning electron micrograph of polished surface for $Bi_{1.8}Pb_{0.2}Sr_2Ca_2Cu_4O_x$ specimen annealed at 1118 K.

for 345.6 ks. J_c for the specimen annealed for long time, was found to be higher than that for the specimen annealed for short time. This is attributed to that connectivity between the grains of superconducting phases is improved by long time heat treatment.

3.3.2 Phase relation

Figure 3.4 shows X-ray powder diffraction patterns for the melt–quenched and heat treated(HT1) specimens of $Bi_2Sr_2Ca_2Cu_3O_x$. The pattern (d) indicates almost halo pattern characteristic of the amorphous phase and a small crystalline peak from CaO phase. Patterns (a), (b) and (c) indicate that various phases crystallized in sequence from the amorphous state during the heat treatment HT1.

Figure 3.5 shows the results of TG-DTA measurements. As shown clearly in DTA curves, a change appeared firstly at about 660 – 670 K, which has been reported [5] to be caused by the glass transition by Komatsu *et al.* The transition temperature decreased by the Pb addition. Three exothermic peaks marked by A, B and C appeared commonly for both specimens with and without Pb additive. The strongest endothermic peak, Y appeared at 1103 or 1113 K was assigned to the onset temperature which associates the appearance of liquid. This temperature corresponds to the temperature of which the weight of the specimen began to decrease. In order to make clear the phase change during crystallization process, the relative X-ray intensities were measured, where the diffraction peaks for each phase mentioned here are cited from references [6–9].

Figure 3.6 shows the dependence of X-ray intensity on annealing temperature for the phases appeared during the heat treatment HT1. The relative intensity indicated here, is the ratio of the intensity of the representative peak to the sum of intensities of all respective peaks, which can be used as a qualitative measure of the volume fraction of each phase. As shown in figure 3.6(a), two crystalline phases, 2201 and CaO were observed to exist in the amorphous matrix at 773 K. Since CaO has already existed in the as quenched specimen, it is suggested that the first exothermic peak at 738 K as shown in figure 3.5 corresponds to the crystallization of 2201 phase. This is consistent with the results

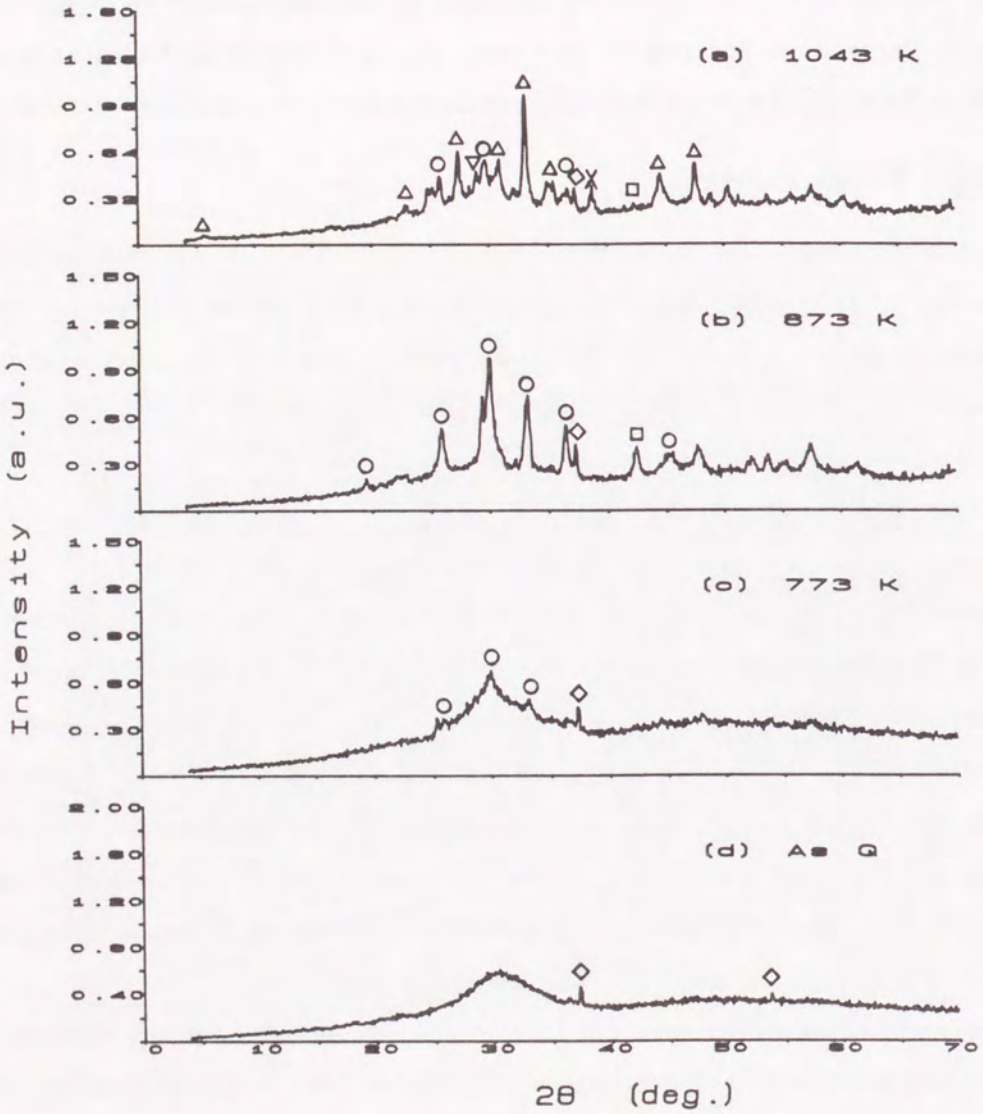

Figure 3.4 X-ray powder diffraction patterns for the none additive specimen as quenched state (a) and after heat treatment HT1 up to various temperatures, where ◯ : 2201, □ : Cu_2O, △ : 2212, ◇ : CaO, ▽ : $(Sr,Ca)_2CuO_3$, × : CuO.

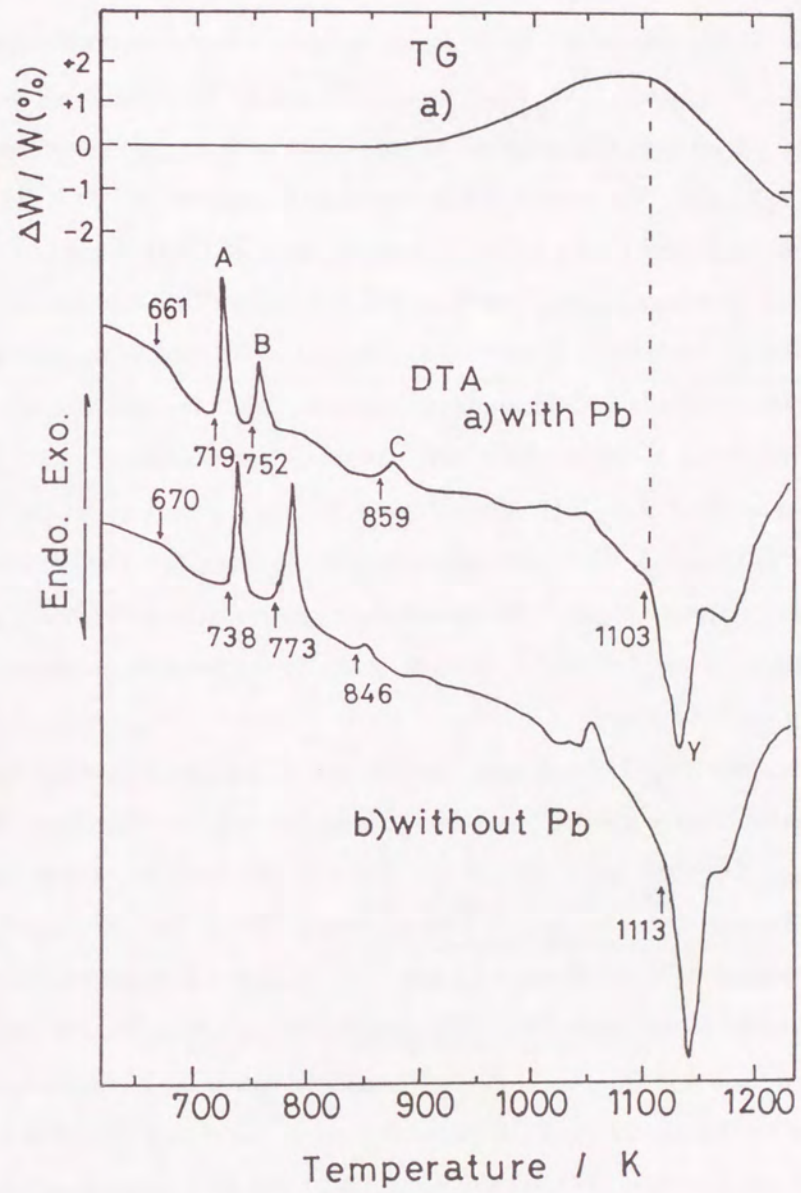

Figure 3.5 TG and DTA curves for the none(a) and Pb additive(b) specimen.

of Ibara *et al.* [10] and Oka *et al.* [11] As shown in figure 3.5, the crystallization of 2201 phase was found to appear at the lower temperature for the Pb additive specimen. According to this, Pb addition is thought to be effective to decrease the crystallization temperature of 2201 phase. The second exothermic peak, B appeared at 773 K for the none additive specimen can be assigned to the crystallization of Cu_2O, because Cu_2O was firstly detected at temperatures lower than 823 K as shown in figure 3.6(a). As shown in figure 3.6(a), the relative X-ray intensity of 2201 phase reached maximum at 823 K and decreased gradually with increasing temperature, while the intensity of 2212 phase was detected at 923 K and increased with increasing temperature up to 1123 K. According to this, the 2212 phase is thought to appear at temperature between 823 and 923 K. As shown in figure 3.5, the third exothermic peak, C began to appear at 846 K for the none additive specimen. Since the appearance of phases detected at 873 K can assigned as mentioned above, the third exothermic peak,C is suggested to correspond to the appearance of the 2212 phase.

Judging from the change of X-ray intensity for 2201 and 2212 phase as shown in figure 3.6(a), it is suggested that the 2201 phase changes continuously into the 2212 phase. Two other phases, Cu_2O and CaO are considered to relate with this reaction. It was found that the Cu_2O phase starts to change into CuO at around 1000 K. The $(Sr,Ca)_2CuO_3$ phase was detected at 1043 K. As shown in figure 3.6(b), Cu_2O phase can be detected at 773 K for the Pb additive specimen. This is due to that the Cu_2O phase already formed at around 752 K as shown in DTA curve for the Pb additive specimen. The behavior on the appearance of 2201 phase for the Pb additive specimen is found to be different from that of none additive specimen. As shown in figure 3.6(b), the 2201 phase disappeared at about 1023 K and appeared again over 1100 K. This reason will be discussed later. Ca_2PbO_4 phase was observed in the temperature region between 973 and 1073 K.

Figure 3.7 shows the annealing temperature dependence of relative X-ray intensity for each phase in the specimens after heat treatment HT2, where the specimen was isothermally annealed for 86.4 ks at various temperatures. In common for both specimens as

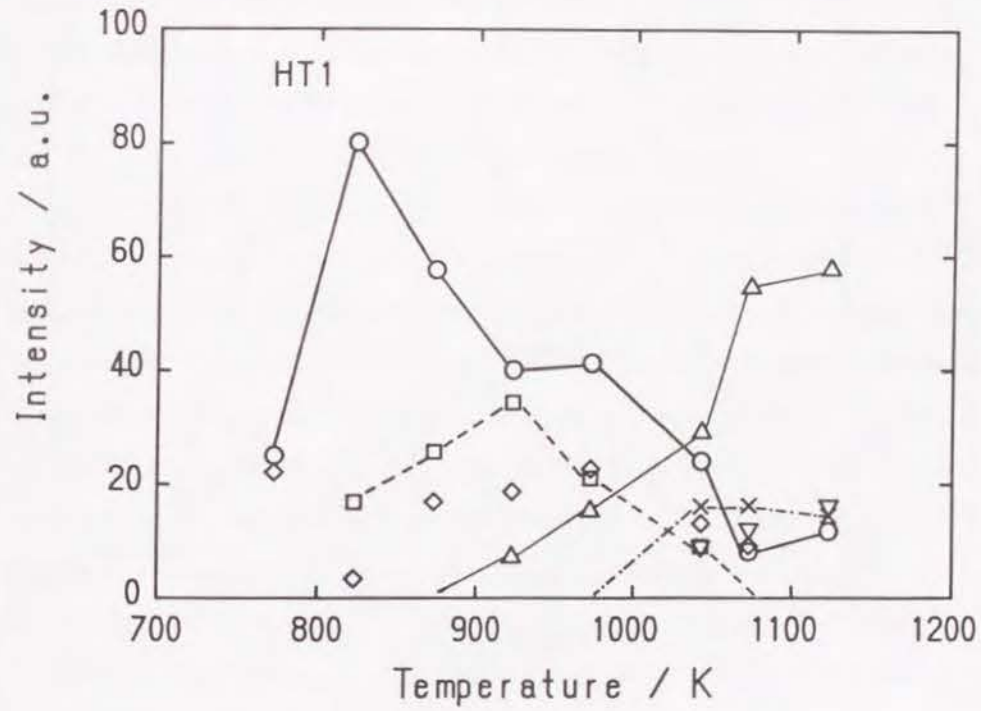

Figure 3.6(a) The relative X-ray intensity of the phases which appeared during heat treatment HT1 as a function of temperature for the none additive specimen, where ○ : 2201, □ : Cu_2O, △ : 2212, ◇ : CaO, × : CuO, ▽ : $(Sr,Ca)_2CuO_3$.

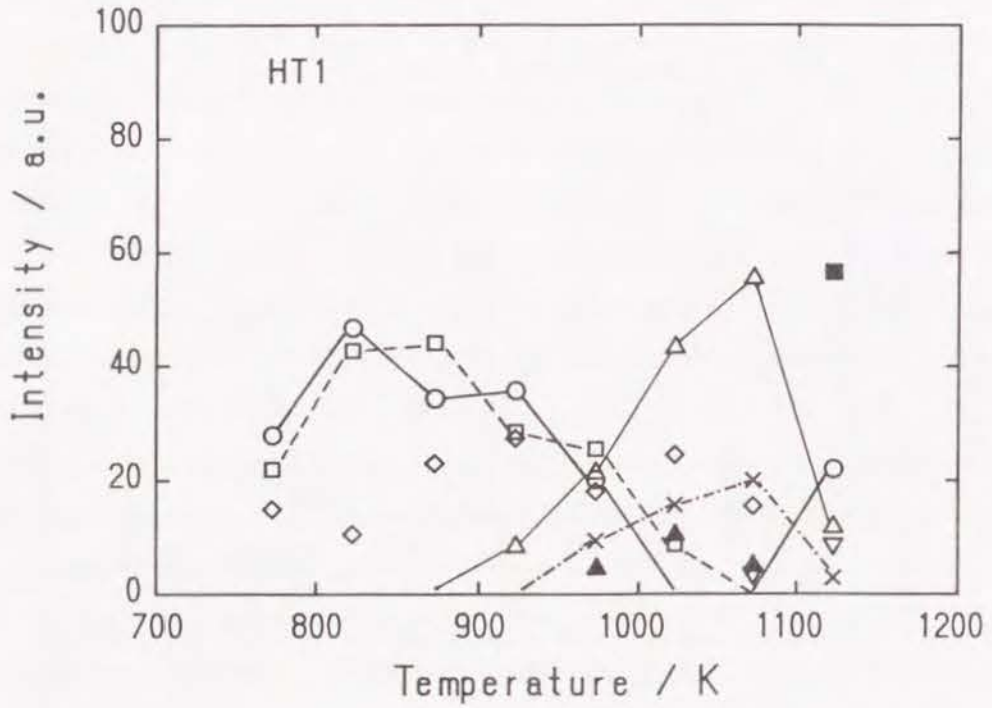

Figure 3.6(b) The relative X-ray intensity of the phases which appeared during heat treatment HT1 as a function of temperature for the Pb additive specimen, where ○ : 2201, □ : Cu_2O, △ : 2212, ◇ : CaO, × : CuO, ▽ : $(Sr,Ca)_2CuO_3$, ▲ : Ca_2PbO_4, ■ : $(Sr,Ca)_3Cu_5O_x$.

shown in figure 3.7(a) and (b), the relative intensity of the 2201 phase decreased with increasing temperature, while 2212 phase appeared at 873 K and its intensity increased with increasing the temperature. Comparing with the result of HT1, Cu_2O could be detected at 773 K and it changed into CuO phase at the lower temperatures for the specimen annealed by HT2. As shown in figure 3.7(b), $(Sr,Ca)CuO_x$ could be detected at 973 and 1073 K for only Pb additive specimen. It should be noted that the 2212, Ca_2CuO_3 and CuO for the none additive specimen exist at 1123 K and the 2212, Ca_2CuO_3 and $(Sr,Ca)_3Cu_5O_x$ for the Pb additive specimen. Judging from X-ray intensity as shown in figure 3.7, the 2212 phase is found to be a major phase at temperatures between 1073 and 1123 K for both none additive and Pb additive specimens.

Figure 3.8 shows the annealing time dependence of relative X-ray intensity for each phase in the Pb additive specimen. The relative X-ray intensity of 2212 phase increased gradually up to near 100 ks, while the 2201 phase decreased gradually and disappeared below 86.4 ks. It was considered that the growth of 2212 phase occurred continuously with increasing annealing time. The 2201 phase was recognized to be unstable at 1123 K from the XRD results. On the other hand, the relative X-ray intensity of the $(Sr,Ca)_2CuO_3$ remained almost constant within the experimental condition. Beyond 604.8 ks, the both relative X-ray intensities of 2212 phase and $(Sr,Ca)_3Cu_5O_x$ decreased and the 2223 phase began to appear and its relative X-ray intensity increased with increasing annealing time. According to this, 2212 and $(Sr,Ca)_3Cu_5O_x$ phases are thought to be associated with the formation and growth of 2223 phase.

According to Noda *et al.* [12] and Oka *et al.* [13], the 2212 phase decomposes to CaO and the liquid at high temperatures above 1373 K. It seems to be reasonable to get the amorphous phase including the crystalline CaO phase by the melt-quenching, when the specimen locates in two phase field of CaO solid phase and the liquid at quenching temperature. As described above, it was made clear that the 2201 phase is crystallized firstly from the amorphous state. By the crystallization of 2201 phase, the element Cu will be enriched around the crystalline phase and then the Cu rich phase is crystallized.

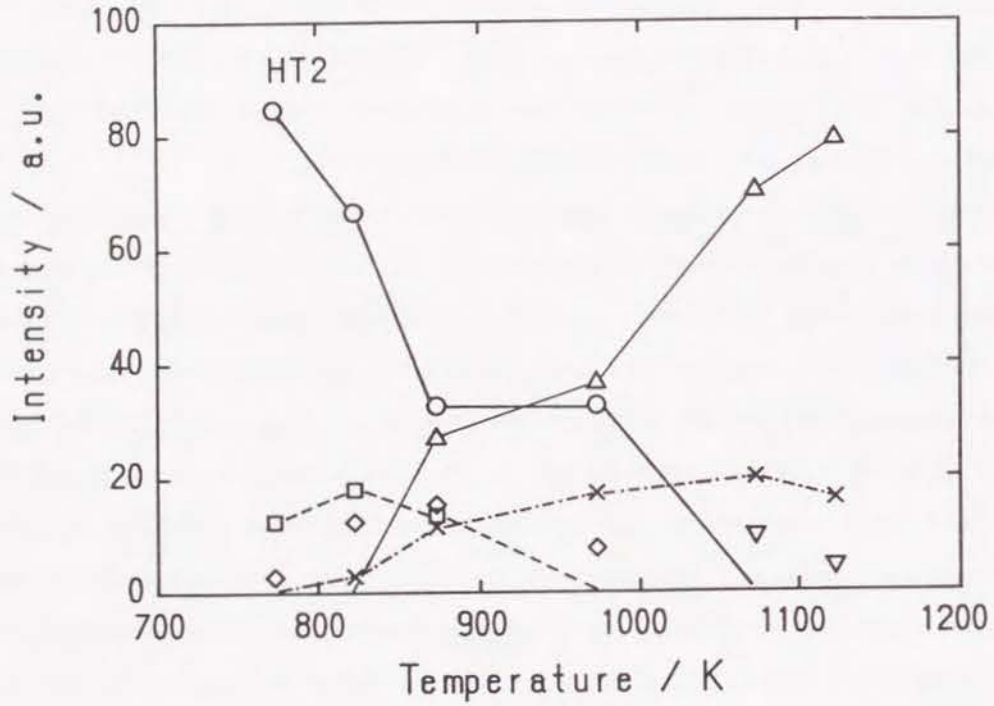

Figure 3.7(a) The relative X-ray intensity of the phases which appeared during heat treatment HT2 as a function of temperature for the Pb additive specimen. For symbol, see Fig. 3.6.

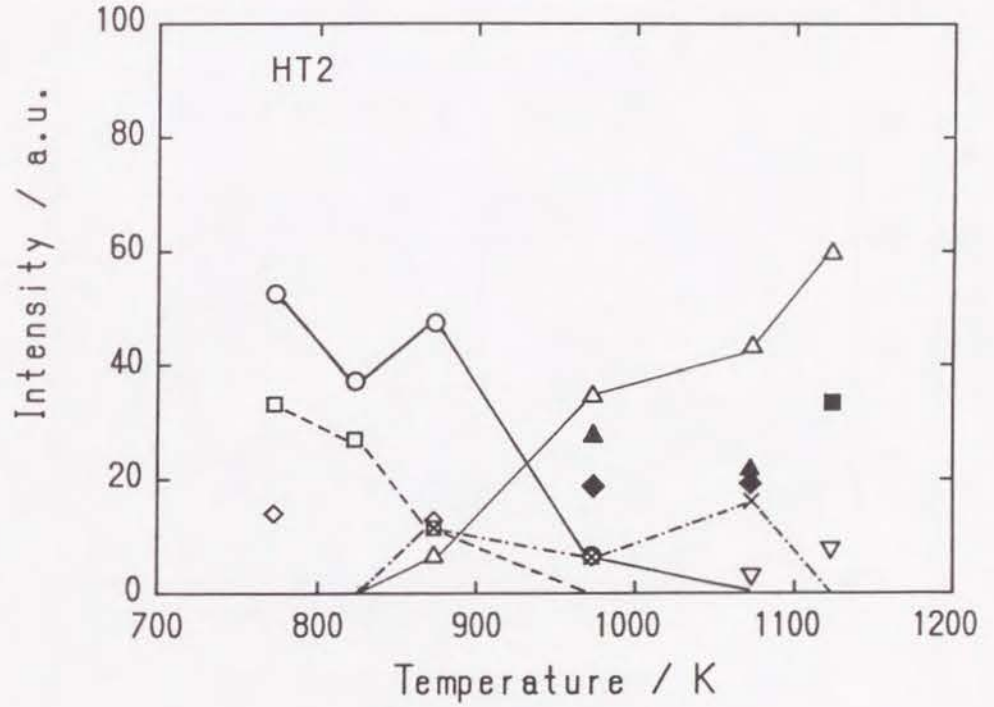

Figure 3.7(b) The relative X-ray intensity of the phases which appeared during heat treatment HT2 as a function of temperature for the Pb additive specimen, where ◆ : $(Sr, Ca)CuO_x$..

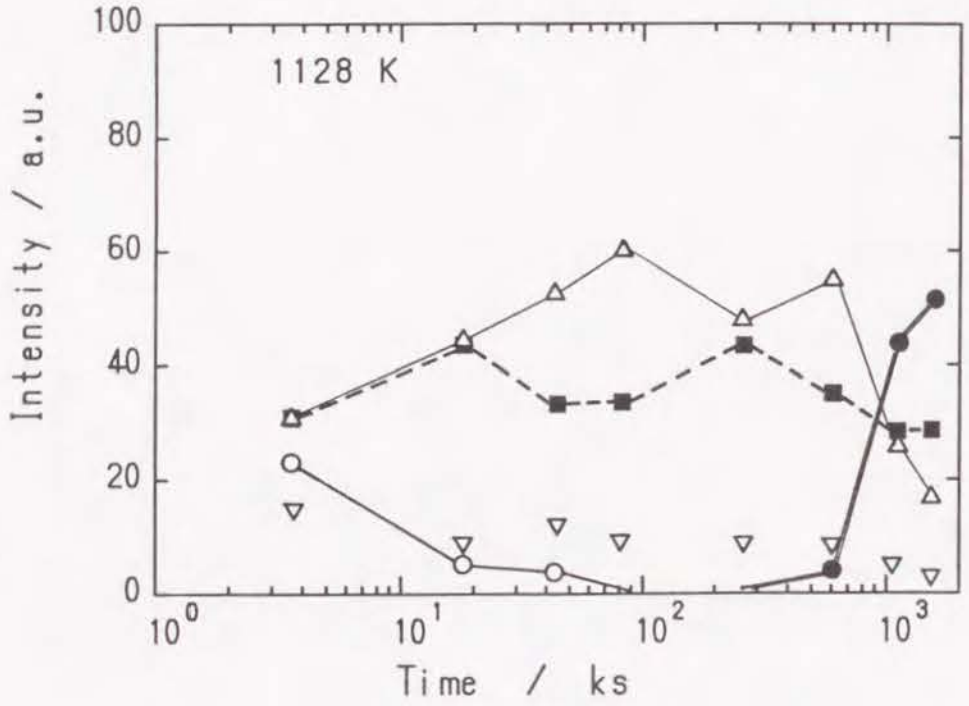

Figure 3.8 The relative X-ray intensity of the phases which appeared during isothermal annealing at 1123 K as a function of temperature for the Pb additive specimen, where ● : 2223 phase.

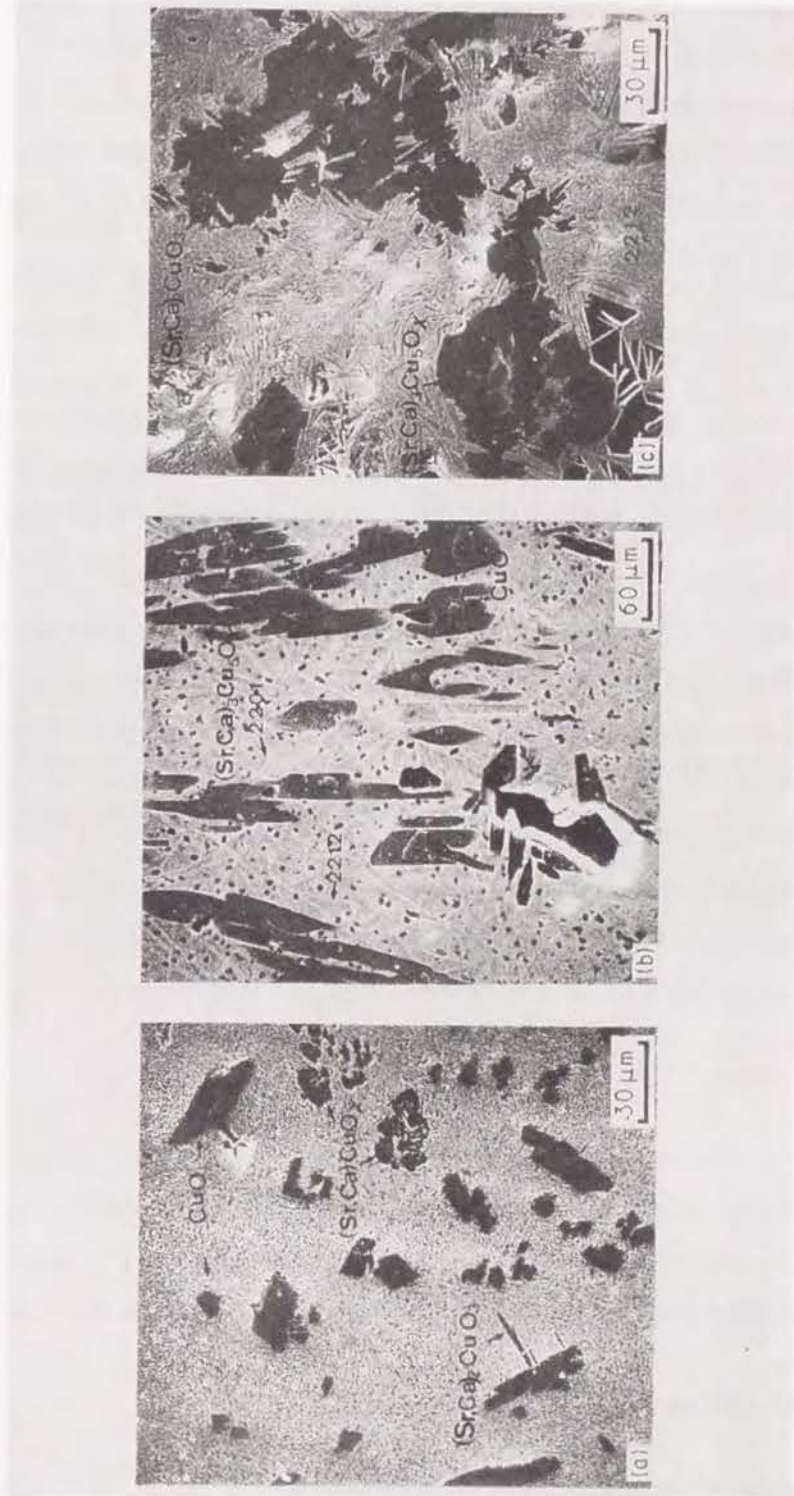

Figure 3.9 Scanning electron micrographs of the polished surface for the Pb additive specimens heat treated by HT1 ((a) 1073 K, (b) 1123 K) or (c) HT2(1123 K, 86.4 ks).

The crystallization of Cu_2O phase was confirmed to occur at temperatures between 752 and 773 K. As shown in figure 3.6(a), the 2212 phase was detected at 923 K, which is crystallized from the remaining amorphous part by the mass balance of elements among the phases. This 2212 phase grows by absorbing the surrounding crystalline phases. During this process, the following reaction may occur;

$$2201 + CaO + 1/2Cu_2O \longrightarrow 2212 \tag{3.1}$$

Meanwhile, Oka *et al.* reported [13] that the structural change of 2201 phase to 2212 phase occurs at temperature range between 1023 and 1073 K for the $Bi_2Sr_2Ca_1Cu_2O_x$ specimens. As shown in figure 3.6, this change was found to occur at the lower temperatures. This difference might be resulted from their different nominal composition.

Figure 3.9(a) shows the microstructure at 1073 K for the specimen annealed by HT1, where $CuO, (Sr, Ca)_2CuO_3$ and $(Sr, Ca)CuO_x$ were observed. The volume fraction of $(Sr, Ca)CuO_x$ phase was evaluated to be negligibly small. As shown in figure 3.9(b), five phases, 2212, 2201, CuO, $(Sr, Ca)_3Cu_5O_x$ and $(Sr, Ca)_2CuO_3$ were detected at 1123 K for HT1 treatment. As CuO is observed inside the $(Sr, Ca)_3Cu_5O_x$ phase, a peritectic reaction is closely related to the formation of $(Sr, Ca)_3Cu_5O_x$ phase. The 2201 phase was observed with large volume fraction. Considering the above results, the following reaction can be suggested in the temperature range between 1073 and 1123 K;

$$2212 + CuO \longrightarrow \text{liquid} + (Sr, Ca)_3Cu_5O_x \tag{3.2}$$

This reaction is accompanying with a partial melting. During quenching, the liquid will be crystallized into 2201 phase. Figure 3.9(c) shows the microstructure annealed at 1123 K for 86.4 ks. It was observed that four phases, 2212, 2201, Ca_2CuO_3 and $(Sr, Ca)_3Cu_5O_x$ coexist. The 2212 phase has grown with plate-like shape and covered over the matrix.

3.4 Conclusion

The main conclusions of the present study are the following;

1. B(P)SCCO amorphous ceramic could be obtained by melt-quenching method. After heat treating $Bi_{1.6}Pb_{0.4}Sr_2Ca_2Cu_3O_x$ amorphous ceramic, superconducting bulk which exhibited 98 K of $T_{c,off}$ could be prepared.

2. Long time heat treatment was effective to increase J_c because the connectivity between the grains of superconducting phases is improved by long time annealing. However, T_c was found to decrease for BPSCCO specimens heat treated for very long time.

3. 2201 phase and Cu_2O were found to be crystallized in sequence from the amorphous phase during heating. These crystallization occurs at the lower temperatures for the specimens with Pb additive.

4. The 2201 phase changed to 2212 phase with increasing temperature up to partial melting.

5. It was suggested that the 2212 phase reacts with CuO, and then the liquid appears accompanying with $(Sr, Ca)_3Cu_5O_x$ phase.

6. The 2223 phase could be formed by prolonged annealing at 1123 K.

References

1. H. Maeda, Y. Takada, M. Fukutomi and T. Asano: Jpn. J. Appl. Phys., **27**(1988)L209.

2. T. Komatsu, R. Sato, K. Imai, K. Matsushita and T. Yamashita : Jpn. J. Appl. Phys., **27**(1988)L550.

3. H. Maeda : *Proc. of Osaka Univ. Int. Symp. on New Developments in Applied Superconductivity* , Osaka, 1988, Ed. by Y. Murakami (World Scientific).

4. M. Takano, J. Takada, K. Oda, H. Kitaguchi, Y. Miura, Y. Ikeda, Y. Tomii and H. Mazaki : Jpn. J. Appl. Phys., **27**(1988)L550.

5. T. Komatsu, R. Sato, C. Hirose, K. Matsushita and T. Yamashita : Jpn. J. Appl. Phys., **27**(1988)L2293.

6. H. Mazaki, T. Ishida and T. Sakuma : Jpn. J. Appl. Phys., **27**(1988)L811.

7. S. Koyama, U. Endo and T. Kawai : Jpn. J. Appl. Phys., **27**(1988)L1861.

8. K. Oda, H. Kitaguchi, J. Takada, A. Osaka, Y. Miura, Y. Ikeda, M. Takano, Y. Bando, Y. Tomii, Y. Oka, N. Yamamoto, Y. Takeda and H. Mazaki : J. Jpn. Soc. of Powder and Powder metallurgy **9**(1988)153.

9. JCPDS card,(*JCPDS International Center for Diffraction Data, Park Lane,1986*)

10. Y. Ibara, H. Nasu, T. Iumura and Y. Osaka : Jpn. J. Appl. Phys., *28*(1989)L37.

11. Y. Oka, N. Yamamoto, H. Kitaguchi, K. Oda and J. Takada : Jpn. J. Appl. Phys., **28**(1989)L213.

12. T. Noda, T. Izumi, A. Nakamura, Y. Shiohara , *in Advances in Superconductivity II*, ed. by T. Ishiguro and K. Kajimura (Spring Velag, 1990)p.239.

13. Y. Oka, N. Yamamoto, Y. Tomii, H. Kitaguchi, K. Oda and J. Takada : J. Jpn. Soc. of Powder and Powder Metallurgy, **36**(1989)37.

Chapter 4

Temperature dependence of phase relation in the Bi-Pb-Sr-Ca-Cu-O superconducting ceramics

4.1 Introduction

Since the discovery [1] of Bi-Pb-Sr-Ca-Cu-O (BPSCCO) superconductor, many efforts have been carried out to investigate the formation mechanism of 2223 high T_c phase. Many groups reported [2–4] that the 2223 phase in BPSCCO system is formed during partial melting and Pb hastens the formation of 2223 phase. The synthesis of 2223 single phase by the usual solid reaction technique has been recognized to be impossible because of the existence of liquid phase. Unknown factors still remain about what phases associate with the formation and decomposition of 2223 phase. From the technical view point for producing high quality BPSCCO bulk, the information of phase relation at respective sintering temperature is very important. Moreover, superconducting properties of ceramic superconductor depend on the volume fraction of superconducting phase as well as the morphology of impurity phases. In this study, we investigated microstructure change and phase relation in BPSCCO bulks sintered at temperatures between 1073 and 1223 K.

4.2 Experimental

High purity Bi_2O_3, PbO, $SrCO_3$, $CaCO_3$ and CuO were weighed and mixed with 1.6:0.4: 1.6:2.0:2.8 in mole ratio of Bi:Pb:Sr:Ca:Cu. After repeating the calcination twice at 1073 K for 43.2 ks and the pulverizing for 10.8 ks, the pellet was prepared by uniaxial cold pressing. It was sintered at temperatures between 1073 and 1223 K for 3.6 – 360 ks in air atmosphere and quenched into liquid nitrogen. The weight of pellet before and after sintering was measured with in accuracy of 0.1 mg. Identification of the phases existed was performed by means of EPMA and XRD analysis (Cu$k\alpha$). By assigning two or more peaks in the powder diffraction pattern, the existence of the phase was registered. TG–DTA was measured with heating rate of 5 K/ min in air atmosphere. Here, calcined powder with 60 mg was used as the specimen for measurement.

4.3 Results and discussion

By using both EPMA and XRD techniques, nine phases have been detected from all the samples examined here. We indicated each phase by using symbol **a** to **i** in this paper as listed in table 4.1.

Table 4.1 Phases existed in the BPSCCO samples sintered at 1073 – 1223 K,detected by the X–ray diffraction (XRD) and electron probe–micro analysis (EPMA).

Symbol	Phase	XRD	EPMA
a	2223	O	X
b	2212	O	X
c	2201	O	O
d	CuO	O	O
e	Ca_2PbO_4	O	O
f	$(Sr,Ca)_2CuO_3$	O	O
g	$(Sr,Ca)_3Cu_5O_x$	X	O
h	$(Sr,Ca)CuO_x$	O	O
i	$(Sr,Ca)O_x$	X	O

By XRD technique, however two phases, **g** and **i** could not be identified because of overlapping with the major superconducting phases. On the other hand, EPMA technique distinguished all phases except the indiscrimination between 2212 and 2223 phase.

Figure 4.1 shows the sintering temperature dependence of bulk density and weight loss, $\Delta W/W$ for the samples sintered for 360 ks at various temperatures. Bulk density decreased continuously with increasing temperature up to 1123 K, but tended to increase at temperatures between 1128 and 1133 K. The decrease or the increase of density of the sample could be explained by the expansion [5] due to the formation and growth of 2223 phase or the appearance of liquid accompanying with the decomposition of 2223 phase, respectively. On the other hand, the weight loss of sample changed with three stages over the temperature range; the rate of weight loss became slightly high at 1103 – 1128 K due to the evaporation of Bi and Pb element during partial melting and the rapid increase beyond 1128 K is attributed to evaporation of volatile element from the increasing liquid.

Figure 4.2 shows the result of TG–DTA measurement in the temperature range between 1023 and 1203 K. As shown in the TG curve, the weight lost continuously and rapidly decreased beyond 1123 K and the decreasing rate became slow above 1143 K. In the DTA curve, some endothermic peaks were observed. The rapid decrease of weight loss and the endothermic peak around 1140 K was due to decomposition of 2212 phase.

Figure 4.3 shows the powder XRD patterns for the samples sintered at temperatures between 1073 and 1113 K. It was found that six different phases were identified for the sample sintered at 1073 K for 360 ks as listed in table 4.2. At temperatures between 1073 and 1113 K, 2212 phase existed as a major phase and the CuO, Ca_2PbO_4, $(Sr,Ca)_2CuO_3$ and $(Sr,Ca)_3Cu_5O_x$ phases were confirmed to coexist. As shown in figure 4.3, three Bragg peaks, (113),(115) and (0010) of 2201 phase were detected at 1073 K. The peak intensity of (0010) decreased with increasing sintering temperature and disappeared at 1113 K. Above 1103 K, it was found that four Bragg peaks of 2223 phase were present. Peak intensities of other phases changed slightly with increasing temperature as shown in figure 4.3. Recently, Ito *et al.* reported [6] that Ca_2PbO_4 reacts with 2201 phase and then

Table 4.2 Phases existed in the sample at temperatures between 1073 and 1223 K, where X indicates a relative amount of the phase.

Temp. (K)	Time (ks)	a 2223	b 2212	c 2201	d CuO	e Ca_2PbO_4	f $(Sr,Ca)_2CuO_3$	g $(Sr,Ca)_3Cu_5O_x$	h $(Sr,Ca)CuO_x$	i $(Sr,Ca)O_x$
1073	360	.	XX	X	X	XXX	X	X	.	.
1093	360	.	XXX	X	X	XX	X	X	.	.
1103	360	X	XX	.	X	XX	X	X	.	.
1108	360	X	XX	.	X	XX	X	X	.	.
1113	360	XX	XX	.	X	XX	X	X	.	.
1118	360	XXX	XXX	.	X	X	X	X	.	.
1123	360	XXXX	X	.	X	X	X	X	.	.
1128	360	XXXXX	.	.	X	.	X	X	.	.
1133	360	XXXX	X	XX	X	.	X	.	XX	.
1143	360	XXX	X	XX	X	.	X	.	XX	.
1153	180	.	.	XXX	.	.	XXX	.	XXX	.
1173	10.8	.	.	XXX	X	.	XXX	.	.	.
1223	3.6	.	.	XXXX	.	.	X	.	.	XXX

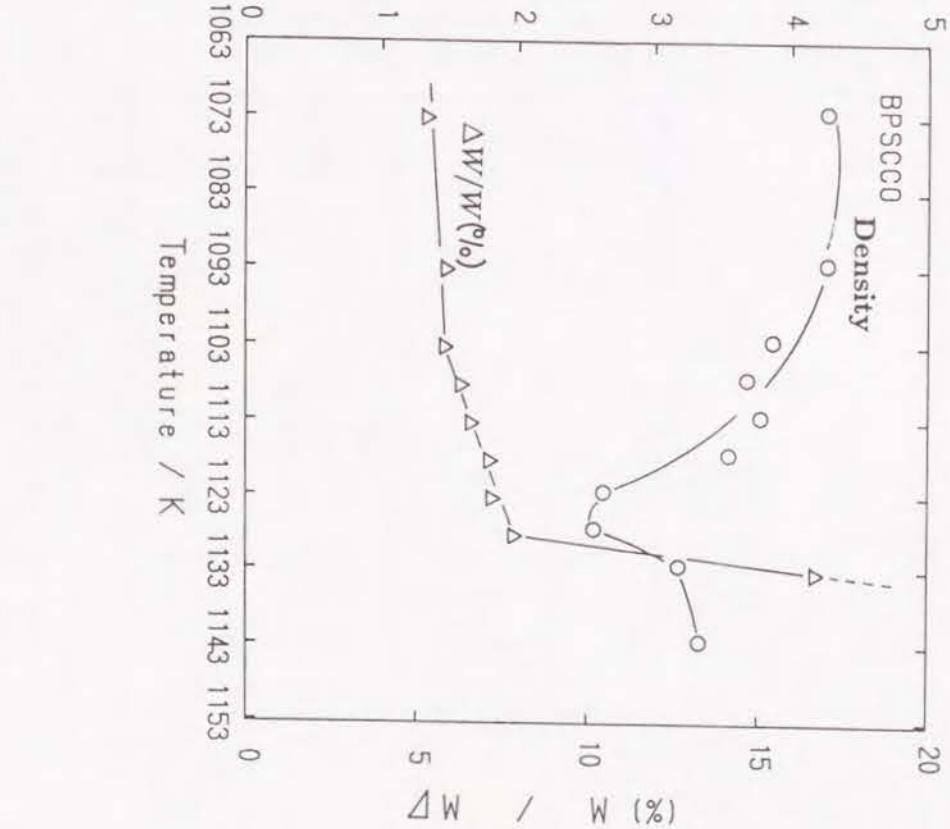

Figure 4.1 The bulk density and weight loss as a function of sintering temperature for the BPSCCO samples sintered for 360 ks .

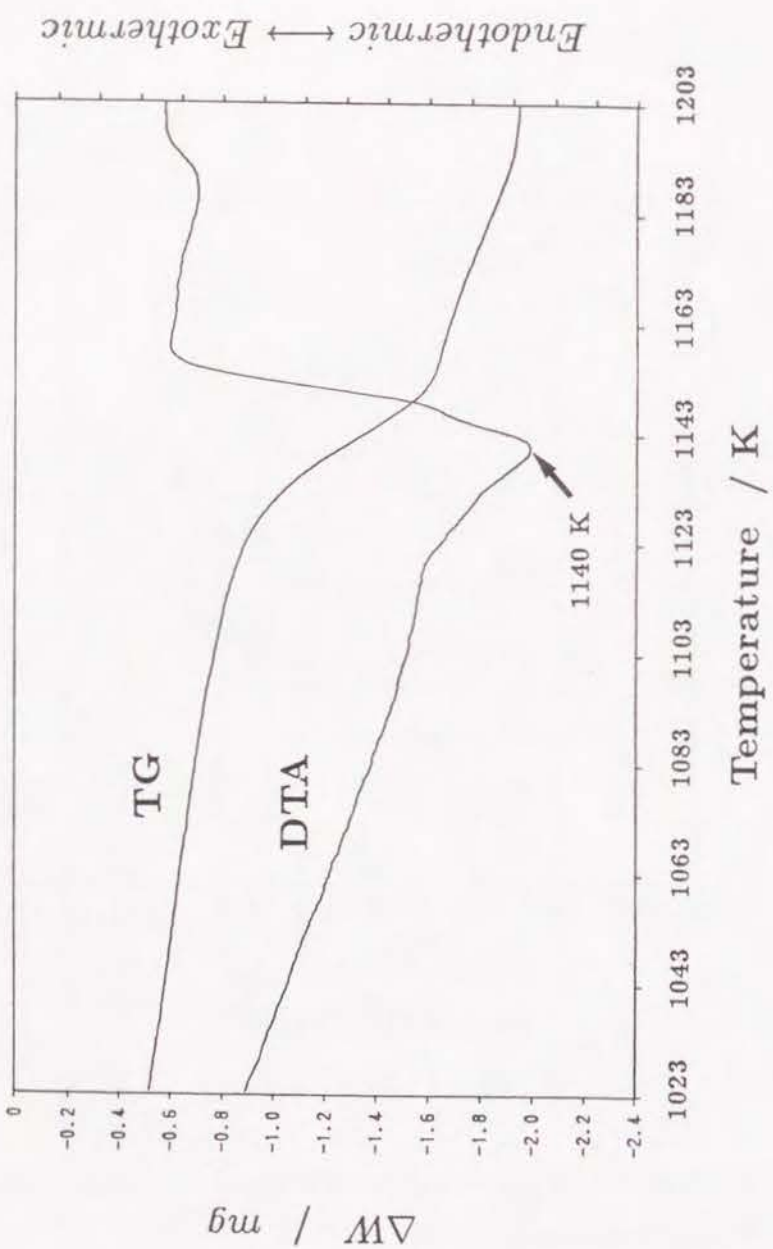

Figure 4.2 TG–DTA curve with heating rate of 5 K / min for the BPSCCO sample sintered at 1073 K for 43.2 ks.

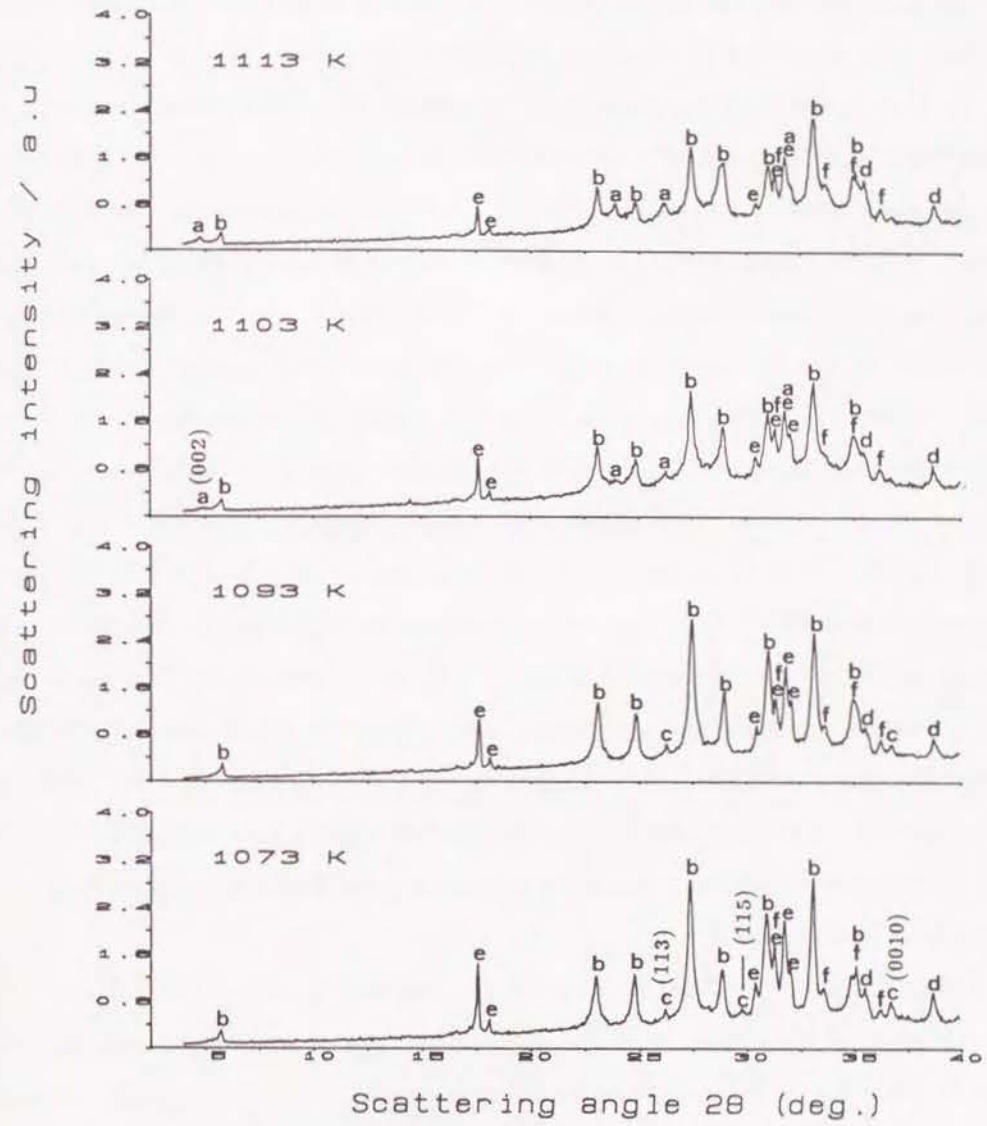

Figure 4.3 X–ray powder diffraction pattern for the samples sintered at 1073 – 1113 K for 360 ks. Here, the phase is denoted by using each symbol listed in table 4.1.

liquid appears. By this eutectic reaction, the 2201 phase is suggested to disappear.

Figure 4.4 shows the powder XRD patterns for the samples sintered at 1118 – 1133 K. At 1128 K, almost X–ray peaks could be assigned to be 2223 phase. Combining the Ito's result and the change of X–ray intensities of 2212,2201, Ca_2PbO_4 and 2223 phases in the temperature range between 1073 and 1128 K, it is suggested that the 2212 phase reacts with the liquid, which was eutectically formed from Ca_2PbO_4 and 2201 phase, and then 2223 phase is formed. Hatano *et al.* [5] suggested that the Pb-enriched-liquid phase enhances dissolution of the 2212 phase and the impurity phases, especially of the high melting temperature compound i.e.$(Sr,Ca)_3Cu_5O_x$. According to this, Ca and Cu is thought to be supplied from the melt and the 2223 phase grew continuously. The X–ray peaks of CuO and $(Sr,Ca)_2CuO_3$ were still observed but the X–ray peaks of 2212 and Ca_2PbO_4 phase diminished at 1128 K. According to this, CuO and $(Sr,Ca)_2CuO_3$ phases are suggested to be inactive with the formation of 2223 phase. Judging from the change of X–ray pattern between 1128 and 1133 K, it is considered that 2223 phase began to decompose into liquid and other phases. At 1133 K, the X–ray peaks of 2212 phase which diminished at 1128 K were again observed and many peaks of 2201 phase were also detected. It was considered that 2212 and 2201 phases were crystallized from the liquid when the sample was quenched into liquid nitrogen from sintering temperature as reported [7] by Oka.*et al.*

Figure 4.5 shows the XRD patterns for the samples sintered at 1143 – 1223 K. The X–ray peaks of 2212 phase were also detected at 1143 K. At 1153 K, 2223 and 2212 phases could not be detected, while the X–ray intensities of $(Sr,Ca)_2CuO_3$, $(Sr,Ca)CuO_x$ and 2201 phase remarkably increased. $(Sr,Ca)CuO_x$ phase was found to diminish over 1173 K.

Figure 4.6 shows the change of X–ray intensity for (002)plane of 2223 phase in the samples sintered for 360 ks and 72 ks against sintering temperature. For the case of 360 ks sintering, 2223 phase could be detected at temperatures between 1103 and 1143 K. The larger amount of 2223 phase was produced in the narrow temperature range between

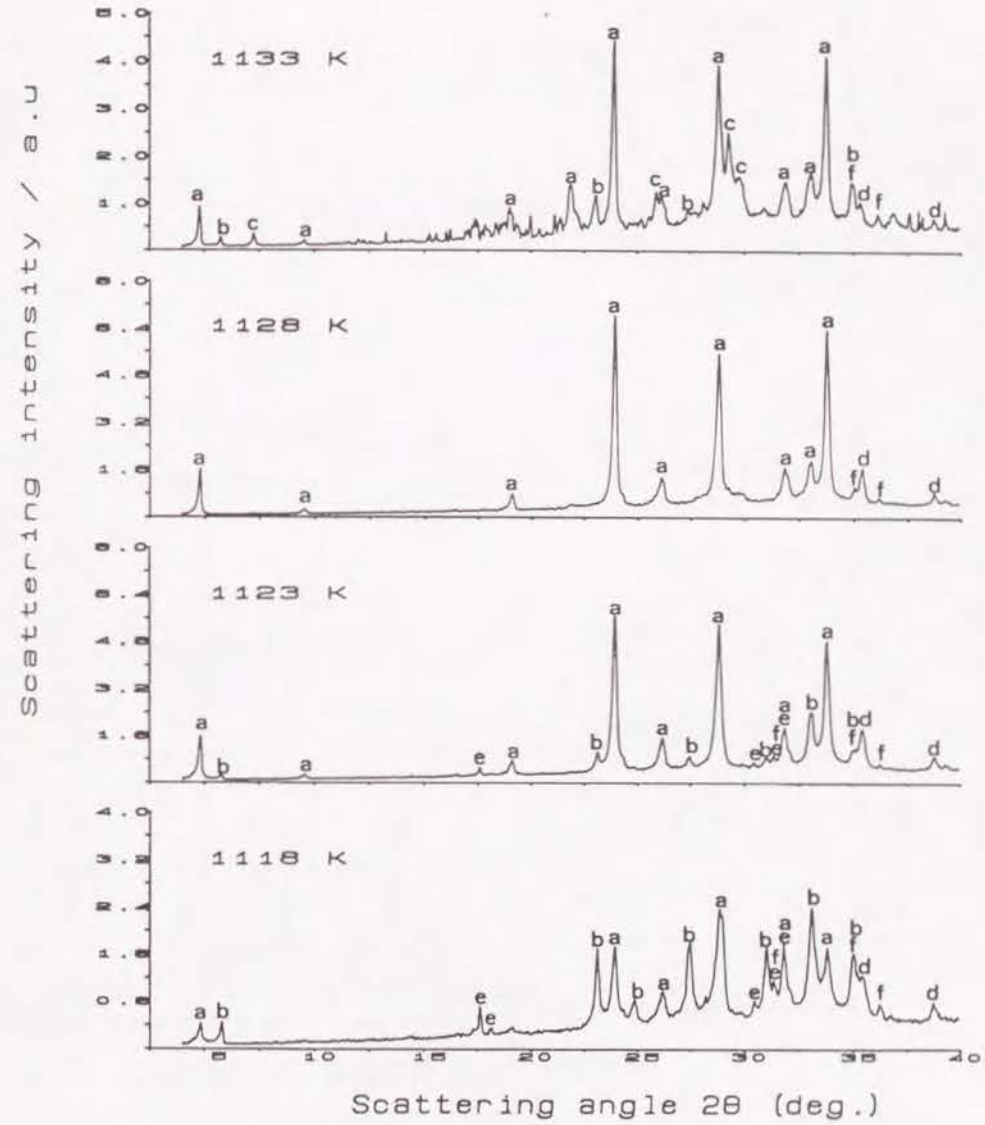

Figure 4.4 X–ray powder diffraction pattern for the samples sintered at 1118 – 1133 K for 360 ks.

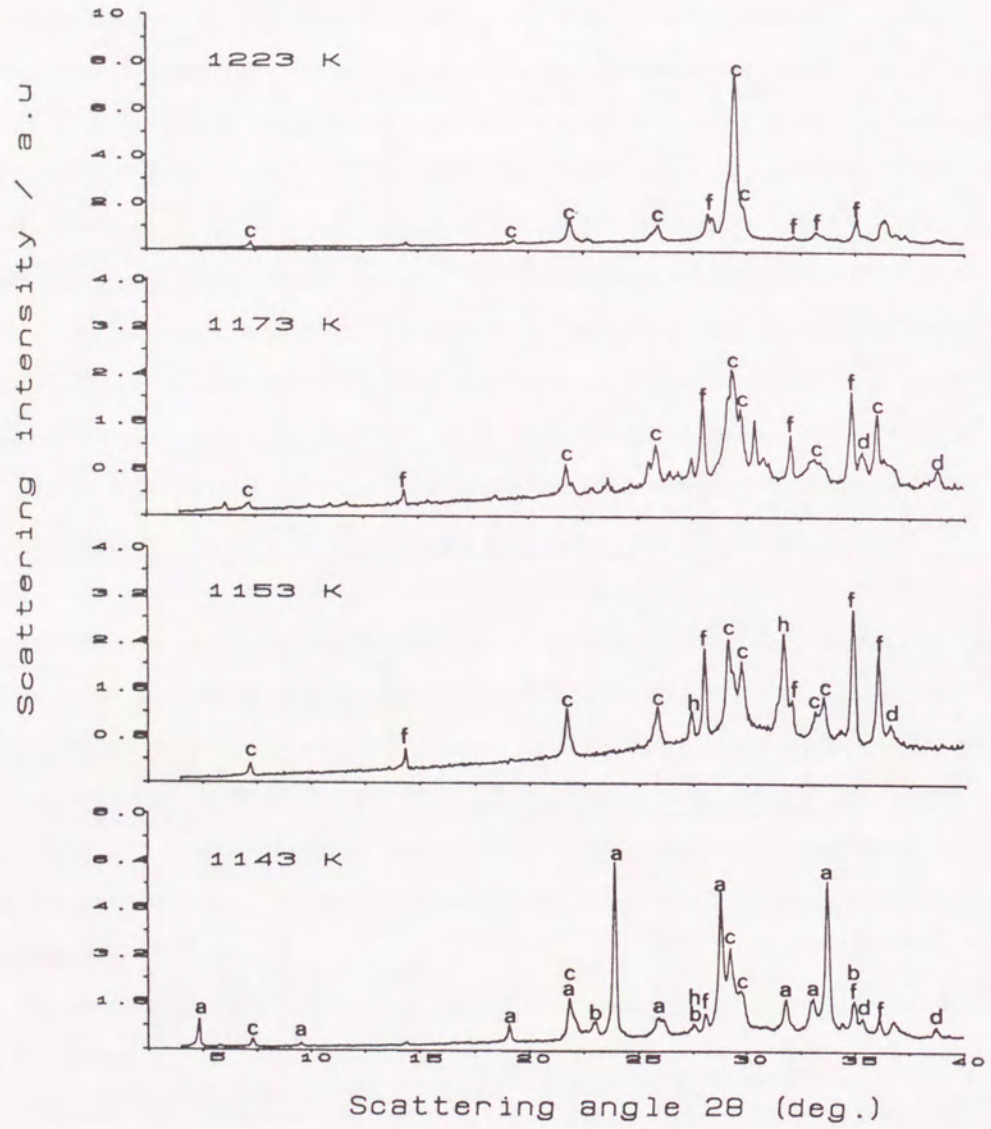

Figure 4.5 X-ray powder diffraction pattern for the samples sintered at 1143 – 1153 K for 360 ks , at 1173 K for 10.8 ks and at 1223 K for 3.6 ks.

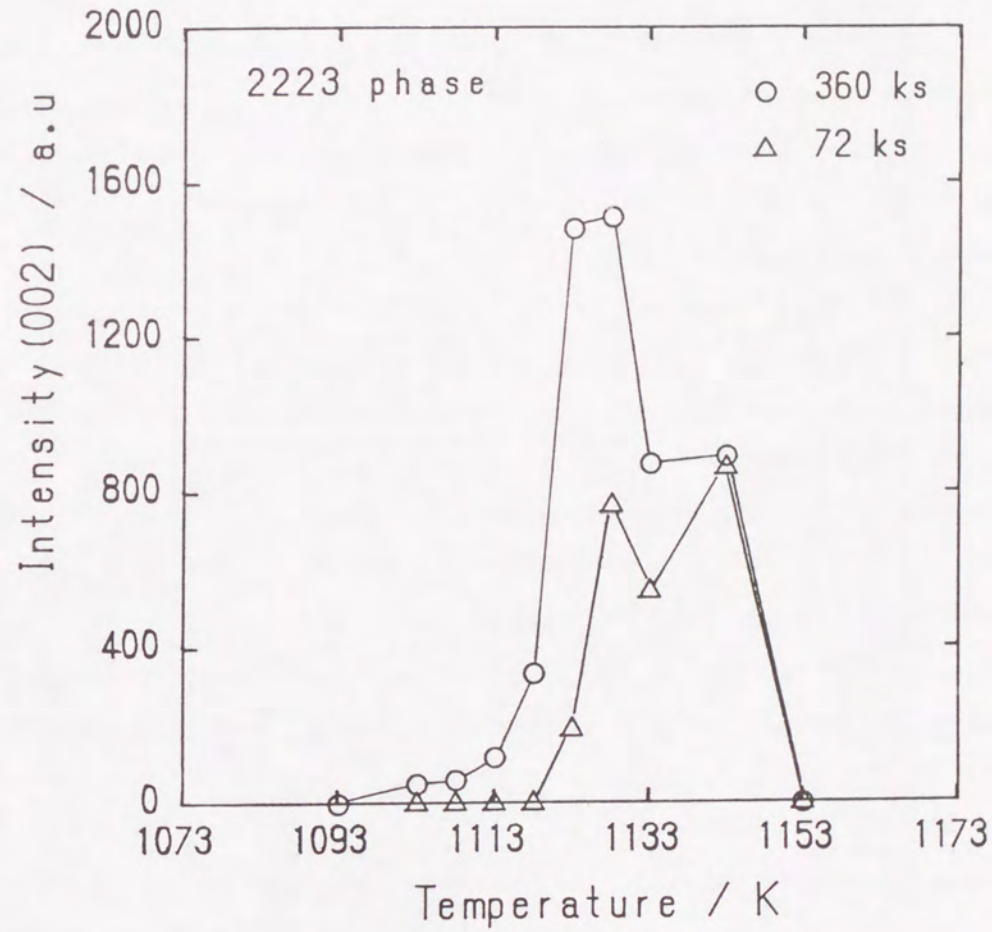

Figure 4.6 The X-ray intensity of (002) plane of 2223 phase as a function of sintering temperature for the samples sintered for 360 and 72 ks.

1123 and 1128 K. The temperature range shifted at the higher temperature for the samples sintered for the shorter time of 72 ks . As clearly shown in figure 4.6, it is concluded that the 2223 phase is produced only at temperatures between 1103 and 1143 K.

Figure 4.7 shows the microstructure of polished surface for the samples sintered at 1093 – 1113 K for 360 ks. It was observed that plate –like grains of 2212 phase distribute randomly together with impurity phases. A coarsening occurred by coalescence among grains of 2212 phase at 1093 – 1108 K. Impurity phases such as Ca_2PbO_4, CuO, $(Sr,Ca)_2CuO_3$ and $(Sr,Ca)_3Cu_5O_x$ were commonly observed at 1098 – 1113 K.

Figure 4.8 shows the microstructure of polished surface for the samples sintered at 1118 – 1133 K. At 1128 K, the major phase was a dense 2223 phase. Impurity phases such as $(Sr,Ca)_2CuO_3$ and $(Sr,Ca)_3Cu_5O_x$ were still observed. At 1133 K, coarse grains of $(Sr,Ca)_2CuO_3$ and $(Sr,Ca)CuO_x$ were observed in the wide region.

Figure 4.9 shows the microstructure of polished surface for the samples sintered at 1143 – 1233 K. $(Sr,Ca)_2CuO_3$ phase which has facet interface and $(Sr,Ca)CuO_x$ phase became large in size at 1143 – 1153 K. Judging from crystal morphology and amount of these two phases,$(Sr,Ca)_2CuO_3$ and $(Sr,Ca)CuO_x$, they are suggested to be formed during decomposition of 2223 phase. No $(Sr,Ca)CuO_x$ phase could be observed over 1173 K. The phase assigned by **i** at 1223 K was estimated to have a chemical form of $(Sr,Ca)O_x$ by means of EPMA analysis, where the composition ratio Sr/Ca was about 0.86/0.14. This phase was firstly identified in the present study.

Combining the results of XRD analysis with EPMA analysis, the temperature dependence of phase relation at respective temperature was evaluated as indicated in table 4.2. The relative amount of each phase is indicated by the number of symbol **X**. The 2223 phase is present maximumly at 1128 K, where no 2212, 2201 and Ca_2PbO_4 are observed, but a small CuO, $(Sr,Ca)_2CuO_3$ and $(Sr,Ca)_3Cu_5O_x$ coexist. The 2201 phase disappeared above 1093 K, but it was detected from the samples quenched from temperatures above 1133 K, because it forms from the melt during quenching. Ca_2Pb0_4 is suggested to

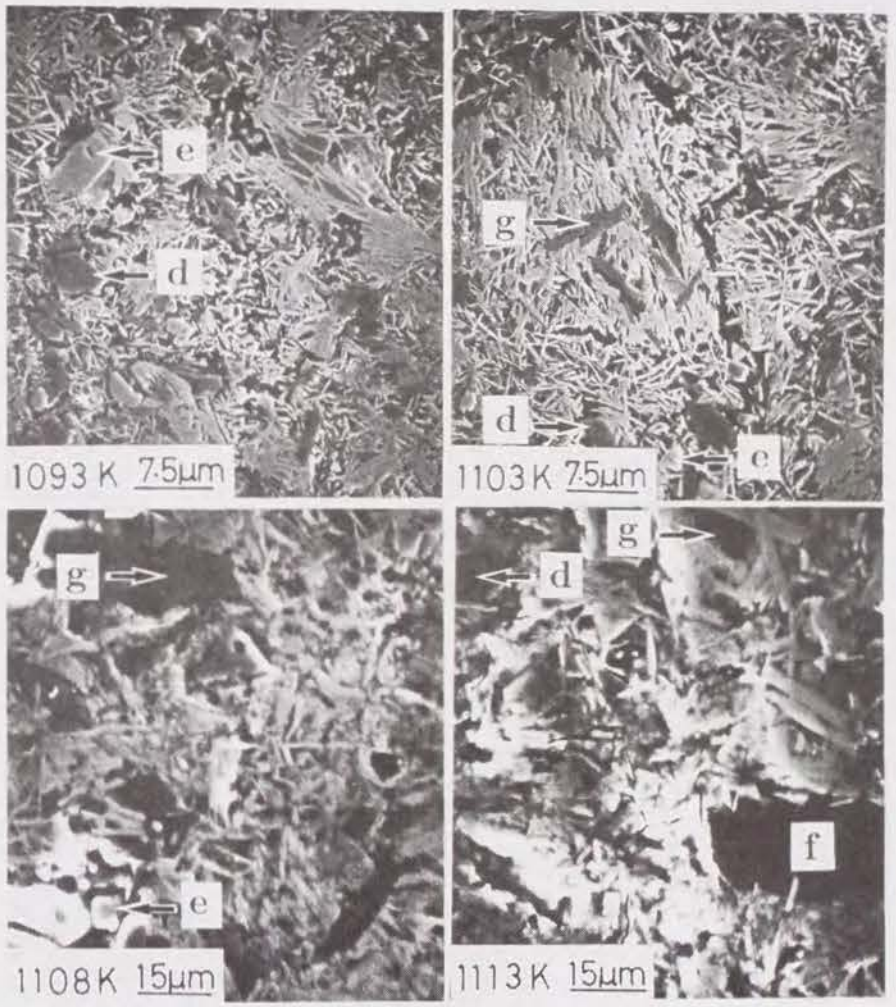

Figure 4.7 Scanning electron micrographs of polished surface for the samples sintered at 1093 – 1113 K for 360 ks.

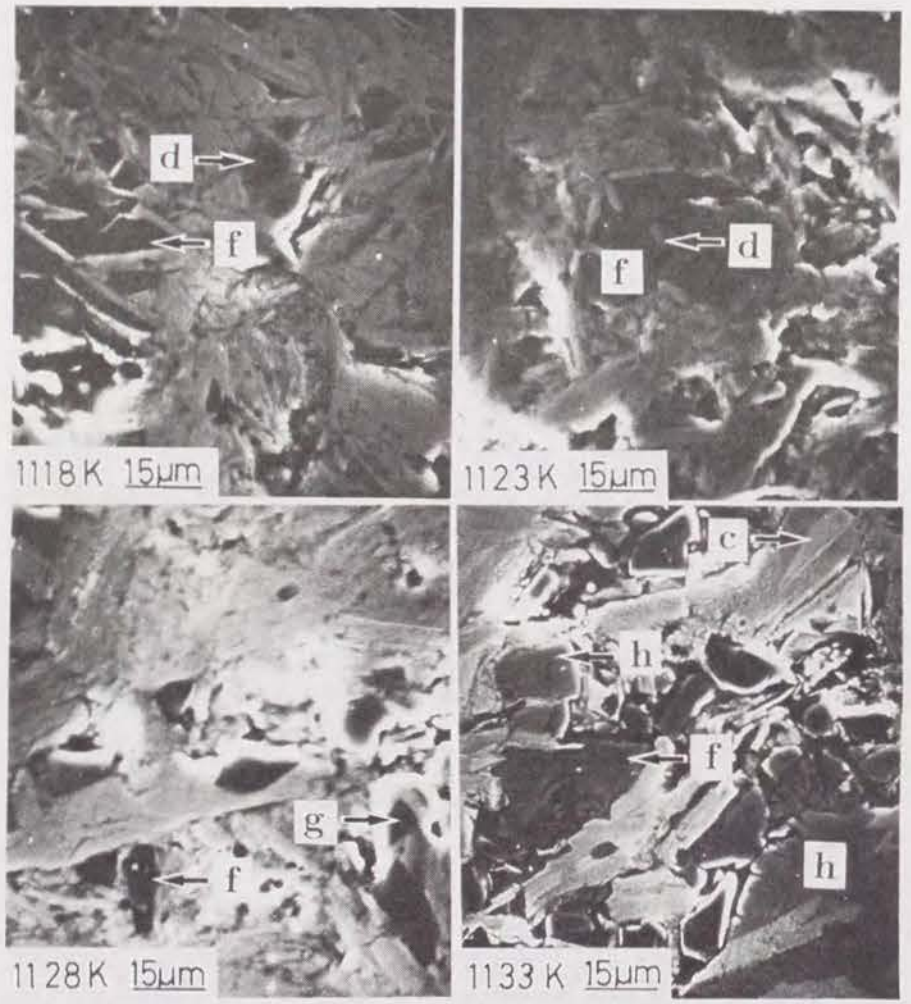

Figure 4.8 Scanning electron micrographs of polished surface for the samples sintered at 1118 – 1133 K for 360 ks.

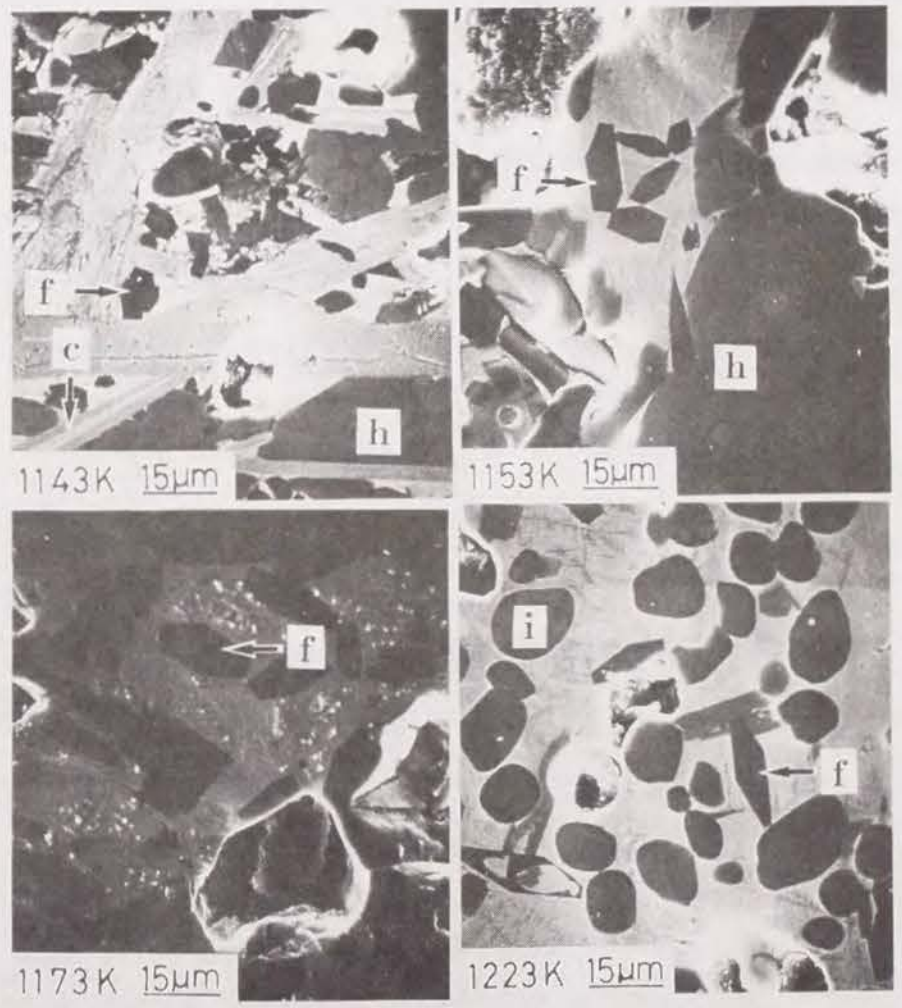

Figure 4.9 Scanning electron micrographs of polished surface for the samples sintered at 1143 – 1153 K for 360 ks, at 1173 K for 10.8 ks and at 1223 K for 3.6ks.

diminish over 1123 K by melting. $(Sr, Ca)_2CuO_3$ phase was confirmed to exist at all temperatures investigated.

4.4 Conclusion

The phase relation and the formation condition of 2223 phase in the BPSCCO system were widely investigated by using samples sintered at various temperatures. The conclusions obtained by present study could be summarized as follow;

1. The 2223 phase was found to be formed by the reaction of 2212 phase with the liquid, which is produced eutectically from 2201 phase and Ca_2PbO_4 and 2223 phase decomposes into liquid and $(Sr, Ca)_2CuO_3$ and $(Sr, Ca)CuO_x$ phases.

2. 2212 and 2201 phases were confirmed to be formed during quenching from the sintering temperature above 1133 K.

3. $(Sr, Ca)O_x$ compound was firstly observed in the sample sintered at 1223 K.

References

1. M. Takano, J. Takada, K. Oda, H. Kitaguchi, Y. Miura, Y. Ikeda, Y. Tomii and H. Mazaki : Jpn. J. Appl. Phys.,**27** (1988)L1041.

2. N. Kijima, H. Endo, J. Tsuchiya, A. Sumiyama, M. Mizuno and Y. Oguri : Jpn. J. Appl. Phys.,**27** (1988)L1852.

3. A. Ono : Jpn. J. Appl. Phys., **27** (1988)L2276.

4. A. Oota, A. Kirihigashi, Y. Sasaki and K. Ohba : Jpn. J. Appl. Phys., **27** (1988)L2289.

5. T. Hatano, K. Aota, S. Ikeda, K. Nakamura and K. Ogawa : Jpn.J.Appl.Phys., **27** (1988)L2055.

6. H. Ito, Y. Ikeda, S. Shimomura, Z. Hiroi, M. Takano, Y. Bando, J. Takada, K. Oda, T. Egi, H. Kitaguchi and Y. Miura : Proc. of 2nd Int. Symp. on Superconductivity (ISS'89) ed. by T. Ishiguro and K. Kajimura (Springer Velag, 1990)137.

7. Y. Oka, N. Yamamoto, Y. Tomii, H. Kitaguchi, K. Oda and J. Takada : Jpn. J. Appl. Phys., **28** (1989)L801.

Chapter 5

Heat treatment dependence of superconducting properties in Ag sheathed Bi-Pb-Sr-Ca-Cu-O tapes

5.1 Introduction

The serial discoveries of high temperature superconductors(HTSC) caused many possibilities to the field of power system and electronics. Comparing with the metallic superconductors, however, many difficulties are involved in HTSC. Especially, low critical current density has been embossed on the development of this material. This is thought to be mainly due to intrinsic physical properties such as short coherence length, anisotropy of property and microstructure factors such as percolation, weak link and pinning centers. Considering the application of high temperature superconductor into electric and electronic field, the development of superconducting wire is indispensable. For realizing this, following conditions are requested.

1. Improvement of superconducting property
2. Improvement of mechanical property
3. Productivity for long wire

Up to date, many processes for wire fabrication shown in table 5.1 have been ceaselessly developed and then, high quality materials of HTSC have been obtained. However, the

Table 5.1 Various fabrication processes for high temperature superconductors

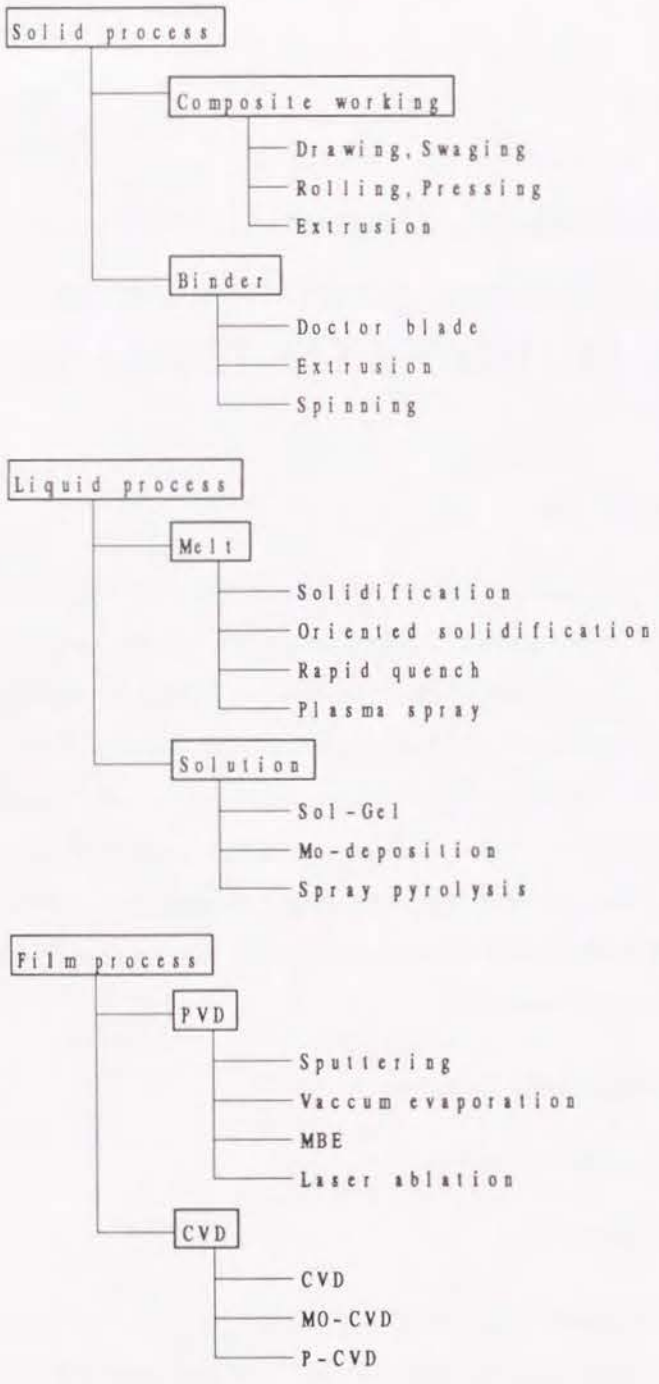

materials which clearly satisfied above conditions are few.

The *powder-in-tube technique* has been known as the most suitable process for wire fabrication because of many potentialities. As a composite processing, thermomechanical treatment (TMT) is employed in the process of this technique and the silver which is chemically stable to other elements involved in oxide and superior to oxygen diffusion is used for tube. The microstructure control of oxide in Bi-(Pb)-Sr-Ca-Cu-O superconducting tapes can be achieved by means of optimizing the TMT condition and choosing the combination of cold working processing.

There are two main currents from the viewpoint for utilizing the B(P)SCCO superconducting phases, which are 2212 low T_c(80 $\sim$ 85 K) phase or 2223 high T_c (105 $\sim$ 110 K) phase. In the meaning of applied superconductivity, superconducting wire made from BSCCO of 2212 phase is expected to be used as a coil of superconducting magnet operated at 4.2 K because of low critical temperature(80 $\sim$ 85 K) . Since single phase of 2212 phase can be obtained, the refinement of microstructure is mainly expected from improvement of textured structure. Recently, critical current densities (at 4. 2 K) with practical level have been reported [1,2] by Enomoto and Kase *et al.* On the other hand, the basic studies for the Ag sheathed BPSCCO superconducting wire which can be utilized at liquid nitrogen temperature has been carried out [3–5] by Sato, Yamada, Oh *et al.*

In the present study, the heat treatment conditions of thermomechanical treatment were minutely investigated as basic research for developing Ag sheathed BPSCCO with high performance; especially influences of TMT cycle, temperature and cooling rate on critical current density have been examined. Based on the present experimental results, the influence of microstructural factors on J_c and T_c has been discussed.

5.2 Experimental

5.2.1 Specimen preparation

High purity(99.9 %) Bi_2O_3, PbO, $SrCO_3$, $CaCO_3$ and CuO powders were weighed with composition of $Bi_{0.8}Pb_{0.2}Sr_{0.8}CaCu_{1.4}O_x$ and mixed sufficiently. The mixture was calcined

at 1073 K for 43.2 ks in air in order to obtain the 2212 phase and pulverized for 10.8 ks. This powder is called A in this article. This process was repeated for preparing homogeneous calcined powders. A part of the powder was further heat treated at 1118 K for 360 ks to produce 2223 phase(powder B). Calcined powders were filled in the silver tube with dimension of 5 or 6 mm outer diameter and 1 mm thickness. The cold working process employed here is described as follows. The diameter of silver tube was reduced by swaging and other techniques such as drawing, rolling with groove, cassette roller die processing, in sequence. Then the thin wire was deformed to tape shaped specimen by cold pressing with uniaxial pressure of about 600 $\sim$ 900 MPa. The specimen was heat treated twice in air. The first and second heat treatment in TMT process is called HT1 and HT2, respectively in the present text. After 1st heat treatment, the specimen was repressed. The procedure of specimen preparation and TMT process was presented in figure 5.1 and 5.2, respectively. The size of tape specimen which was finally obtained was presented in figure 5.3.

5.2.2 Measurement of superconductivity

The critical transition temperature, T_c was resistively measured. Here, $T_{c,off}$ and $T_{c,on}$ were defined by the temperature at which the resistivity becomes zero, and the temperature of intersection of normal state line against the transition line, respectively. This definition was presented in figure 5.4 The critical transport current measurements have been performed at 77.3 K without magnetic field. This measurements were automatically performed by using personal computer system as shown in figure 5.5 and the I_c was defined by 1 μV / cm criterion. The critical current density was calculated as the critical current divided by the cross-sectional area of the oxide layer in specimen.

5.2.3 Microstructure analysis

In order to prepare the specimen for observation, the specimens after measurements were cut out and mounted to resin. The surface was ground with emery papers of silicon carbide and finally polished with alumina dust by using rotating polishing wheel.

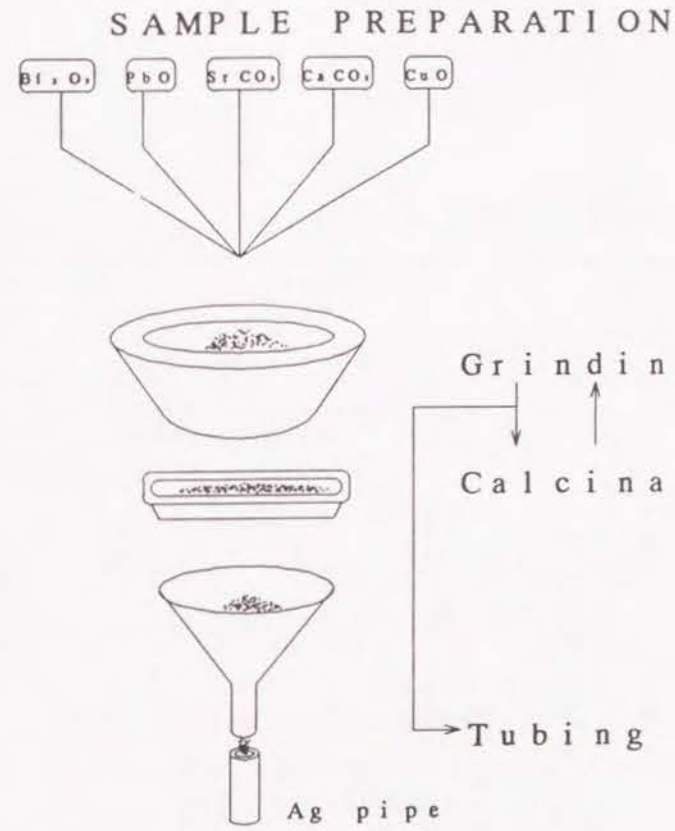

Figure 5.1 Schematic illustration of specimen preparation.

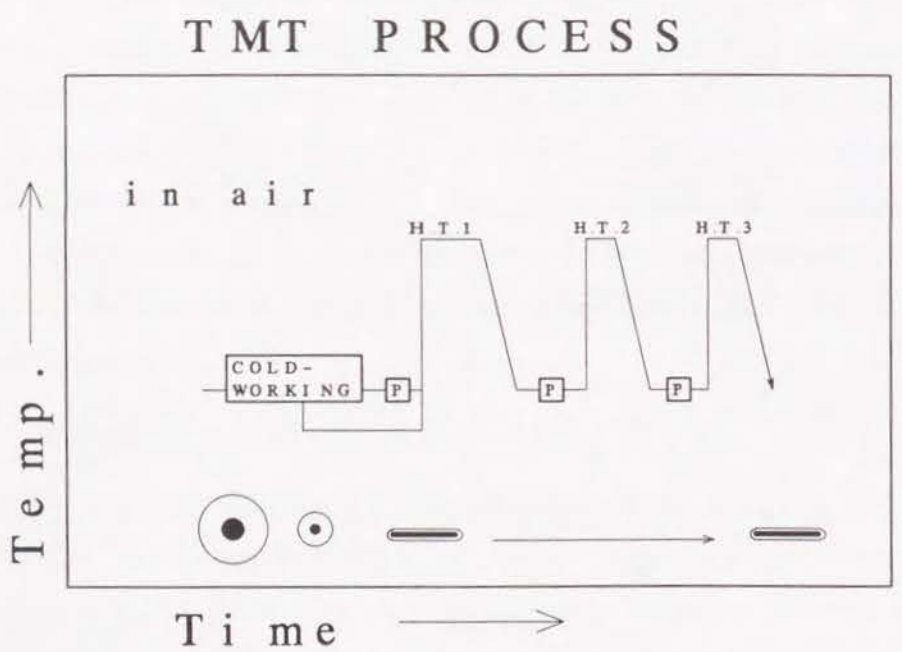

Figure 5.2 Schematic illustration of thermomechanical treatment.

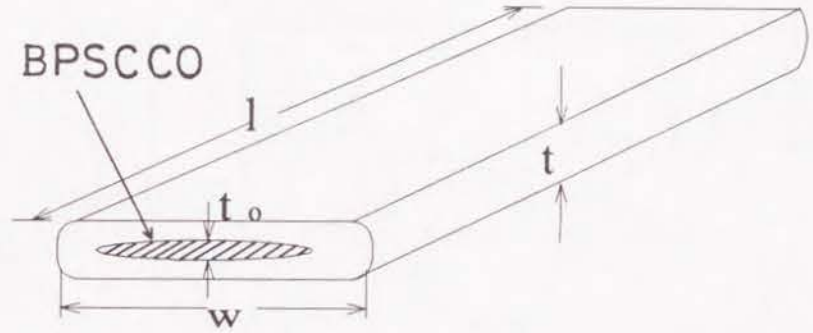

t : 0.05 ~ 0.3 mm

w : 2 ~ 4 mm

l : 17 ~ 25 mm

Figure 5.3 Size of tape specimen.

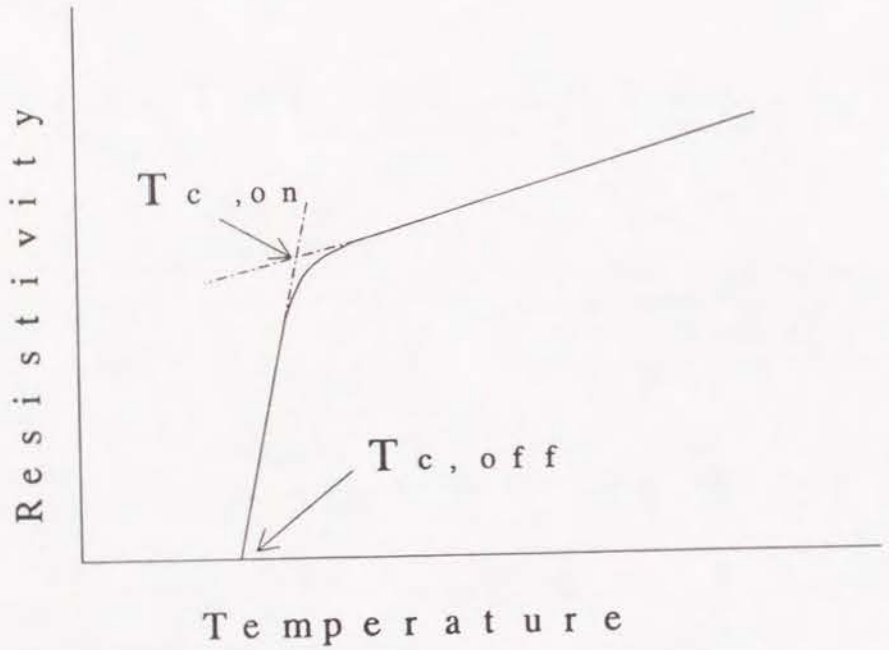

Figure 5.4 Schematic illustration of definition for critical transition temperatures, $T_{c,on}$ and $T_{c,off}$.

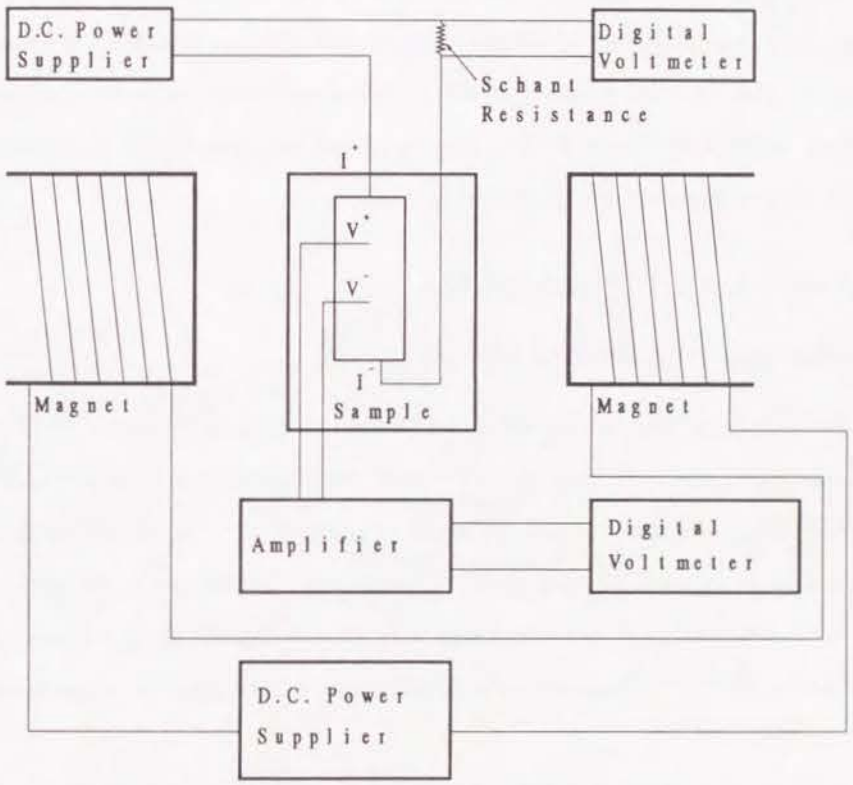

Figure 5.5 Schematic illustration of electric circuit for the critical transport current measurement by automatic system.

The microstructure of polished surface was observed by means of secondary electron images using scanning electron microscope(SEM). The identification of phases existed in BPSCCO oxide was carried out by means of electron probe micro analyser(EPMA) and X–ray powder diffractomer(PHILLIPS PW-1700) with Cu $k\alpha$, where the specimen for XRD measurement was prepared by stripping the Ag sheath and attaching it to silicon sheet of single crystal. In order to evaluate the preferred orientation of grain of superconducting phases, Schultz reflection method was employed as a pole figure measurement. The geometry of measurement was presented in figure 5.6.

5.3 Results and discussion

5.3.1 Influence of calcined powders

Figure 5.7 shows the X–ray powder diffraction pattern for calcined powders. 2212 phase as a major phase was observed together with other impurity phases such as Ca_2PbO_4, CuO, $(Sr,Ca)_2CuO_3$, and 2201 phase. A small amount of $(Sr,Ca)_3Cu_5O_x$ phase was confirmed to exist in calcined powder by EPMA analysis. During the cyclic process of calcination and pulverization, it was considered that the mixed particles of starting materials became to fine and 2212 phase and other phases were formed after the decomposition of oxide and carbonates .

Figure 5.8 shows the influence of kind of calcined powder on critical current density. The oxide layer thickness, t_o dependence tends to equalize irrespective of the different types of powder used, within experimental accuracy. The effect of different powders will be eliminated by the following heat treatment and pressing and therefore the results for powder A are mainly mentioned hereafter.

5.3.2 Microstructure change by TMT process

Figure 5.9 shows the comparison of XRD pattern between the tape specimen prepared SDPHT1PHT2 and the bulk sintered at 1113 K for 540 ks. Nevertheless, the heat treatment condition was same for two cases, different microstructure appeared due to the

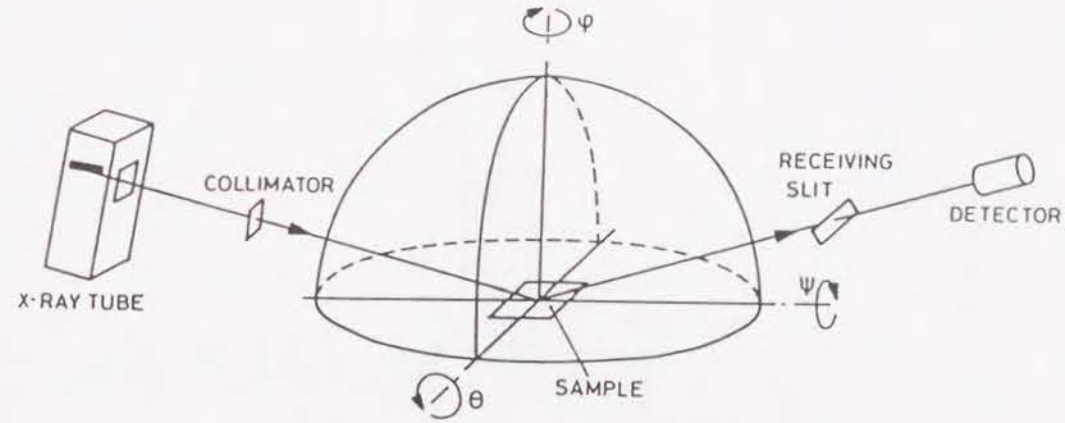

Figure 5.6 Schematic illustration of specimen configuration in the pole figure measurement.

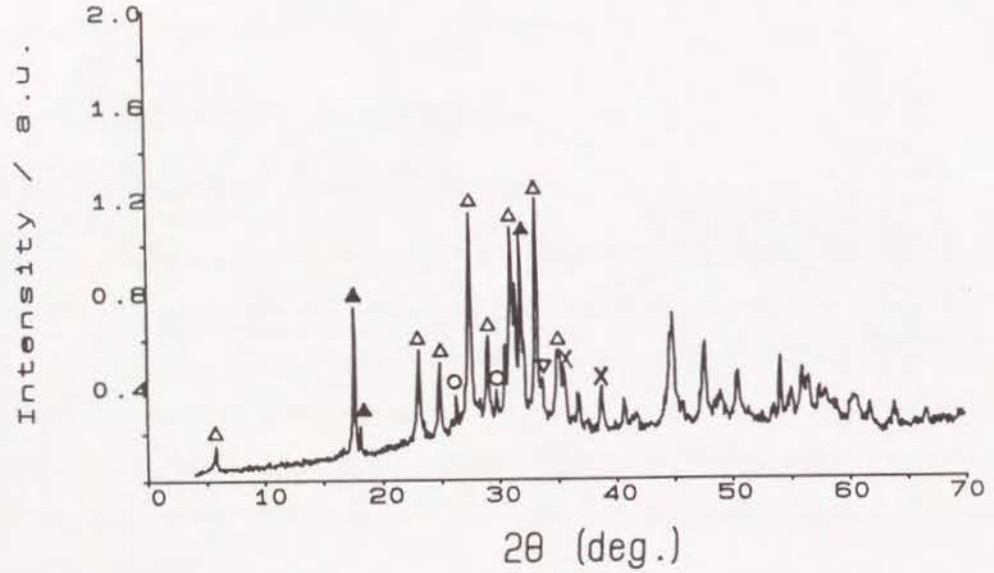

Figure 5.7 X-ray powder diffraction pattern of calcined powder, where ○ : 2201 phase, △ : 2212 phase, ▲ : Ca_2PbO_4, × : CuO and ▽ : $(Sr, Ca)_2CuO_3$.

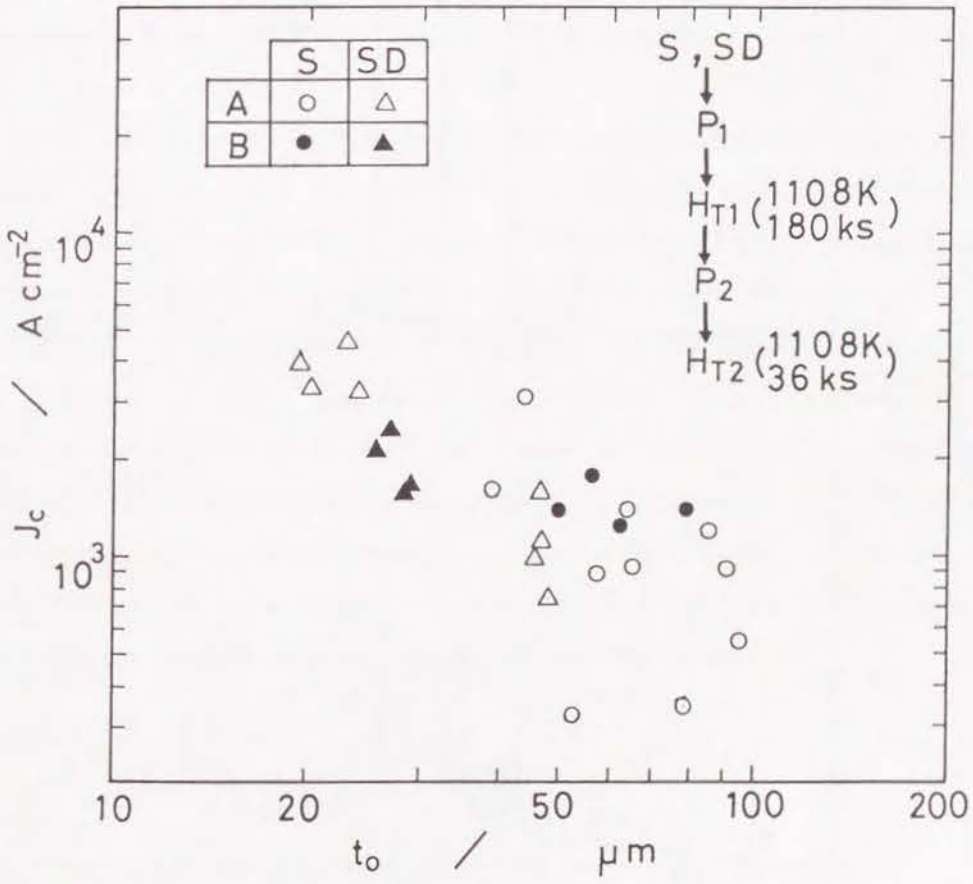

Figure 5.8 The critical current density as a function of oxide layer thickness for the specimens prepared by two kinds of calcined powders of 2212 phase (A), and 2223 phase (B), respectively as major phase.

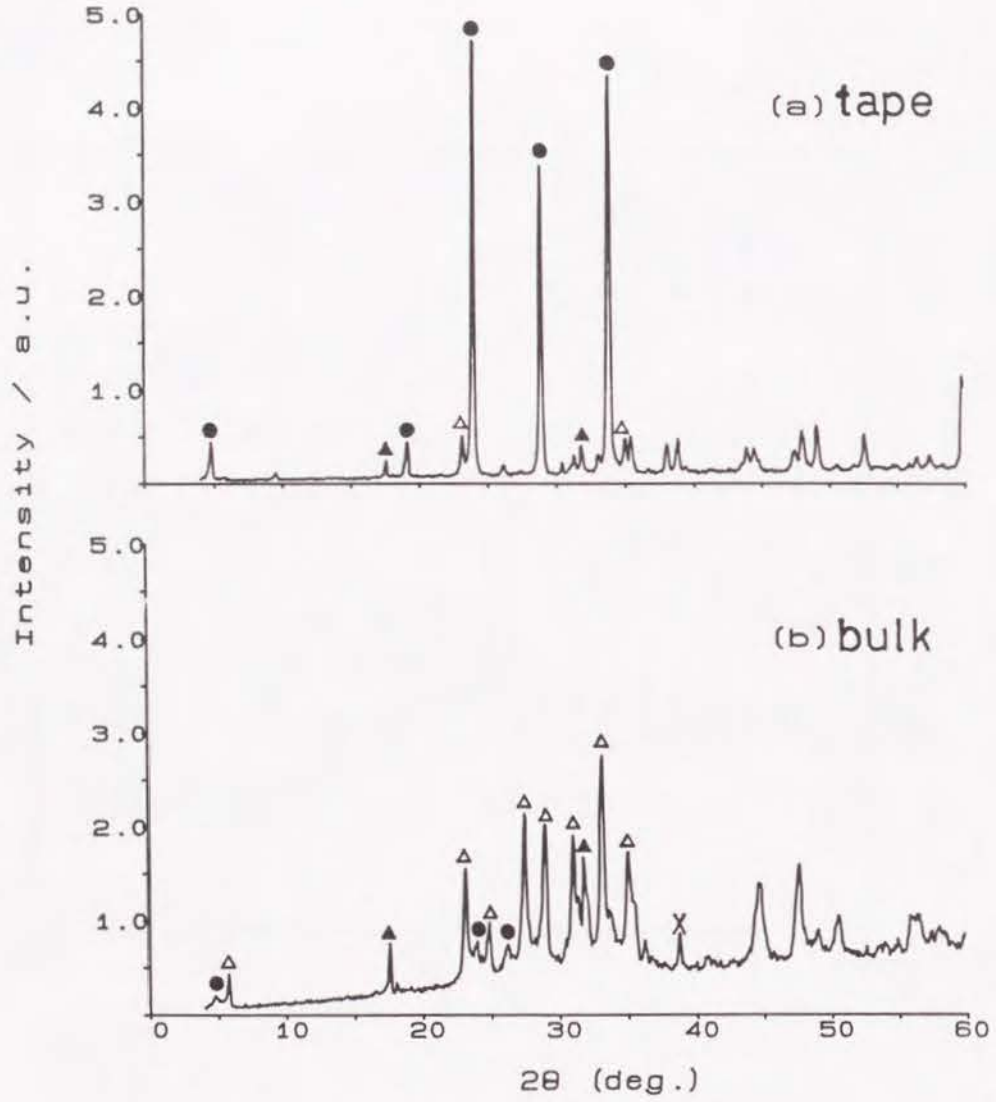

Figure 5.9 The X-ray powder diffraction patterns for the tape specimen prepared with SDPHT1PHT2 and the bulk heat treated at 1113 K for 540 ks, where ● : 2223 phase(other symbols are indicated in figure 5.7).

difference of production method. It can be confirmed that the 2223 phase with preferred orientation of a-b plane appeared as a major one for the Ag sheathed BPSCCO tape. On the other hand, for the bulk specimen, it was found that the 2212 phase becomes major one and the volume fraction of impurity phase is larger than that of Ag sheathed one. This is thought to be attributed to the difference of cold working and formation temperature of 2223 phase by Ag sheath.

Figure 5.10 shows the XRD patterns for the specimens with various cycles of TMT process. During first heat treatment, 2223 phase is thought to nucleate and grow by the reaction in calcined powders consisting of 2212 phase and impurity phases as shown in figure 5.7. In the pattern(a) and (b) for the specimen with SPHT1PHT2PHT3 and SPHT1PHT2, it was found that the X-ray intensities for 2223 phase increased, but they for 2212 phase decreased. The intensity of 2223 phase was found to increase for the specimen prepared with SPHT1PHT2(b), compared to that for specimen prepared with SPHT1P(c). According to this, the volume fraction of 2223 phase is thought to increase during second heat treatment. In order to examine the degree of preferred orientation for (a-b) plane of 2223 phase, the following conventional technique [4] is available. The factor $F(\%)$ which reflects the preferred orientation is defined as follows;

$$F(\%) = \frac{(P_1 - P_2)}{(1 - P_2)} \times 100 \tag{5.1}$$

where,

$$P_i = \frac{\Sigma I(00L)}{\Sigma I(HKL)} \tag{5.2}$$

$I(HKL)$ is the X-ray intensity of HKL plane of the 2223 phase measured by the usual θ - 2θ diffractometor. $\Sigma I(HKL)$ indicates the summation of all diffraction intensities for the 2223 phase in the measured range of scattering angle and $\Sigma I(00L)$ is the sum for the (00L) diffraction intensities, P_1 and P_2 are the measured one from the reference value from the randomly oriented specimen and the preferred oriented specimen, respectively. It was made clear that the preferred orientation of (a-b) plane for 2223 phase occurs during

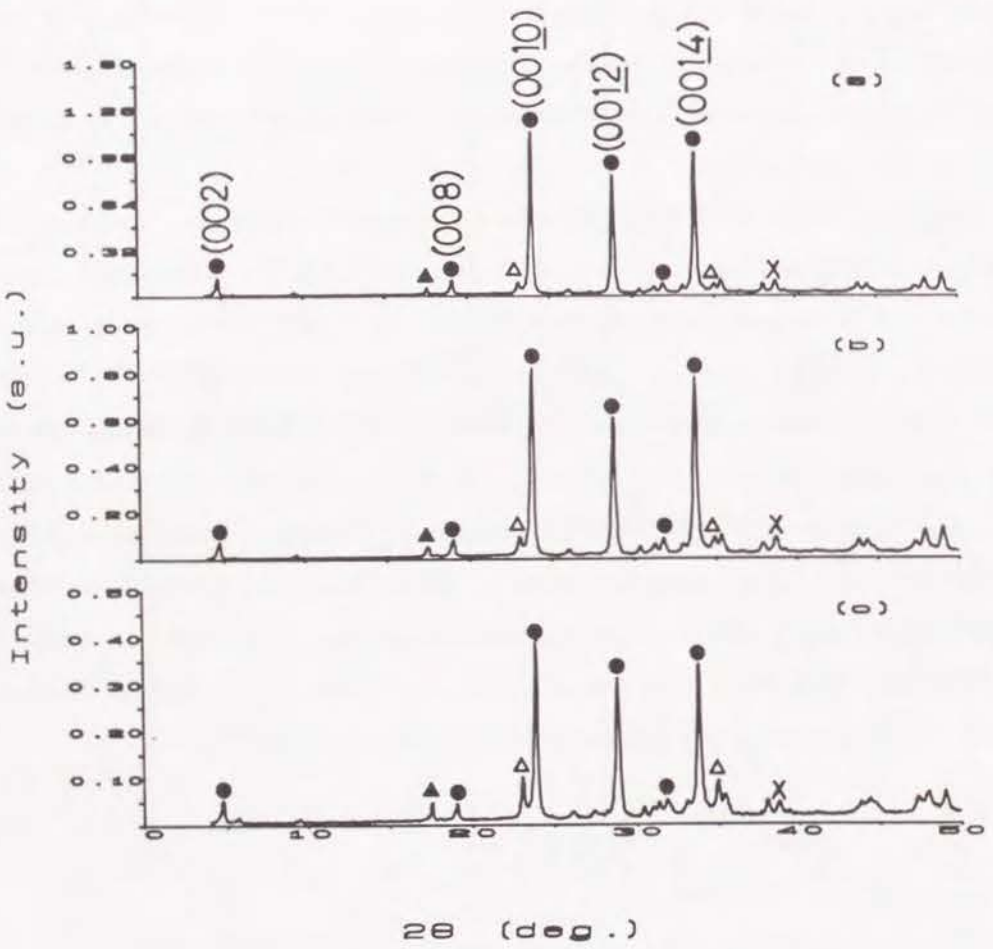

Figure 5.10 X-ray powder diffraction patterns for the specimens prepared with various TMT cycles. (a) : SPHT1PHT2HT3, (b) : SPHT1PHT2, (c) : SPHT1P , where symbols are indicated in figure 5.7 and 5.9.

second heat treatment as indicated F values of each specimen in table 5.2.

Table 5.2 F factor(%) for the specimens prepared with various TMT cycle.

TMT	SPHT1P	SPHT1PHT2	SPHT1PHT2PHT3
F(%)	78.4	84.3	86.3

The degree of preferred orientation for a-b plane can be directly evaluated by pole figure analysis. Figure 5.11 shows the pole figure of (00$\underline{12}$) plane in 2223 phase for the tapes prepared with different TMT cycles. The experimental data are presented in the region of tilting angle (ψ) between 0° to 85°. The pole figure(a) is for the specimen prepared with 1 TMT cycle. Relatively high intensities which distributed anisotropically were found near 30° tilting angle. This implies that the degree of preferred orientation of (a-b) plane is considered to be low for the specimen after 1 TMT cycle. For the case of (b), the intensity distribution exhibited symmetric contour and the intensity increased isotropically with decreasing the tilting angle and maximum intensity is found to be high compared to be (a). This result suggests that the plate-like grains of 2223 phase aligns parallel to the tape surface. According to this, textured structure is considered to be improved by repeating TMT cycle.

5.3.3 Influence of TMT cycle

Figure 5.12 shows the effect of TMT cycle(P $\rightleftharpoons$ HT) on the critical current density. After SD or S treatment, the pressing and heat treatment were repeated according to S(D)P1HT1P2HT2...., where first heat treatment HT1 was performed at 1108 K for 360 ks and further heat treatment at 1108 K for 36 ks. For cycle of up to three times J_c increased, but on further cycle J_c decreased. Figure 5.13 shows the layer thickness dependence of critical current density for the specimen processed by S(D)PHT1PHT2 or S(D)PHT1PHT2PHT3, where temperature of heat treatment(HT1 = HT2 = HT3) is 1113 K and time is 360 ks(HT1) and 180 ks(HT1 = HT2). Irrespective of the different cycle in TMT process, both specimens exhibited almost similar J_c with respect to t_o.

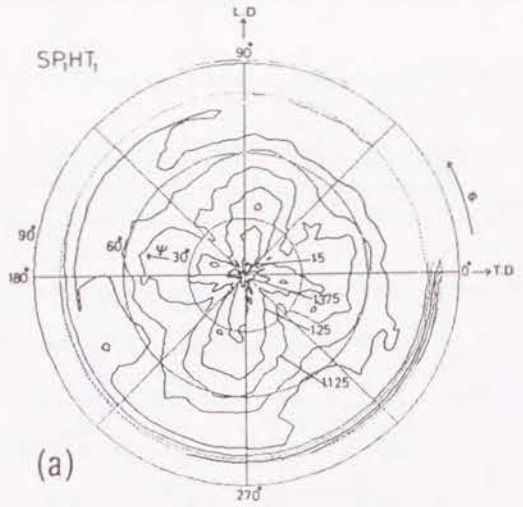

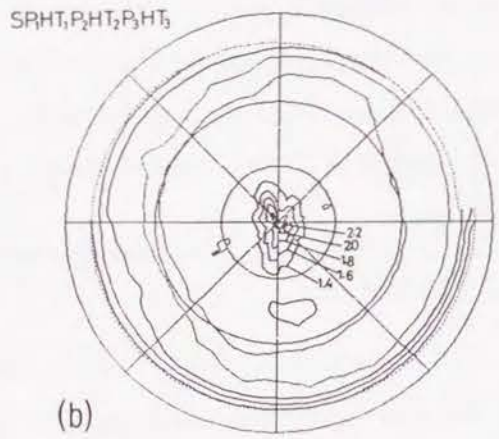

Figure 5.11 Pole figure of (00$\underline{12}$) plane in 2223 phase for the tapes prepared with different TMT cycles. (a) : 1 TMT cycle, (b) : 3 TMT cycles.

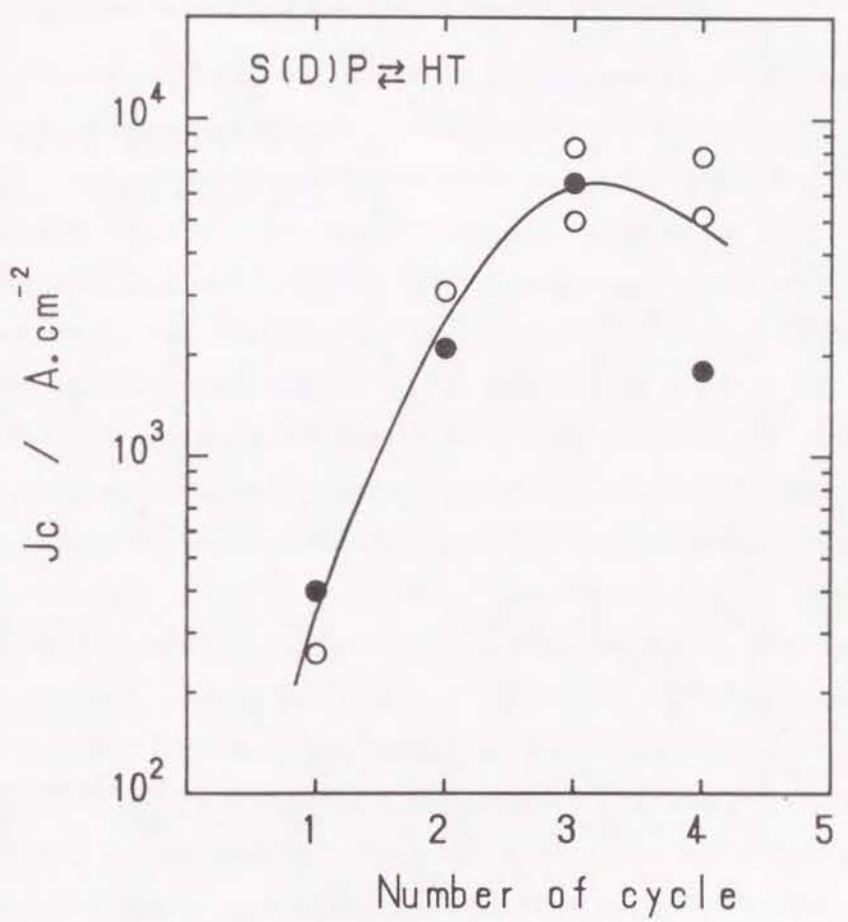

Figure 5.12 The critical current density as a function of number of TMT cycle.

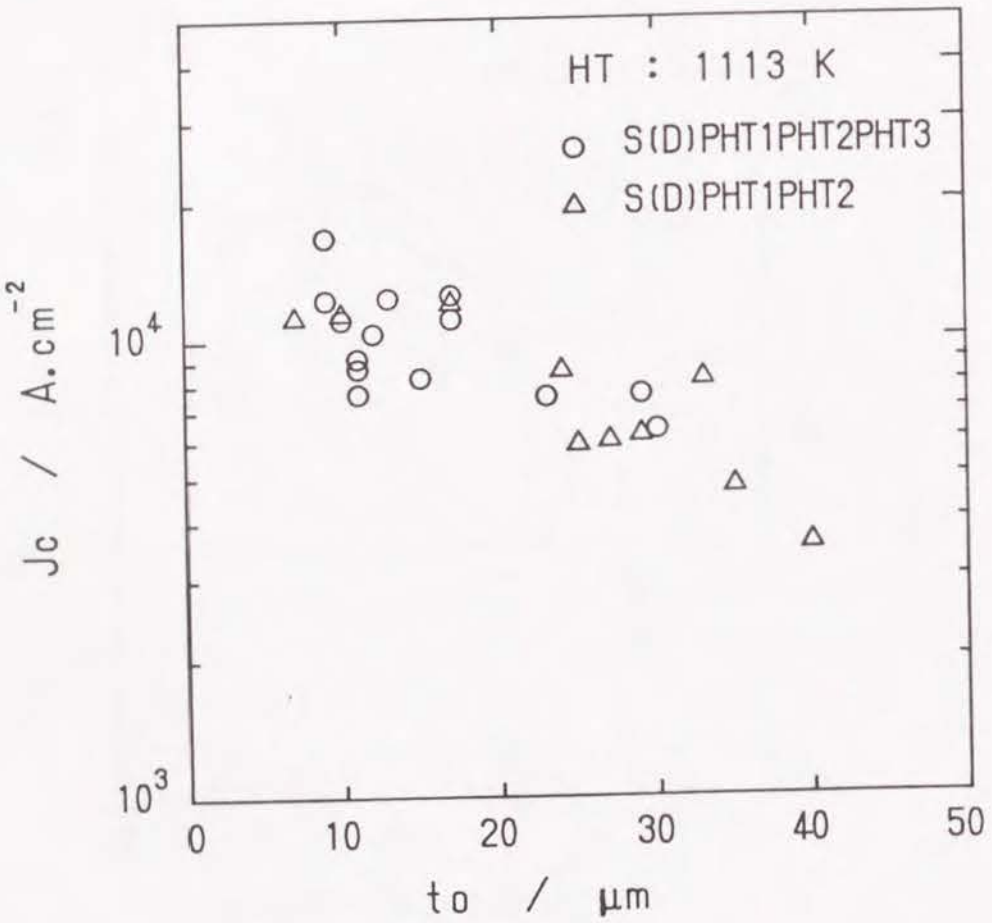

Figure 5.13 The critical current density as a function of layer thickness for the specimens prepared with different TMT cycle.

Comparing with the result from figure 5.12, it was found that the dependence of number of cycle on J_c depends on heat treatment temperature and time.

5.3.4 Influence of heat treatment temperature

Figure 5.14 shows the influence of heat treatment temperature for HT1 and HT2 on critical current density, where temperatures for both HT1 and HT2 were the same. It was found that the specimen heat treated at higher temperature exhibits higher J_c. Figure 5.15 shows the influence of first heat treatment temperature on critical current density, where the second heat treatment was fixed at 1113 K. The specimen heat treated at 1113 K for first heat treatment exhibited higher J_c with respect to t_o. Figure 5.16 shows the influence of second heat treatment temperature on the critical current density for the specimens annealed at 1108 K in first heat treatment. It was found that the critical current density increases with increasing temperature and reaches to a maximum at range of 1113 ~ 1118 K, then decreases with further increase of temperature. It should be noted that J_c changes remarkably in a so narrow temperature range between 1093 and 1123 K. Figure 5.17 shows the second heat treatment temperature dependence of critical temperature for the specimen plotted as solid circle in figure 5.16. The critical temperature was higher than 100 K for all specimens examined here and became highest at 1113 K, while $\Delta T = T_{c,on} - T_{c,off}$ became narrowest. This suggests that the crystal grains of 2223 phase are well connected with each other. The annealing temperature dependence of T_c is well consistent with that of the J_c as seen from figures 5.16 and 5.17. When the specimen was heat-treated at 1123 K, both J_c and T_c decreased remarkably. Figure 5.18 also shows the influence of second heat treatment temperature on the critical current density for the specimens annealed at 1113 K in first heat treatment.

It was found that J_c was maximized at 1113 K. Comparing with the results from figure 5.16, similar temperature dependence of J_c was observed with irrespective of first heat treatment temperature.

Figure 5.19 shows the change of X-ray diffraction pattern for the specimens heat treated

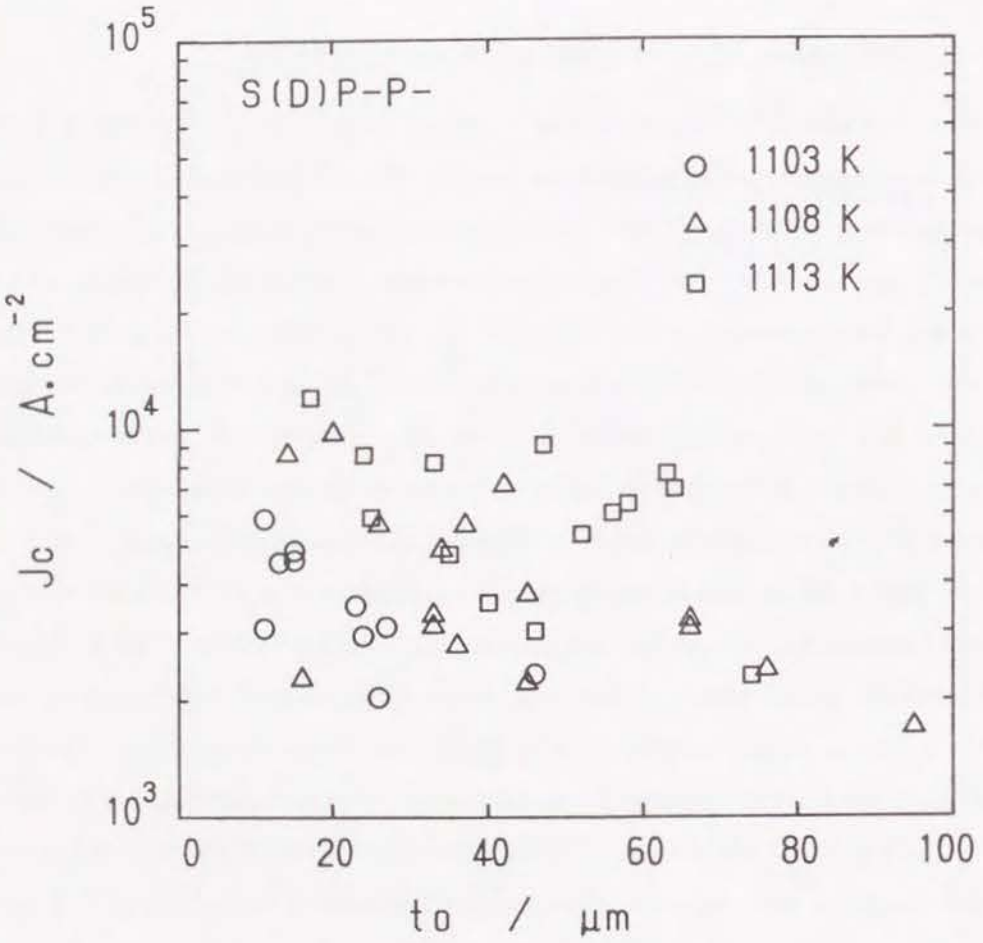

Figure 5.14 The critical current density as a function of layer thickness for the specimens prepared at different temperature for both HT1 and HT2.

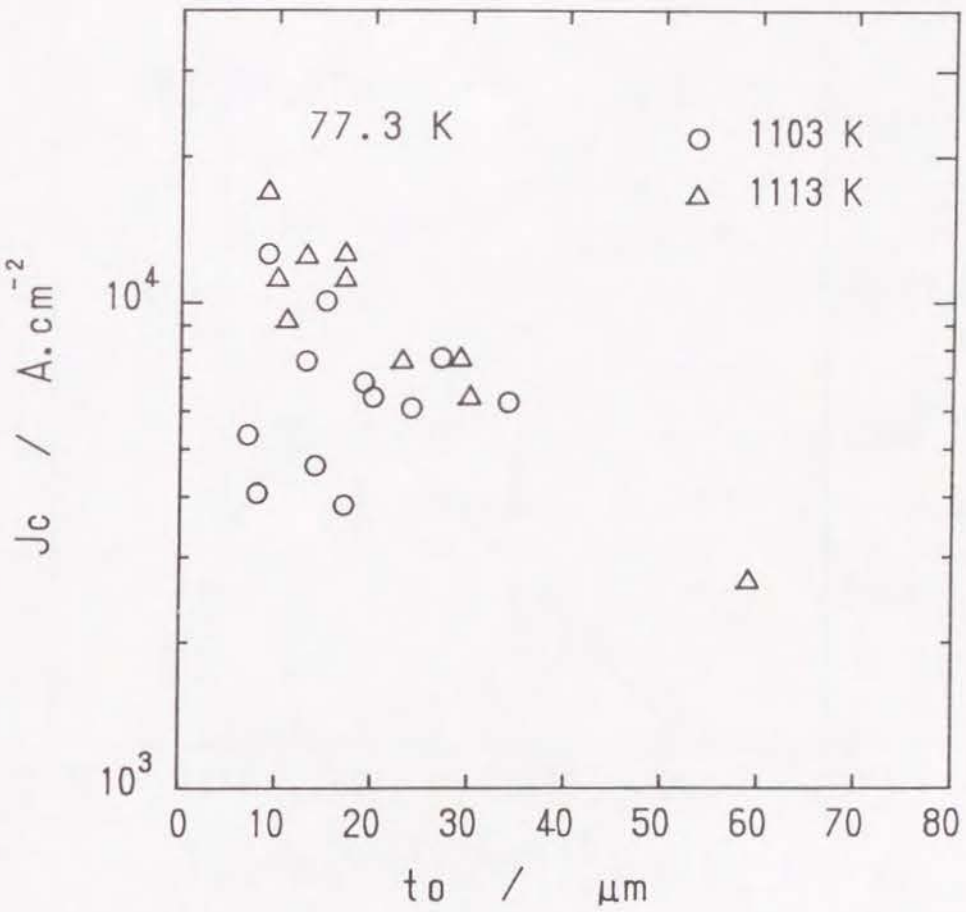

Figure 5.15 The critical current density as a function of layer thickness for the specimens prepared at different temperature for HT1, where temperature for HT2 was 1113 K.

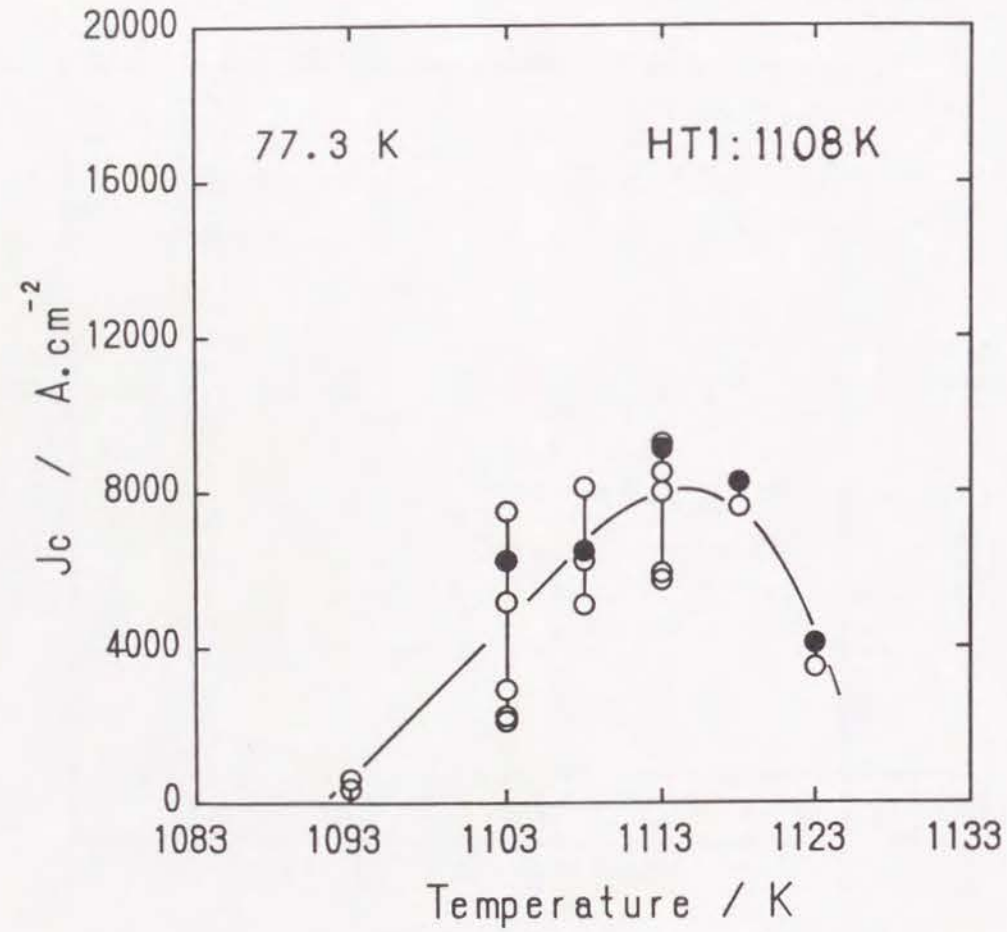

Figure 5.16 The critical current density as a function of temperature for HT2, where temeprature for HT1 was 1108 K.

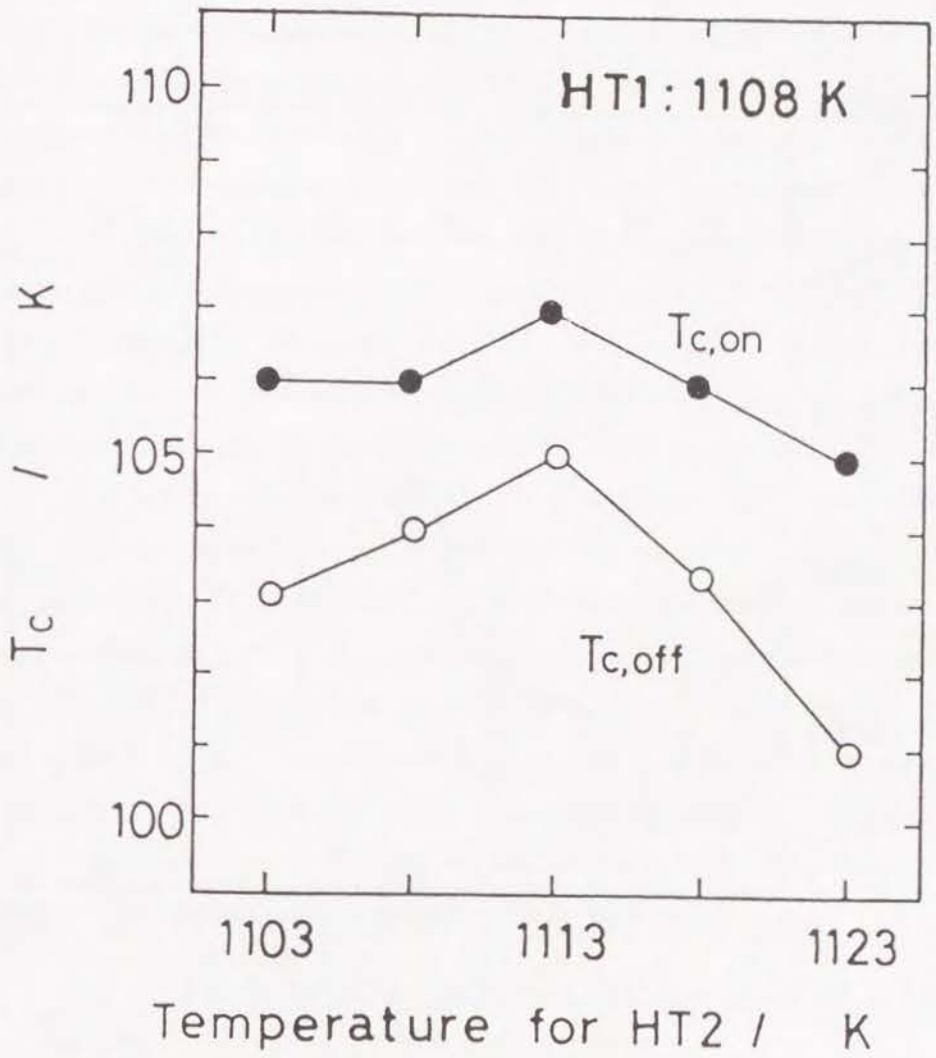

Figure 5.17 The critical transition temperature as a function of temperature for HT2.

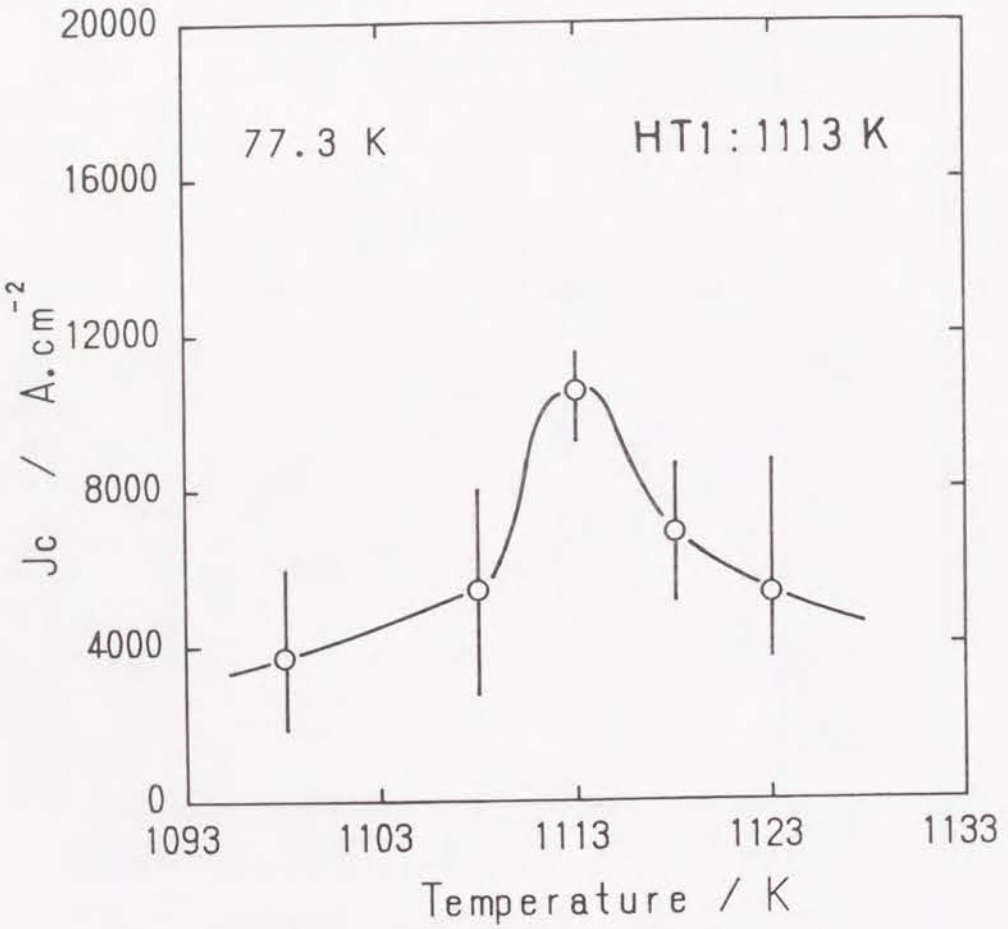

Figure 5.18 The critical current density as a function of temperature for HT2, where temperature for HT1 was 1113 K.

at various temperatures for HT2, where the first heat treatment was fixed at 1108 K. It is difficult in general to identify $(Sr, Ca)_3Cu_5O_x$ phase by X-ray diffraction because its diffraction patterns overlap with peaks of 2223 phase. But it can be easily detected by EPMA analysis. It was confirmed that 2223 phase existed as a main phase and 2212 phase also existed with smaller amount than 2223 phase at any temperature and other two impurity phases Ca_2PbO_4 and CuO were commonly detected for all specimens heat treated at different temperatures. For the specimen heat treated at 1123 K for HT2, 2201 phase could be detected. In a previous study [6], it was confirmed that 2223 phase for sintered bulk dissolves liquid and other solid phase at about 1128 K, and then 2201 phase was crystallized during cooling. According to this, the decomposition of 2223 phase which was formed in first heat treatment was thought to occur during second heat treatment at 1123 K for present Ag sheathed tape. Figure 5.20 shows the intensity distribution from $(00\underline{1}0)$ plane against tilting angle, which was obtained from the pole figure analysis. For all the specimens, the intensity became maximum at $\psi = 0$ and decreases with increasing angle. Judging from intensity level and FWHM(Full width at half maximum), it was clearly shown that the preferred orientation of a-b plane is improved for the specimen heat treated at higher temperature. $F(\%)$ values were calculated and summarized in table 5.3. $F(\%)$ increased for the specimen heat treated at higher temperature. This tendency is consistent with result from the pole figure analysis.

Table 5.3 F factor(%) for the specimens heat treated at various temperatures for HT2.

Temp.(K)	1093	1113	1123
$F(\%)$	66.1	86.0	91.73

Figure 5.21 shows the microstructure of polished surface in the cross-section perpendicular to the current flow for the specimens heat treated at various temperatures for HT2. The elongated plate-like grains were assigned as superconducting phase. As shown in figure 5.19, the coexistence of both 2212 and 2223 phases are indicated from the X-ray

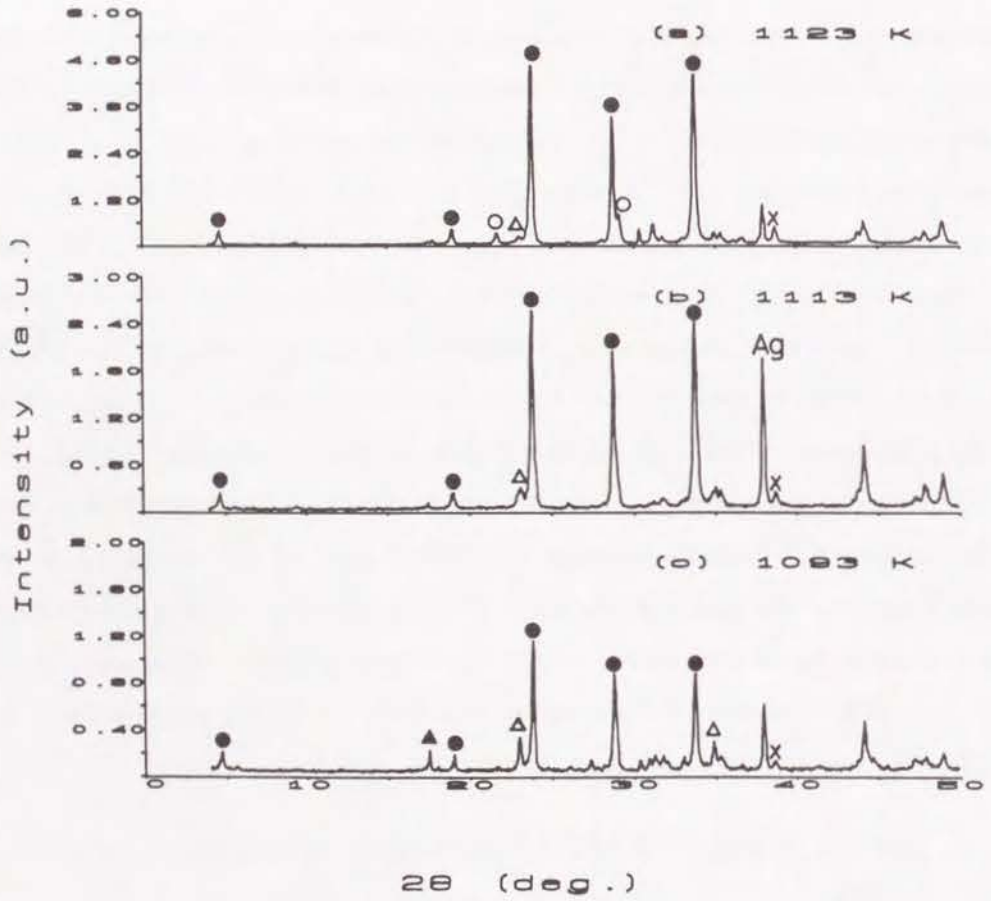

Figure 5.19 The X–ray diffraction patterns for the specimens heat treated at various temperatures for HT2, where temperature for HT1 was 1108 K, where the symbols are indicated in figure 5.7 and 5.9.

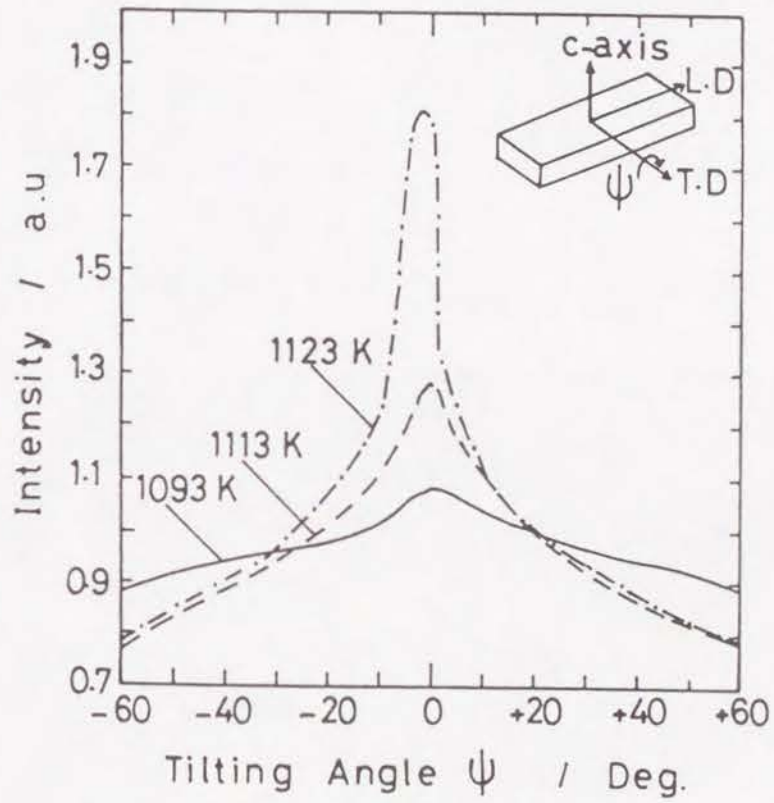

Figure 5.20 The intensity distribution from (00$\underline{1}$0) plane against the tilting angle, ψ.

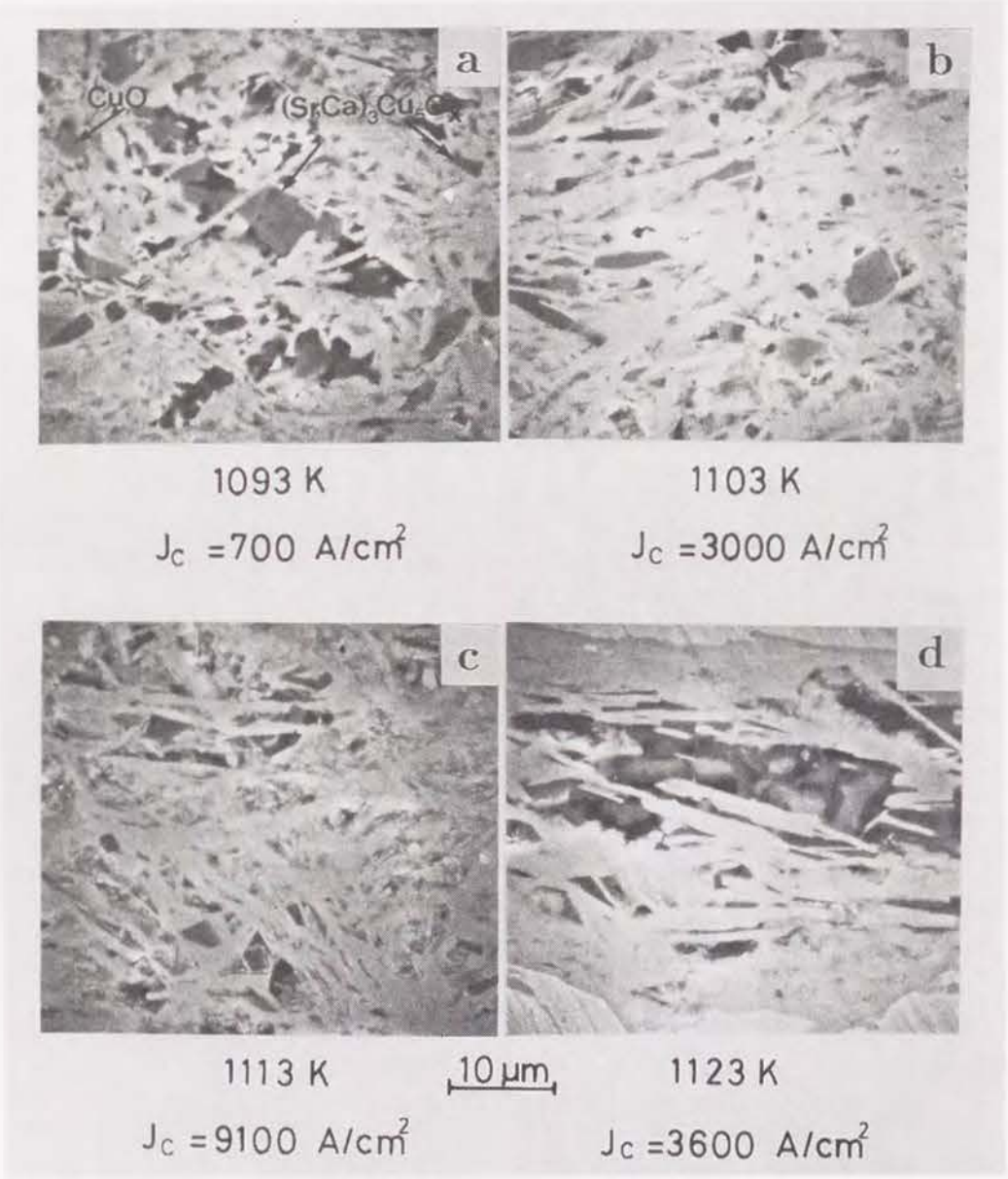

Figure 5.21 Scanning electron micrographs of polished surface for the specimens heat treated at various temperatures for HT2, where a,b,c,d are for 1093, 1103, 1113 and 1123 K, respectively, where temperature for HT1 was 1108 K.

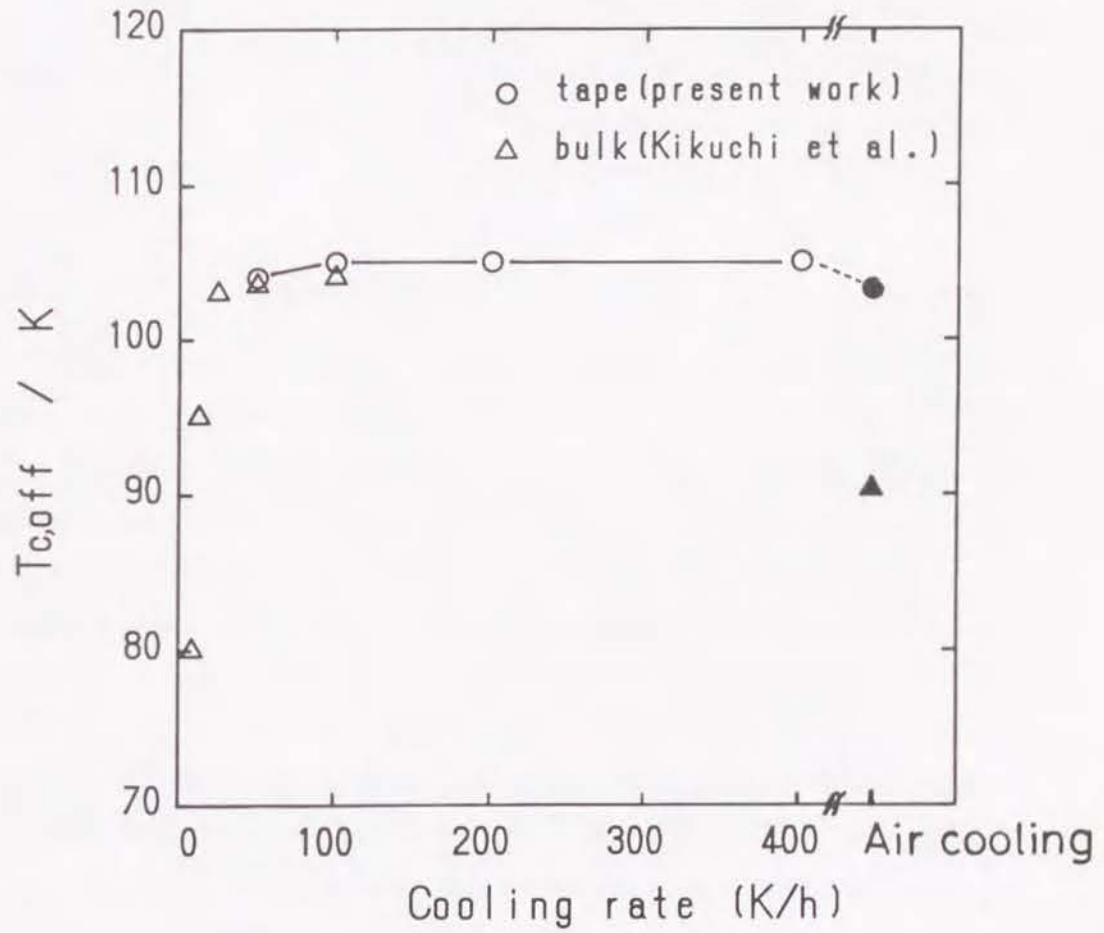

Figure 5.22 Cooling rate dependence of critical temperature, $T_{c,off}$, where solid symbols are data for air cooling.

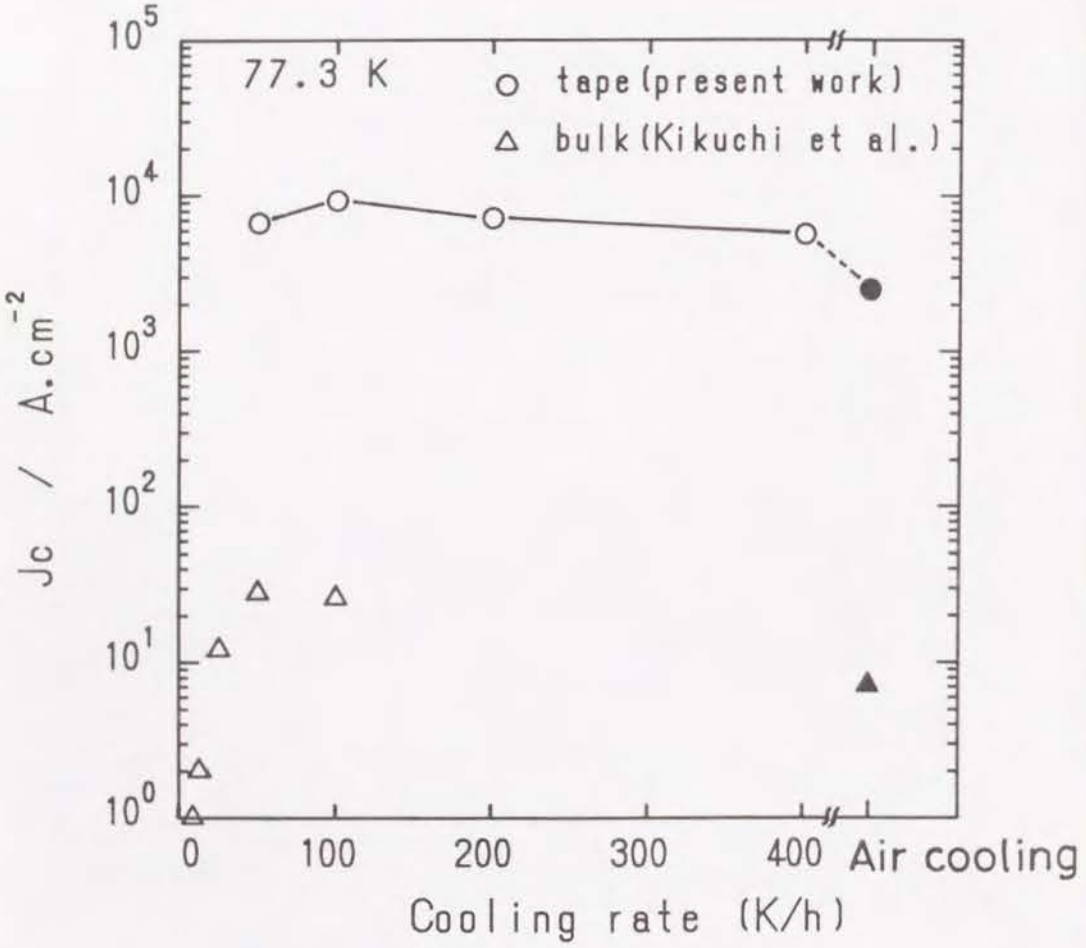

Figure 5.23 Cooling rate dependence of critical current density, where solid symbols are data for air cooling.

analysis. It is, however, difficult to distinguish both phases from the SEM photos. Except these superconducting phases, a $(Sr,Ca)_3Cu_5O_x$ impurity phase disperses commonly for all specimens. For the specimen of 1113 K, it was observed that the volume fraction of $(Sr,Ca)_3Cu_5O_x$ decreased remarkably. The J_c increases for the specimen including the smaller amount of $(Sr,Ca)_3Cu_5O_x$ phase. For the case of 1123 K, it was observed that the superconducting phase became coarser. This oriented structure observed at 1123 K is consistent with the result of pole figure as shown in figure 5.20.

5.3.5 Influence of cooling rate

Figure 5.22 shows the cooling rate dependence of critical temperature. After final heat treatment, the specimen was cooled with various rate. The data reported by Kikuchi *et al.* [8] for bulk($Bi_{1.6}Pb_{0.4}Sr_{1.6}Ca_2Cu_4O_x$) prepared by conventional solid state reaction method are also plotted in the graph. Combining present tape's data with bulk ones, critical temperature was found to decrease at very slow cooling rate and air cooling. For the case of present tape, optimum cooling rate to maximize $T_{c,off}$ was in the range from about 100 K/h to 400 K/h. The decrease of $T_{c,off}$ for the air cooled specimen is thought to be related with the thermal stress [8] and change of oxygen content [9] at and near grain boundaries by quenching. The degradation of $T_{c,off}$ for the air cooled tape was found to small as compared to that of bulk. Figure 5.23 shows the cooling rate dependence of critical current density for the same specimens shown in figure 5.22. J_c was also strongly dependent on the cooling rate. The tape specimen cooled with 100 K/h exhibited highest J_c. Cooling rate dependence of J_c shows similar trend with that of $T_{c,off}$. Degradation of J_c for air cooled specimen was thought to be associated with decrease of $T_{c,off}$.

5.4 Conclusion

BPSCCO(2223 phase) superconducting tape could be successfully prepared by *powder-in-tube technique*. The main conclusions are the following;

1. A refined structure with high volume fraction of 2223 phase was obtained by employing the thermomechanical treatment, compared to bulk prepared with conventional sintering.

2. Both superconducting properties, J_c and T_c have been made clear to become best for the heat treatment at 1113 K.

3. Superconducting properties degraded for the specimen heat treated at 1123 K because of appearance of 2201 phase.

4. The volume fraction of 2223 phase was confirmed to increase during second heat treatment.

5. The preferred orientation of (a-b) plane was improved by repeating TMT cycle.

6. The optimum cooling rate to maximize both $T_{c,off}$ and J_c was found to be typically of 100 K/h.

References

1. N. Enomoto, H. Kikuchi, N. Uno, H. Kumakura, K. Togano and K. Watanabe : Jpn. J. Appl. Phys., **29**(1990)L447.

2. J. Kase, K. Togano, H. Kumakura, D. R. Dietderich, N. Irisawa, T. Morimoto and H. Maeda : Jpn. J. Appl. Phys., **29**(1990)L1096.

3. K. Sato, T. Hikata, H. Mukai, T. Masuda, M. Ueyama, H. Hitotsuyanagi, T. Mitsui and M. Kawashima : *Proc. 2nd Inter. Symp. on Superconductivity (ISS'89)* ed. by. T. Ishiguro and K. Kajimura(Spring Velag,1990).

4. Y. Yamada, K. Jikihara, T. Hasebe, T. Yanagiya, S. Yasuhara and M. Ishihara : Cryo.Eng., **25**(1990)82.

5. S. S. Oh, K. Osamura and S. Ochiai : *Proc. 2nd Inter. Symp. on Superconductivity (ISS'89)* ed. by T. Ishiguro and K. Kajimura(Spring Velag, 1990).

6. S. S. Oh and K. Osamura : Supercond. Sci. Technol. **4**(1991)239.

7. S. Koyama, U. Endo and T. Kawai : Jpn. J. Appl. Phys., **27**(1988)1861.

8. A. Kikuchi, M. Matsuda, M. Takata, M. Ishii, T. Yamashita and H. Koinuma : Jpn. J. Appl. Phys., **28**(1989)L371.

9. W. Carrilo and W. Göpel : Physica C, **161**(1989)373.

Chapter 6

Influence of cold working on the critical current density of Ag sheathed Bi-Pb-Sr-Ca-Cu-O tapes

6.1 Introduction

Although the cuprate high temperature superconductors(HTSC) are known as promising materials from the view point of their high transition temperature, the critical current density (J_c) for bulk oxide are known to very low, compared with that of metallic superconductors. For considering the large scale application as magnet coil, improvement of J_c for oxide superconductors is requested greatly. Larbalestier pointed out [1] that many of eventual applications of HTSC depend on the realization of transport critical current density of order 10^5 A/cm^2 or more at 77 K. The critical current density in magnetic field is considered to depend on the microstructure of oxide. At the grain boundaries the crystal structure is not regular and there is a tendency, where impurities concentrate at the grain boundaries owing to the irregular structure. It has been known that dislocation networks, small voids, cracks, [2] carbon [3] and amorphous layer [2] exist at the grain boundaries and grain boundary act as barrier against superconducting current because of weak link behavior and makes J_c decrease in polycrystalline specimens. Therefore, favorable grain boundary structure and eliminating the defects at grain boundary would be necessary for obtaining high J_c. Dimos *et al.* made clear [4] that transport J_c is roughly proportional to the inverse of misorienting angle between grains. This result imply that

achieving a degree of texture is important for obtaining of very high critical current. Jin *et al.* have reported [5] that oriented polycrystalline bulk solid materials produced from the melt has achieved high J_c of 1.7×10^4 A/cm^2. On the other hand, wires and tapes of superconducting materials are necessary for many applications, but, these configurations recognized to be difficult because of the brittle nature of these materials. Among various processing techniques, the powder-in-tube technique is considered to be powerful for long and uniform wire fabrication. Textured structure can be obtained during the process of thermomechanical treatment and high J_c was achieved. Recently, high critical current densities (77.3 K, zero magnetic field) exceeding 2×10^4 A/cm^2 have been reported [3,6,7] for Ag sheathed BPSCCO tapes. But it is not easy to understand the deformation mechanism of the composite consisting of ductile metallic sheath and brittle oxide powder. In this study, microstructure change and work instability by cold working and their influence on critical current density and its field dependence were investigated in detail, when the specimen was prepared by powder-in-tube technique.

6.2 Experimental

The powder with composition of $Bi_{1.6}Pb_{0.4}Sr_{1.6}Ca_2Cu_{2.8}$ for tubing to Ag pipe was prepared by similar process mentioned in Chapter 5.2.1. In order to change the degree of cold working, Ag pipes with various size(12 mm, 6 mm and 5 mm outer) were used here. Many kinds of cold working techniques have been tried to reduce the diameter of composite specimen and to deform to tape specimen by mainly cold pressing and rolling for some specimen. The various cold working techniques were employed as follow.

- S : Swaging
- D : Drawing
- Dc : Casset roller die processing
- Rc : Cross rolling

- Rg : Grooved rolling
- R : Conventional rolling
- P : Uniaxial cold pressing

Heat treatment at 1113 K and cold working were repeated for producing superconducting tapes. An example of the schedule of the TMT is presented by SDP-P-, which means that after swaging(S) and drawing(D) treatments, the pressing(P) and heat treatments(-) were repeated twice. Microstructure was investigated by the means mentioned Chapter 5.2.2. Critical current was measured at magnetic field ranges from 0 to 0.5 T at 77.3 K and 0 to 15 T at 4.2 K, respectively.

6.3 Results and discussion

6.3.1 Macrostructure change of oxide layer by cold working

It is not clear how the composite specimen filled with oxide powder is deformed during cold working. First, the change of shape of oxide core during swaging was investigated. Figure 6.1 shows the relation between the ratio of cross sectional area of oxide core to total area of composite and outer diameter of composite. The composite specimen filled with oxide powder was swaged from 5 mmϕ to 0.8 mmϕ in outer diameter. The volume fraction of oxide core decreased at the first step of swaging and kept constant within some error range with decreasing outer diameter of composite. The powder particle filled in Ag tube is thought to be pulverized and the number of void involved in oxide core is reduced by continuous vertical movement of vibrating dies and then, the densification occurs during swaging. Figure 6.2 shows the cross sectional views perpendicular to the longitudinal direction of the composite with different outer diameter after swaging. The shape of oxide core becomes irregular with increasing reduction rate. The Ag sheath is deformed plastically, while the oxide core is deformed inhomogeously owing to nonuniform flowage of powder particle by swaging. For estimating work instability during swaging, the variation of oxide layer thickness parallel to the longitudinal direction of tape was

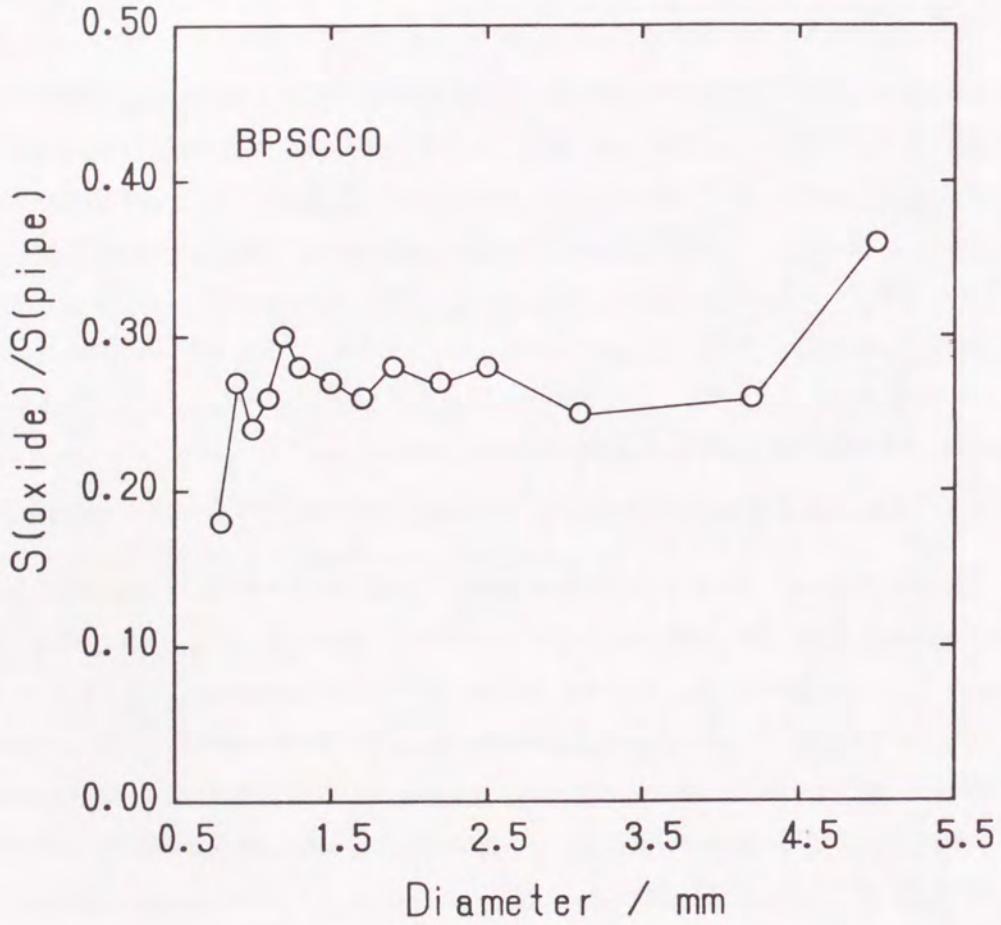

Figure 6.1 Change of the area ratio of the oxide core to the tube as a function of outer diameter of tube during swaging.

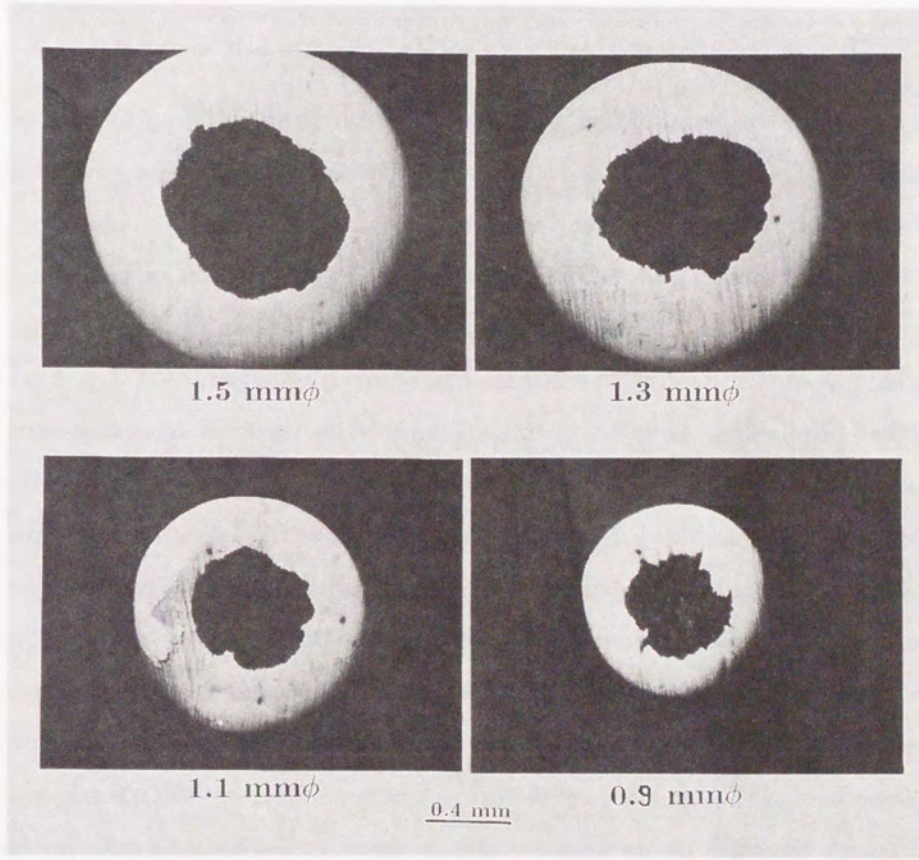

Figure 6.2 Cross sectional views perpendicular to the longitudinal direction of the composite.

measured for the tape specimen finally obtained after TMT and it was evaluated using the coefficient of variation(COV), which is the standard deviation divided by average layer thickness. The COV increased with decreasing the diameter as shown in figure 6.3. This implies that the work instability by swaging depends greatly on the reduction rate.

6.3.2 Pressure dependence of critical current density

The composite was reduced in size by swaging(S) and drawing(D) up to 0.9 mm outer diameter and then pressed into a tape shape. Pressing (P) and heat treatment(HT) were repeated by two times. The load of pressing was changed to control the oxide layer thickness. Figure 6.4 shows the pressure dependence of critical current density. J_c increased with increasing the pressure. As shown in figure 6.4, an increase of J_c by three times could be obtained owing to increase of pressure. It was found that J_c is dependent on the load of pressing. As shown in figure 6.5, the oxide layer thickness decreased with increasing pressure. According to this, it was confirmed that there is a correlation between oxide layer thickness and load of pressing. Figure 6.6 shows the relation between the ratio of cross sectional area of oxide layer to the total area of the tape and pressure. The ratio decreased with increasing pressure. This indicates that the oxide layer becomes dense by pressing. According to this, the uniaxial cold pressing is considered to be very effective for increasing J_c. This tendency in the pressure dependence of J_c is consistent with results [8] from Yamada *et al.* Figure 6.7 show the microstructure of fracture surface perpendicular to the length direction of the tape for the specimen processed with different load of pressing, where (a) and (b) are for tapes pressed with 386 and 930 MPa, respectively. Large voids and randomly distributed grains were found for the specimen prepared with low pressure. The connectivity between the grains is very bad for the specimen(a). A dense textured structure that the grains align parallel to tape surface(current flow) was observed for the specimen prepared with higher pressure. According to this, increasing the load of pressing is effective to not only densification of oxide layer, but the texturing of grains.

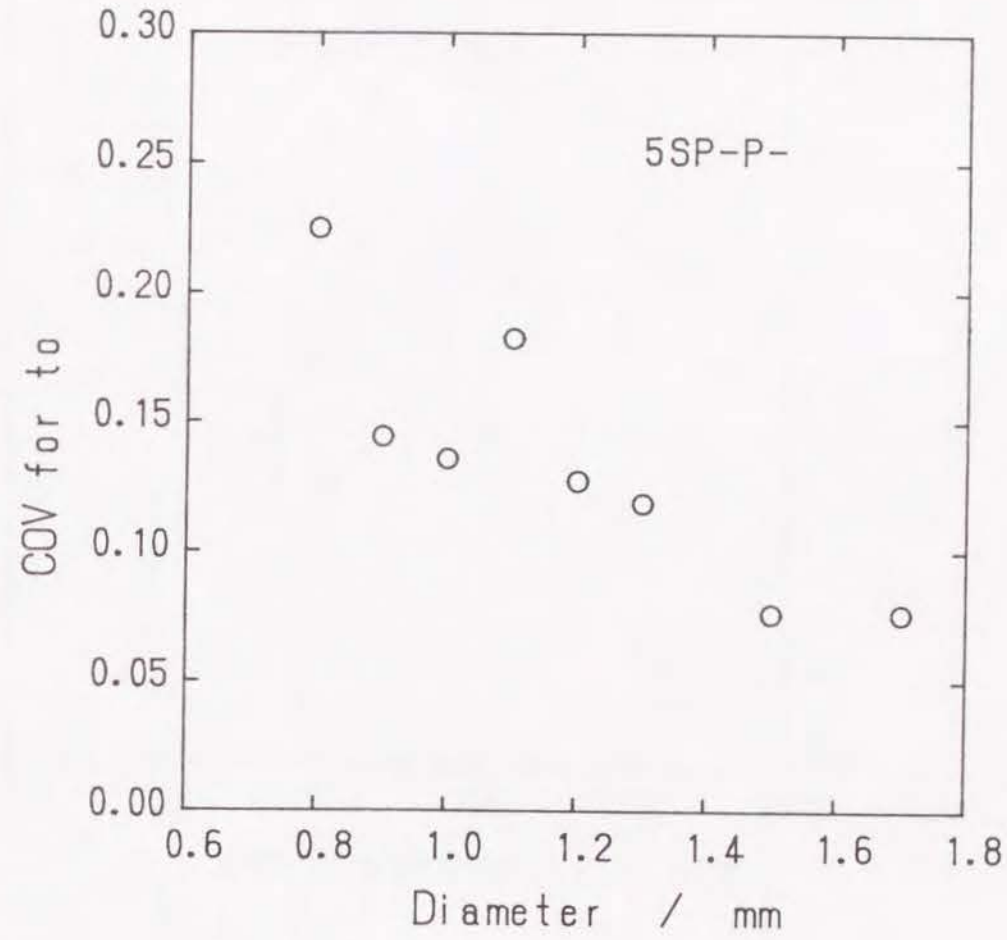

Figure 6.3 The relation between the outer diameter of composite and the coefficient of variation (COV) of oxide layer thickness.

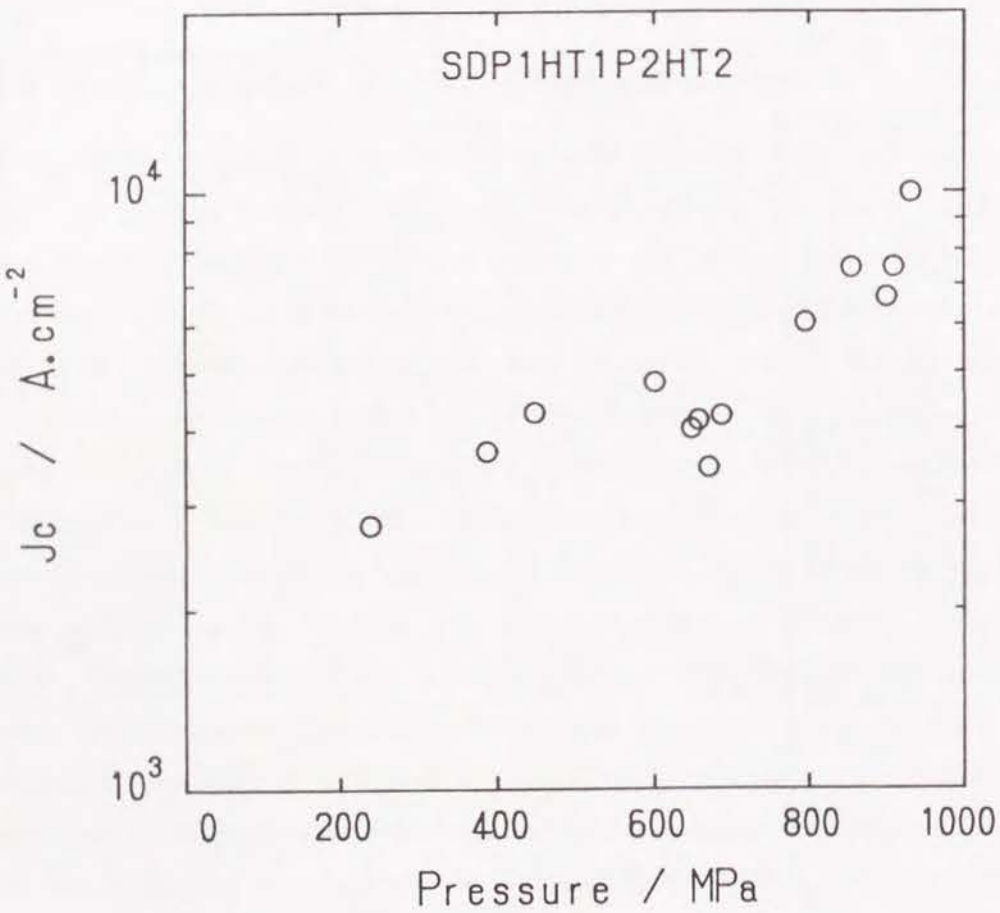

Figure 6.4 Pressure dependence of J_c, for the tapes prepared by a TMT process of SDP-P-.

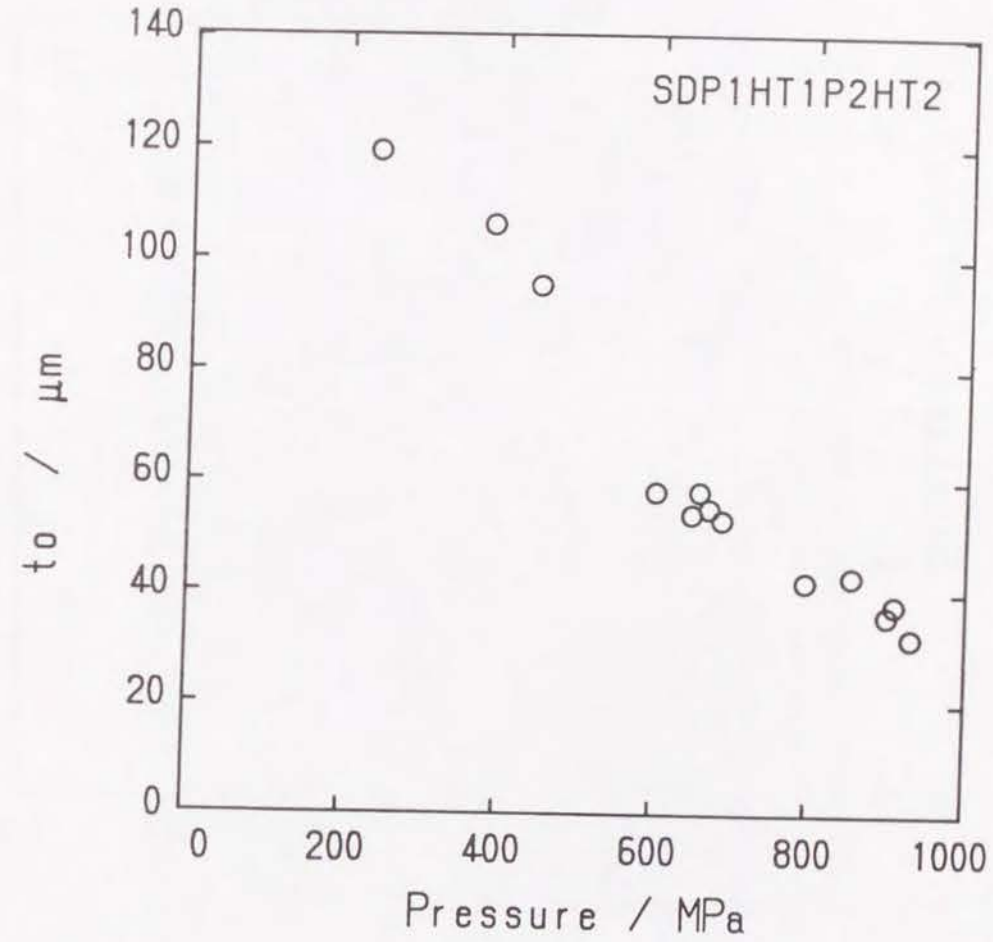

Figure 6.5 Pressure dependence of the oxide layer thickness (t_o) for the same specimens presented in figure 6.4.

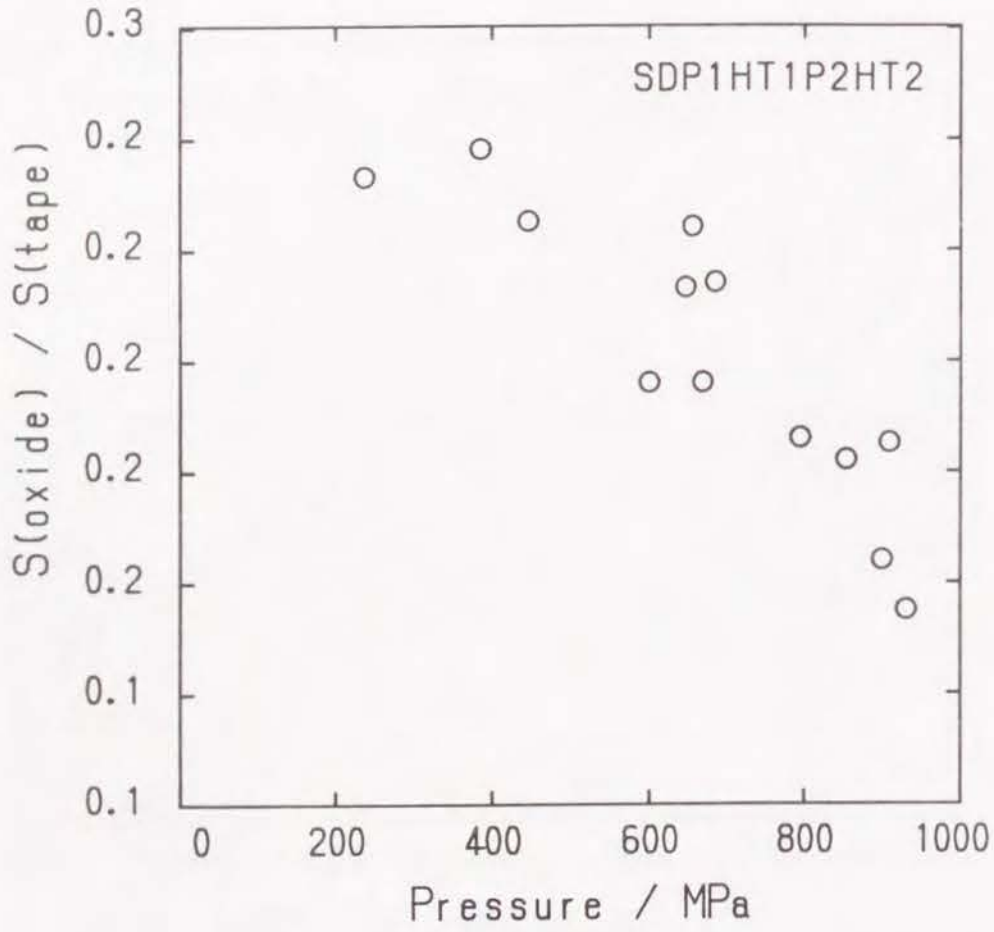

Figure 6.6 Pressure dependence of the area ratio of oxide layer to the whole cross sectional area for the same specimens presented in figure 6.4.

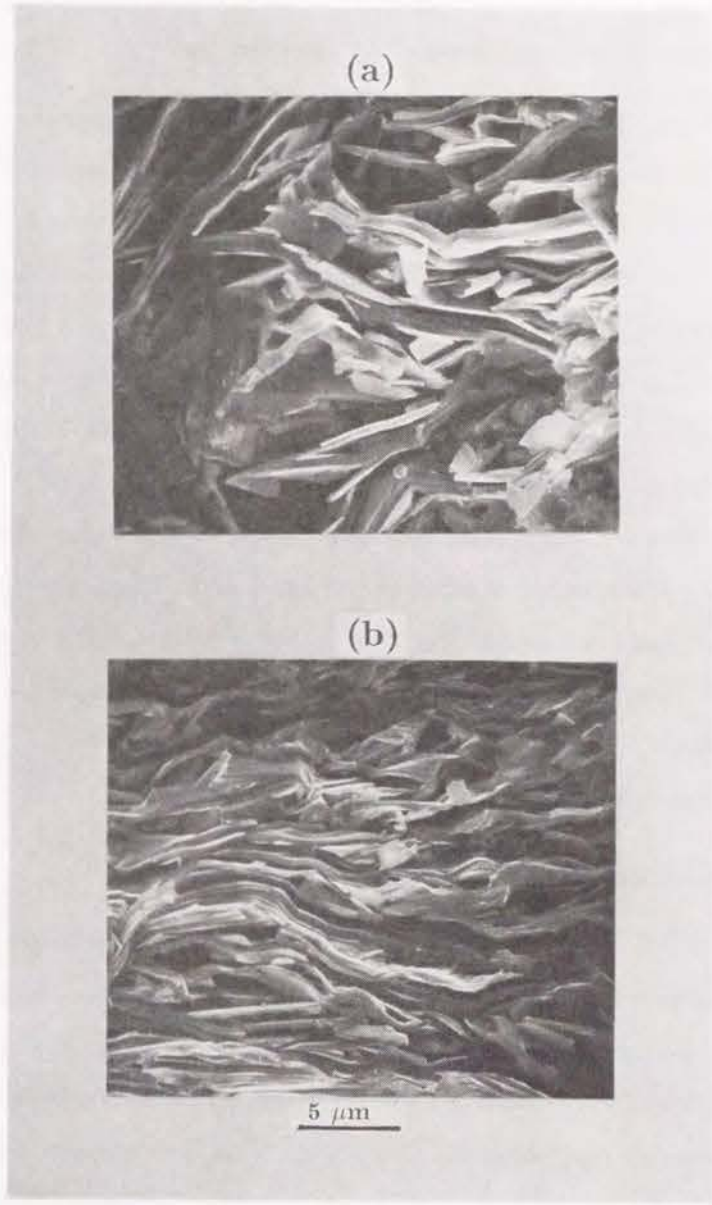

Figure 6.7 Microstructures of fracture surface for the specimens prepared with different pressure.

6.3.3 Influence of cold working technique

Figure 6.8 shows the oxide layer thickness(t_o) dependence of critical current density for the specimens prepared with various cold working. Here, the diameter of composite was reduced by using some kind of combinations from swaging, drawing and casset roller die processing and the tape was made by conventional rolling, cross rolling or pressing as indicated in figure 6.8. Although the data are scattered with some extent, there is a tendency that J_c increased with decreasing the oxide layer thickness t_o, except for the data from the specimens processed by rolling. A TMT process of DcRc-R-, where rolling was used to deform the tape after second heat treatment turned out to be no effective to increase J_c. However, the J_c was found to be improved by pressing after second heat treatment. The microstructure of oxide layer parallel to the length direction of tape for the specimen prepared by DcRc-R- was investigated and its photographs were shown in figure 6.9. Work instability was found to be large when the tape was deformed by rolling. Furthermore, large pore was observed in necked region of oxide layer. The transport current is thought to be interrupted at this region.

6.3.4 Influence of the degree of cold working

Figure 6.10 shows a summary of the critical current density for various tapes prepared by different degree of cold working in RgP-P- process. The experimental data of both J_c and thickness are very scattered even for the tapes prepared by same condition. There is, however, a tendency in the oxide layer thickness dependence. Obviously the J_c increases with decreasing oxide layer thickness. The highest J_c at zero magnetic field is recorded to be 22400 A/cm^2. For the tapes prepared by the same condition, the average values of J_c and layer thickness were calculated as shown in figure 6.11, where the straight line attached with each average value indicates the maximum and minimum. This figure gives a clear information about the layer thickness dependence of J_c. It increases with decreasing layer thickness and reaches a maximum and then degrades rapidly for the further decrease of oxide layer thickness. Its critical thickness is evaluated to be about 20

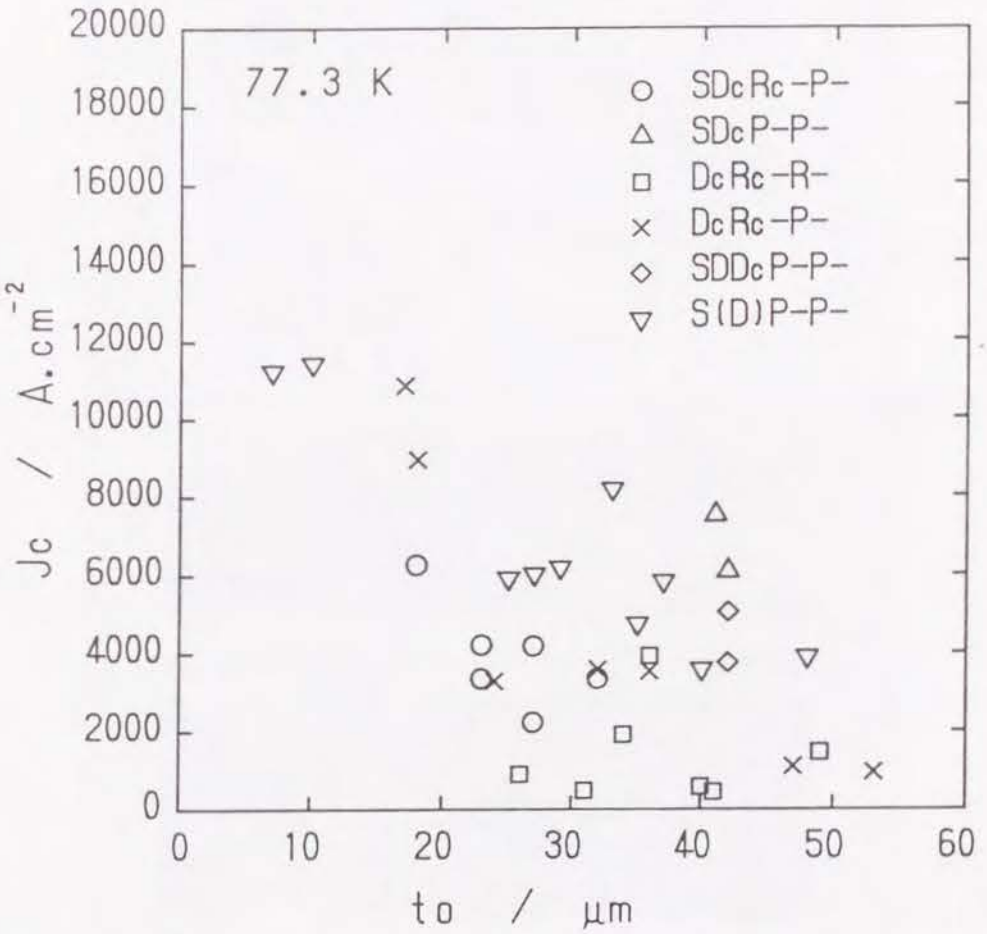

Figure 6.8 Oxide layer thickness dependence of J_c for the various specimens prepared with different cold working.

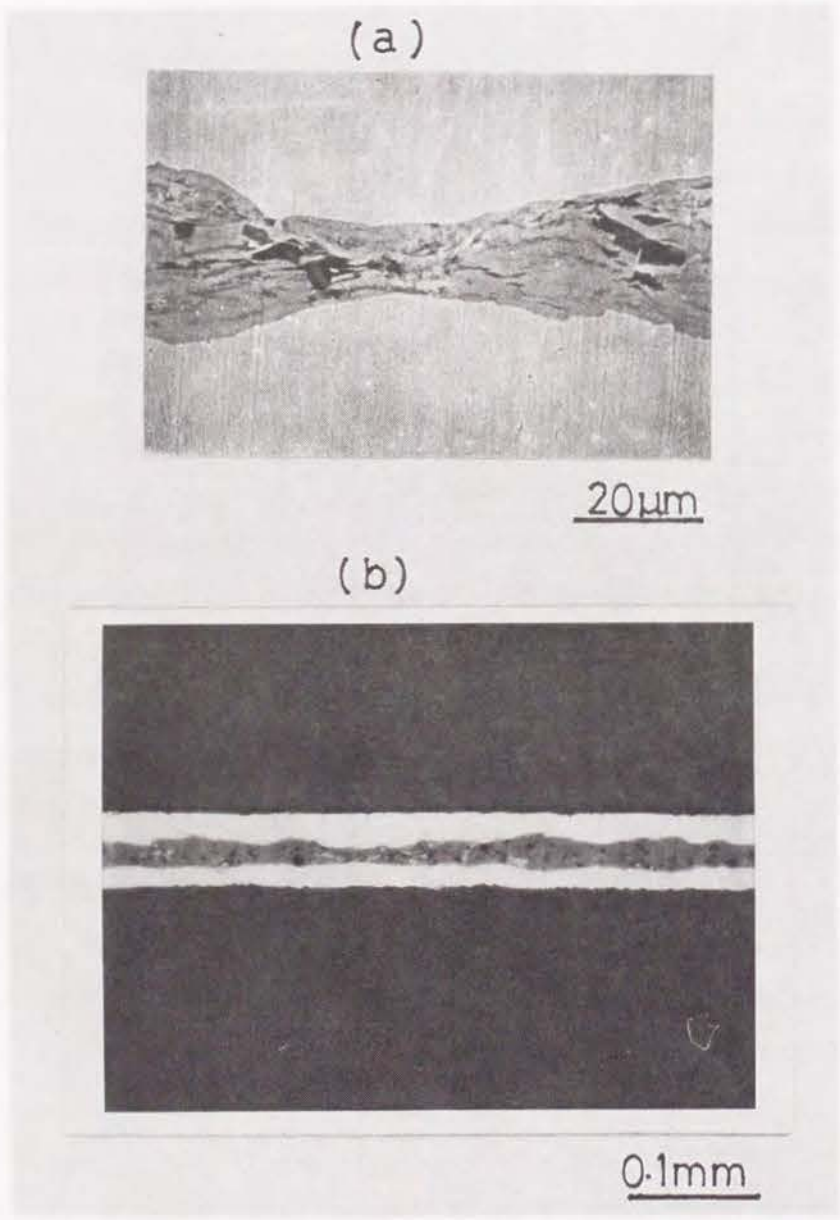

Figure 6.9 Microstructures of the specimen prepared by TMT process of DcRc-R-.

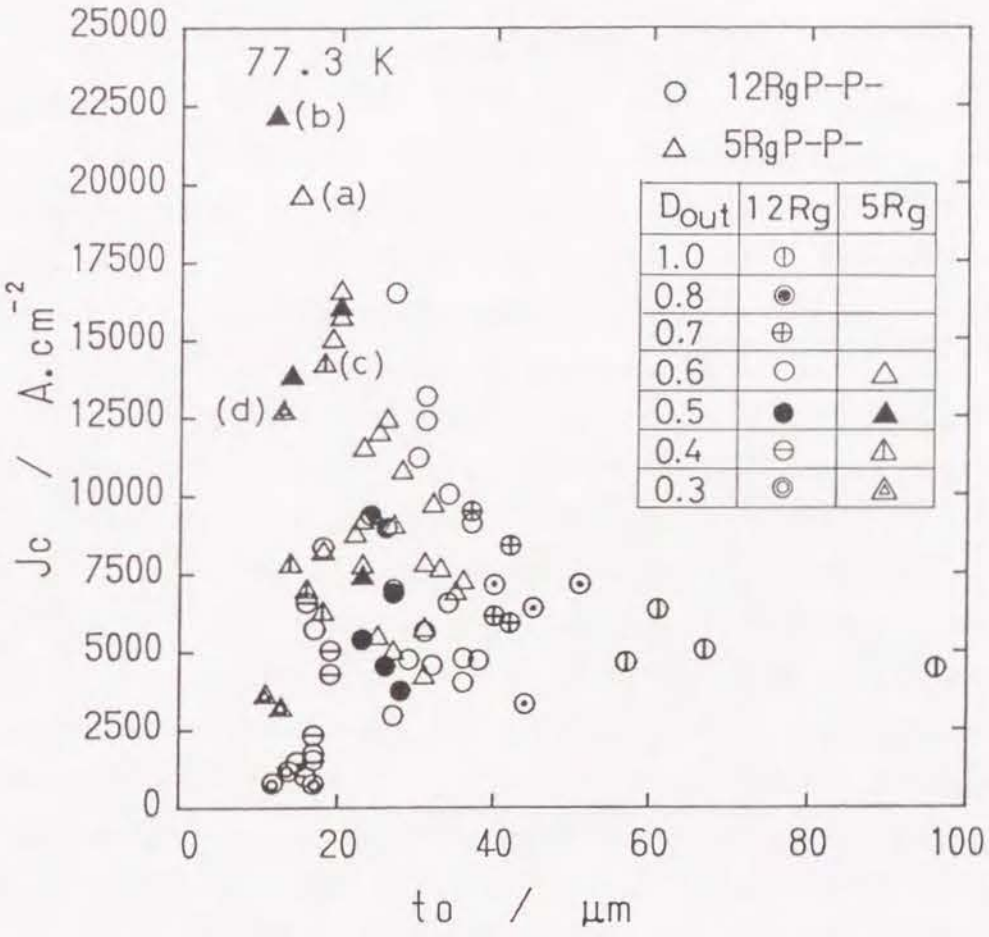

Figure 6.10 Change of critical current density at 77.3 K as a function of oxide layer thickness for the tapes prepared from different starting-tubes, where the data are classified by the same signs for the tapes with same value of D_{out} in dimension of mm.

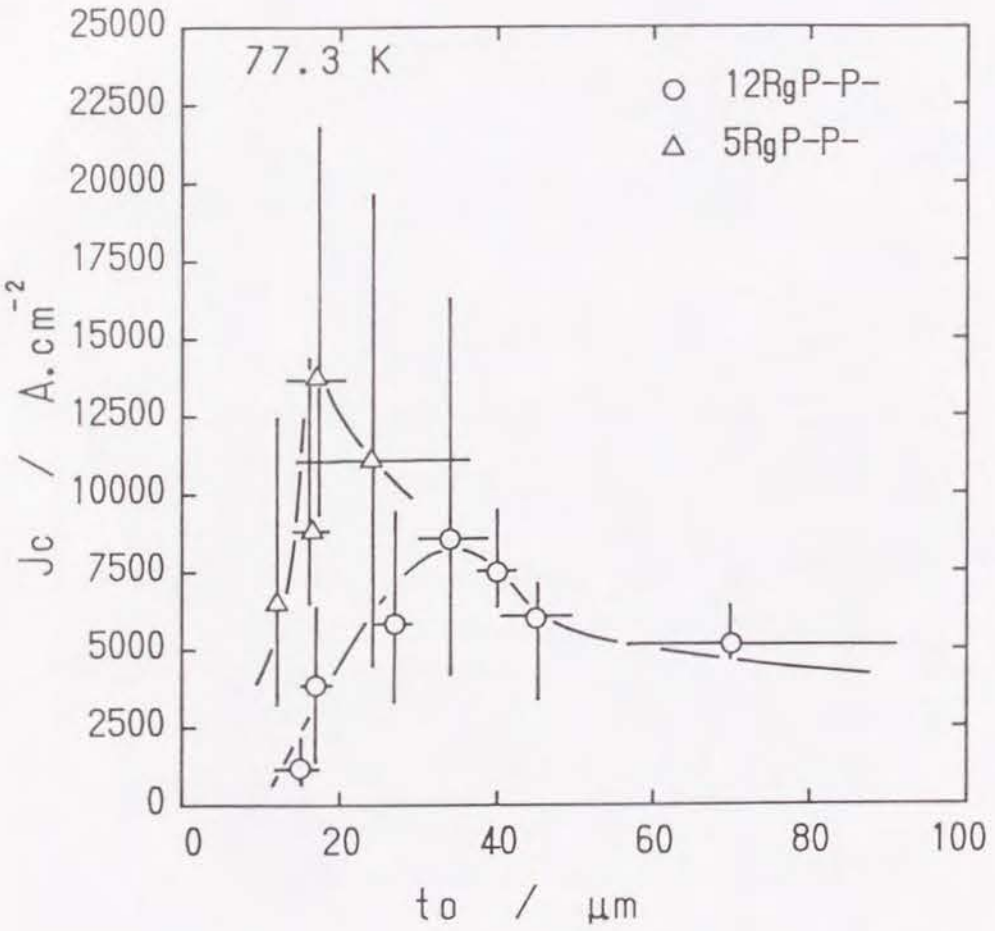

Figure 6.11 Averaged J_c vs averaged oxide layer thickness for the tapes prepared by the same condition.

and 30 μm for the 5 ϕ and 12 ϕ tapes, respectively. Figure 6.12 shows the change of J_c as a function of degree of reduction of cross sectional area, where S_o(i) and S_o(f) are the total cross sectional area of the composites before and after a series of the thermomechanical treatment, respectively. When the degree of reduction increases, the J_c increases and reaches maximum and then degrades. It was found that the J_c increases with increasing degree of reduction as shown in low reduction area. In this region, however, the absolute value of J_c is quite different for both tapes prepared from the different tubes. This result suggests that the degree of reduction has no direct correlation to the change of critical current density. In order to clarify the degradation of J_c due to the heavy reduction, the deviation of layer thickness has been examined. Figure 6.13 shows the views of the composite parallel to the current flow for the specimens with different reduction ratio. The oxide layer thickness fluctuates in place to place Figure 6.14 shows the oxide layer thickness dependence of COV. The COV becomes large when the oxide layer thickness is less then 30 μm for 12 ϕ tapes and 20 μm for 5 ϕ tapes, respectively. This result is consistent with the layer thickness dependence of J_c as shown in figure 6.10. Therefore it is suggested that the degradation of J_c is attributed to the work instability. Figure 6.15 shows the sheath thickness dependence of COV. The thickness dependence is identical for two types of tape. When the sheath thickness is smaller than about 0.1 mm, the COV became large and the work instability appeared. Therefore, it is suggested that the work instability depends primarily on sheath thickness. As shown in figure 6.13, the thickness fluctuates along the current direction. To calculate the critical current density, the smallest thickness should be adopted. In the statistical viewpoint, the probability finding the event by 99.7 % is given 3 σ, where σ is the standard deviation and the coefficient of variation is equal to σ/t_o. Therefore it is assumed that the smallest thickness is put as $t_o - 3\sigma$ statistically. The average values shown in figure 6.11 were corrected using this minimum cross sectional area. The result is shown in figure 6.16. Here, the corrected values are indicated by solid symbols tend to increase monotonously with decreasing thickness. It seems that the effect of work instability is eliminated. From the above-mentioned arguments, it is made clear

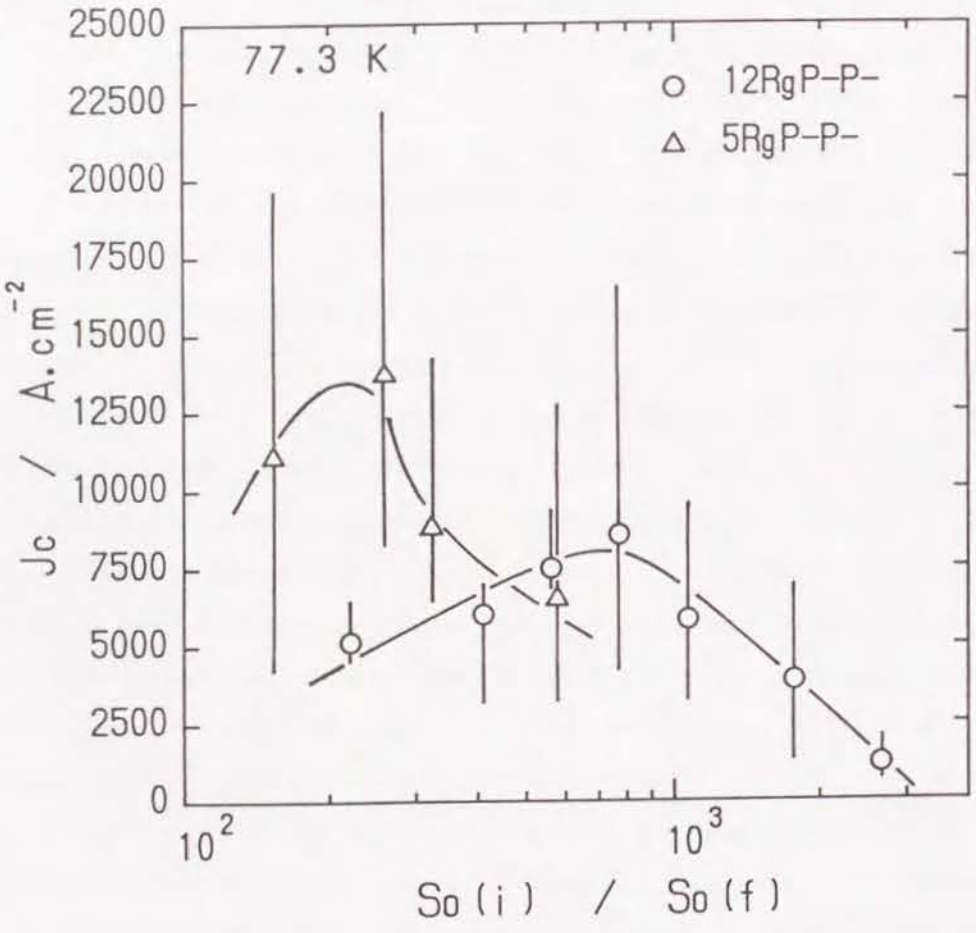

Figure 6.12 Change of critical current density as a function of the area ratio of the final tape to the starting tube for the tapes prepared from the tubes with different D_{out}.

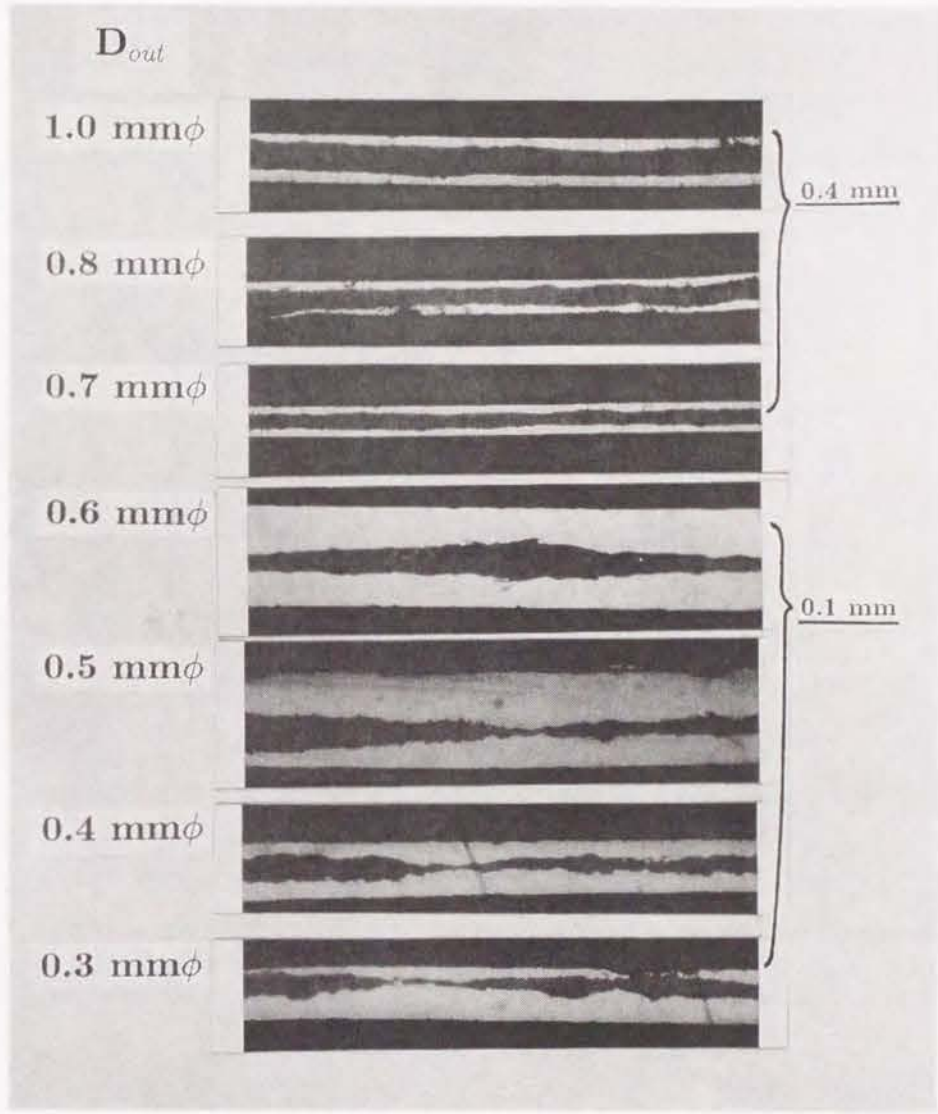

Figure 6.13 Photographs of the cross section parallel to the current flow direction for several tapes prepared from the tubes with different D_{out}.

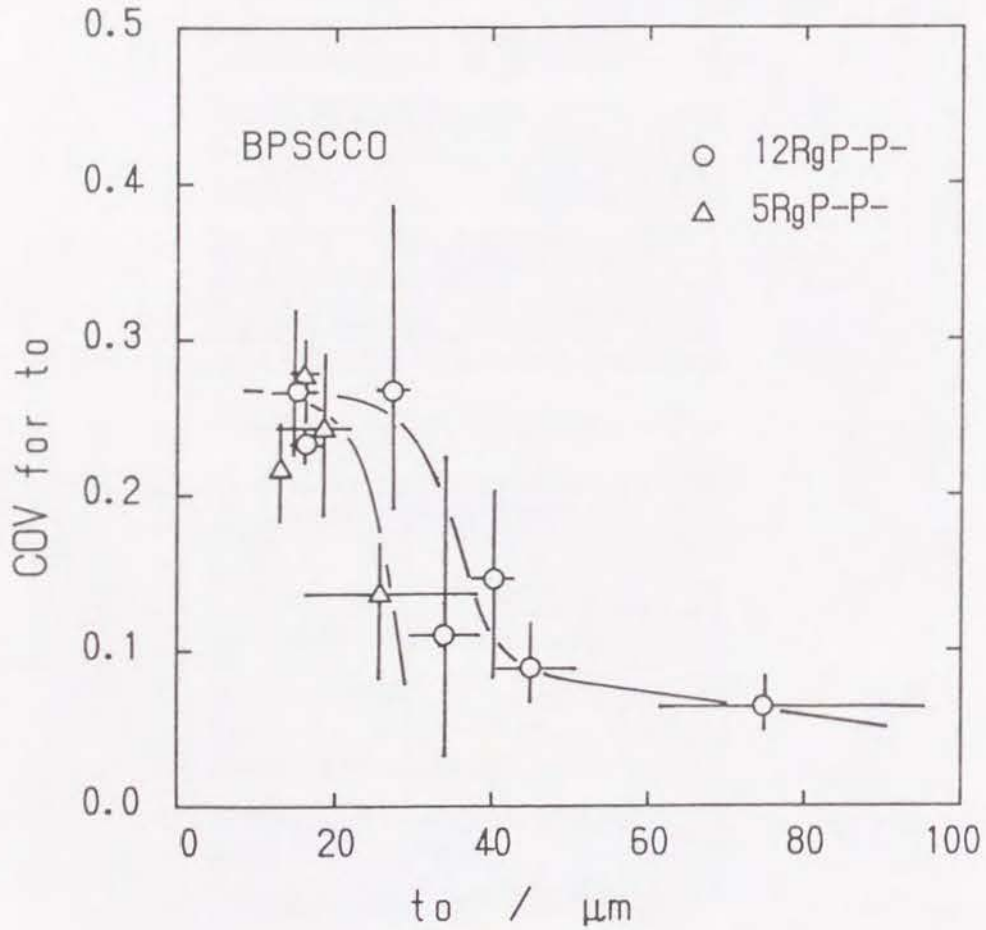

Figure 6.14 The oxide layer thickness dependence of COV for the tapes prepared from the tubes with different D_{out}.

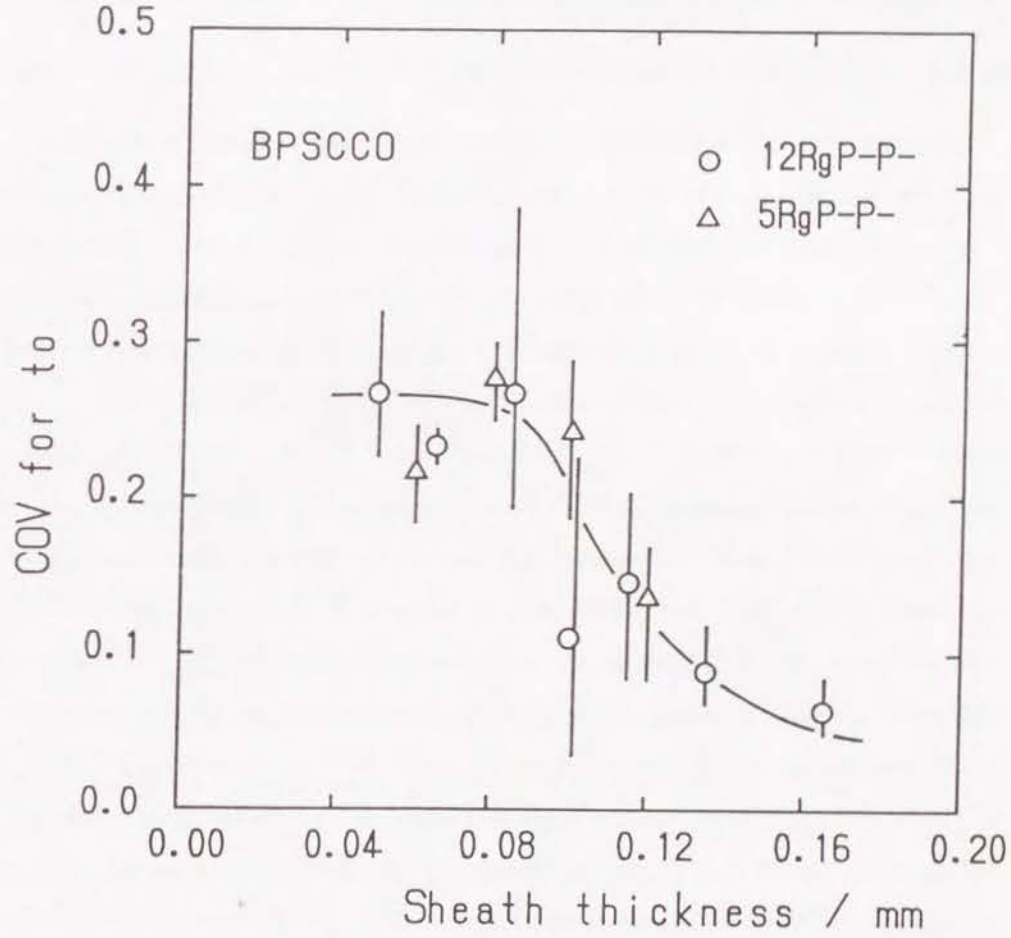

Figure 6.15 Change of COV as a function of sheath thickness for the tapes prepared from the tubes with different D_{out}.

that a very high J_c value exceeding the 10^5 A/cm^2 is obtainable when the present powder-in-tube technique. Figure 6.17 shows the temperature dependence of critical current density at zero magnetic field. At both temperatures, J_c increased with decreasing the layer thickness. J_c at 4.2 K was found to be higher by $5 \sim 6$ times than that for 77.3 K.

6.3.5 Magnetic field dependence of critical current density

The magnetic field dependence of critical current density at 4.2 K and 77.3 K, respectively was investigated for the tapes prepared with various cold working conditions. Figure 6.18 shows the magnetic field dependence of normalized critical current density J_c(B)/ J_c(0 T) at 4.2 K for the specimens with various oxide layer thicknesses. Here, external magnetic field was applied parallel and perpendicular to the tape surface and the current. The critical current was measured at static magnetic field with increasing magnetic field from 0 to 15 T. For all the specimens, J_c dropped drastically at low field and kept almost constant up to 15 T. It was confirmed that the degradation ratio of J_c with respect to increase of magnetic field depends on the oxide layer thickness of the specimen. It was found that a drop of J_c to magnetic field becomes large for the thick tape specimen. Figure 6.19 shows the magnetic field dependence of J_c for the specimen different oxide layer thickness, t_o. Magnetic field was applied parallel and perpendicular to the tape surface and the current from zero up to 15 T and down to 0 T. The J_c over 20,000 A/cm^2 could be obtained at high field region of 15 T for the specimen with thinner t_o, where J_c(77.3 K, 0 T) was 23000 A/cm^2. The J_c of the specimen with thinner t_o exceeded the value of 10^5 A/cm^2 at zero magnetic field. The hysteresis effect of J_c–B due to increasing and decreasing the external magnetic field was observed for both specimens. It was found to be slightly reduced for the specimen with thinner t_o. This hysteresis effect was known to be related with existence of weak link such as grain boundary in the superconductor. When the external magnetic field is applied to superconductor, the self-field with opposite direction is induced due to the shielding current against penetration of flux line by external magnetic field as shown in figure 6.20. The transport J_c decreases

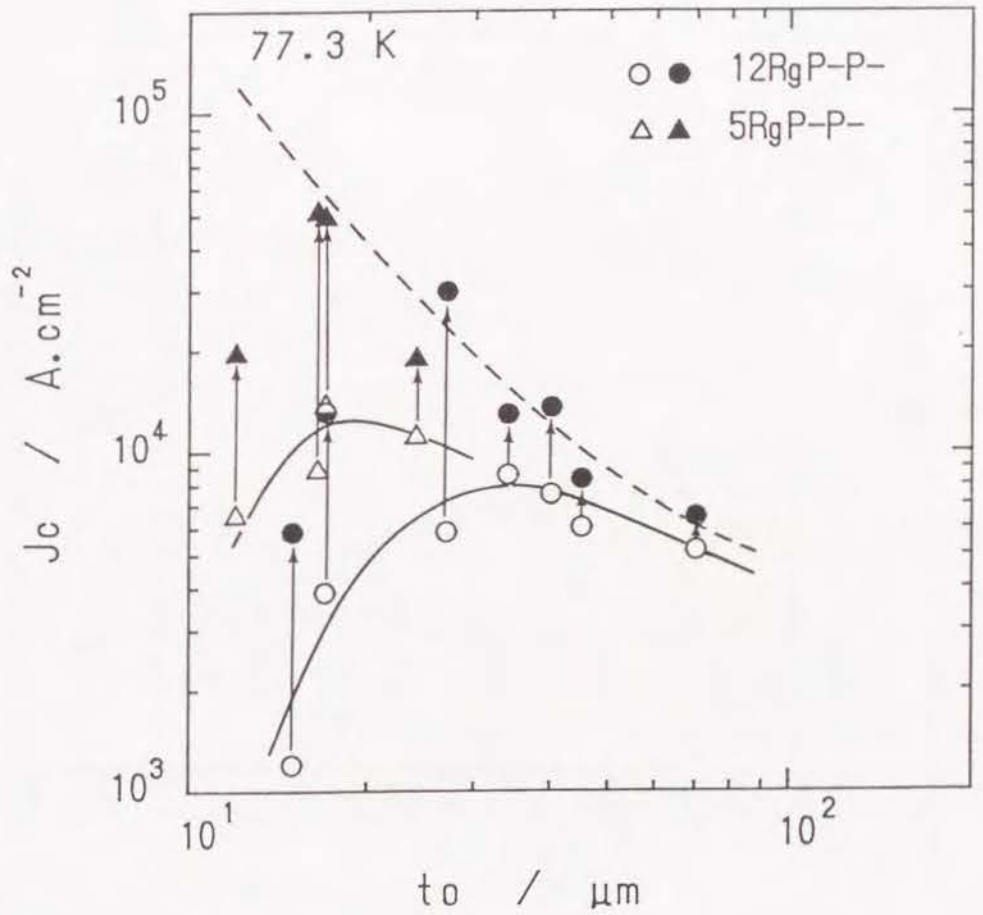

Figure 6.16 Correction of critical current density by using the statistically smallest oxide layer thickness for the tapes prepared by the same condition.

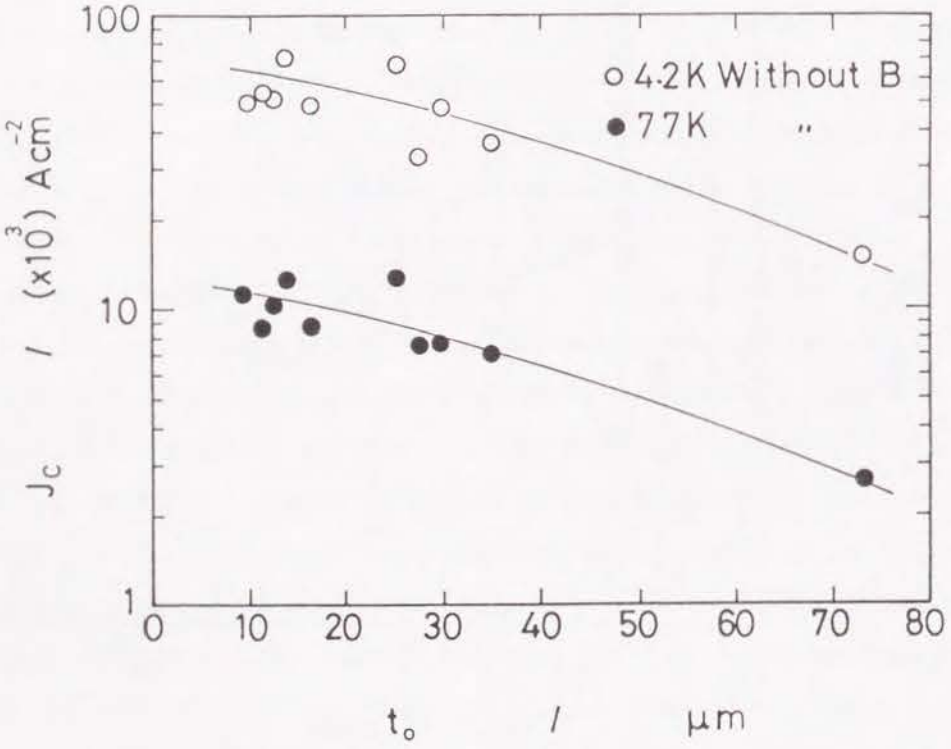

Figure 6.17 Oxide layer thickness dependence of J_c at different temperatures of 77.3 K and 4.2 K.

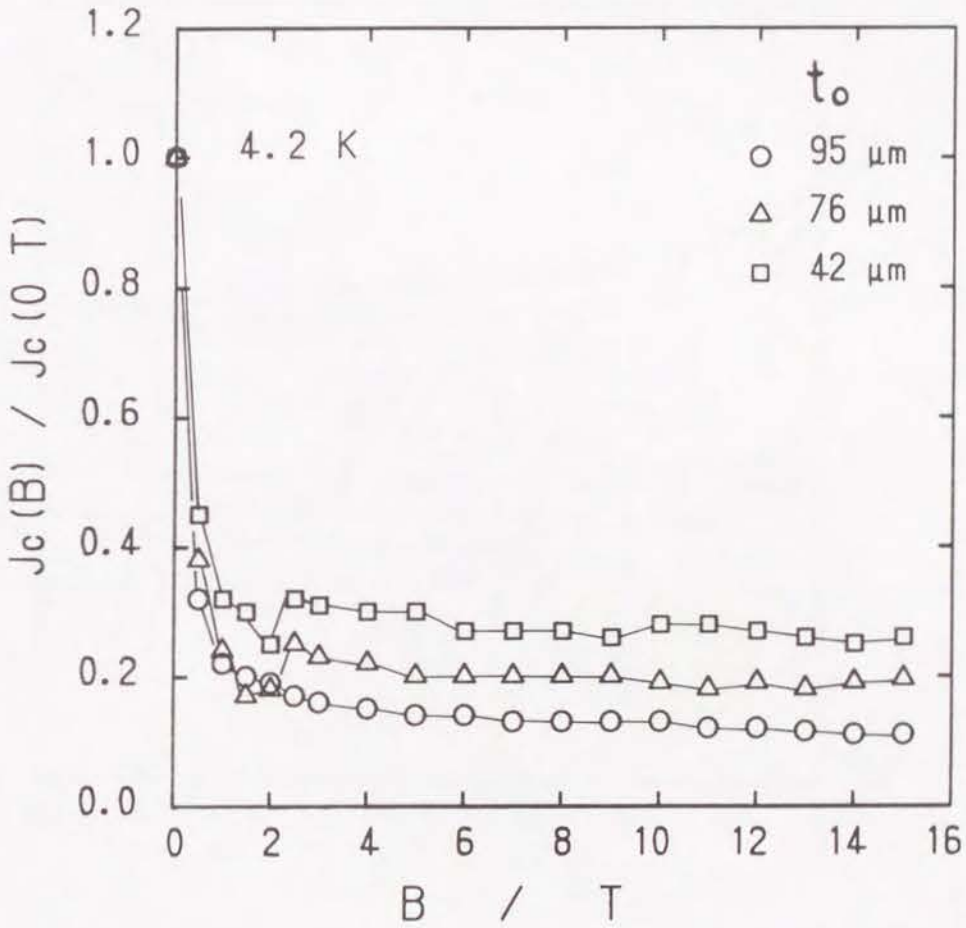

Figure 6.18 Magnetic field dependence of normalized critical current density at 4.2 K, J_c(B) / J_c(0 T) for the tapes with different oxide layer thickness.

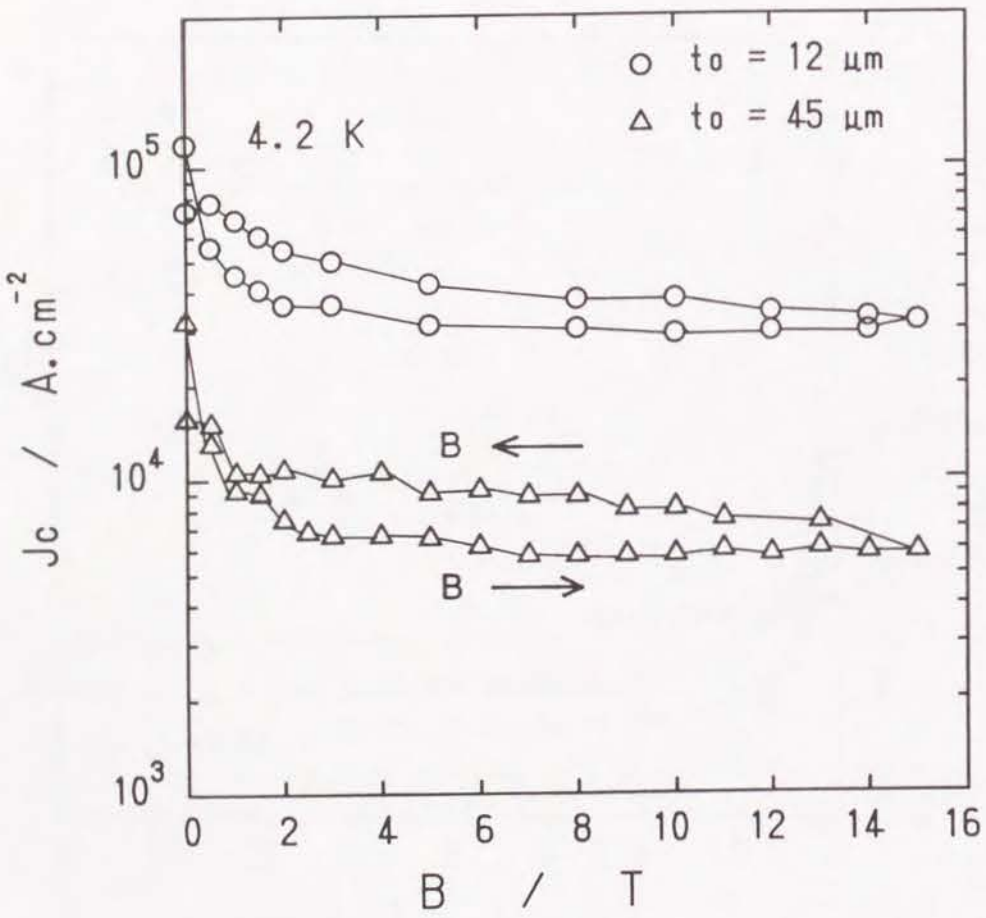

Figure 6.19 Magnetic field dependence of critical current density at 4.2 K for the tapes with different oxide layer thickness, where magnetic field was applied up to 15 T and down to 0 T.

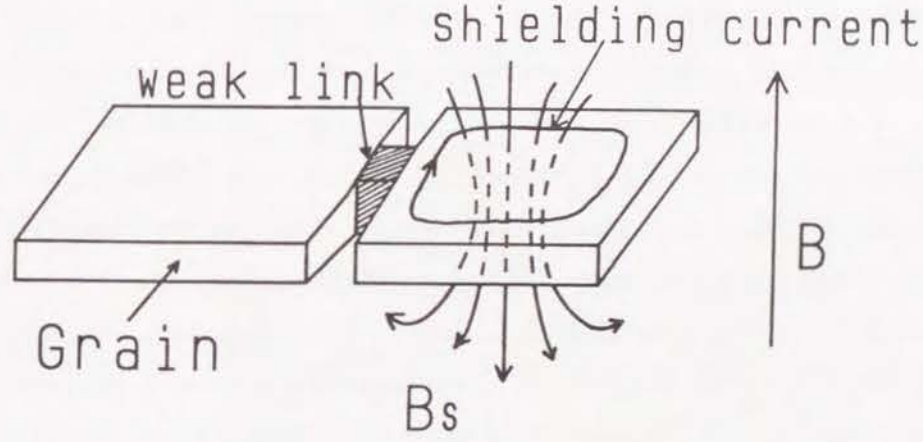

Figure 6.20 Schematic explanation for a generation of self-field due to shielding current.

because the magnetic field superposes to the self-field with same direction at grain boundary when the external magnetic field is applied increasingly, while J_c increases because the direction of self-field at grain boundary becomes opposite against the direction of external magnetic field owing to magnetic flux line trapped at defects in crystal when the external magnetic field is applied decreasingly. It was reported [9] by Sato *et al.* that the hysteresis effect is reduced by improvement of grain boundary structure. Figure 6.21 shows the dependence of magnetic field direction on J_c at 4.2 K. In the whole range of magnetic field, J_c appeared to be high when the magnetic field was applied parallel to tape surface and perpendicular to the current. Figure 6.22 shows the microstructures of polished(a) and fracture surface(b) parallel to current flow. The plate like 2223 superconducting phase, the thickness of which is $1 \sim 3$ μm and impurity phases such as $(Sr, Ca)_3Cu_5O_x$ and $(Sr, Ca)_2CuO_3$ were observed in photograph (a). As shown in photograph (b), it was found that the plate like grains are composed of laminated thin grains well coupled with each other. Because of layered structure and weak bonding between the two Bi-O layers in Bi-based material, twist boundary is easily formed by overlapping and sliding layers along one another [10,11]. According to this, planar boundaries observed in photograph (b) can be assigned as twist boundaries. Due to the theory suggested [12] by Sato *et al.* flux lines can be possibly pinned by layered crystal structure, and then flux pinning is considered to be large when the magnetic flux lines penetrate parallel to twist boundaries and perpendicular to the current because the Lorentz force acts perpendicular to twist boundaries. When magnetic field is applied both perpendicular to the tape surface and the current, J_c is thought to be reduced because J_c is mainly determined by the pinning property of bulk material. According to this, texturing is considered to be effective for improving flux pinning. Figure 6.23 shows the magnetic field dependence of normalized critical current density, $J_c(B)/J_c(0\ T)$ at 77.3 K for the specimens with different J_c value at zero magnetic field. The cold working condition and oxide layer thickness for the specimens indicated in figure 6.23 are summarized in table.1. The magnetic field was applied parallel to the tape surface and perpendicular to the current up to 0.5 T.

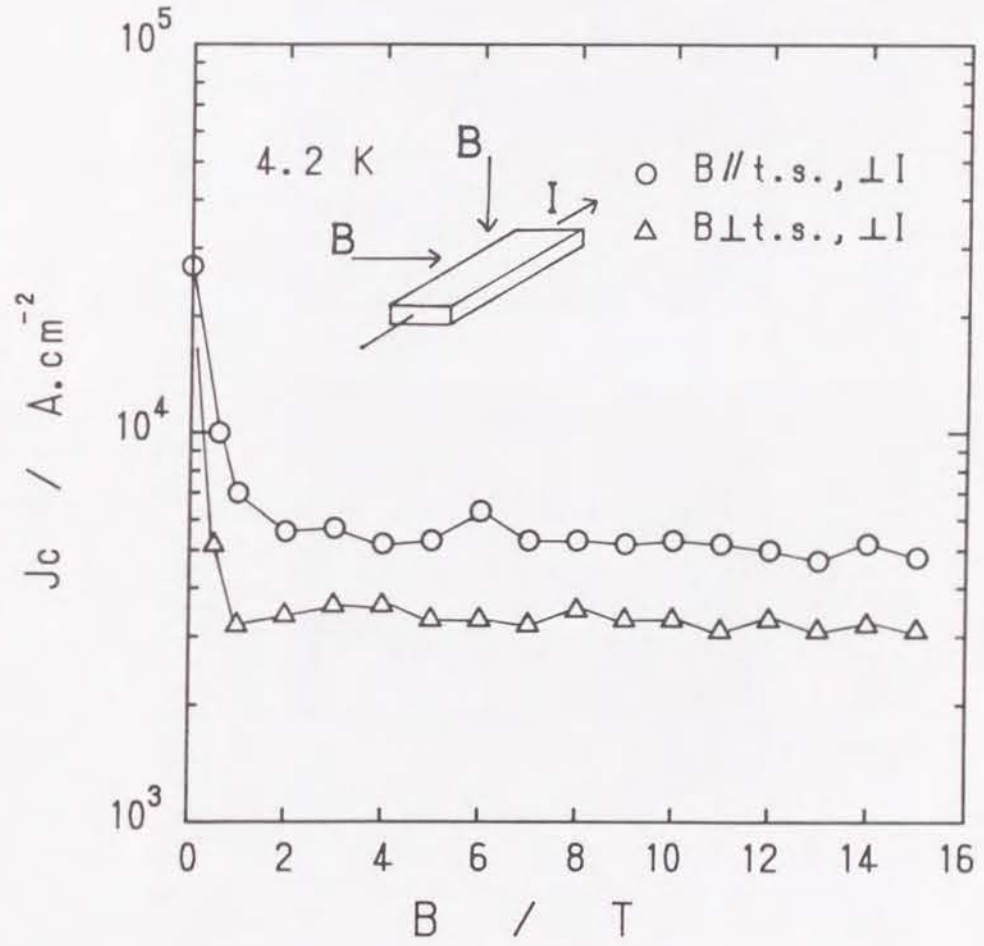

Figure 6.21 Magnetic field dependence of critical current density at 4.2 K , where the direction of magnetic field was change to tape surface(t.s.).

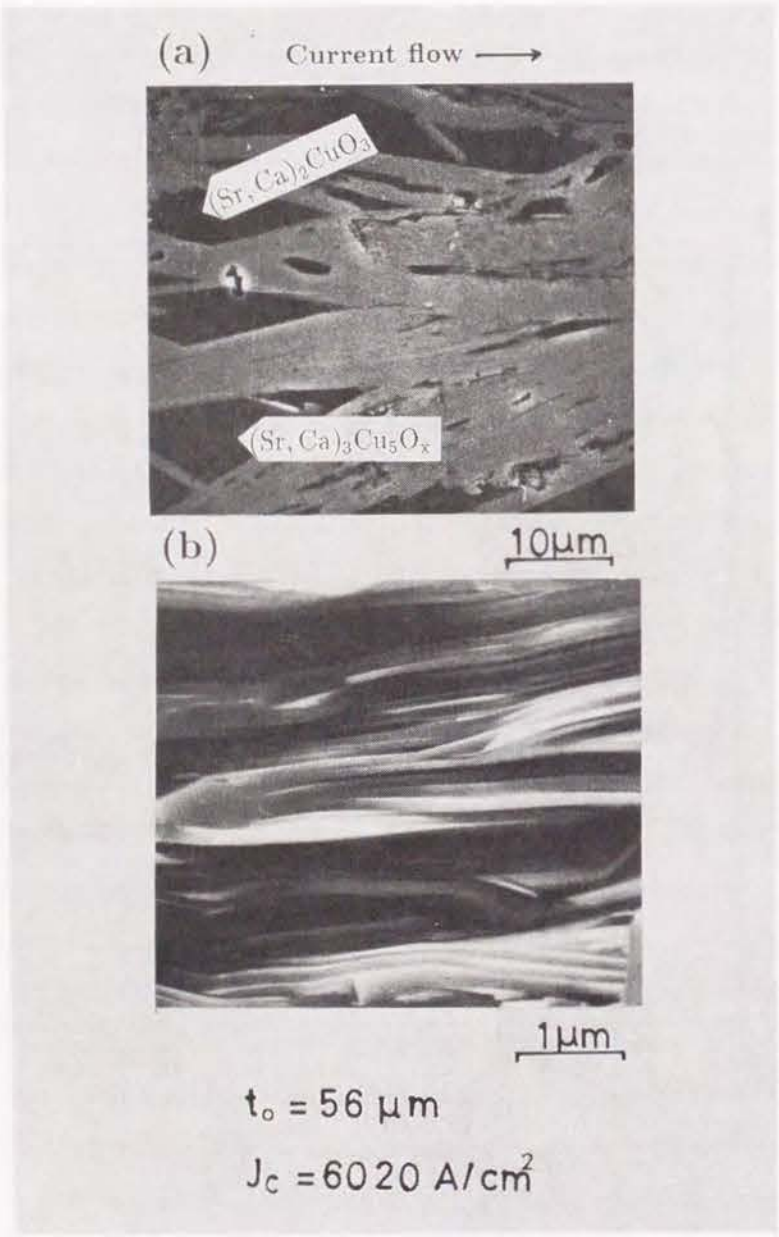

Figure 6.22 Microstructures of polished (a) and fracture surface (b).

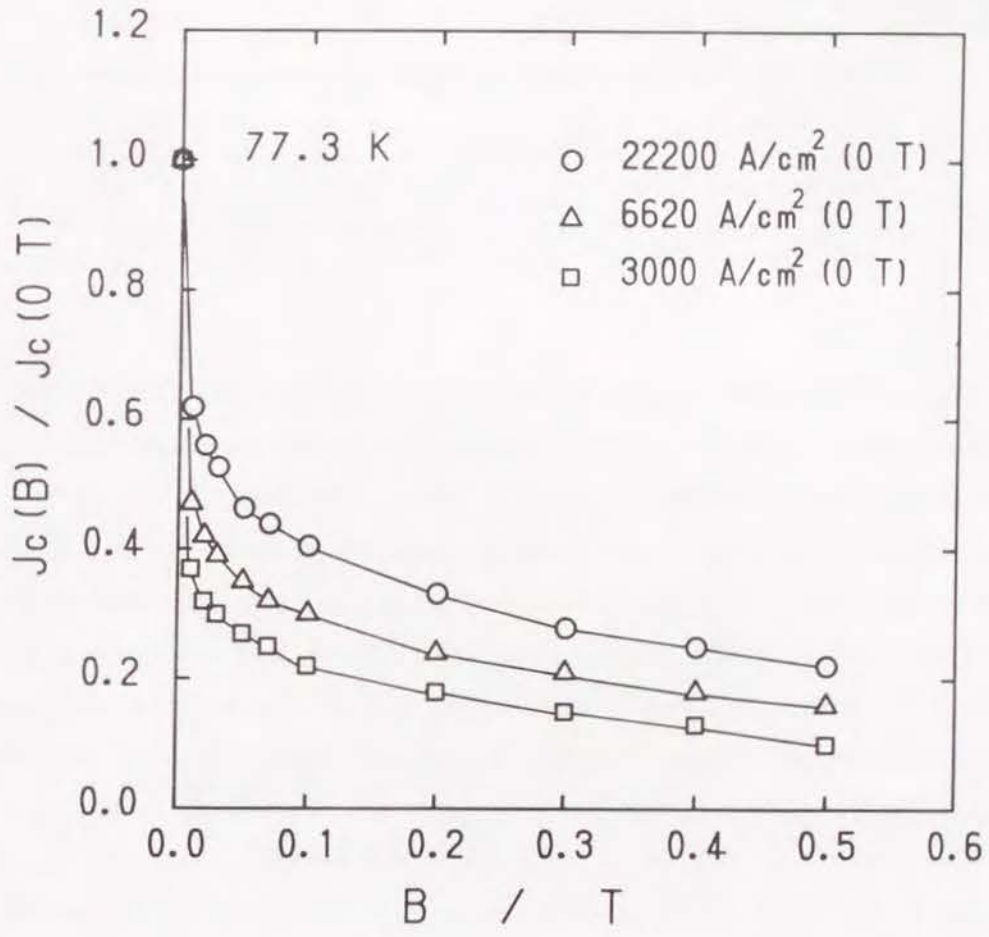

Figure 6.23 Magnetic field dependence of normalized critical current density at 77.3 K, J_c(B) / J_c(0 T) for the tapes with different J_c at zero magnetic field.

For all the specimen, J_c dropped largely at the region of low magnetic field below 0.1 T and its tendency depends on the value of J_c at zero magnetic field. It was found that the magnetic field dependence of J_c can be improved for the specimen with higher J_c at zero magnetic field.

Table 6.1 Preparation conditions, t_o and J_c for various specimens

TMT	t_o / μm	Heat Treatment	J_c / Acm^{-2}
Rg(0.6)P-P-	12	1113 K, 360 ks - 1113 K, 180 ks	22200
S(1.0)P-P-	52	1113 K, 360 ks - 1113 K, 180 ks	6620
S(1.2)P-P-	106	1113 K, 360 ks - 1113 K, 180 ks	3000

Figure 6.24 shows the magnetic field dependence of global pinning force (F_p) for above two specimens. For all the specimens, global pinning force increased monotonously with increasing the magnetic field. The F_p for the specimen prepared by RgP-P- increases at a much faster rate than that for other specimens. It can be found that global pinning force is remarkably improved for the specimen with higher J_c at zero magnetic field, which was prepared by RgP-P-. The global pinning force was found to be saturated at 0.5 T for the specimen with the lowest J_c. For Bi–based materials, planar defects such as twist boundaries and stacking faults can occur by cold working and then, severe cold working is expected for improving pinning force. This seems to be reasonable because the sever cold worked specimen with thinner oxide layer thickness exhibited large pinning force as shown in figure 6.24. Figure 6.25 shows the magnetic field dependence of J_c for various specimens, where the reference data [13] by Dou *et al.* were also indicated. It was known that the sintered bulk exhibits double step behavior [14] of J_c vs magnetic field. In the low field region below 0.01 T, J_c for bulk rapidly drops. This is known to be due to that the J_c is limited by Josephson weak links, rather than flux pinning. At very low fields, the supercurrents flows through the whole volume of the sample and J_c is determined by the maximum Josephson current of the grain boundary weak links, while at the higher field where the weak links are normal conducting, the supercurrent flows through percolative

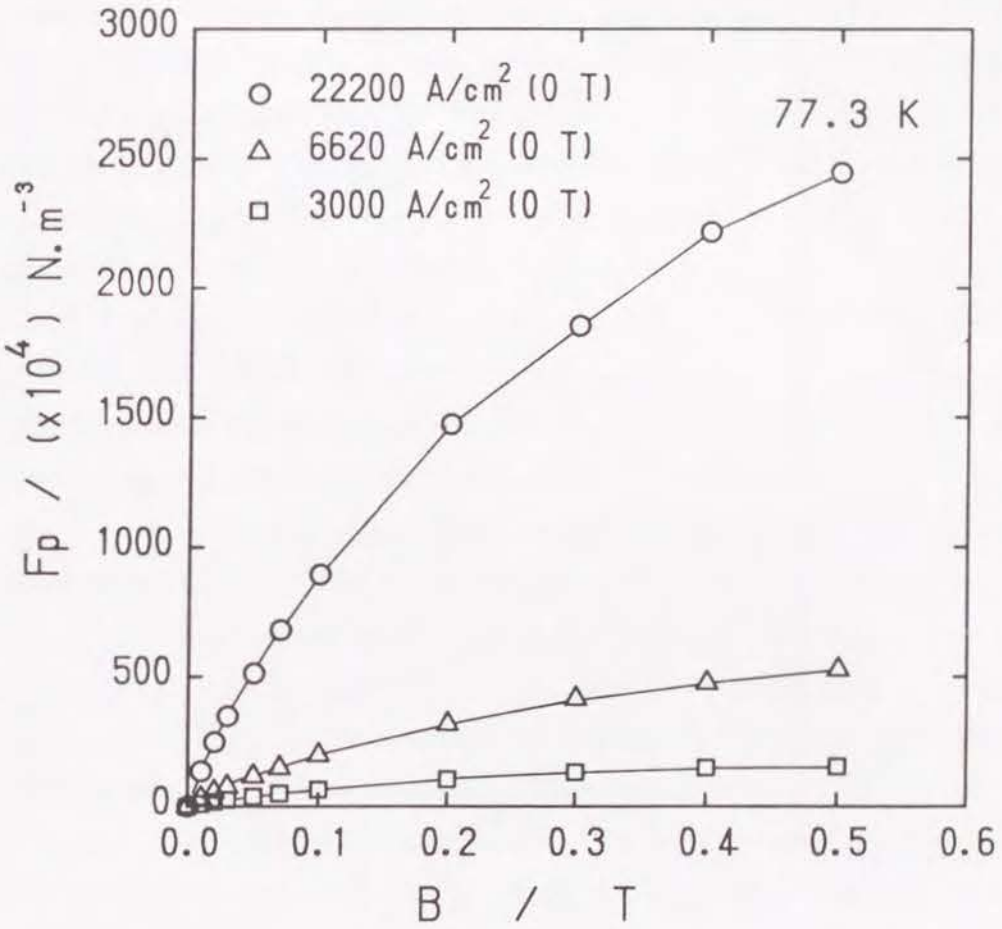

Figure 6.24 Magnetic field dependence of global pinning force for the same specimens presented in figure 6.23.

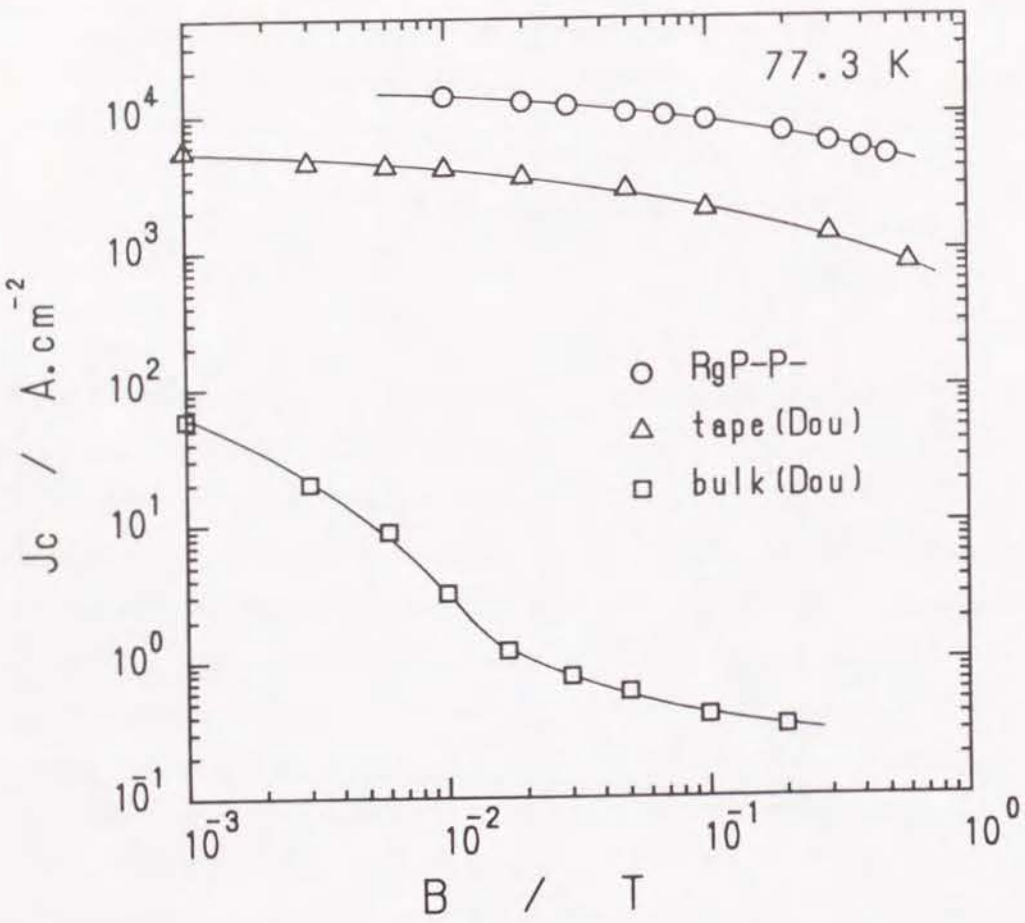

Figure 6.25 Magnetic field dependence of critical current density at 77.3 K for the present tape, where reference data are also indicated in figure.

paths and J_c is determined by flux pinning. The J_c for both tape specimen decreased at much slower rate than the that for bulk one. This is attributed to that grain boundary weak links are considerably improved for both tape specimens processed by TMT, compared to that for bulk one. The present tape processed by RgP-P- exhibited better magnetic field dependence of J_c than that for the Dou's tape processed by cold rolling and heat treatment. Figure 6.26 shows the magnetic field dependence of critical current density for the specimens prepared with different cold working. It was found that the hysteresis effect of J_c – B can be improved by optimizing the cold working condition. This is attributed to that the weak links are improved due to refinement of microstructure such as densification and texturing. Comparing with result at 4.2 K from figure 6.19, the hysteresis effect is found to be relatively reduced at 77.3 K. Figure 6.27 shows the microstructure of polished surface which are parallel to the direction of current flow for the specimens with various oxide layer thickness. As shown in photograph A, the thick tape specimen processed with relatively low cold working degree has a very porous structure and the connectivity between the grains was observed to be bad. The transport current for the specimen shown in photograph A is considered to be limited at void and large impurity phase. It can be observed that the oxide layer becomes dense and grain alignment parallel to the tape surface(current flow) is improved for the specimens with thinner layer thickness and then, the good aligned specimen showed higher J_c. In average, the a-b plane which is more superconductive than other plane in crystal structure was found to parallel to tape surface by analysis of pole figure as mentioned Chapter 5. It was confirmed that the higher critical current density is obtained from refinement of structure such as high density and textured structure. Figure 6.28 shows the relation between the J_c(0 T) and J_c(0.5 T) for various specimens processed by combination of grooved rolling and other techniques. Almost positive linear relationship was observed between J_c (0 T) and J_c (0.5 T) for all the specimens. The J_c value of 19600 A/cm^2 at 0 T corresponded to the J_c value of 4100 A/cm^2. It was found that magnetic field dependence of J_c is not associated with cold working method.

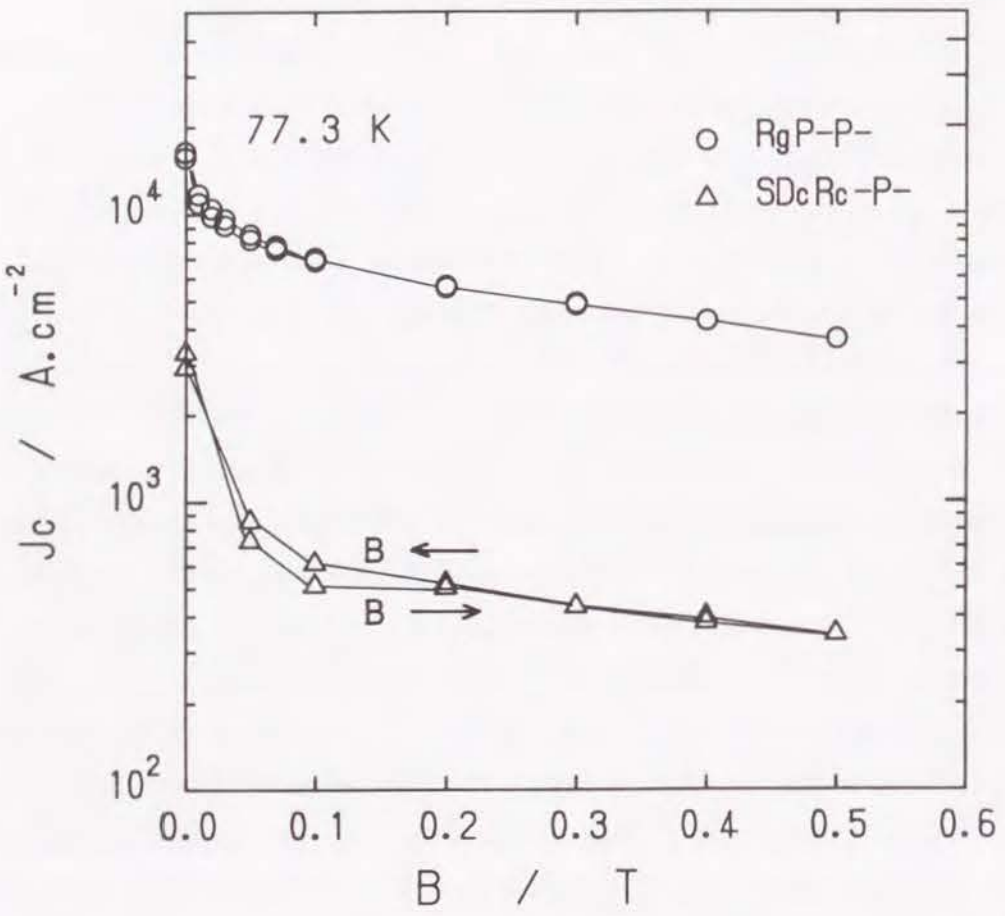

Figure 6.26 Magnetic field dependence of critical current density at 77.3 K for the tapes with different cold working, where magnetic field was applied up to 0.5 T and down to 0 T.

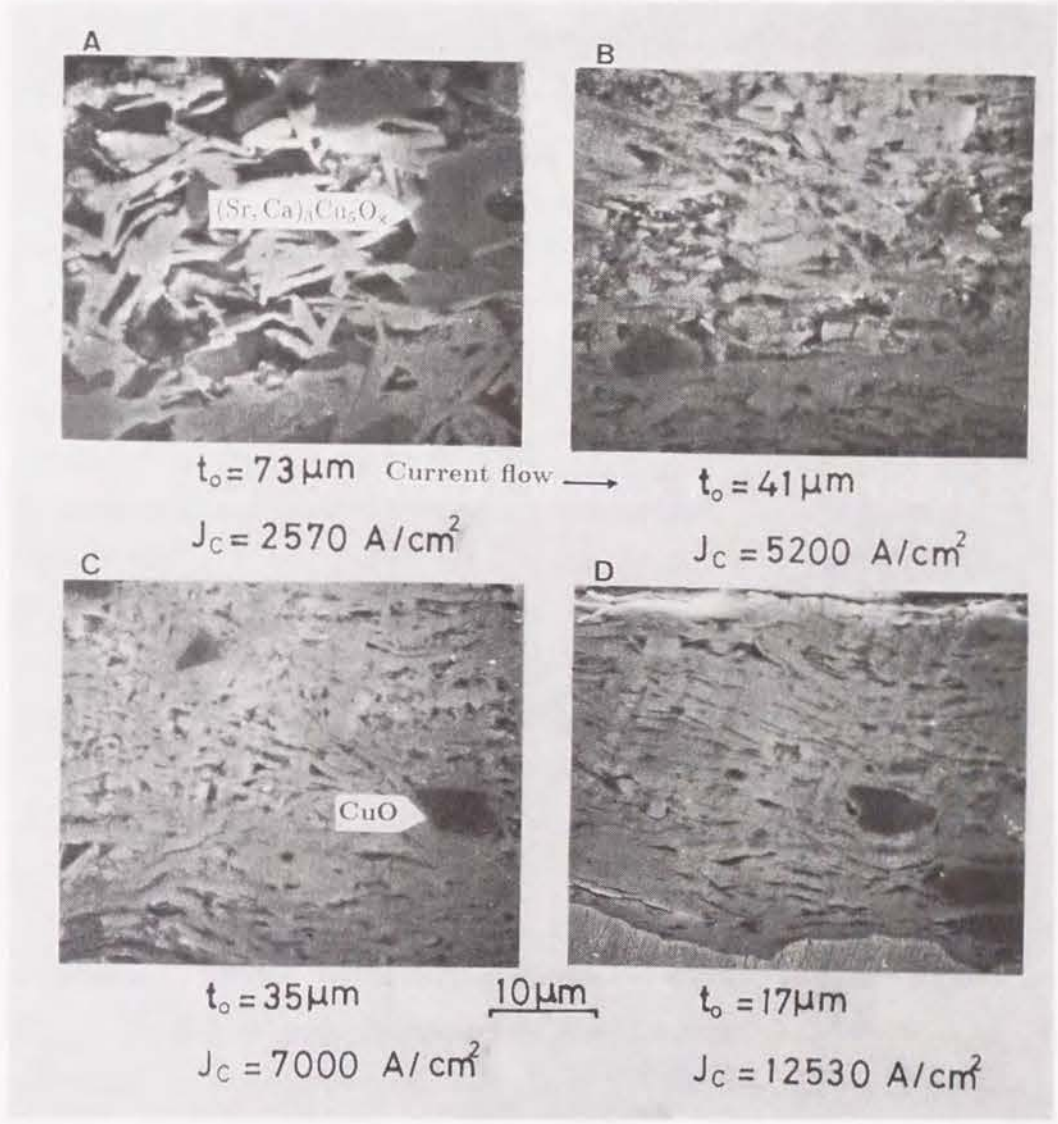

Figure 6.27 Microstructures of polished surface parallel to direction of current flow for the tapes with different oxide layer thickness.

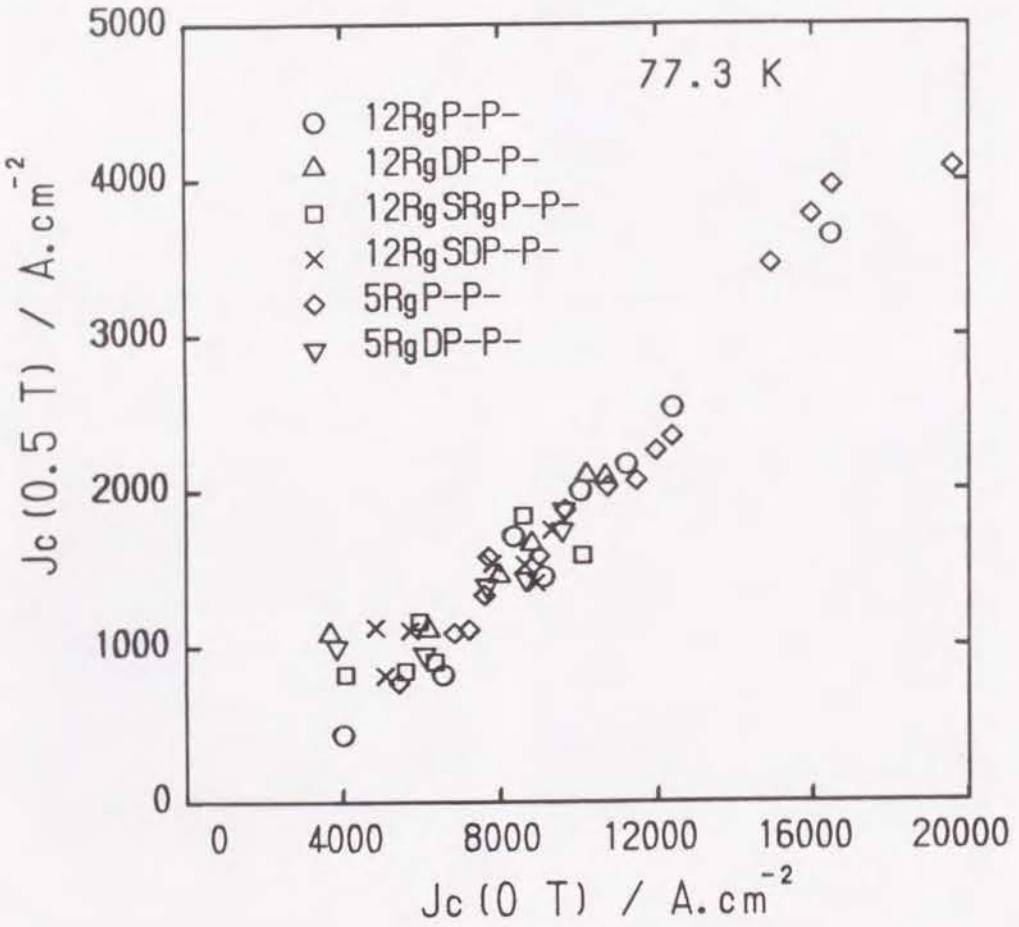

Figure 6.28 The relation between the J_c (0 T) and J_c(0.5 T) at 77.3 K for the specimens prepared with different cold working combination and outer diameter of starting tube.

6.3.6 I–V characteristic

When a transport current,I is applied to the oxide superconductor at a given magnetic field, $I-V$ characteristic appears as shown in figure 6.29. In the early stage of transition, the curve can be expressed by the power law($V \propto I^n$). The index, n is a measure of the sharpness of the resistive transition; when the transition is sharp, n value becomes large. Figure 6.30 shows the relation of log$I$ vs log$V$ derived from the figure 6.29. Almost linear relationship was found at all range of magnetic field, except for the curvature of log I-log V appeared at high magnetic field. The n values were estimated at the range between 0.3 and 5 μV by the least square method and magnetic field dependence of n value for the specimen prepared with different reduction ratio was shown in figure 6.31, where the J_c at zero magnetic field was indicated in figure. The field dependence of n value depends on J_c value and the reduction ratio and it is similar to field dependence of J_c as shown in figure 6.23. The specimen with lower J_c exhibited relatively small n value especially at low magnetic fields. The n values of BPSCCO tape specimen turned out to be small, compared to that of metallic superconductor such as NbTi composite [15]. This implies that the resistive transition of oxide superconductor is not sharp. One origin of this behavior can be thought to be associated with flux creep. Flux creep occurs by hopping of flux lines thermally excited even in the state that the pinning force is larger than Lorentz force. This phenomena [16] is known to be a characteristic in the oxide superconductor which has short coherence length and small pinning force. In addition to this, weak link and work instability of the sample is suggested [17,15] to be associated with the low n value in resistive transition. Figure 6.32 shows the relation between the n value and cold working degree expressed as outer diameter of composite for various tapes prepared with 12 ϕ RgP-P-. It was found that the positive correlation exist between the outer diameter of composite before pressing and n value. This implies that the n value tend to decrease with increasing the cold working reduction ratio. Figure 6.33 shows the relation between the work instability expressed as COV and n value. Although the data are scattered, the n value decreased with increasing the COV. It can be known that the

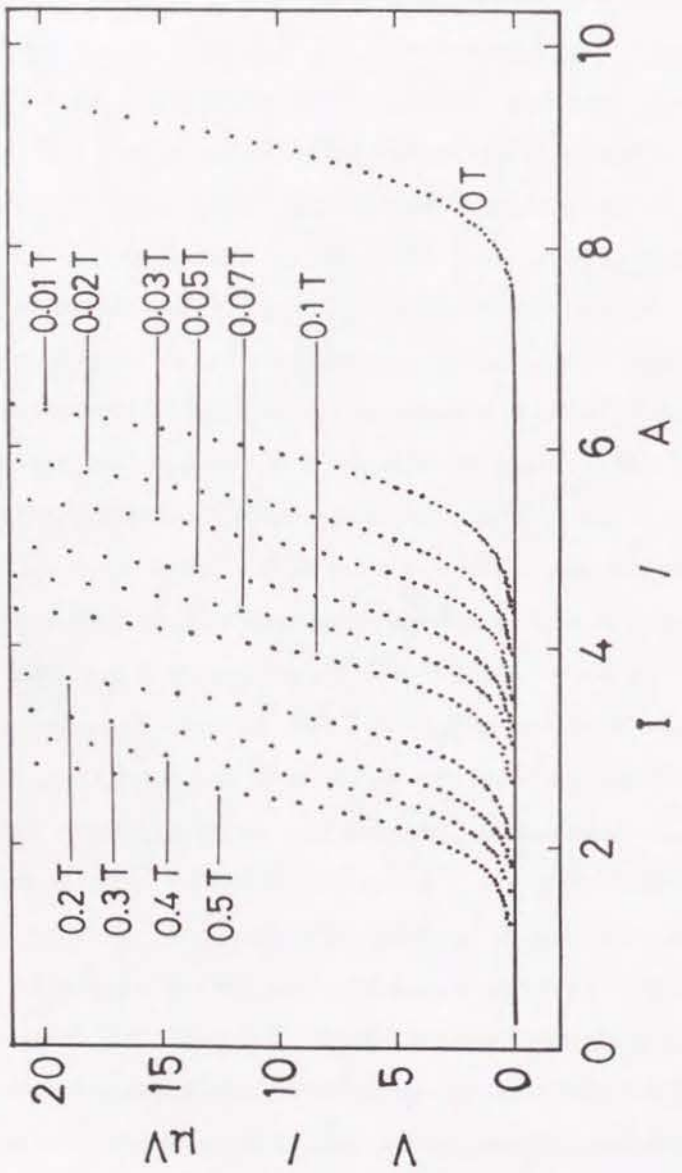

Figure 6.29 I–V curve at range of 0 ~ 0.5 T.

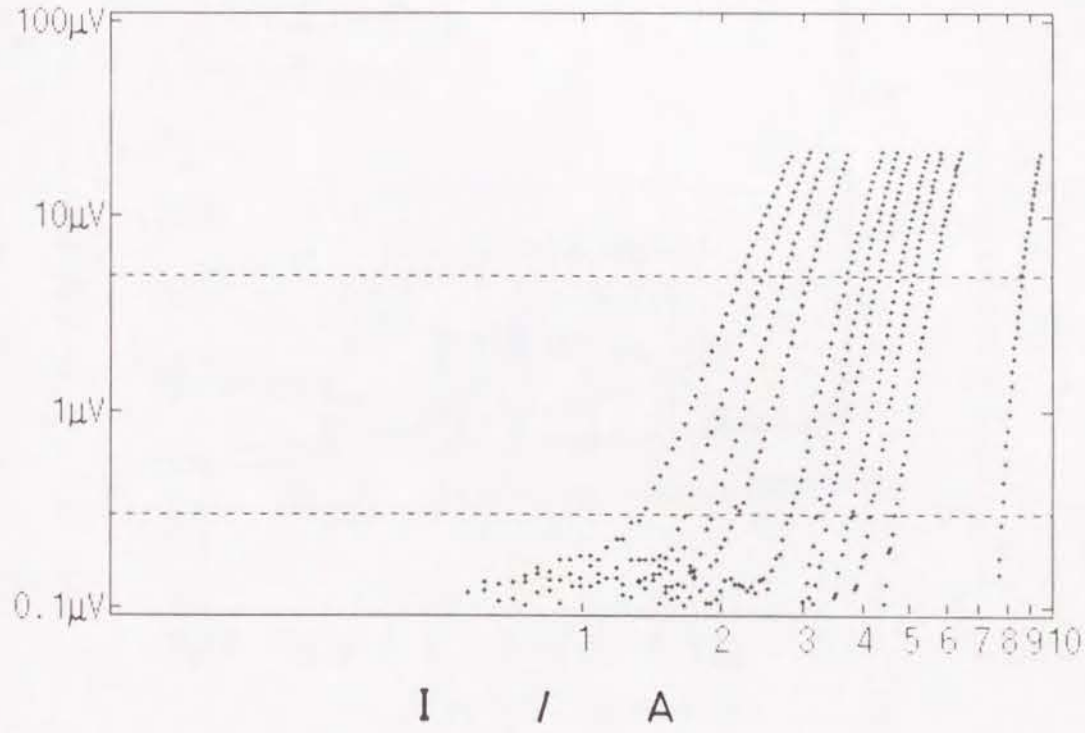

Figure 6.30 log V vs log I for the specimen presented in figure 6.29.

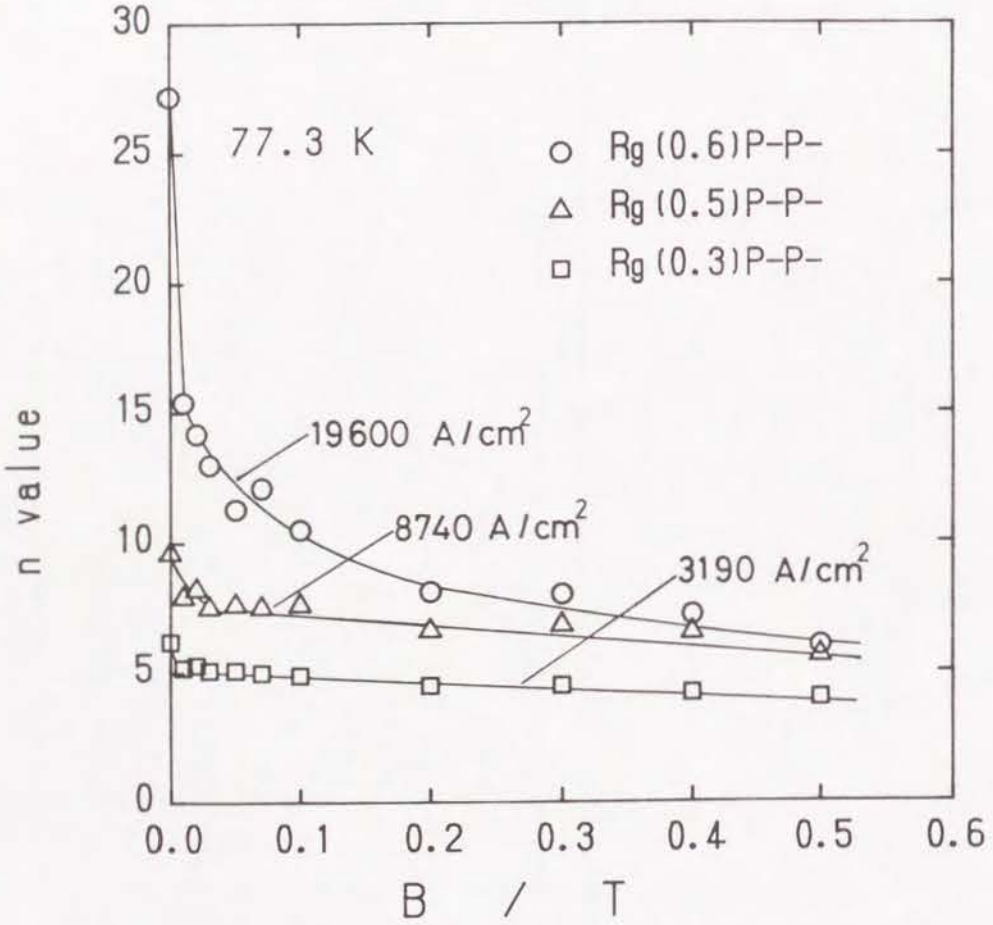

Figure 6.31 Magnetic field dependence of n value for the specimens with different reduction ratio.

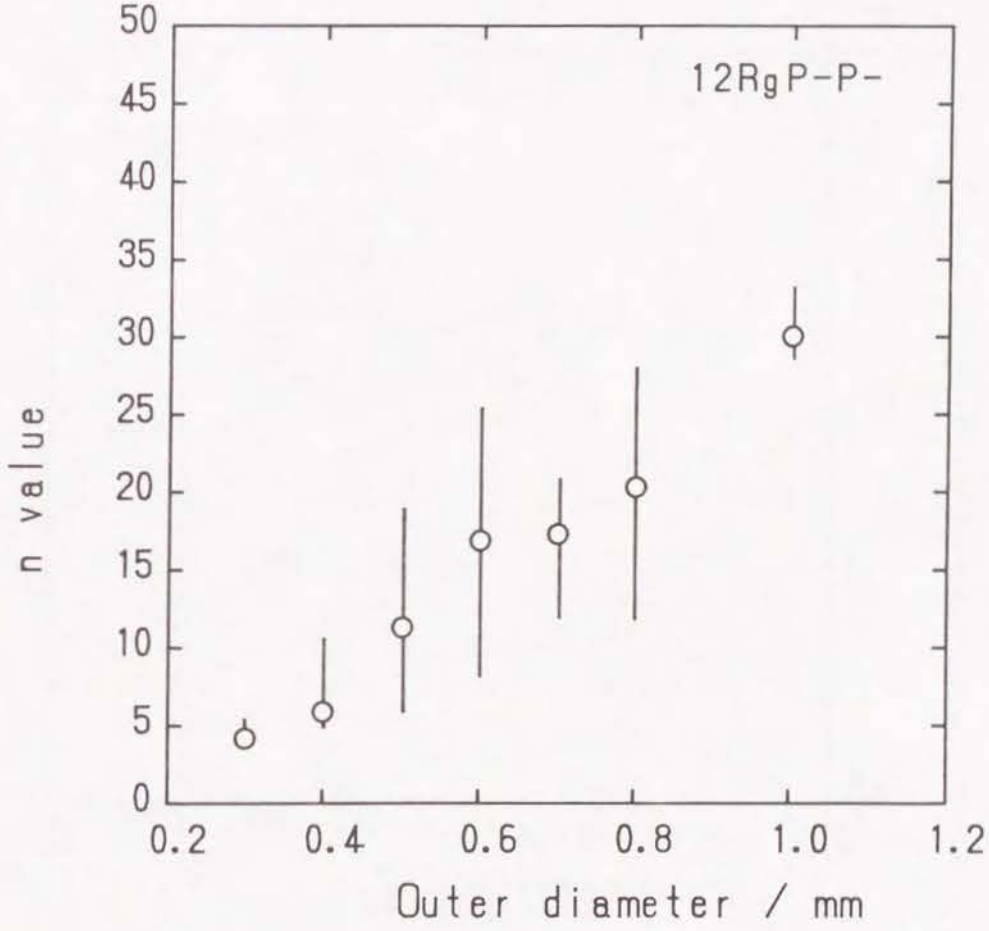

Figure 6.32 Change of n value as a function of D_{out} for the specimens prepared with a TMT combination of 12RgP-P-.

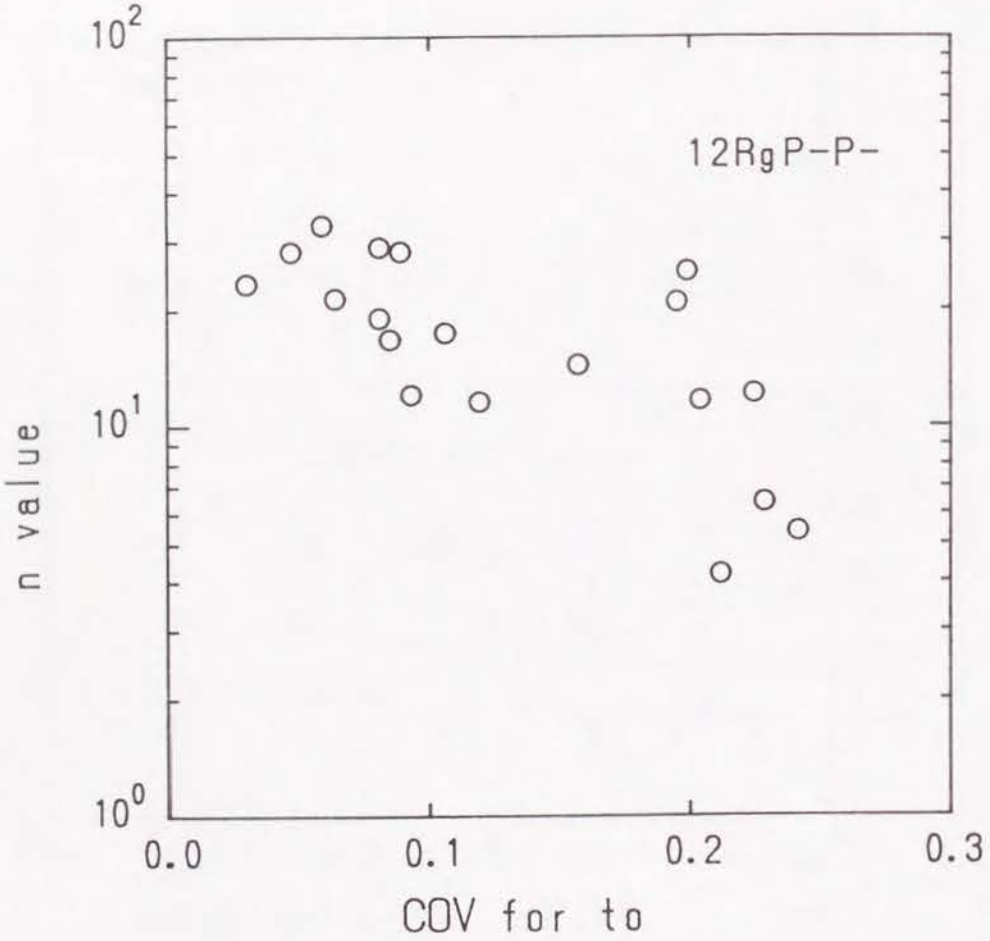

Figure 6.33 Change of n value as a function of COV for t_o for the specimens prepared with a TMT combination of 12RgP-P-.

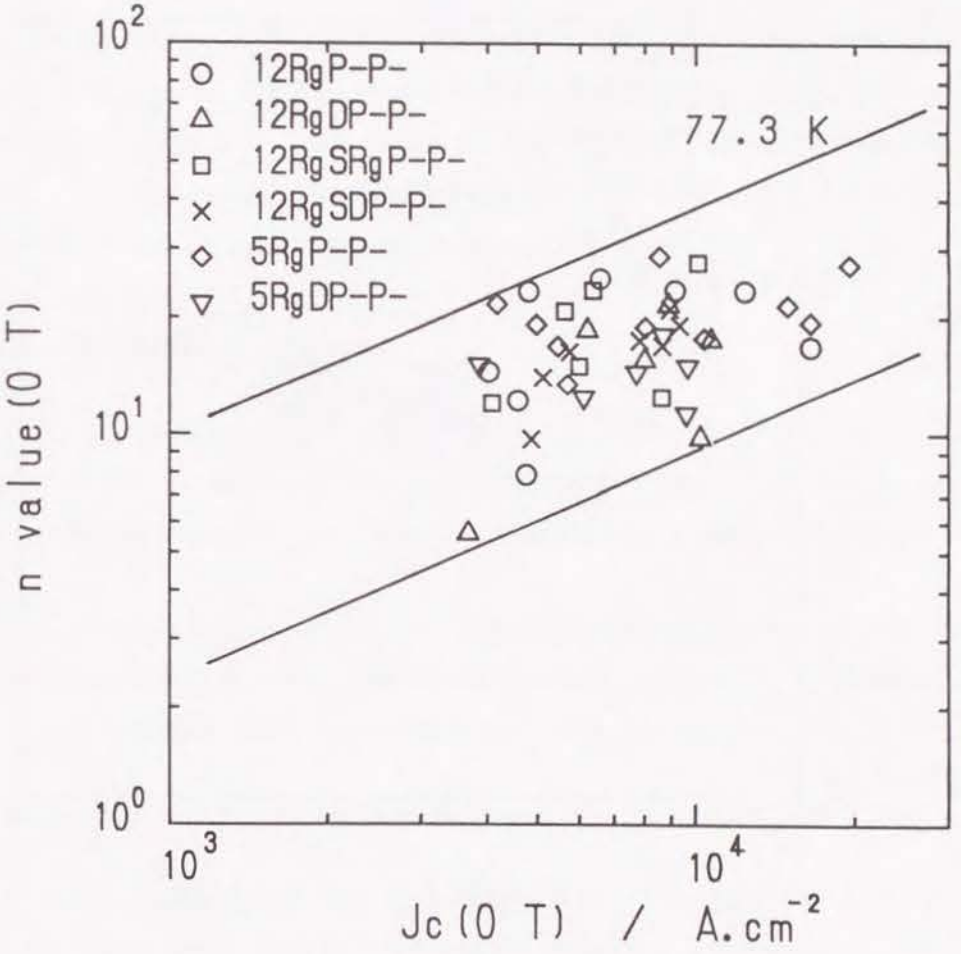

Figure 6.34 The n value(0 T) vs critical current density at zero magnetic field for the specimens with different cold working combination and D_{out}.

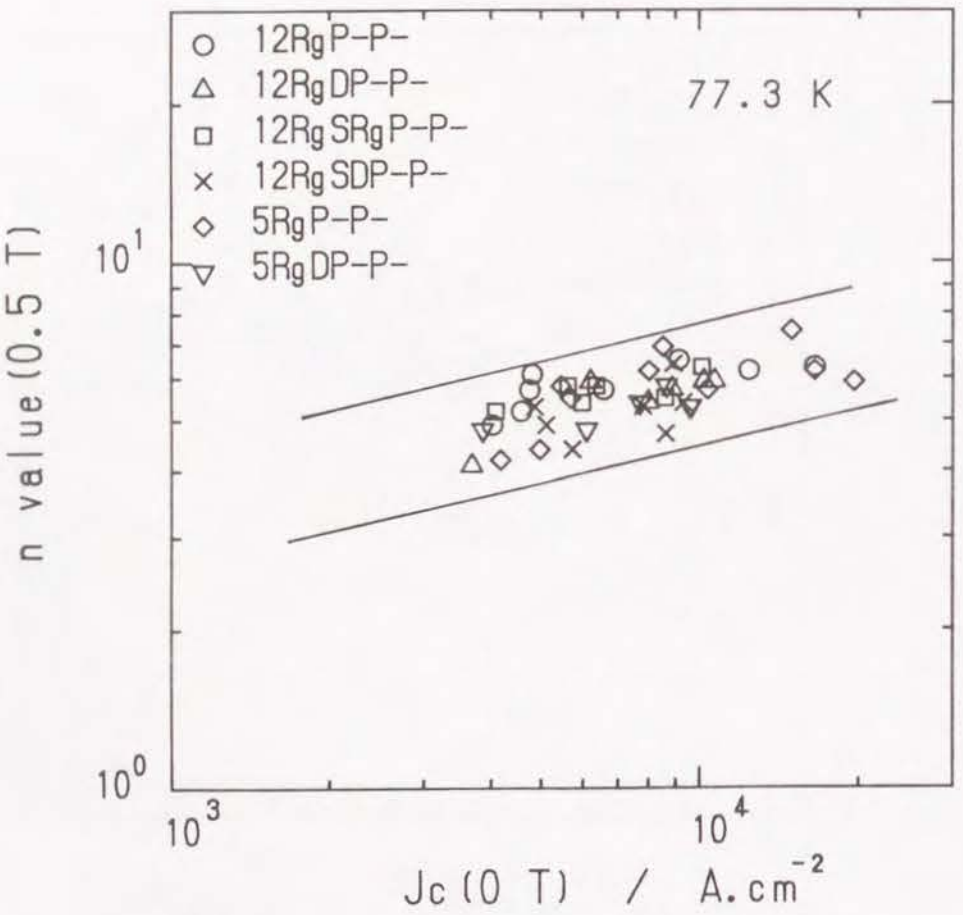

Figure 6.35 The n value(0.5 T) vs critical current density at zero magnetic field for the specimens with different cold working combination and D_{out}.

sharpness of resistive transition becomes small for the specimen with instable oxide layer. It can be confirmed that the n value depends on the work instability of oxide layer like the case of NbTi composite superconducting wire [15]. Figure 6.34 show the relation between the n value(0 T) and critical current density at zero magnetic field. Though the data are scattered, it was observed that n value increases with increasing the J_c, irrespective of cold working condition. Figure 6.35 show the relation between the n value(0.5 T) and critical current density. Positive correlation was also confirmed between the n value(0.5 T) and J_c. n value(0.5 T) distributed at range of $0.4 \sim 0.76$, deviation degree of data was found to be small for the case of n value at 0.5 T.

6.4 Conclusion

The macroscopic and microscopic change by cold working and its influence to critical current density was investigated when the Ag sheathed BPSCCO tapes was prepared by powder-in-tube technique. The main conclusions could be summarized as follow.

1. J_c increases with decreasing oxide layer thickness and reaches maximum, but degrades rapidly by further reduction of oxide layer thickness. The increase of J_c is suggested to be mainly attributed to the densification and texturing.

2. The degradation of J_c was found to be related to the work instability.

3. A correction of J_c was done in the statistical view point by assuming the smallest thickness of oxide layer as the lowest limit of thickness distribution.

4. Among various cold working techniques, the pressing turned out to be effective for increasing the critical current density. A dense and textured structure could be obtained for the specimen prepared with higher pressure.

5. Magnetic field dependence of J_c and hysteresis effect of J_c – B could be improved by optimizing the cold working condition.

6. The correlation between the sharpness of resistive transition expressed as n value and work instability or J_c was confirmed.

References

1. D. C. Larbalestier, S. E. Babcock, M. Daeumling, D. P. Hampshire, T. F. Kelly, L. A. Lavanier, P. J. Lee and J. Seuntjens : Physica C **153-155**(1988)1580.

2. S. Nakahara, G. J. Fisanick, M. F. Yan, R. B. Van Dover and T. Boone : J. Cryst. Growth, **85**(1987)639.

3. R. Flükiger, A. Jeremie, B. Hensel, E. Seibt, J. Q. Xu and Y. Yamada : *ICMC* (Huntsville,1991).

4. D. Dimos, P. Chaudhari, J. Mannhart, F. K. Legoues : Phys. Rev. Lett., **61**(1988)219.

5. S. Jin, T. H. Tiefel, R. C. Sherwood, R. B. Van Dover, M. E. Davis, G. W. Kammlott and R. A. Fastnacht : Phys. Rev.B, **37**(10)(1988)5828.

6. M. Ueyama, T. Hikata, T. Kato and K. Sato : Jpn. J. Appl. Phys., **30** (1991)L1384.

7. K. Osamura, S. S. Oh and S. Ochiai : Supercond. Sci. & Technol, Submitted(1991).

8. Y. Yamada, K. Jikihara, T. Hasebe, T. Yanagiya, S. Yasuhara and M. Ishihara : Jpn. J. Cryogenics, **25**(1990)28.

9. K. Sato, N. Shibuta, H. Mukai, T. Hikata, T. Masuda, M Ueyama, T. Kato, M. Nagata, K. Iwata, T. Mitsui : Jpn. J. Sumitomo electric, **138**(1991)145.

10. S. X. Dou, H. K. Liu, J. Wang, M. H. Apperley and C. C. Sorrell : Physica C **172**(1990)63.

11. Y. Feng, K. E. Hautanen, Y. E. High, D. C. Larbalestier, R. Ray II, E. E. Hellstrom and S. E. Babcock : Submitted to Phisica C(1991).

12. K. Sato, T. Hikata, H. Mukai, T. Masuda, M. Uneyama, H. Hitotsuyanagi, T. Mitsui and M. Kawashima : *Proc. of ISS'89* (Tsukuba, Japan, Nov. 14–17, 1989).

13. S. X. Dou, H. K. Liu, J. Wang and K. H. Song and G. J. Bowden : Physica C **171**(1990)293.

14. J. W. Ekin, T. M. Larson, A. M. Hermann and Z. Z. Sheng, K. Togano and H. Kumakura : Physica C **160**(1989)489.

15. W. H. Warnes and D. C. Larbalestier : Cryogenics **26**(1986)643.

16. Y. Yeshurun, A. P. Malozemoff, T. K. Worthington, R. M. Yandrofski, L. Kurushin-Elbaum, F. H. Holtzberg, T. R. Dinger, G. V. Chandrashekhar : Cryogenics **29**(1989)258.

17. J. Tenbrink, K. Heine, H. Krauth : *Proc. of Critical Currents in High T_c Superconductors* 24–25 Oct, 1989, Karlsruhe, FRG.

Chapter 7

Composition dependence of critical current density in Ag sheathed Bi-Pb-Sr-Ca-Cu-O tapes

7.1 Introduction

In Bi-Pb-Sr-Ca-Cu-O system, it has been known [1] that 2223 phase can be formed by long time heat treatment at restricted temperature range and some impurity phases such as Ca_2PbO_4, CuO and Sr-Ca-Cu compound easily appear at heat treatment temperatures. Considering the percolative behavior of transport current property, volume fraction of superconducting phase and morphology of impurity phase becomes important factors [2] and this is related to preparation conditions especially such as the nominal composition. Since the discovery [3] that 2223 phase is stably formed by partial substitution of Pb for Bi, a lot of studies have been carried out to investigate optimum composition for obtaining real high T_c 2223 phase in BPSCCO system. Added Pb atom has been reported to be substituted with Bi and Sr atom in crystal structure [2]. Oota *et al.* suggested [5] that the amount of Pb suitable for the formation of 2223 phase is limited by the competition between the reaction to form the 2223 phase by the catalytic effect of Pb and the one to form the Ca_2PbO_4. Endo *et al.* reported [6] that the almost single 2223 phase which was confirmed by X-ray powder diffraction can be obtained by the strict selection of nominal composition and the deviation from ideal composition delicately affects the superconducting properties. Comparing with the study for BPSSCO bulk prepared by conventional solid state

reaction method, however, it has not been studied enough for the case of Ag sheathed BPSCCO tapes. In this study, the microstructure change in BPSCCO tapes prepared by changing mole ratio of Bi, Pb, Sr, Ca and Cu and their effect on the superconducting properties were investigated.

7.2 Experimental

High purity $Bi_2O_3, PbO, SrCO_3, CaCO_3$ and CuO powders were mixed with various nominal composition. For Bi and Ca, their starting composition were changed independently with respect to other element, while for Pb, it was changed substitutionally with Bi. The composition of Sr, Ca and Cu was changed with relative ratio. Figure 7.1 shows the composition map for preparing specimens, where mole ratio of Sr, Ca and Cu elements were changed as indicating composition parameter x in the chemical formular of $Bi_{1.6}Pb_{0.4}Sr_{1.6-0.1x}Ca_{2+0.04x}Cu_{2.8+0.06x}O_y$. As shown in figure 7.1, parameter, x was changed in two directions from x = 0, where Sr increases with decreasing Ca and Cu, and Sr decreases with increasing Ca and Cu. After mixing the powders sufficiently, they were calcined at 1023 K for 43. 2 ks. By this heat treatment, the oxide powders consisting of 2212 phase and some other impurity phases were prepared. Calcination and pulverization were repeated two times. This powders were filled into Ag pipe and reduced the diameter by swaging or swaging–drawing and the composite specimen was deformed to tape by uniaxial cold press. This tapes were heat treated firstly at 1108 K ~ 1113 K for 360 ks and repressed and heat treated at same temperature with first heat treatment for 180 ks. Critical transport current and transition temperature were measured by 4 terminal method at 77.3 K. Microstructure was observed by scanning electron microscope and identification of phases existed in oxide layer was performed by powder XRD (Cu kα) analysis and EPMA.

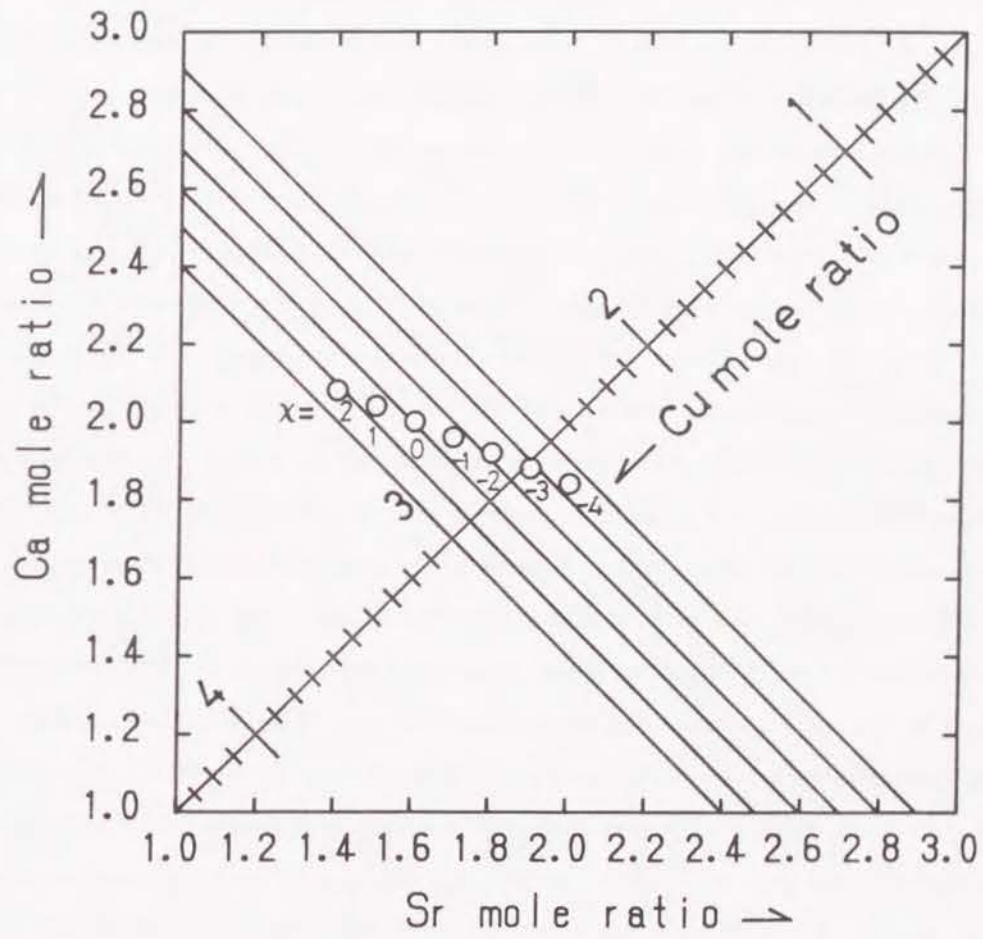

Figure 7.1 Composition map for preparing $Bi_{1.6}(Bi_{1.8})Pb_{0.4}Sr_{1.6-0.1x}Ca_{2+0.04x}Cu_{2.8+0.06x}O_y$ specimen by changing composition parameter, x of starting element.

7.3 Results and discussion

Figure 7.2 shows the Bi composition dependence of critical current density for the specimens heat treated at 1113 K. J_c increased and reached maximum at x = 1.6 and decreased with increasing Bi mole ratio. It was found that critical current density remarkably decreased for the specimens prepared with the higher Bi mole ratio.

Figure 7.3 shows the relation between the substitution ratio of Pb and critical current density for the specimen[$(Bi_{1-x}Pb_x)_2Sr_{1.6}Ca_2Cu_{2.8}O_y$] heat treated at 1108 K. Here, reference data, bulk.1($(Bi_{1-x}Pb_x)_2Sr_2Ca_2Cu_3O_y$) and bilk.2($(Bi_{1-x}Pb_x)_2Sr_2Ca_2Cu_{3.6}$) by Hiraoka [7] were also plotted in the figure. In the whole range of x, the present Ag sheathed tape exhibited higher J_c than that of bulk. This is mainly thought to be due to the difference of fabrication processes between the conventional solid state reaction and the powder-in-tube technique. The mean values of J_c for the present tape increased and became highest at x = 0.2 and then dropped with increasing substitution ratio of Pb. Comparing with the reference data from bulk, the appropriate substitution ratio of Pb exhibiting highest J_c was found to shift to low substitution ratio of Pb. This is considered to be resulted from the difference from compositions of Sr, Ca and Cu. Under the present fixed Sr, Ca and Cu composition, it was found that the 20 % substitution of Pb for Bi was most effective for increasing the critical current density. In the result [4] of Murayama *et al.* for bulk which has the same composition system with present one, a large amount of Ca_2PbO_4 was confirmed to exist. According to this, low J_c for the specimen with high substitution ratio of Pb is thought to be associated with larger formation of Ca_2PbO_4.

Figure 7.4 shows Ca composition dependence of critical current density for the specimen prepared with SDPHT1PHT2, where the temperatures of HT1 and HT2 were 1108 and 1113 K, respectively. J_c increased and reached maximum at x = 2.0 and decreased with increasing Ca mole ratio. As shown in microstructures from figure 7.5, CuO with size of about 10 μm was observed with large amount for the specimen with Ca poor composition, while a lot of $(Sr,Ca)_3Cu_5O_x$ compound phase was observed to be distributed for the specimen with Ca rich composition. The volume fraction of $(Sr,Ca)_3Cu_5O_x$ was

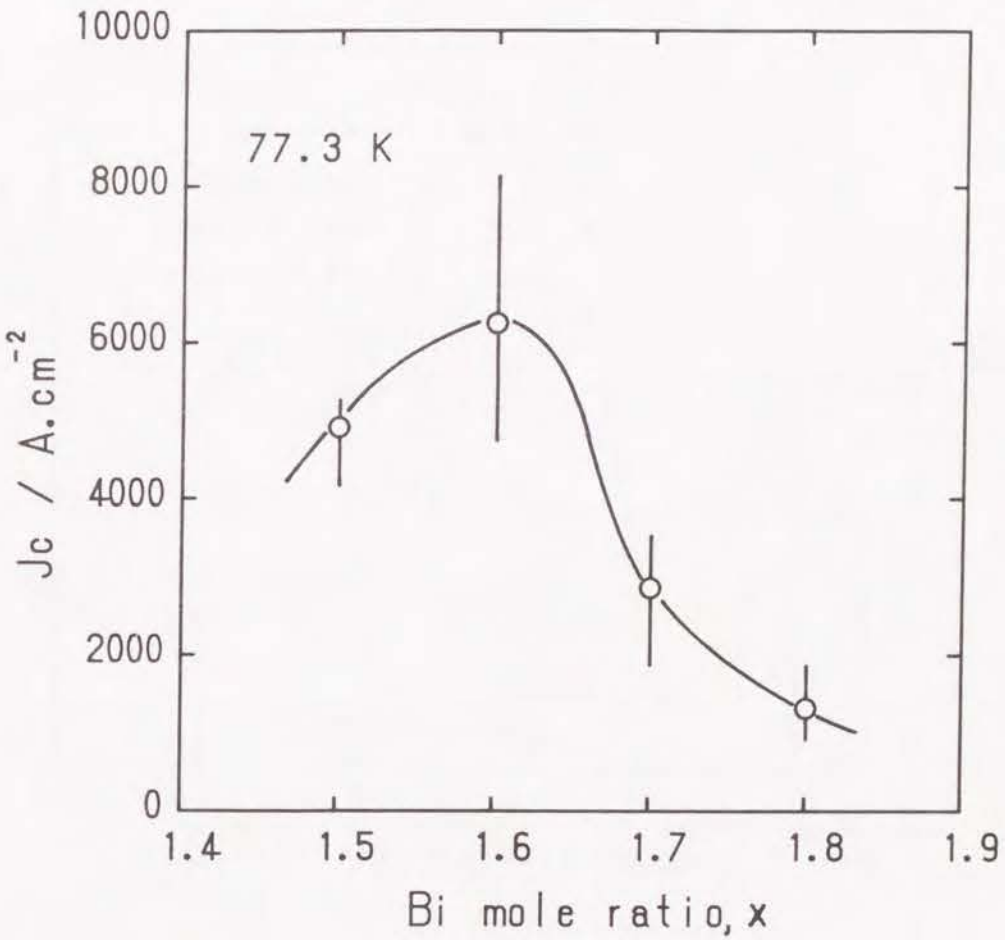

Figure 7.2 The critical current density as a function of Bi mole ratio, x in $Bi_xPb_{0.4}Sr_{1.6}Ca_2Cu_{2.8}$ specimen.

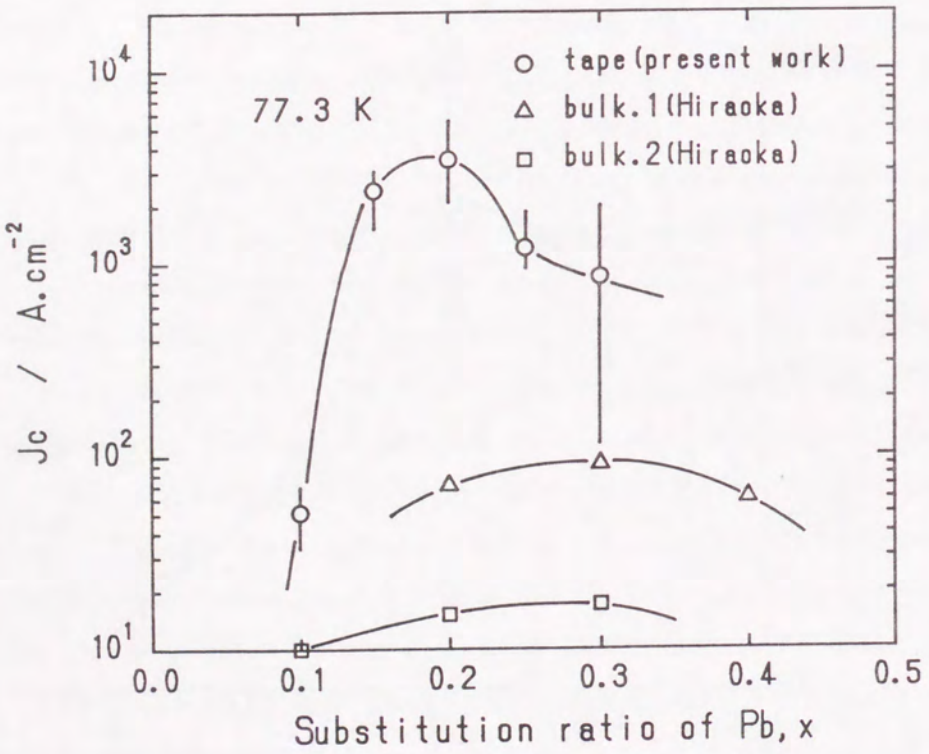

Figure 7.3 The relation between substitution ratio of Pb, x and critical current density for $(Bi_{1-x}Pb_x)_2Sr_{1.6}Ca_2Cu_{2.8}O_y$ specimen.

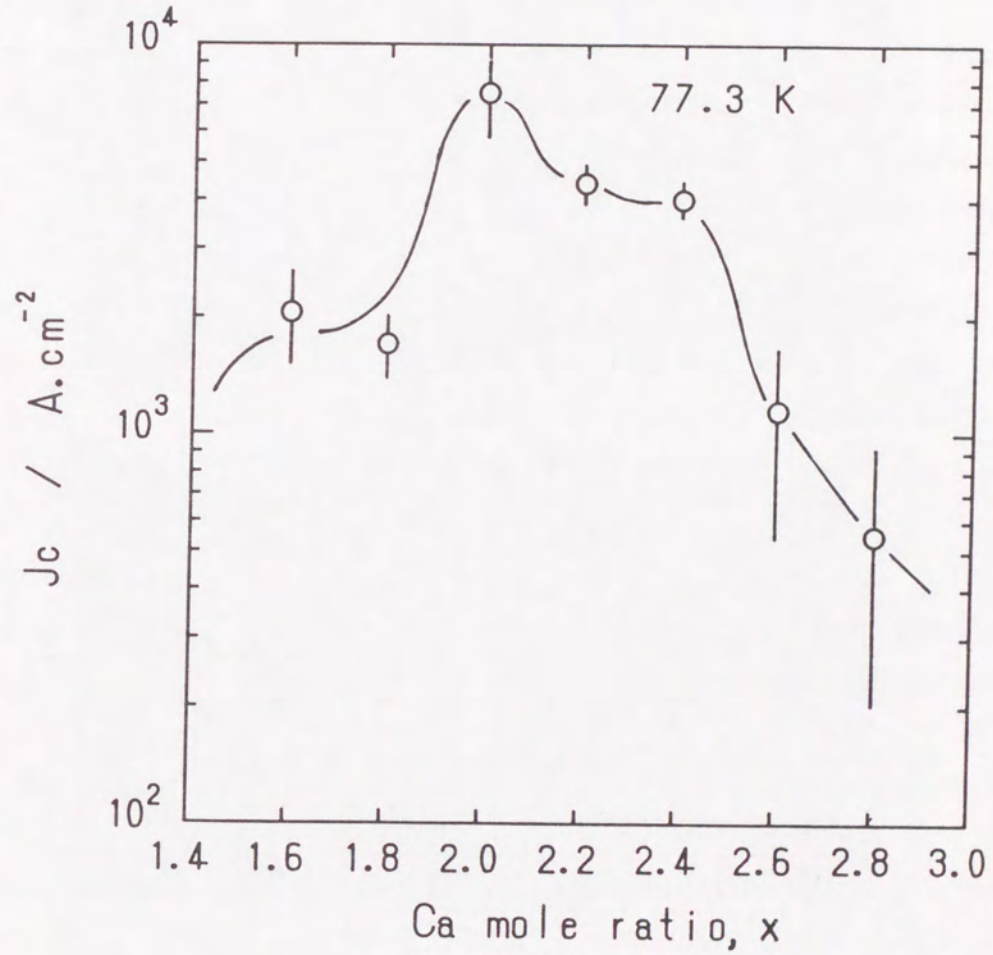

Figure 7.4 The critical current density as a function of Ca mole ratio, x in $Bi_{1.6}Pb_{0.4}Sr_{1.6}Ca_xCu_2$ specimen.

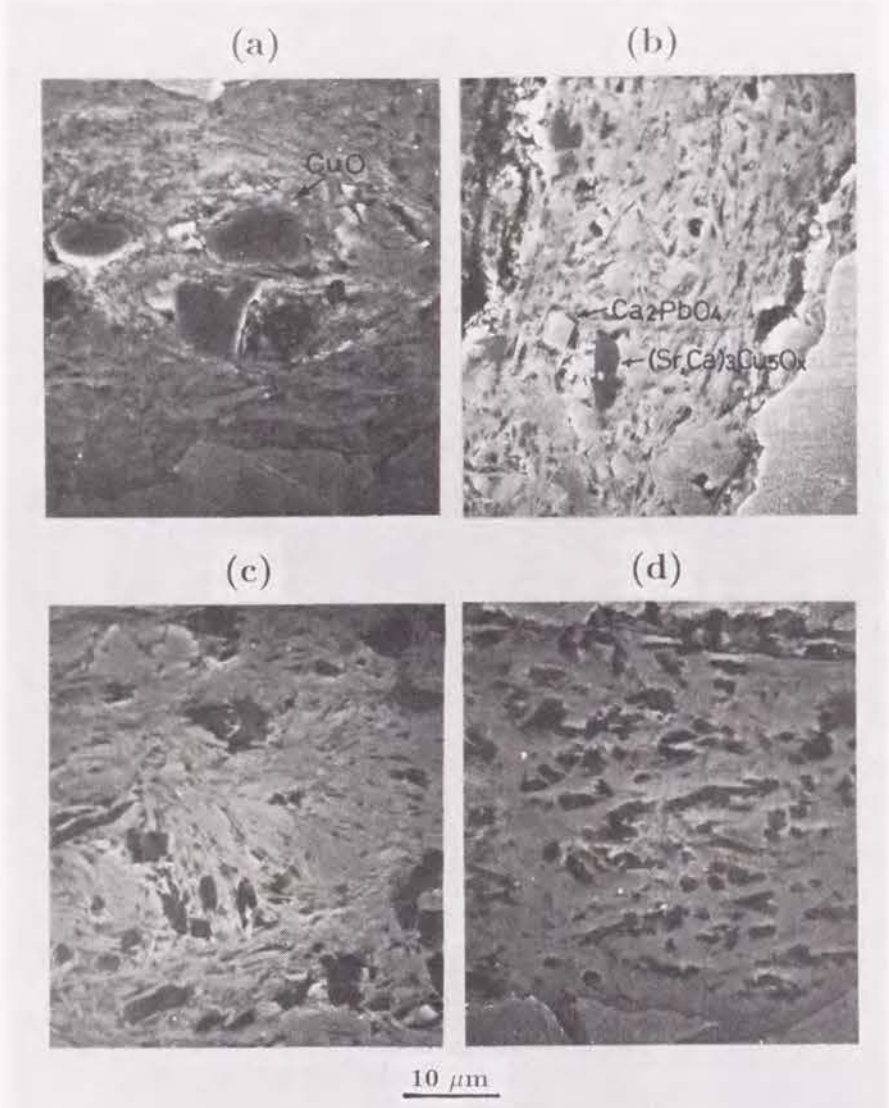

Figure 7.5 Scanning electron micrographs of polished surface for the various $Bi_{1.6}Pb_{0.4}Sr_{1.6}Ca_xCu_{2.8}O_y$ specimen, where (a) x = 1.6, (b) x = 2, (c) x = 2.4 and (d) x = 2.8.

confirmed to increase with increasing Ca mole ratio. Therefore low J_c at Ca rich region is thought to be attributed to this. Due to existence of insulating phase such as CuO and $(Sr,Ca)_3Cu_5O_x$, critical current density is considered to decrease because the total area which transport current can flow in the specimen is reduced.

Figure 7.6 shows the relation between the superconducting properties(J_c, $T_{c,off}$) and composition parameter, x which represents a sub composition of Sr, Ca and Cu in the chemical formula of $Bi_{1.6}Pb_{0.4}Sr_{1.6-0.1x}Ca_{2+0.04x}Cu_{2.8+0.06x}O_y$ for the specimens heat treated at 1108 K. The specimen with x = 0 exhibited high J_c and $T_{c,off}$. It was found that the degradation of superconducting properties is remarkable at composition region where both Ca and Cu are rich, compared to the composition region where Sr is rich. Figure 7.7 shows the X-ray diffraction patterns for the various specimens prepared with different composition parameter x. The X-ray intensity of 2212 phase increased with decreasing the x value. This means that the volume fraction of 2212 phase increased with increasing amount of Sr. This is consistent with the result [6] of Endo *et al.* Therefore, the degradation of J_c shown in figure 7.6 is thought to be mainly resulted from the decrease of volume fraction of 2223 phase. On the other hand, 2201 phase was detected with a small amount for the specimens x = 1 and 2, respectively. This phase was thought to be crystallized from the liquid formed by decomposition of 2223 phase accompanying with partial melting [8]. When the decomposition occurred at grain boundary of 2223 phase, it is suggested that both J_c and T_c decrease by precipitation of 2201 phase at grain boundary. Figure 7.8 shows microstructures for the specimens prepared with different composition parameter x. $(Sr,Ca)_3Cu_5O_x$ impurity phase was observed in the specimen with Sr rich composition, while Ca_2PbO_4 and $(Sr,Ca)_2CuO_3$ were observed for the specimen with Ca and Cu rich composition. By the analysis of EPMA, 6% Sr was found to be substituted with Ca element in the $(Sr,Ca)_2Cu0_3$ compound. Figure 7.9 shows the composition parameter x dependence of critical current density for the specimen ($Bi_{1.8}Pb0.4Sr_{1.6-0.1x}Ca_{2+0.04x}Cu_{2.8+0.06y}$) heat treated at 1113 K. J_c maintained similar value of J_c till x = –2 and decreased remarkably at x is –3 and –4 with decreasing

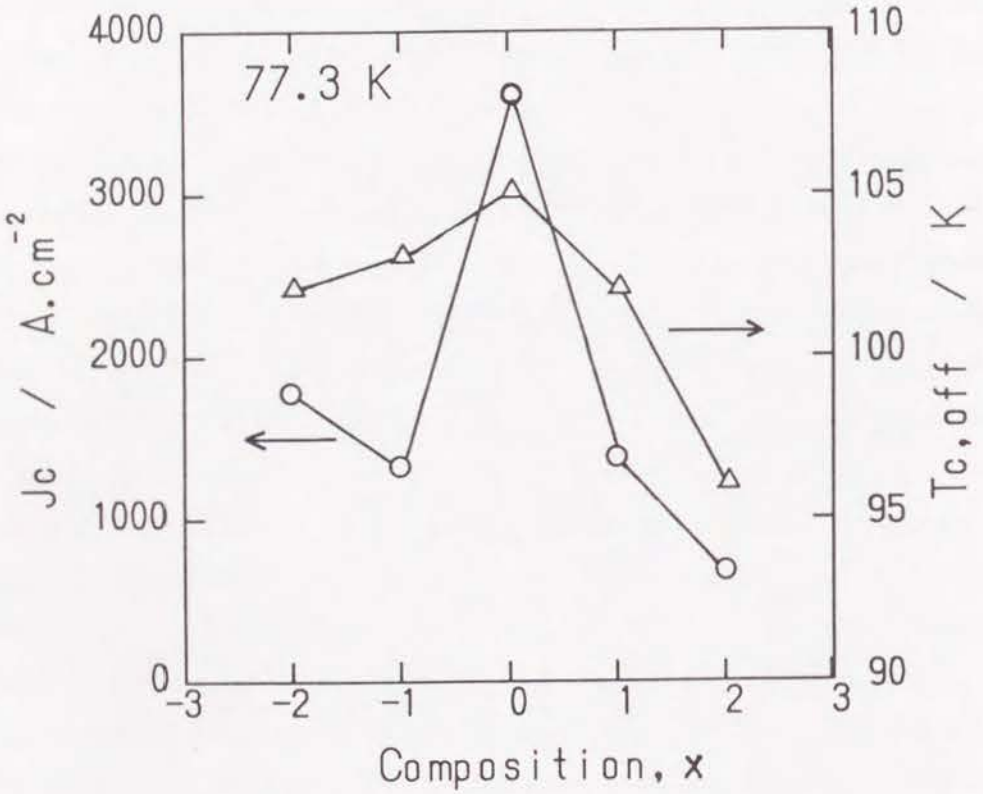

Figure 7.6 The critical current density and temperature, $T_{c,off}$ as a function of composition parameter, x for the $Bi_{1.6}Pb_{0.4}Sr_{1.6-0.1x}Ca_{2+0.04x}Cu_{2.8+0.06x}O_y$ specimen.

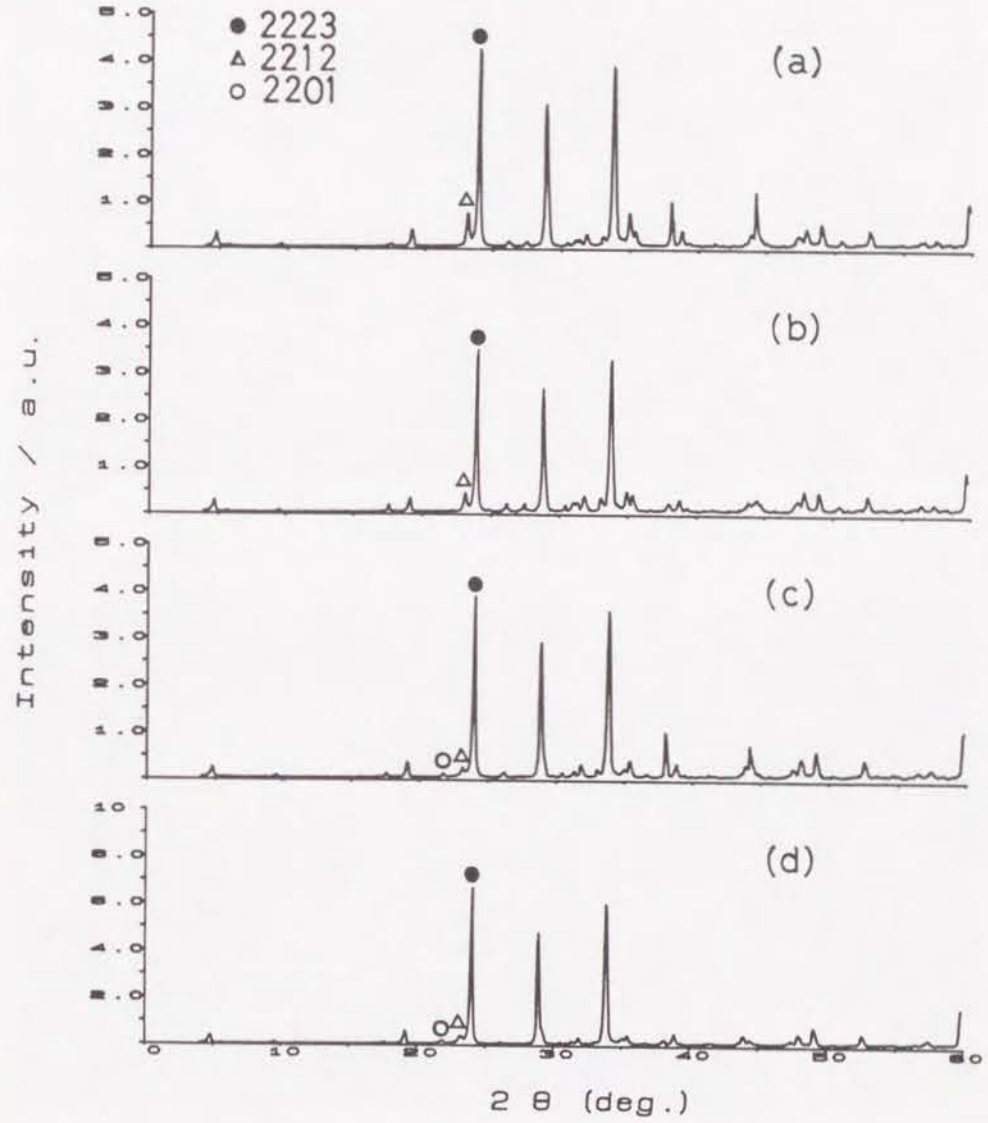

Figure 7.7 X-ray powder diffraction patterns for the various $Bi_{1.6}Pb_{0.4}Sr_{1.6-0.1x}Ca_{2+0.04x}Cu_{2.8+0.06x}O_y$ specimen, where (a) x = –2, (b) x = –1, (c) x = 1 and (d) x = 2.

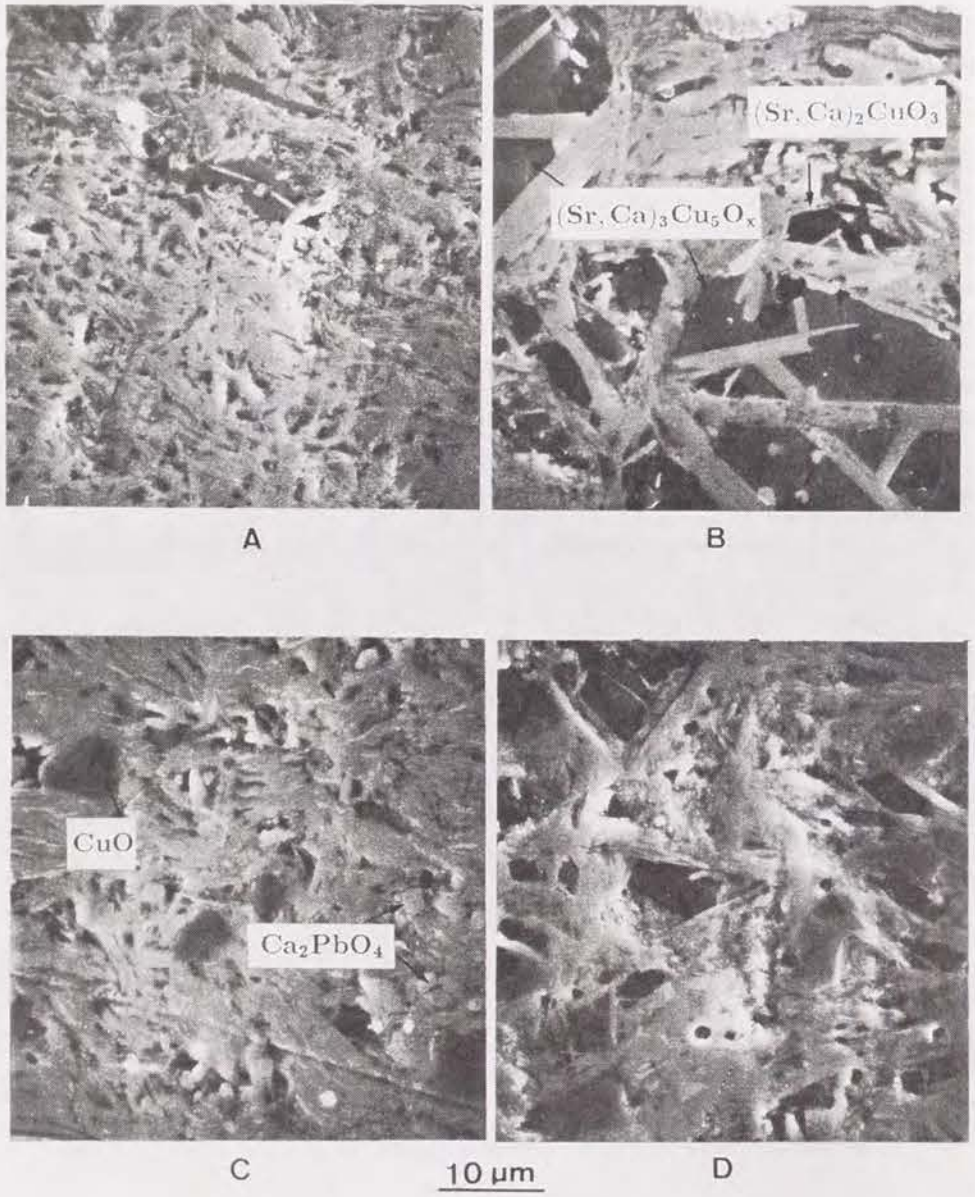

Figure 7.8 Scanning electron micrographs of polished surface for the $Bi_{1.6}Pb_{0.4}Sr_{1.6-0.1x}Ca_{2+0.04x}Cu_{2.8+0.06x}O_y$ specimen, where A : x = −2, B : x = −1, C : x = 1 and D : x = 2.

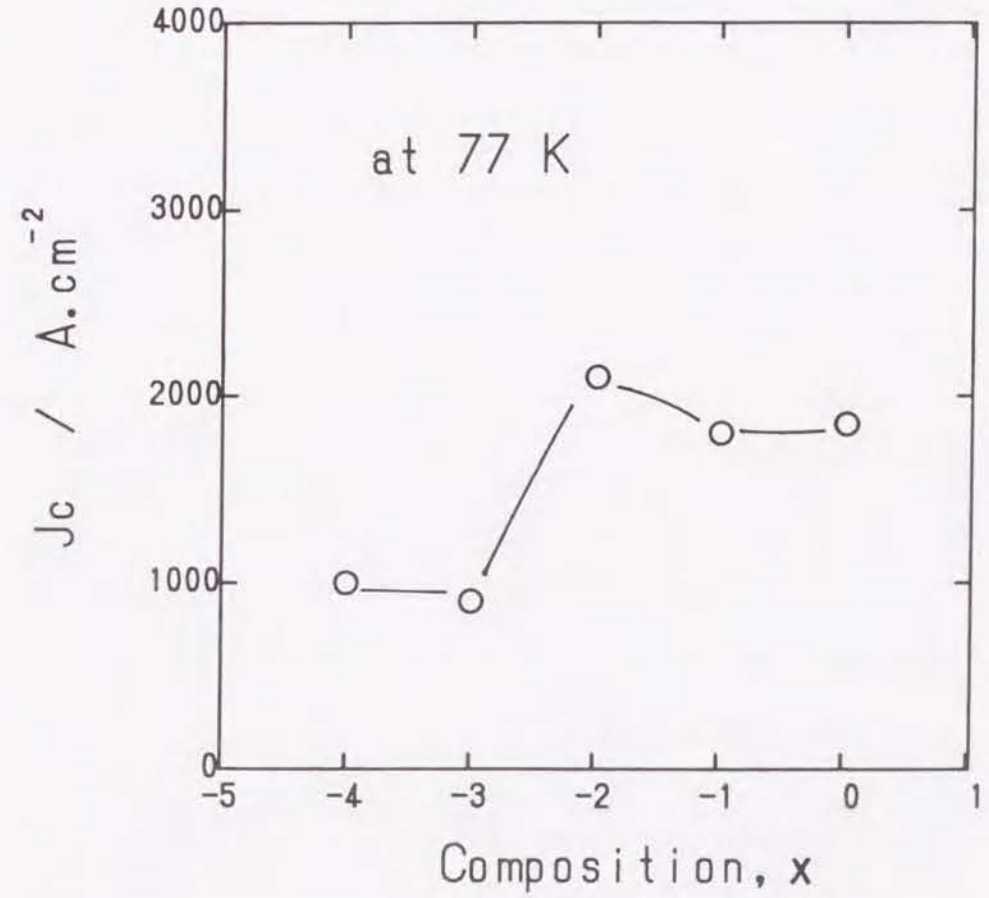

Figure 7.9 The critical current density as a function of composition parameter, x for the $Bi_{1.8}Pb_{0.4}Sr_{1.6-0.1x}Ca_{2+0.04x}Cu_{2.8+0.06x}O_y$ specimen.

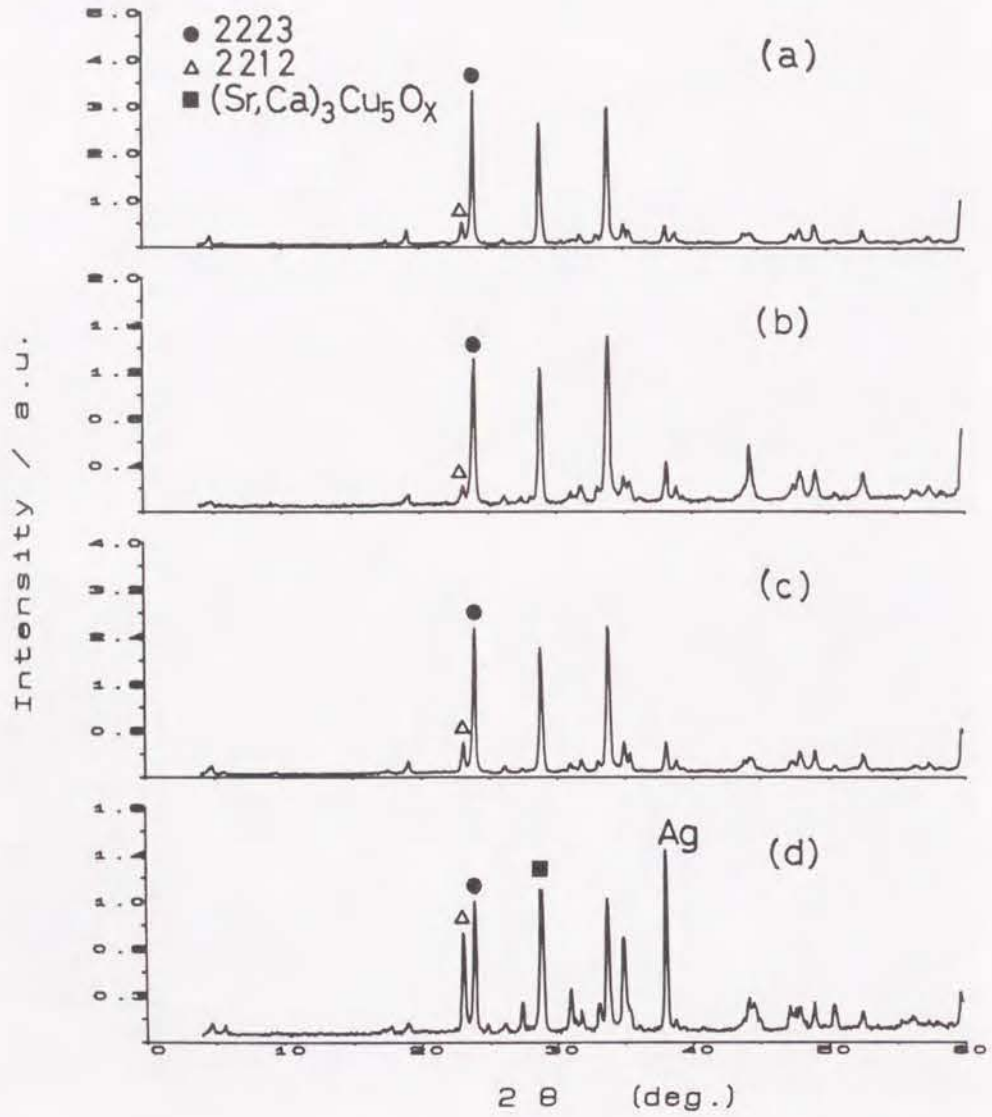

Figure 7.10 X-ray powder diffraction patterns for the various $Bi_{1.8}Pb_{0.4}Sr_{1.6-0.1x}Ca_{2+0.04x}Cu_{2.8+0.06x}O_y$ specimens, where (a) x = 0, (b) x = –1, (c) x = –2 and (d) x = –4.

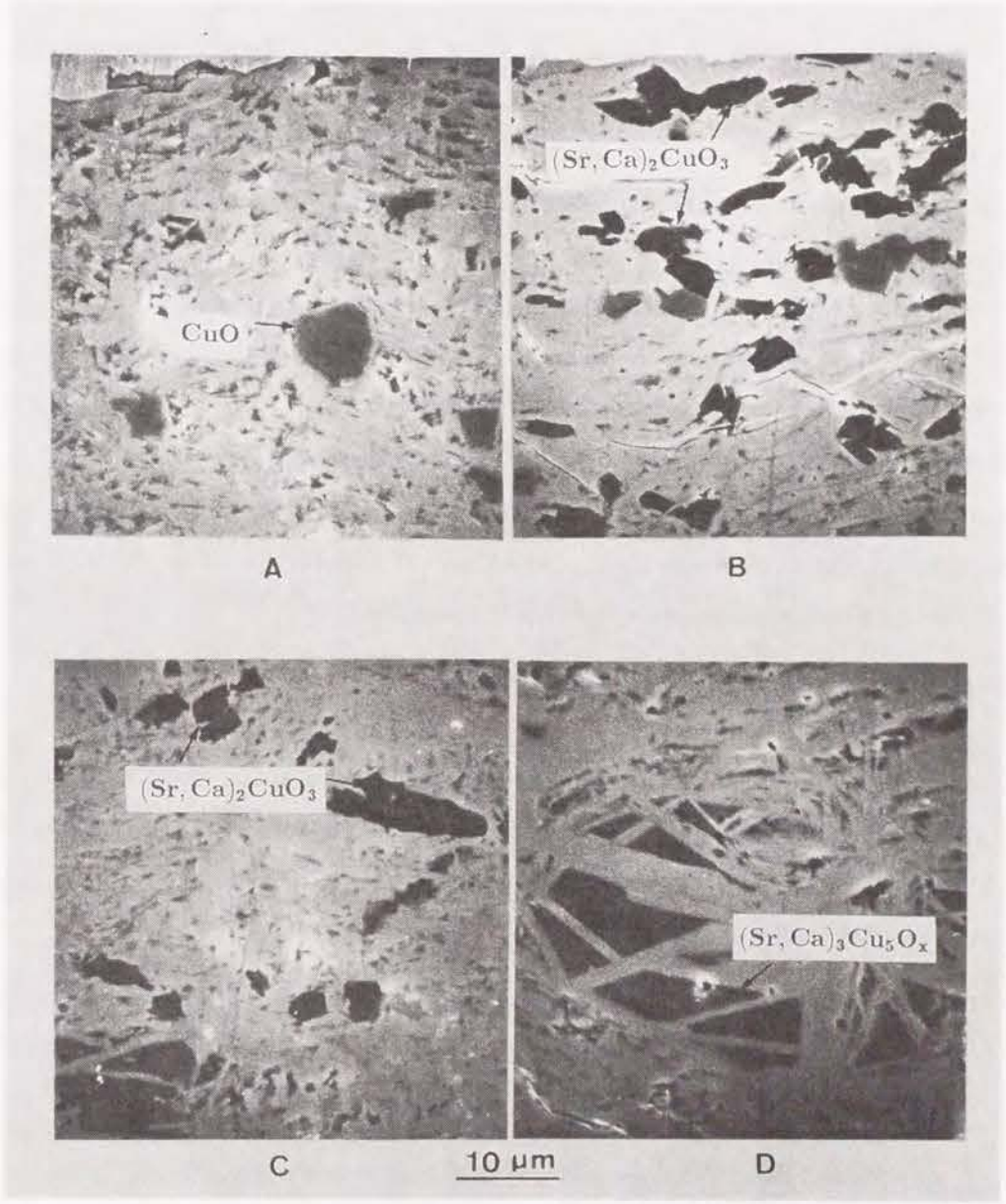

Figure 7.11 Scanning electron micrographs of polished surface for the $Bi_{1.6}Pb_{0.4}Sr_{1.6-0.1x}Ca_{2+0.04}Cu_{2.8+0.06x}O_y$ specimen(A) and the $Bi_{1.8}Pb_{0.4}Sr_{1.6-0.1x}Ca_{2+0.04x}Cu_{2.8+0.06x}O_y$(B,C,D) , where A : x = 0, B : x = 0, C : x = –1 and D : x = –2.

composition parameter x. Figure 7.10 shows the X-ray diffraction patterns for the specimens($Bi_{1.8}Pb0.4Sr_{1.6-0.1x}Ca_{2+0.04x}Cu_{2.8+0.06x}O_y$) with different composition parameter x. The X-ray intensity of 2212 phase increased continuously with decreasing x value. The fact that the increasing volume fraction of 2212 phase with increasing mole ratio of Sr is consistent with the result from figure 7.7. The peak of $(Sr, Ca)_3Cu_5O_x$ which is overlapped with the peak of 2223 phase was found to increases relatively for the specimen with x = −4. Figure 7.11 shows the microstructure for the specimens with different composition parameter x. It was observed that $(Sr, Ca)_2CuO_x$ phase, which has sharp interface with matrix distributed with large amount for the $Bi_{1.8}$.... (x = 0). It was found that the amount of $(Sr, Ca)_3Cu_5O_x$ increased and CuO decreased with increasing the amount of Sr as shown in photographs C and D. Especially, coarse $(Sr, Ca)_3Cu_5O_x$ and superconducting phases were observed in photograph, D.

7.4 Conclusion

Microstructure change due to the difference of nominal composition in Bi-Pb-Sr-Ca-Cu-O system and its influence to superconducting properties were investigated when the Ag sheathed BPSCCO tapes were prepared by powder-in-tube technique. The main conclusions are the following;

1. Critical current density of BPSCCO tape was confirmed to depend on the variation of nominal composition. This was considered to be due to volume fraction of 2223 superconducting phase and existence of impurity phase.

2. Ag sheathed BPSCCO tapes prepared with composition of $Bi_{1.6}Pb_{0.4}Sr_{1.6}Ca_{2.0}Cu_{2.8}$ exhibited the highest J_c. When the composition of starting elements was changed from the above one, amount of impurity phases such as CuO, Ca_2PbO_4, $(Sr, Ca)_3Cu_5O_x$ and $(Sr, Ca)_2CuO_x$ was found to increase.

3. 2201 phase could be detected for the specimen($Bi_{1.6}Pb_{0.4}Sr_{1.6-0.1x}Ca_{2+0.04x}Cu_{2.8+0.06}O_y$) with high ratio of Ca and Cu.

References

1. S. Narumi, H. Ohtsu, I. Iguchi and R. Yoshizaki : Jpn. J. Appl. Phys., **28**(1988)L27.

2. T. Matsushita, B. Ni, Y. Sudo, M. Iwakuma, K. Hunaki, M. Takeo and K. Yamafuji : Jpn. J. Appl. Phys.,**6**(1988)929.

3. M. Takano, J. Takada, K. Oda, H. Kitaguchi, Y. Miura, Y. Ikeda, Y. Tomii and H. Mazaki : Jpn. J. Appl. Phys., **27**(1988)L1041.

4. N. Murayama, M. Awano, E. Sudo and Y. Torii : Jpn. J. Appl. Phys., **27**(1988)L2280.

5. A. Oota, A. Kirihigashi, Y. Sasaki and K. Ohba : Jpn. J. Appl. Phys., **27**(1988)L2289.

6. U. Endo, S. Koyama and T. Kawai : Jpn. J. Appl. Phys., **28**(1989)L190.

7. M. Hiraoka : Jpn. J. of Mitsubishi electric., **78**(1989)1.

8. S. S. Oh, K. Osamura : Supercond. Sci & Technol. **4**(1991)239.

Chapter 8

Influence of additive elements on the superconducting properties of Ag sheathed Bi-Pb-Sr-Ca-Cu-O tapes

8.1 Introduction

For developing the oxide superconducting wire which can be used as magnet coil, the improvement of critical current density in magnetic field is requested with high level. The critical transport current density in magnetic field has been known to depend on the weak links and flux pinning. From this view point, not only the refinement of microstructure but the introduction of effective pinning center against flux flow has been recognized to be important. For the ceramic superconductor which has layered structure, the intrinsic pinnings [1] by weakly superconductive layers in crystal structure was reported by Tachiki *et al.* On the other hand, the extrinsic pinnings by structural imperfections such as precipitates and irradiation-induced defects have been reported. Murakami *et al.* made clear [2] that the Y_2BaCuO_5 precipitates formed by peritectic reaction from $YBa_2Cu_3O_x$ can act as effective extrinsic pinning centers. The critical transport current density is remarkably improved by the fine dispersion of 211 phase in the 123 matrix. Also, the study for introducing pinning center by addition of other elements has been also carried out. Osamura *et al.* reported [3] that the intragrain critical current density of YBCO is

remarkably improved by addition of SnO_2. Improvement of intragrain J_c was confirmed to be due to dispersion of $BaSnO_3$ precipitates. For Bi-(Pb)-Sr-Ca-Cu-O system, recently, some studies [4,5,6,7] have been carried out for improving superconducting property of bulk specimen by addition of other element such as Ag, Sb, Ba and Mg. In this study, SnO_2, $BaCO_3$ and MgO were added to Bi-Pb-Sr-Ca-Cu-O system when the Ag sheathed BP-SCCO tapes were prepared by "powder-in-tube technique". Microstructure changes by addition of other elements and their influence on critical current density in magnetic field were investigated.

8.2 Experimental

8.2.1 Specimen preparation

SnO_2, $BaCO_3$ and MgO were added with different mole ratio into mixture of $Bi_{1.6}Pb_{0.4}Sr_{1.6}Ca_2Cu_{2.8}O_x$ as follow.

- SnO_2 addition
  - $Bi_{1.6}Pb_{0.4}Sr_{1.6}Ca_2Cu_{2.8}\underline{Sn_x}O_y$
- $BaCO_3$ addition
  - $Bi_{1.6}Pb_{0.4}\underline{Sr_{1.6-x}Ba_x}Ca_2Cu_{2.8}O_y$
- MgO addition
  - $Bi_{1.6}Pb_{0.4}Sr_{1.6}Ca_2Cu_{2.8}\underline{Mg_x}O_y$

After repeating calcination(1073 K, 43.2 ks) and pulverization twice, the powder was filled in Ag tube with dimension of 5 mm outer diameter and 1 mm thickness. The composite specimen was reduced by the swaging and drawing. Then, the thin wire was deformed to tape shaped specimen with uniaxial pressure of 600 $\sim$ 900 MPa . The specimen was heat treated at 1113 K in air and the cycle of uniaxial cold pressing and heat treatment was repeated one or two times.

8.2.2 Measurements

Outline of A.C inductive measurement was shown in figure 8.1, where cancel coil is for detecting the signal from only specimen by canceling a noise surrounding the specimen. The A.C inductive measurement has been developed [8] as a nondestructive methods to characterize sintered oxide specimens and inter- and intragrain current densities in oxide superconductors under given magnetic fields are obtained by analysis. Both the dc and superposed ac magnetic fields were applied parallel to the long axis of the specimen at liquid nitrogen temperature. The magnetic flux Φ going in and out of the specimen was measured as a function of the ac field amplitude b, and the penetration depth λ' of the ac filed was derived [9] :

$$\lambda' = \frac{1}{2w}\frac{\partial \Phi}{\partial b} \tag{8.1}$$

where w is the width of the specimen. Plotting λ' against b, a linear relation is obtained in ordinary bulk superconductors; the slope of the linear line gives $1/\mu J_c$(μ denoting the permeability of the vacuum) and λ' saturates to a constant representing the center of the specimen for large b value. For deriving intragrain J_c, it was assumed that the J_c is the same in all grains and the shape of grain is plate.

The intragrain J_c was determined by a best fit of the calculated $\lambda' - b$ curve, the region of which is that the flux penetrate slowly as shown in figure 8.2. Critical transport current measurement and microstructure analysis were mentioned in Chapter 6.

8.3 Results and discussion

8.3.1 Influence of Sn addition

The temperature dependence of resistivity for none and various Sn additive specimens was shown in figure 8.3. All the specimens exhibited almost 105 K of $T_{c,on}$ except for the specimen prepared with 0.05 mole ratio of Sn. It was observed that $T_{c,off}$ decreased with increasing the mole fraction of Sn. Sn addition turned out to destroy the superconducting property of BPSCCO. Figure 8.4 shows the magnetic field dependence of normalized

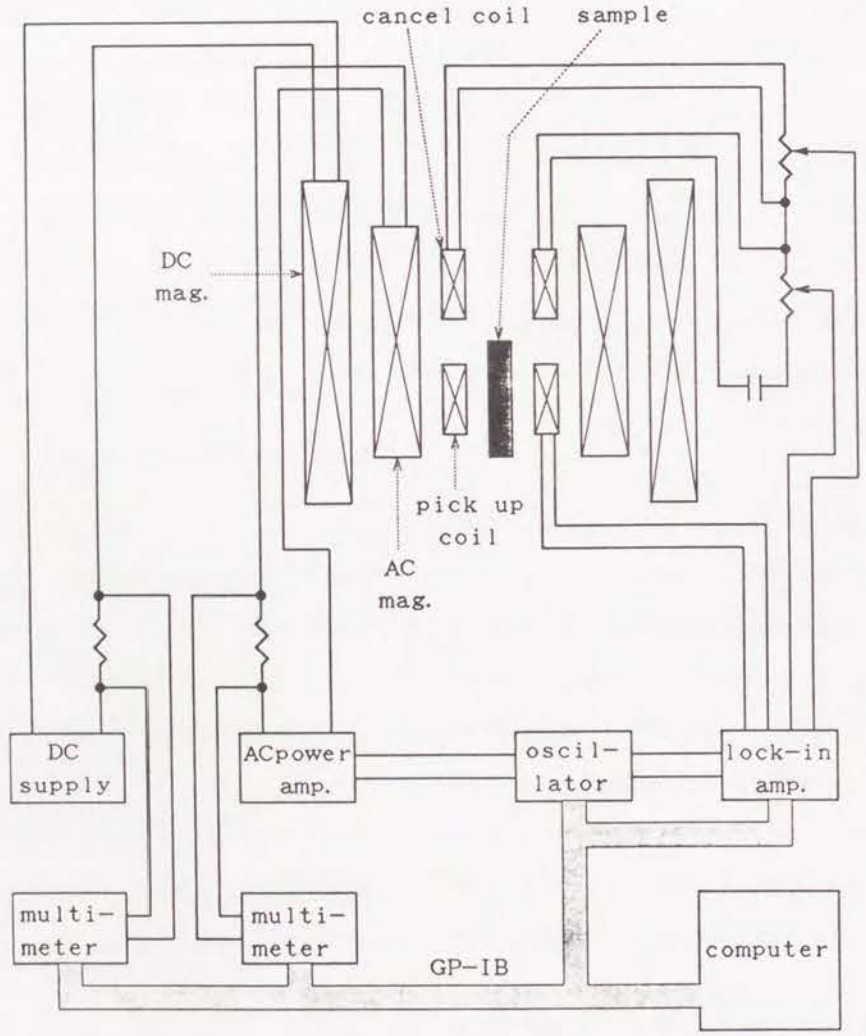

Figure 8.1 Schematic illustration of electric circuit for A.C inductive measurement.

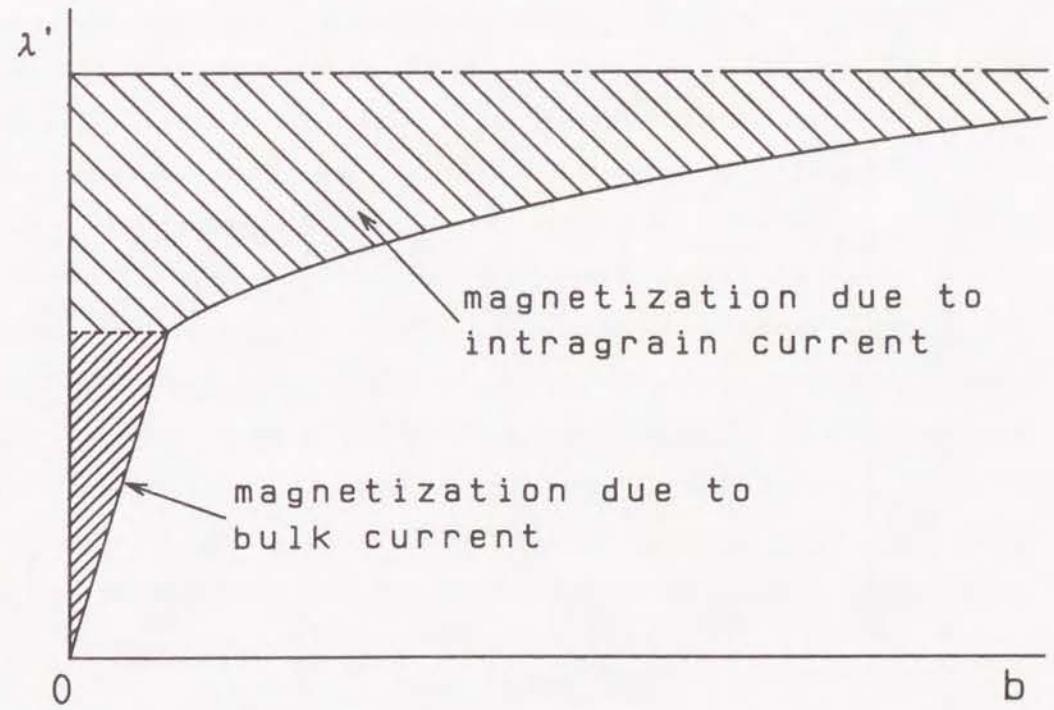

Figure 8.2 Schematic illustration of λ' vs b curve, where the areas of two hatched regions represent contribution to the magnetization from respective shielding currents.

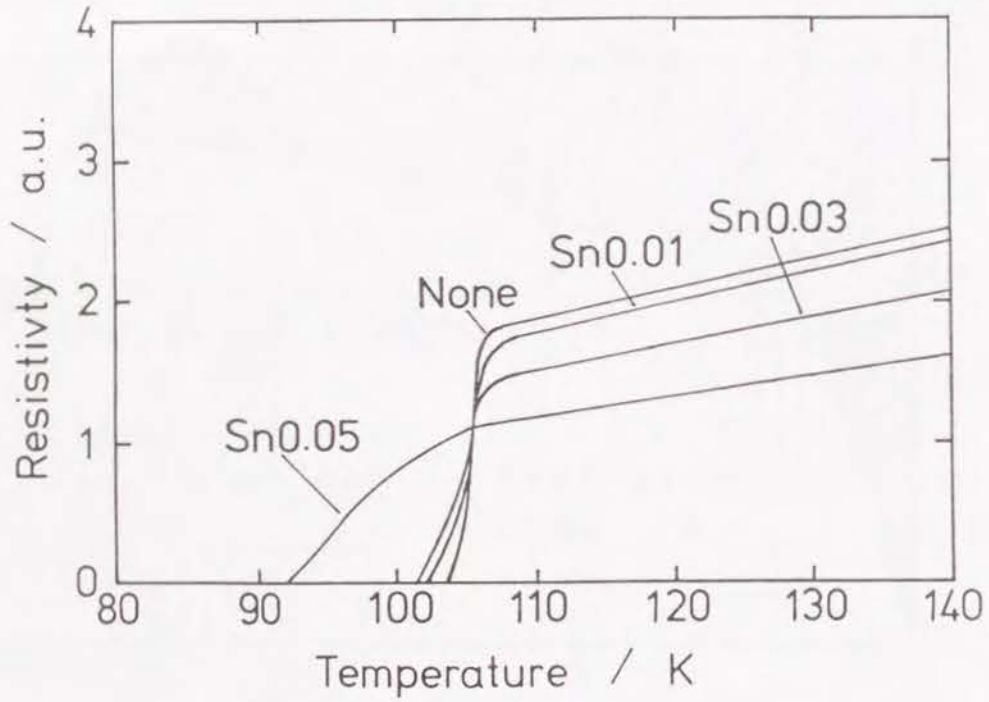

Figure 8.3 The temperature dependence of resistivity for none and Sn additive specimens.

critical transport current density measured by 4 terminal method, $J_c(\mathrm{B})/J_c(0\ \mathrm{T})$ for none and various Sn additive specimens. A decrease of J_c at low field was observed to be large for Sn additive specimen as comparison with that for none additive one. Magnetic field dependence of J_c was found to degrade with increasing Sn content. A large drop of J_c at the magnetic field of 0.01 T for Sn additive specimen is considered to be associate with weak link of superconducting grains [8,9]. Figure 8.5 shows the X-ray powder diffraction patterns for the none and Sn(0.01) additive specimens. Judging from the change of X-ray intensity ratio of (00$\underline{10}$) peak for 2223 phase to (008) peak for 2212 phase, the volume fraction of 2223 phase is considered to be low for the Sn additive specimen. According to this, the formation of 2223 phase is thought to be suppressed by Sn addition.

Figure 8.6 shows the microstructures of polished surface for the various Sn additive specimens. Sintering density of oxide was observed to be poor and a lot of impurity phases such as Ca_2PbO_4, CuO and $(Sr,Ca)_3Cu_5O_x$ were found to exist in the specimen prepared with larger mole fraction of Sn. The degradation of superconducting property by Sn addition is thought to be resulted from lower volume fraction of 2223 phase, poor grain connectivity and the existence of impurity phases. By the analysis of EPMA, Sn was detected in Ca_2PbO_4 as shown in EDX pattern as shown in figure 8.7. Considering the ionic radius and crystal structure of compound possibly formed, the added Sn was thought to be partially substituted for Pb atom in Ca_2PbO_4.

8.3.2 Influence of Ba addition

Figure 8.8 shows the temperature dependence of resistivity for various Ba additive specimens. Resistivity for Ba additive specimen in normal state was found to be low, compared to that for none additive specimen. Both $T_{c,on}$ and $T_{c,off}$ were observed to be slightly increased by Ba addition. This is consistent with the result of bulk sintered by usual solid reaction [10].

Figure 8.9 shows the magnetic field dependence of normalized critical current density, $J_c(\mathrm{B})/J_c(0\ \mathrm{T})$ for none and Ba additive specimens. The decreasing rate of J_c with respect

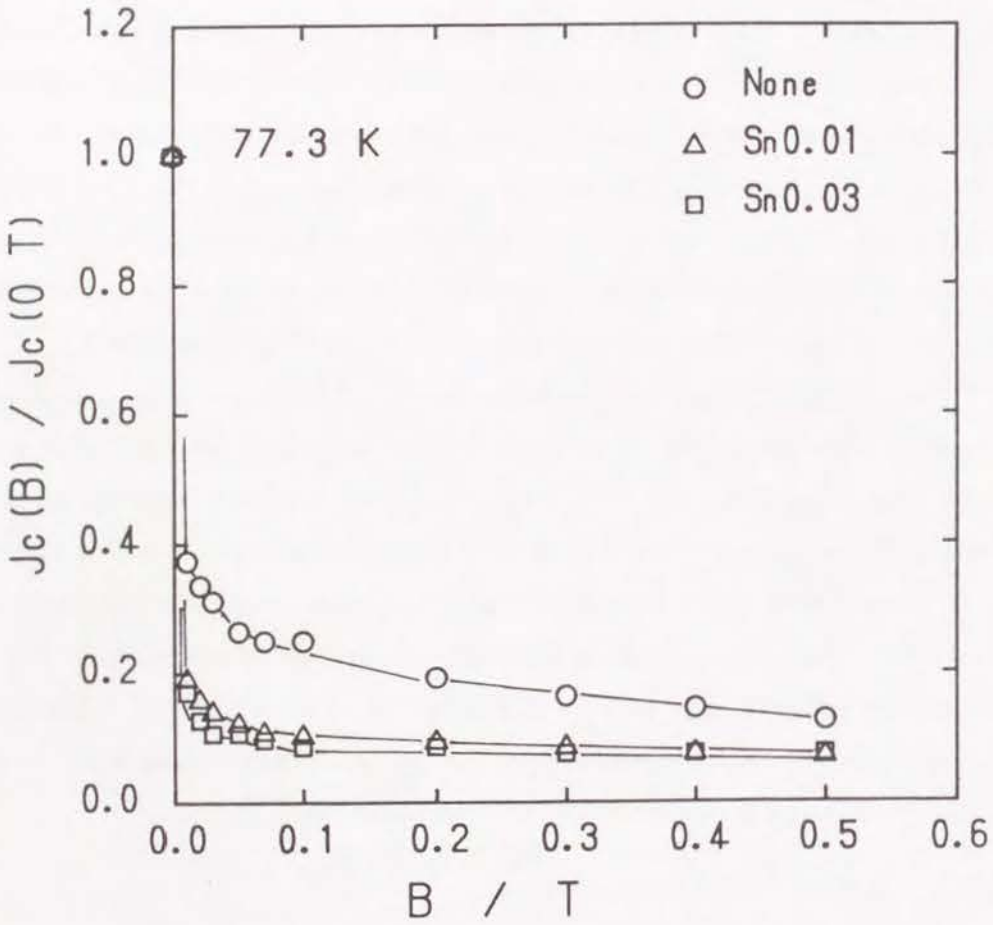

Figure 8.4 The magnetic field dependence of normalized critical current density, $J_c(B)/J_c(0$ T) for none and Sn additive specimens.

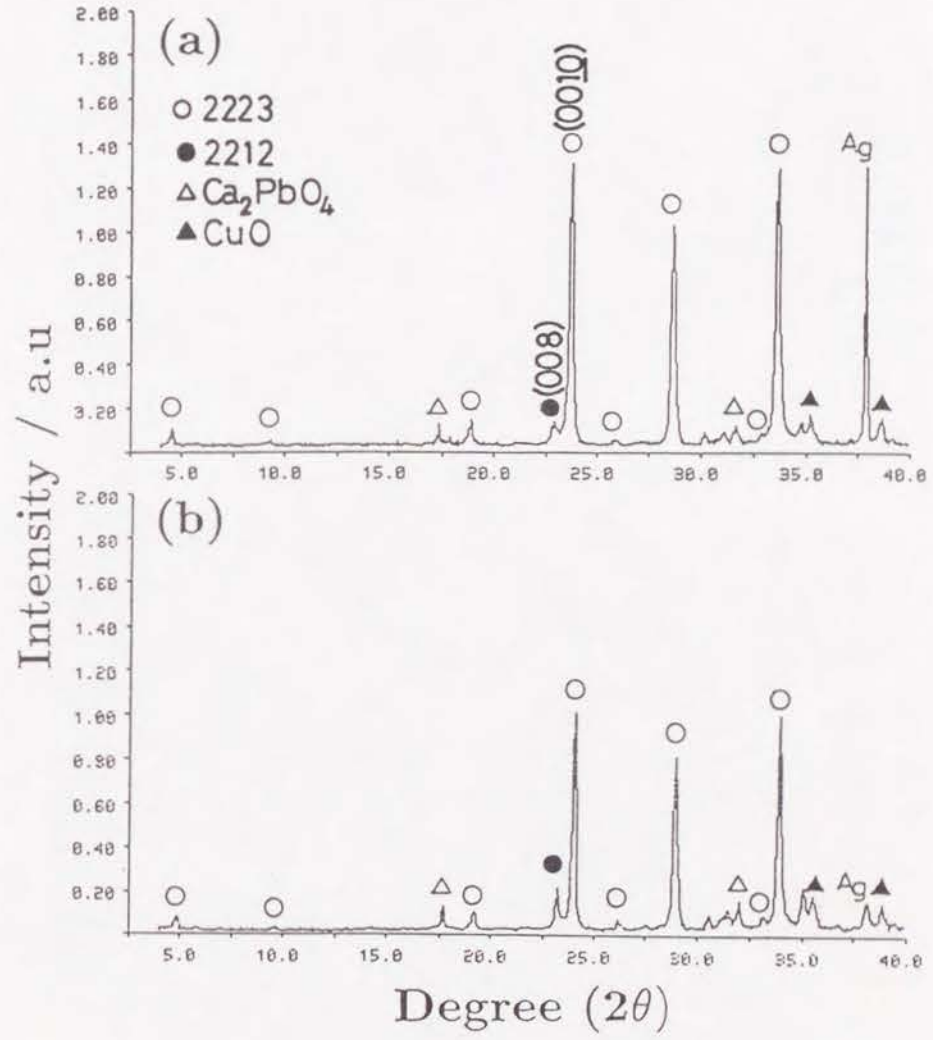

Figure 8.5 X-ray powder diffraction patterns for the none(a) and Sn(0.01) additive specimen(b).

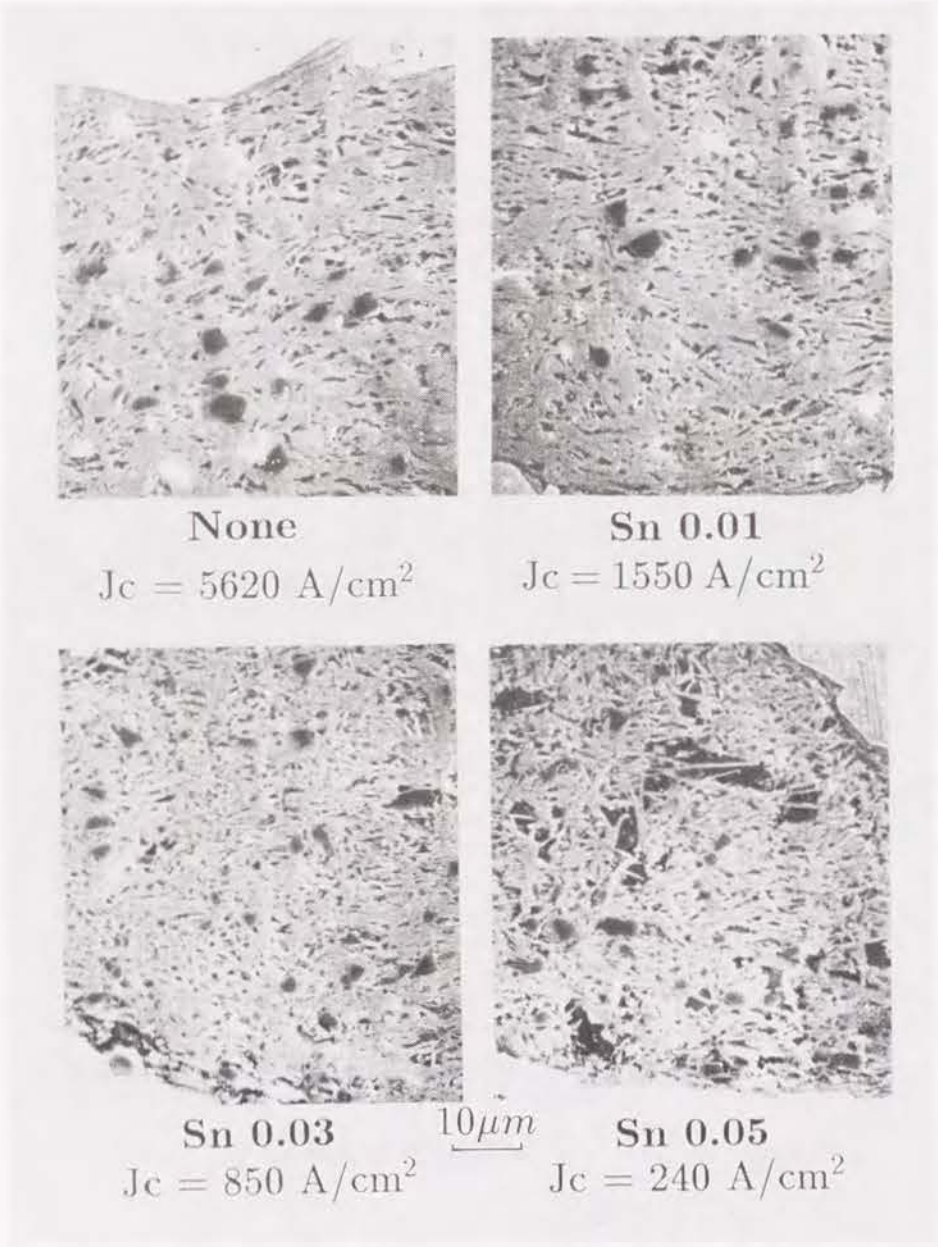

Figure 8.6 The microstructures of polished surface for the various Sn additive specimens.

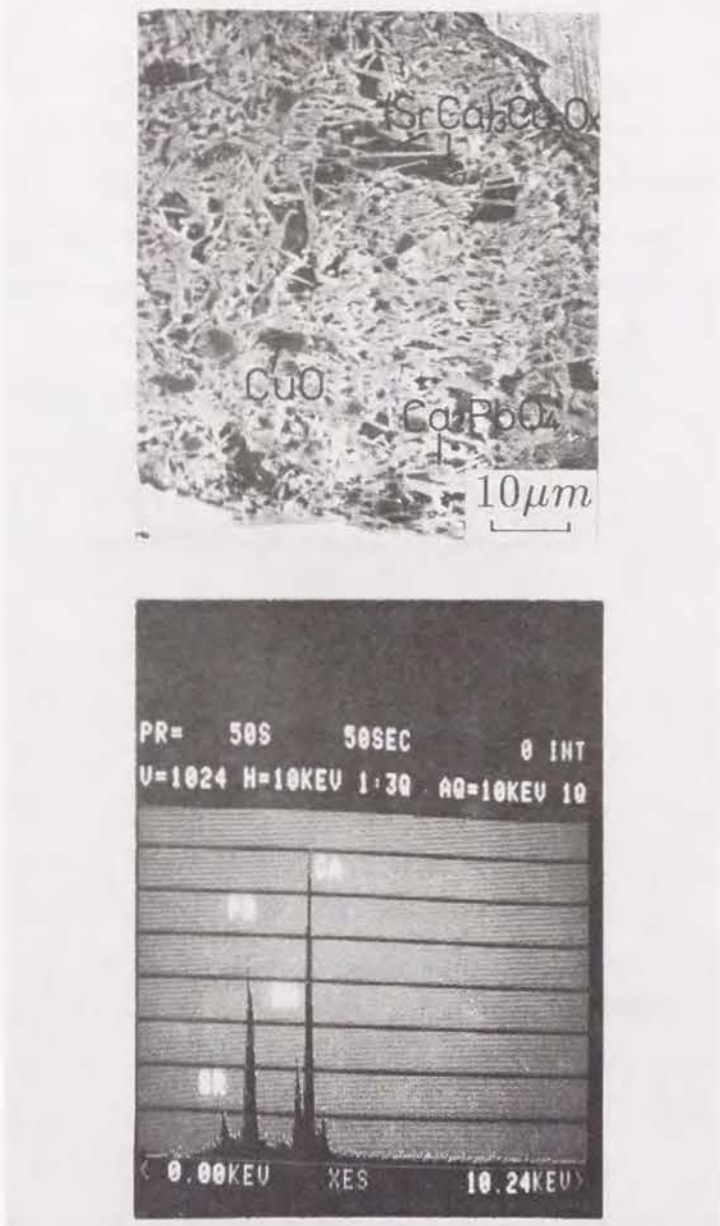

Figure 8.7 The microstructure and EDX pattern in site of Ca_2PbO_4 for Sn additive specimen.

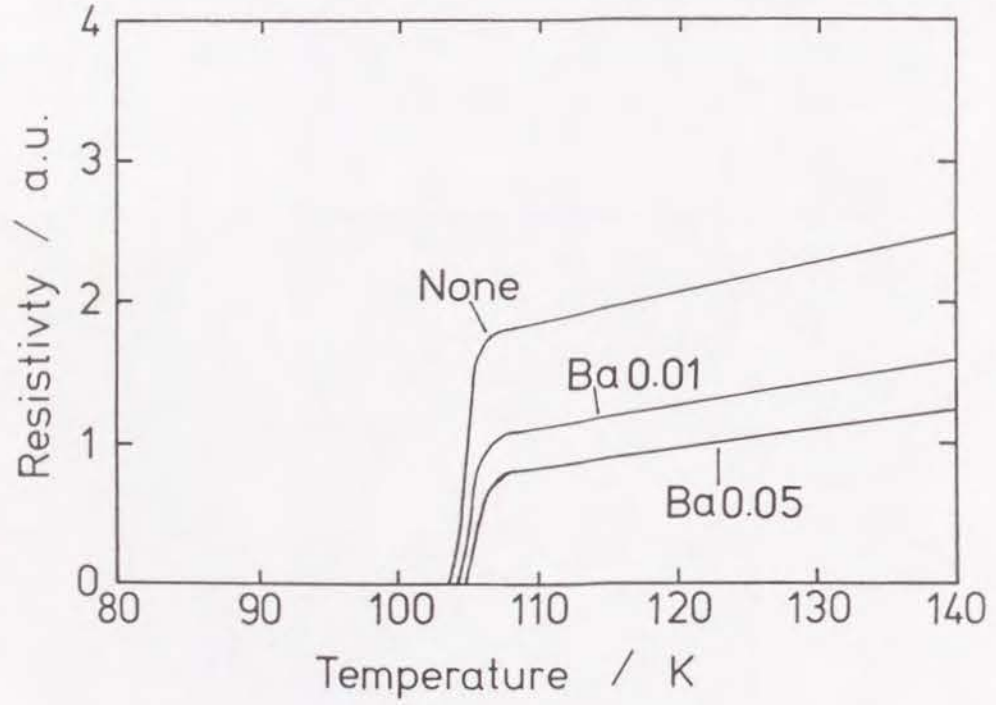

Figure 8.8 The temperature dependence of resistivity for various Ba additive specimens.

to increase of magnetic field became small for Ba additive specimen. Magnetic field dependence of J_c was confirmed to be improved for the specimen prepared with the higher Ba mole ratio. Judging from change of X-ray intensity ratio of peaks for 2223 phase to peaks for 2212 and impurity phase shown in figure 8.10, it was found that volume fraction of 2223 phase became high, while they for 2212 phase and impurity phases became low by Ba addition. According to this, the growth of 2223 phase is thought to be enhanced by Ba addition, similar to the Pb addition of Bi–Sr–Ca–Cu–O system. This is consistent with the result [4] for bulk prepared with conventional solid state reaction. By XRD and EPMA analysis, the Ba compound phases could not be detected in oxide layer. Ba was confirmed to exist in 2223 phase by EPMA analysis. Hakuraku *et al.* suggested [12] that the Ba which was added to Bi–Pb–Sr–Ca–Cu–O system is substituted for Sr in crystal structure of 2223 phase. According to study [7] by Ashizawa *et al.*, the effect of Ba substitution for Sr was suggested to that the partial melting temperature decreased and the range of formation of 2223 phase was extended. Figure 8.11 shows the microstructure of polished surface for none and Ba additive specimens. A dense structure was obtained for the specimen prepared with the higher Ba mole ratio. The Ba addition turned out to be effective to densify the BPSCCO crystal structure and the increase of J_c at magnetic field is considered to be due to the improvement of grain connectivity by densification of crystal structure. On the other hand, it was known that the superconducting property is anisotropic and then critical current is large in a-b plane. Therefore, textured structure is expected for obtaining high J_c. Figure 8.12 shows the change of X-ray intensity reflected from (00$\underline{12}$) plane of 2223 phase against tilting angle Φ, where rotation angle is 0. The X-ray intensity increased with decreasing tilting angle Φ. Considering the full half width and maximum intensity, the degree of a-b plane orientation that aligns parallel to the tape surface (direction of current flow) was confirmed to be improved by Ba addition.

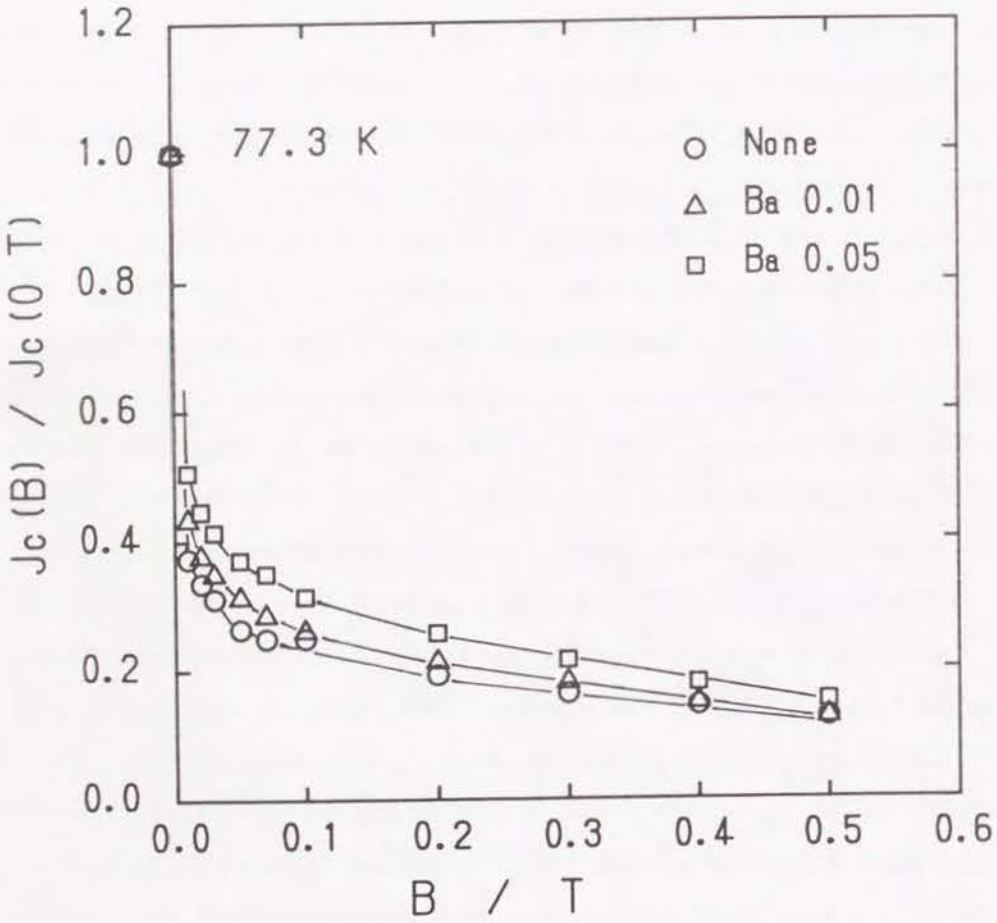

Figure 8.9 The magnetic field dependence of normalized critical current density, $J_c(B)/J_c(0\ T)$ for none and Ba additive specimens.

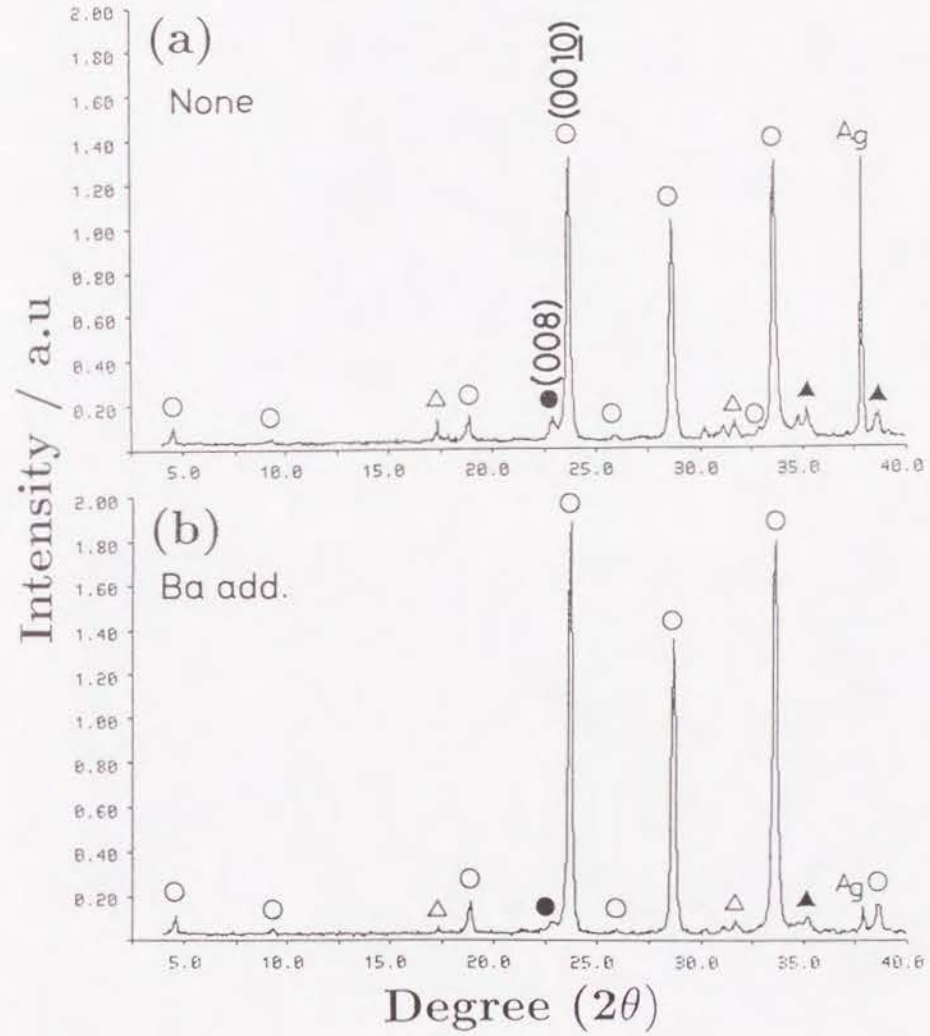

Figure 8.10 X-ray powder diffraction pattern for none and Ba additive specimens, where the symbols are indicated in figure 8.5.

Figure 8.11 The microstructure of polished surface of none and Ba additive specimens.

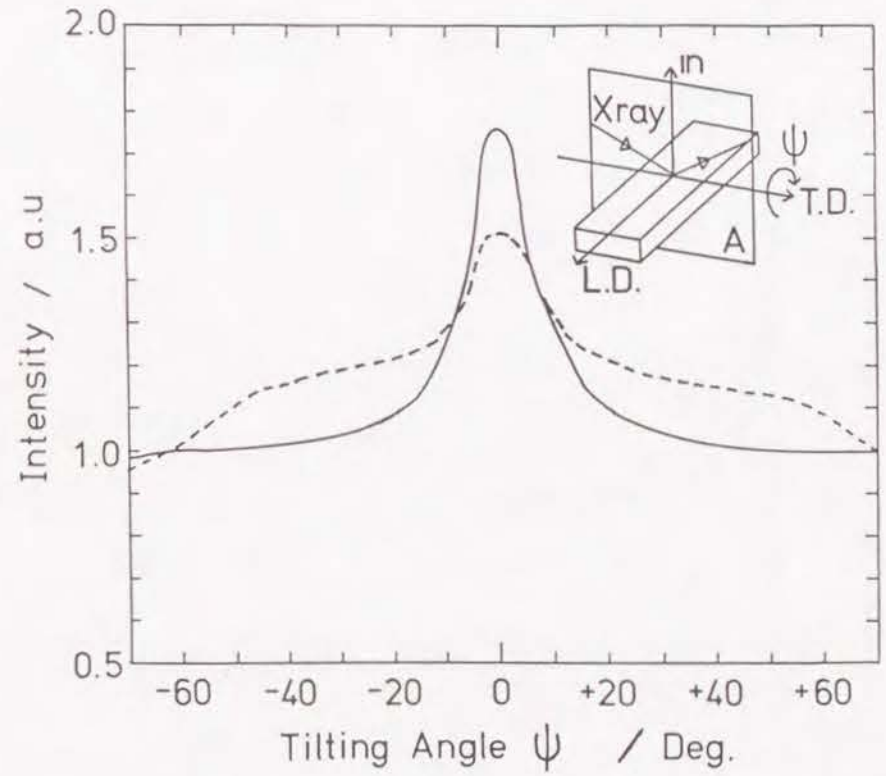

Figure 8.12 X-ray intensity reflected from (00$\underline{12}$) plane of 2223 phase vs tilting angle Φ, where rotation angle Ψ is 0, where dashed line and solid one are for none and Ba(0.05) additive specimen, respectively.

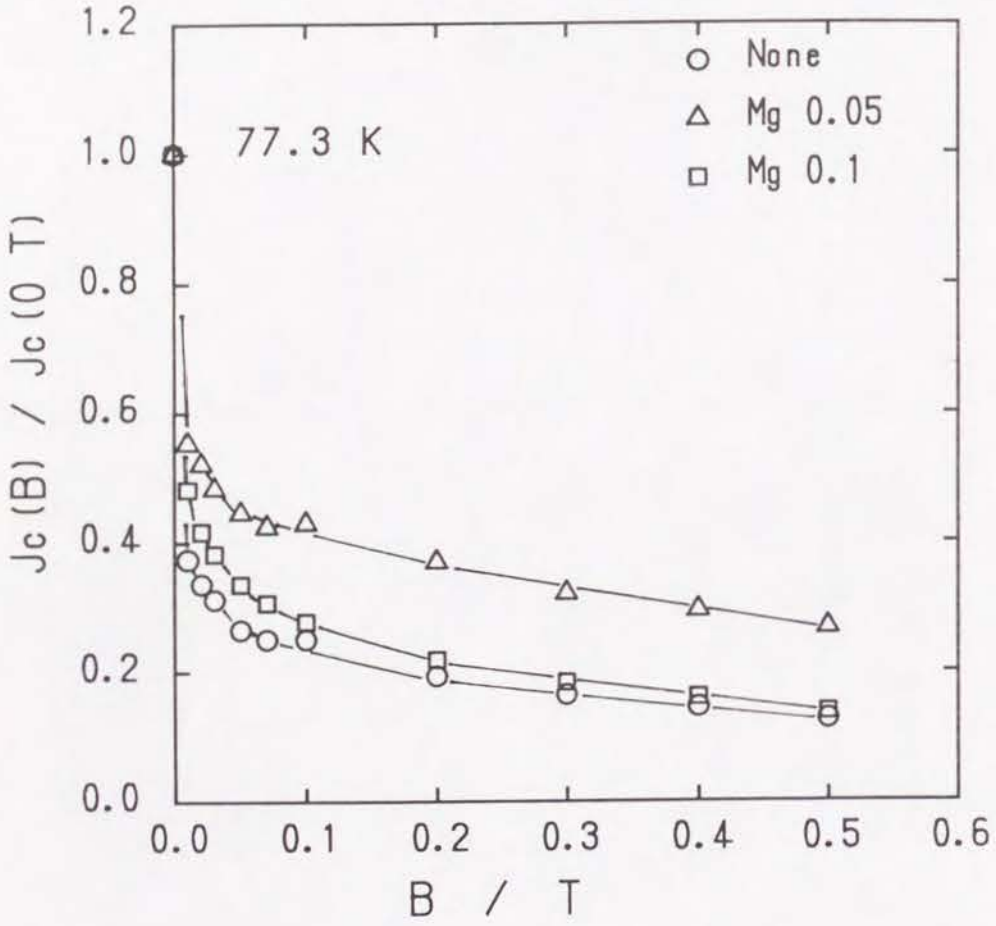

Figure 8.13 The magnetic field dependence of normalized critical current, $J_c(B)/J_c(0\ T)$ for none and Mg additive specimen.

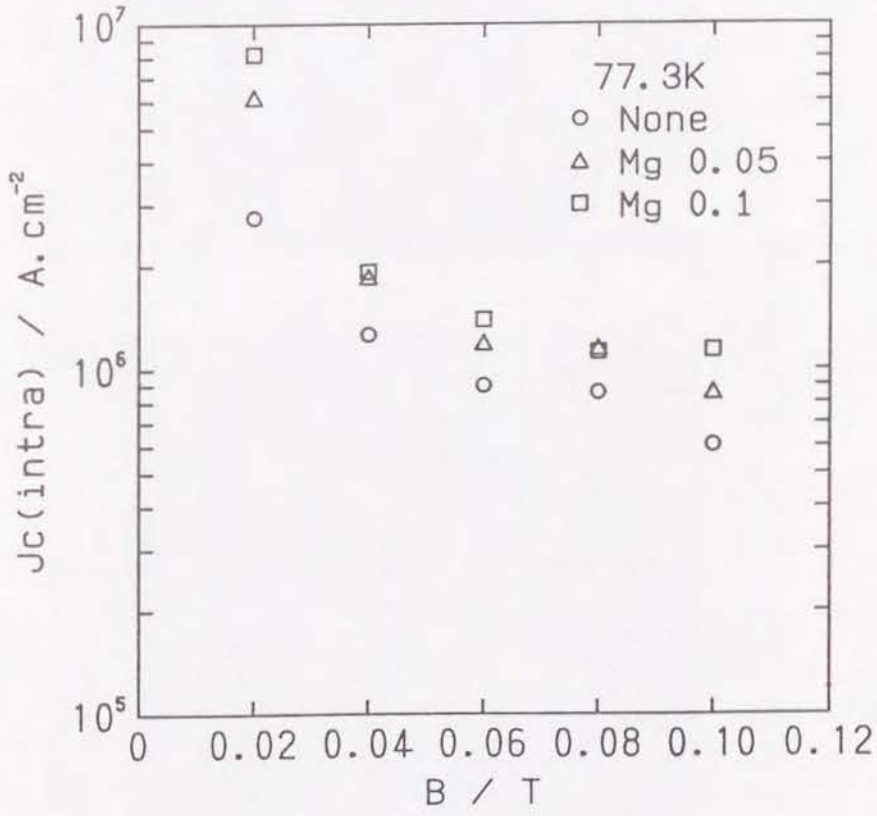

Figure 8.14 The magnetic field dependence of intragrain critical current density measured by A.C inductive method for none and Mg additive specimens.

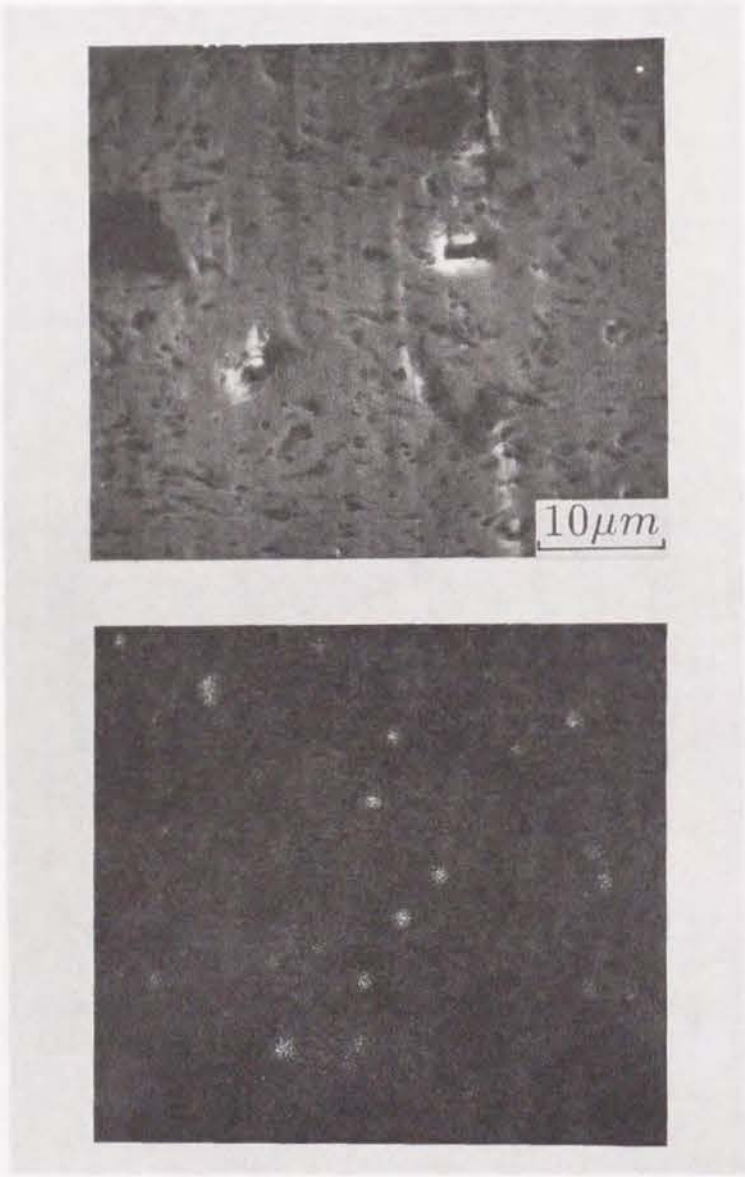

Figure 8.15 The microstructure of polished surface and distribution image of MgO particle.

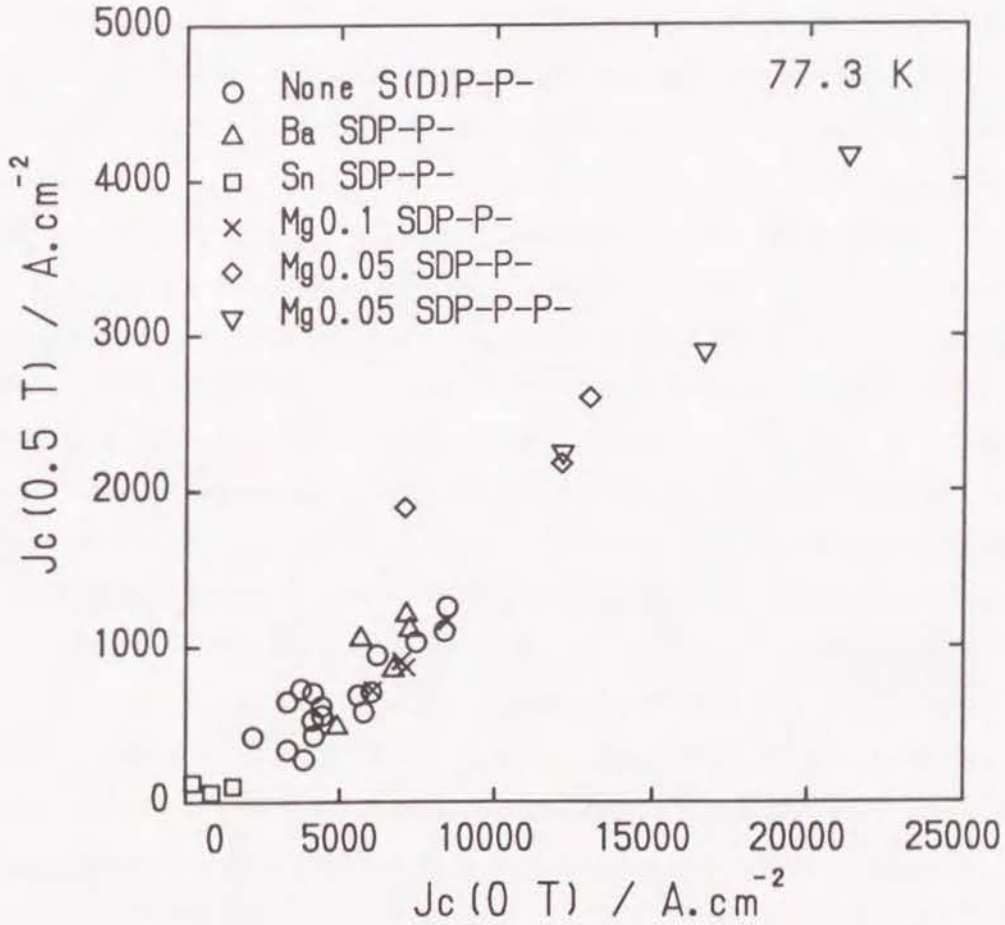

Figure 8.16 The relation between J_c(0 T) and J_c(0.5 T) at 77.3 K for none and various additive specimens.

8.3.3 Influence of Mg addition

Figure 8.13 shows the magnetic field dependence of normalized critical current density, J_c(B)/J_c (0 T) for none and Mg(0.05) additive specimen. The magnetic field dependence of J_c was found to be improved by Mg addition. Its tendency was observed to be remarkable for the specimen prepared with 0.05 mole ratio of Mg. The intragrain J_c of tape specimen was measured by A.C inductive method and its result was plotted in figure 8.14. This result was obtained with assuming the size of grain with normal to magnetic field is 1μm. The intragrain critical current density might be related to the pinning of magnetic flux lines against Lorentz force, where the Lorentz force is defined as $F = J_c \times B$. Mg additive specimen exhibited higher intragrain J_c than that for none additive specimen. Figure 8.15 shows the microstructure of polished surface and distribution image of MgO particle, which was analyzed by EDX. Dispersed MgO particles were observed in the matrix. Additive MgO was thought to become fine during the process of calcination and pulverization and dispersed in matrix. No Mg compound phase could be detect in the oxide layer by EPMA and XRD analysis. The improvement of magnetic field dependence of J_c by Mg addition as shown in figure 8.13 and 14 is thought to be attributed from the increase of pinning force owing to dispersion of MgO particles.

Figure 8.16 shows the relation between J_c(0 T) and J_c(0.5 T) for various specimens. J_c at 0.5 T increased almost linearly with increasing J_c at 0 T for all kinds of specimens. It was observed for Mg additive specimen that the J_c at 0.5 T against J_c at zero magnetic field becomes high, compared to that for other specimens. J_c over 4000 A/cm^2 at 0.5 T can be obtained for the specimen prepared with 0.05 mole ratio of Mg.

8.4 Conclusion

SnO_2, $BaCO_3$ and MgO have been attempted to be added in Bi-Pb-Sr-Ca-Cu-O system when the Ag sheathed tapes were prepared by "powder–in–tube technique". The main conclusions are the following;

1. For the SnO_2 additive specimen, critical current density was found to become lower than that of none doped tapes. This was resulted from the lower volume fraction of 2223 phase and poor connectivity of grains due to low sintering density.

2. The critical current density was confirmed to be improved by $BaCO_3$ and MgO addition. This is attributed to the refinement of microstructure such as densification of BPSCCO oxide layer and dispersion of MgO particles, respectively.

References

1. M. Tachiki and S. Takahashi : Solid State Communications, **72**(1989)1083.

2. M. Murakami : Jpn. J. KOTAIBUTSURI **4**(1990)51.

3. K. Osamura, N. Matsukura, Y. Kutsumoto, S. Ochiai, B. Ni and T. Matsushita : Jpn. J. Appl. Phys., **29**(1990)L1621.

4. T. Kawai, S. Kawai, S. Tanaka, T. Horiguchi, Y. Miura, S. Takaki, K. Ogura, S. Kambe and M. Kawai: Jpn. J. Appl. Phys, **27**(1988)L2296.

5. R. Sato,T. Komatsu, K. Matsushita and T. Yamashita : Jpn. J. Appl. Phys., **28**(1989)L1922.

6. Y. Kubo, K. Michishita, N. Shimizu, Y. Higashida, H. Yokoyama, Y. Hayami, E. Inukai, A. Saji, N. Kuroda and H. Yoshida

7. T. Ashizawa, S. Shimoda, S. Yamana, K. Sumiya, M. Ishihara and H. Kuwajima : Jpn. J. Appl. Phys., **28**(1989)L1140.

8. B. Ni, T. Munakata, T. Matsushita, M. Iwakuma, K. Funaki, M. Takeo and K. Yamafuji : Jpn. J. Appl. Phys., **27**(1988)1658.

9. A. M. Campbell : J. Phys., **C2**(1969)1492.

10. J. W. Ekin, T. M. Larson, A. M. Hermann, Z. Z. Sheng, K. Togano and H. Kumakura : Physica C **160**(1989)489.

11. S. X. Dou, H. K. Liu, J. Wang and K. H. Song : Physica C **171**(1990)293.

12. Y. Hakuraku, M. Ohara, F. Sumiyoshi and T. Ogushi : Jpn. J. Appl. Phys., **29**(1990)L749.

Chapter 9

Summary

In this thesis, microstructure change and its relation to critical current density have been investigated in detail when two kind of superconducting materials, V_3Ga and Bi-Pb-Sr-Ca-Cu-O high temperature superconductor were fabricated in various conditions. In Chapter 2, crystal growth of V_3Ga compound as well as the relationship between microstructure and critical current density or global pinning force for V_3Ga prepared with addition of Zr and Mg element were investigated. Crystal growth of V_3Ga compound was found to be enhanced by Mg addition and overall growth of V_3Ga compound layer was confirmed to be controlled by bulk diffusion in compound layer. V_3Ga grains tend to columnar and this tendency is enhanced by Mg addition. Critical current density is improved by Mg addition because of increase in elementary pinning force and B_{c2}. The degradation ratio of J_c in high magnetic field becomes small for the long time annealed specimen. In low magnetic field, it was confirmed that global pinning force increased linearly with decreasing grain size.

In Chapter 3, the crystallization process of B(P)SCCO amorphous ceramic which was prepared by melt-quenching method and superconducting property for annealed specimen were investigated. After heat treating $Bi_{1.6}Pb_{0.4}Sr_2Ca_2Cu_3O_x$ amorphous ceramic, superconducting bulk which exhibited 98 K of $T_{c,off}$ could be prepared. It could be confirmed that the 2201 phase and Cu_2O are crystallized in sequence from the amorphous phase during heating. These crystallization occurs at the lower temperatures for the specimens with Pb additive. The 2201 phase changed to 2212 phase with increasing temperature

up to partial melting . Also, it was suggested that the 2212 phase reacts with CuO, and then the liquid appears accompanying with $(Sr, Ca)_3Cu_5O_x$ phase. The 2223 phase could be formed by prolonged annealing at 1123 K.

In Chapter 4, the phase relation and the microstructural features in Bi-Pb-Sr-Ca-Cu-O superconducting ceramics were investigated. Various samples were prepared by sintering at temperatures between 1073 and 1223 K for a long time and quenching into liquid nitrogen. The phase existing at those temperatures have been identified by means of XRD and EPMA. The 2223 phase was found to be formed by the reaction of 2212 phase with the liquid, which is produced eutectically from the 2201 phase and Ca_2PbO_4. It was confirmed that the volume fraction of 2223 phase became largest in the sample sintered at 1128 K, with small amount of impurity phases CuO, $(Sr, Ca)_2CuO_3$ and $(Sr, Ca)_3Cu_5O_x$. The amounts of $(Sr, Ca)_2CuO_3$ and $(Sr, Ca)CuO_x$ phases increased during the decomposition of the 2223 phase at temperatures above 1133 K. The $(Sr, Ca)O_x$ compound was identified as a new phase for the sample sintered at temperatures higher than 1223 K.

In Chapter 5, the microstructure of BPSCCO(2223 phase) superconducting tape prepared by *powder-in-tube technique* in various heat treatment and cooling conditions and its influence to superconducting property were investigated in detail. A refined structure with high volume fraction of 2223 phase was confirmed to be obtained by employing the thermomechanical treatment, compared to bulk conventionally sintered at the same condition. Both superconducting properties, J_c and T_c have been made clear to become best for the heat treatment at 1113 K. Superconducting properties degraded for the specimen heat treated at 1123 K because of appearance of 2201 phase. It was confirmed that the volume fraction of 2223 phase increases during second heat treatment and the preferred orientation of (a-b) plane is improved by repeating TMT cycle. The optimum cooling rate to maximize both $T_{c,off}$ and J_c was found to be typically of 100 K/h.

In Chapter 6, cold working effect on the microstructure and critical current density was investigated when the BPSCCO tapes was prepared by powder-in-tube technique. It was confirmed that J_c increases with decreasing oxide layer thickness and reaches maximum,

but degrades rapidly by further reduction of oxide layer thickness. The increase of J_c is suggested to be mainly attributed to the densification and texturing. It is found that the degradation of J_c is related to the work instability. A correction of J_c was done in the statistical view point by assuming the smallest thickness of oxide layer as the lowest limit of thickness distribution.

Among various cold working techniques which were tried for fabricating Ag sheathed BPSCCO superconducting tape, the pressing turned out to be effective for increasing the critical current density. A dense and textured structure could be obtained for the specimen prepared with higher pressure.

It was confirmed that the magnetic field dependence of J_c and hysteresis effect of J_c – B can be improved by optimizing the cold working condition. The correlation between the sharpness of resistive transition expressed as n value and work instability or J_c was confirmed.

In Chapter 7, the microstructure of BPSCCO tapes which were prepared with various nominal compositions by powder-in-tube technique and its influence on critical current density were investigated. Critical current density of BPSCCO tape was confirmed to depend on the variation of nominal composition. This was considered to be due to volume fraction of 2223 superconducting phase and existence of impurity phase. Ag sheathed BPSCCO tapes prepared with composition of $Bi_{1.6}Pb_{0.4}Sr_{1.6}Ca_{2.0}Cu_{2.8}$ exhibited the highest J_c. When the composition of starting elements was changed from the above one, amount of impurity phases such as CuO, Ca_2PbO_4, $(Sr, Ca)_3Cu_5O_x$ and $(Sr, Ca)_2CuO_x$ was found to increase. 2201 phase could be detected for the specimen $(Bi_{1.6}Pb_{0.4}Sr_{1.6-0.1x}Ca_{2+0.04x}Cu_{2.8+0.06x}O_y)$ with high ratio of Ca and Cu.

In Chapter 8, the influence of Sn, Ba and Mg addition on the superconducting properties of BPSCCO tapes was investigated. For Sn added tapes, the superconducting property was found to be inferior to that of none added tape, because the volume fraction of 2223 phase decreased by Sn addition. On the other hand, the superconducting properties were confirmed to be improved by Ba and Mg addition. This is attributed to

the dense and textured structure by Ba addition or the fine dispersion of Mg particles.

In conclusion, the basic knowledge about the relation between microstructure and superconducting properties has been made clear through the present study. The author believes that this results would be helpful in understanding and further improving the superconducting materials.

List of Publication

1. *Journal of the Japan Institute of Metals*, **52**(1988)886.
"Microstructure and Superconducting Properties of Bronze-processed V_3Ga Compound"(in Japanese)
K. Kawaguchi, S. S. Oh, S. Ochiai and K. Osamura

2. *Journal of the Japan Copper and Brass Research Association*, **27**(1988)127.
"Study on the Diffusion in Crystal Growth of Bronze Processed V_3Ga Compound" (in Japanese)
S. S. Oh, K. Osamura and S. Ochiai

3. *Journal of Materials Science*, **26**(1991)4220.
"Microstructure change during crystallization of amorphous $Bi(Pb) - Sr - Ca - Cu - O$ ceramics"
S. S. Oh and K. Osamura

4. *Supercond. Sci. & Technol*, **3**(1990)143.
"Effect of thermomechanical treatment on the critical current density of Ag-sheathed B(Pb)SCCO tapes"
K. Osamura, S. S. Oh and S. Ochiai

5. *Proceedings of the 2nd International Symposium on the Superconductivity(ISS'89)*, Nov.14-17,1989,Tsukuba Japan edited by T.Ishiguro and K.Kajimura(Spring-Velag) p389.

"Effect of Cold-Working on the Critical Current Density of Ag-Sheathed Bi(Pb)-Sr-Ca-Cu-O Tapes"
S. S. Oh, K. Osamura and S. Ochiai

6. *Physica C*, **171**(1990)265.
"Annealing temperature dependence of the superconducting properties of Ag-sheathed Bi-Pb-Sr-Ca-Cu-O tapes"
S. S. Oh, T. Kubota and K. Osamura

7. *Appl. Phys. Lett.*, (to be submitted)
"Temperature Dependent Critical Current Density of Bi(Pb)-Sr-Ca-Cu-O Tapes in Fields Up To 20 Tesla"
D. P. Hampshire, S. S. Oh, K. Osamura and D. C. Larbalestier

8. *Proceedings of the 3rd International Symposium on the Superconductivity(ISS'90)*, Nov.6-9,1990,Sendai Japan, edited by K. Kajimura and H. Hayakawa(Spring-Velag)p651.
"Composition Dependence of Critical Current Density in Ag sheathed Bi-Pb-Sr-Ca-Cu-O tapes"
S. S. Oh, K. Osamura and S. Ochiai

9. *Journal of Japan Society of Powder and Powder Metallurgy*, **38**(1991)97.
"Microstructure Control and Current Density of Silver Sheathed Oxide Superconducting Tapes" (in Japanese)
K. Osamura and S. S. Oh

10. *Journal of Korea Institute of Metals*, **29**(1991)337.

"Influence of Thermomechanical Treatment on Critical Current Density of Ag Sheathed Ceramic Superconducting Bi-Pb-Sr-Ca-Cu-O Tapes"(in Korean)
S. S. Oh and K. Osamura

11. *Supercond. Sci. & Technol*, **4**(1991)239.
"Temperature Dependence of Phase Relation in the Bi-Pb-Sr-Ca-Cu-O Superconducting Ceramics"
S. S. Oh and K. Osamura

12. *Proceedings of Int. Conf. M²S-HTSC III*, Jul. 22, Kanazawa, Japan(in press)
"Influence of Additive Elements on the Critical Current Density of Ag Sheathed BPSCCO Tapes"
S. S. Oh, M. Kamo and K. Osamura

13. *Supercond. Sci. & Technol.*,(Submitted, 1991)
"Work Instability and Its Influence to Critical Current Density of Silver Sheathed Bi2223 Tapes"
K. Osamura, S. S. Oh and S. Ochiai

14. *Proceedings of the 4th International Symposium on the Superconductivity(ISS'91)*, Oct,1991, Tokyo Japan (in press)
"Microstructure Control and Critical Current Density of Silver Sheathed Bi2223 Tapes"
K. Osamura, S. S. Oh and S. Ochiai

15. *Journal of the Japan Institute of Metals*, (Submitted, 1991)

"Influence of Sn, Ba and Mg Addition on the Superconducting Properties of Ag Sheathed Bi2223 Tapes" (in Japanese)

M. Kamo, S. S. Oh and K. Osamura